DESIGN OF PIEZOELECTRIC GYRO-SENSOR USING

LANTHANUM GALLIUM SILLICATE (La$_3$Ga$_5$SiO$_{14)}$ AND

TEMPERATURE BEHAVIOR OF LANGASITE

By

GOBONG CHOI

A Dissertation submitted to the

Graduate School – New Brunswick

Rutgers, The State University of New Jersey

In partial fulfillment of the requirements

For the degree of

Doctor of Philosophy

Graduate Program in Civil and Environmental Engineering

Written under the direction of

Yook-Kong Yong

And approved by

—————————————

—————————————

—————————————

—————————————

New Brunswick, New Jersey

January 2016

ABSTRACT OF THE DISSERTATION

Design of Piezoelectric Gyro-Sensor Using

Lanthanum Gallium Silicate (La$_3$Ga$_5$SiO$_{14}$) and Temperature Behavior of Langasite

By GOBONG CHOI

Dissertation Director

Yook-Kong Yong

Lanthanum Gallium Silicate (La$_3$Ga$_5$SiO$_{14}$, Langasite, LGS) and its isomorphs are gaining in popularity due to their superior piezoelectric material properties. These materials have similar crystal properties as the quartz crystal, which is widely used in BAW applications such as resonators and piezoelectric vibratory gyroscopes. The langasite and langatate have better stability at high temperatures that have no phase transition up to the melting point at 1475℃ and 1450℃, respectively. Additionally, quartz, langasite, and langatate crystals are trigonal class crystals that belonging to the same point group 32, for which well-known methods of trapping energy of piezoelectric resonator can be easily and accurately applied.

Quartz, langasite and langatate crystals are used for studying and designing piezoelectric vibratory gyroscopes. The three-dimensional finite element models are developed to simulate the characteristic of the vibratory gyroscopes. The piezoelectric double-ended tuning fork gyroscope is used to verify and validate the finite element analysis. The geometric and gyroscopic sensitivity of the finite element models of the quartz doubled-ended tuning fork gyroscope showed the excellent agreement with the

experimental data. The results show that langasite and langatate crystal are more effective than quartz crystal for high precision piezoelectric gyroscopes.

A length-extension vibratory gyroscope is our newly designed gyroscope, which utilizes a length extension mode as a driving mode and a flexure mode as a sensing mode to detect the Coriolis force generated by the rotation of the system. The sizes of the gyroscopes vary due to the material properties and length of the driving arms. The langasite and langatate gyroscopes are nearly the same size and are smaller than the quartz gyroscope. The results show that the newly designed length-extension gyroscope can be used as a gyro-sensor, and that langasite and langatate gyroscopes provide the stronger sensitivity to angular velocity than the quartz gyroscope. The length extension gyroscope is also able to detect the angular velocities about the other two axes(x- and y-axes).

The three-dimensional Langrangian formulations are used to calculate the frequency-temperature behaviors of the langasite. Normally, the piezoelectric effect is ignored in analysis of the quartz crystal due to their weak piezoelectric coupling. The piezoelectric coupling factor of the langasite crystal is much larger than that of the quartz crystal, which cannot be ignored. However, the analysis shows that the piezoelectric effect on the frequency-temperature behavior of langasite is negligible. The study on the temperature behaviors of the langatate cannot be completed, since the third-order non-linear elastic constants have not been published. The results show that no zero-temperature compensated cuts for A- and B- mode exist, while a more than sufficient number of the zero-temperature compensated orientations of langasite for C-mode have been identified. The temperature compensated cuts of langasite for any order higher than the first were not found.

Dedication

I dedicate this dissertation to my family and my wife for

their constant support and unconditional love.

I love you all dearly.

Acknowledgements

Table of Contents

List of Table

List of Figure

Introduction

In 1880, Jacques and Pierre Curie brothers discovered the piezoelectric effect. They found some materials, which generate electrical charges when a mechanical stress was applied. The word "piezo" is a Greek word means "to press or to squeeze" [1]. Therefore, piezoelectric means electricity generated from the pressure. Those piezoelectric materials have asymmetric crystal structure. The piezoelectric materials can be divide into three main categories; crystals, ceramics and thin films [2]. The most well-known and widely used piezoelectric material is quartz crystal (SiO_2).

Ever since micro-electromechanical systems are introduced, the piezoelectric gyro-sensors are dramatically gained the popularly due to its manufacture cost, power consumption and its size. Due to these reasons, the piezoelectric gyro-sensors are widely used in many industries such as automotive, aerospace, telecommunications, consumer electronics and entertainment industries. However, the piezoelectric gyro-sensors have to overcome many technical problems. The problems are related to the performance, complexity of the geometry and shock resistance due to the decrease of the size of the sensors. Quartz crystal gyro-sensors are more durable and have much simple geometry compared to other piezoelectric gyro-sensors based on ceramic piezoelectric materials.

The gyroscopic sensitivity of the gyroscope is one of the most important criteria in the design of gyro-sensor, which directly related to type of material and the geometry of the gyroscope. Quartz and ceramic type piezoelectric materials are widely used material for gyro-sensor. Lanthanum gallium silicate ($La_3Ga_5SiO_{14}$) and lanthanum gallium tantalite ($La_3Ga_{5.5}Ta_{0.5}O_{14}$), also known as langasite and langatate, respectively, are other piezoelectric materials that have same crystal properties as quartz crystal. They all belong

to point group 32 and trigonal class. Langasite and langatate crystals are fairly newer piezoelectric materials, which introduced in early 1980s by Russian scientists. Due to the number of reasons, the crystals are not utilized for any applications until recent years. Both crystals started to get attention after scientist found that they are suitable for high temperature condition and they perform better than quartz crystal due to their piezoelectric material properties. Both langasite and langatate have stronger electro-mechanical coupling factor, heavier mass density and higher temperature frequency coefficient constant than the quartz crystal. These material properties make langasite and langatate gyro-sensors perform superior to quartz gyroscope. The geometry of the gyroscope is also affecting the gyroscopic characteristics which can be analyzed by parametric modal analysis.

In this dissertation work, the langasite and langatate doubled-ended tuning fork gyro-sensor are analyzed and compared with the quartz gyroscope. Design of the gyroscopes and analyses were done using finite element method. The Furthermore, the length extension gyroscopes are introduced and analyzed with the same analysis method. The temperature behavior of the langasite is also analyzed by numerical method. Since, third order non-linear constants of langatate are not published; the temperature analysis on langatate has been omitted.

Thesis Organization:

The work carried out in this dissertation has been organized into six chapters.

- Chapter 1 provides a brief introductory of piezoelectric crystals

- Chapter 2 contains the introductory of piezoelectric vibratory gyroscope and its governing equations. The equations derived in this chapter are used to design and analyze the piezoelectric gyroscopes.

- Chapter 3 consists of evaluating the characteristics of the piezoelectric doubled-ended tuning fork. The finite element analysis is used to analyze the double-ended tuning forks gyro-sensors.

- Chapter 4 includes design of length extension gyroscopes. The gyroscopic and geometric sensitivity analyzes are also includes in this chapter.

- Chapter 5 contains the analysis of temperature nonlinearly behavior of langatate crystal

- Chapter 6 includes the conclusion and future improvement of this dissertation.

Chapter 1. Basics of Piezoelectric Crystals

1.1 Crystal systems and basic terminology

The crystal means a solid in which the atoms are arranged in a single pattern repeated through the body. The crystal atoms are occurring in small groups, all groups being exactly alike, similarly oriented, and regularly aligned in all three dimension. Each group are bounded by a parallelepiped and each parallelepiped can be considered as an ultimate building blocks of crystal. The crystal is formed by stacking the basic parallelepiped without any spaced between them. Such a building block is called a unit cell. Since the choice of a particular set of atoms to form a unit cell is arbitrary, it is evident that there is a wide range of choices in the shape and dimensions of the unit cell. In practice, the unit cell is selected by the symmetry of the crystal and by simply related to the actual crystal faces and X-ray reflections.

In crystallography, the properties of a crystal is represents in terms of natural coordinate system which the axes are indicated by the latter a, b and c. For example, theses axes are equal length and are mutually perpendicular in a cubic crystal while the axes are unequal lengths and no two axes are mutually perpendicular in triclinic crystal. The faces of any crystal are all parallel to the planes whose intercepts on the a, b, and c axis are small multiples of unit distances or infinity, in order that their reciprocals, when multiplied by a small common factor, are all small integers or zero, which represent the indices of the plane. In the orthorhombic, tetragonal, and cubic systems, these faces are normal to a, b and c axes. Even in the monoclinic and triclinic systems, these faces contain, respectively, the b and c, a and c, and a and b axes. As referred to the set of rectangular axes X, Y, Z, these indices are in general irrational except for cubic crystals.

The crystals are commonly classified into seven systems; triclinic, monoclinic, orthorhombic, tetragonal, trigonal, hexagonal, and cubic [3]. The seven systems are further divided into point groups, also known as classes, based on their symmetry with respect to a point. For example, the trigonal crystals all possess a three-fold axis, while those of the tetragonal and hexagonal crystal systems possess a four-fold and six-fold axis, respectively. The cubic crystal groups all have multiple threefold axes. The orthorhombic point groups have two-fold symmetry either 2 or *m* with respect to each of the X-, Y-, Z-directions of an orthogonal axis system, while the monoclinic point groups are limited to two-fold symmetry with respect to a single axis direction. Finally, the triclinic point groups can only have an axis of order 1. Overall, there are total 32-point groups. Table 1.1.1 and 1.1.2 gives the summary of crystal system and provides clarification by identifying the symmetry directions for each crystal system.

Table 1.1.1 Summary of crystal systems [IEEE Standards on Piezoelectricity]

Crystal System		International Point Groups		Axis Identification, Crystallographic			Axis Identification, Rectangular			+/- Axes (Note 3)		Schoenflies Symbol	Example	Formula
		Short	Full	c	a	b	X	Y	Z					
Triclinic	p	1	1					1(010)		Z	X	C_1	Aminoethyl ethanolamine hydrogen *d*-tartrate (AET)	$C_8H_{17}O_7N_2$
$c_0 < a_0 < b_0$; α, β > 90°								1(010)				$C_1(S_2)$	Copper sulfate pentahydrate	$CuSO_4 \cdot 5H_2O$
	p	2	2			2	1(100)	b	c	Y		C_2	Ethylene diamine tartrate (EDT)	$C_6H_{14}N_2O_6$
Monoclinic	p	m	m			/m	1(100)	b	c	Z	X	$C_8(C_{1h})$	Lithium trihydrogen selenite	$LiH_3(SeO_3)_2$
$c_0 < a_0$, β > 90°; α = γ = 90°		2/m	$\frac{2}{m}$				1(100)	b	c			C_{2h}	Gypsum	$CaSO_4 \cdot 2H_2O$
	p	222	222	2	2	2	a	b	c			$D_2(V)$	Rochelle salt, except between Curie points	$NaKC_4H_4O_6 \cdot 4H_2O$
Orthorhombic	p	mm2	mm2	(See Note 1)			(See Note 1)			Z		C_{2v}	Barium sodium niobate	$Ba_2NaNb_5O_{15}$
$c_0 < a_0 < b_0$; α = β = γ = 90°		mmm	$\frac{2}{m}\frac{2}{m}\frac{2}{m}$	2	2	2	a	b	c			$D_{2h}(V_h)$	Barite	$BaSO_4$
Tetragonal $a_0 = b_0$: α = β = γ = 90°				c	a_1	a_2								
	p	4	4	4	†		(a_1)	(a_2)	c	Z		C_4	Potassium strontium niobate	$KSr_2Nb_5O_{15}$
	p				†		(a_1)	(c_2)	c	Z		S_4	Anorthite	$Ca_2Al_2SiO_7$
		4/m	$\frac{4}{m}$	4	†		(a_1)	(a_2)	c			C_{4h}	Scheelite	$CaWO_4$
	p	422	422	4	2	2	(a_1)	(a_2)	c	*		D_4	Nickel sulfate hexahydrate, Paratellurite	$NiSO_4 \cdot 6H_2O$, TeO_2
	p	4mm	4mm	4	/m	/m	(a_1)	(a_2)	c	Z		C_{4v}	Barium titanate	$BaTiO_3$
	p	2m	2m		2	2	(See Note 2)			Z		$D_{2d}(V_d)$	Ammonium dihydrogen phosphate (ADP)	$NH_4H_2PO_4$
		4/mmm	$\frac{4}{m}\frac{2}{m}\frac{2}{m}$	4	2	2	(a_1)	(a_2)	c	*		D_{4h}	Zircon	$ZrSiO_4$
Trigonal $(a_0)_1 = (a_0)_2 = (a_0)_3$				c	a_1	a_2	a_3			Any two				
Trigonal	p	3	3	3	†			(a_1)		c			C_3	Sodium periodate trihydrate	$NaIO_4 \cdot 3H_2O$
$(a_0)_1 = (a_0)_2 = (a_0)_3$					†			(a_1)		c			$C_{3i}(S_6)$	Dolomite	$CaCo_3MgCO_3$
	p	32	32	3	2	2	2	(a_1)		c	X		D_3	α-quartz	SiO_2
	p	3m	3m	3	/m	/m	/m	(a_1)		c	Z	Y	C_{3v}	Lithium niobate	$LiNbO_3$

Crystal System		International Point Groups		Axis Identification, Crystallographic			Axis Identification, Rectangular			+/- Axes (Note 3)		Schoenflies Symbol	Example	Formula
		Short	Full	c	a	b	X	Y	Z					
(See 2.2.5)		m	$\bar{3}\frac{2}{m}$		2	2	2	(a_1)		c			D_{3d}	Calcite	$CaCO_3$
Hexagonal	p	6	6	6	†			(a_1)		c	Z		C_6	Lithium iodate	$LiIO_3$
$(a_0)_1 = (a_0)_2 = (a_0)_3$ (See 2.2.5)	p				†			(a_1)		c	X	Y	C_{3h}	Lithium peroxide	Li_2O_3
		6/m	$\frac{6}{m}$	6				(a_1)		c			C_{6h}	Apatite	$CaF_2, 3Ca_3P_2O_8$
	p	622	622	6	2	2	2	(a_1)		c			D_6	β-quartz	SiO_2
	p	6mm	6mm	6	/m	/m	/m	(a_1)		c	Z		C_{6v}	Cadmium sulfide	CdS
	p	m2	m2		2	2	2	(a_1)		c	X		D_{3h}	Benitoite	$BaTiSi_3O_9$
		6/mmm	$\frac{6}{m}\frac{2}{m}\frac{2}{m}$	6	2	2	2	(a_1)		c			D_{6h}	Beryl	$3BeO \cdot Al_2O_3 \cdot 6SiO_2$
Cubic $a_0 = b_0 = c_0$; α = β = γ = 90°				a_1	a_2	a_3								
Cubic	p	23	23	2	2	2	(a_1)	(a_2)	(a_3)	Z		T	Bismuth germanium oxide	$Bi_{12}GeO_{20}$
		m3	$\frac{2}{m}\bar{3}$	2	2	2	(a_1)	(a_2)	a_3	*		T_h	Pyrite	FeS_2
		432	432	4	4	4	(a_1)	(a_2)	a_3	*		O	Cadmium fluoride	CdF_2
	p	3m	3m				(a_1)	(a_2)	(a_3)	Z		T_d	Gallium arsenide	$GaAs$
		m3m	$\frac{4}{m}\bar{3}\frac{2}{m}$	4	4	4	(a_1)	(a_2)	(a_3)	*		O_h	Sodium chloride	$NaCl$

Significant Symmetry Directions for the International (Hermann-Mauguin) Symbol[*]

Crystal System	First Symbol	Second Symbol	Third Symbol
Triclinic	None		
Monoclinic	b (1)		
Orthorhombic	a (1)	b (1)	c (1)
Tetragonal	c (1)	a (2)	[110] (2)
Trigonal	c (1)	a (3)	
Hexagonal	c (1)	a (3)	Digonal (3) [1010 axis]
Cubic	a (3)	[111] (4)	[110] (6)

*The number after each direction indicates the multiplicity of that direction in the crystal.

Table 1.1.2 Symmetry direction for each crystal system [IEEE Standards on

Piezoelectricity]

1.2 Trigonal class piezoelectric material

The primary piezoelectric materials of interest in this dissertation are quartz, langasite and langatate, which all have a trigonal system [4] [5]. The trigonal system is one of the seven crystal systems in crystallography. Crystallography is the branch of the science of determining the arrangement of the atoms in the crystalline solid. Although quartz, langasite and langatate belong to the trigonal system, their unit cells are hexagonal. The Bravais-Miller system is often used to specify the hexagonal crystal system. This is the only crystal system that has a four-axis coordinate system as shown in figure 1.2.1   The system consist with three equivalent secondary axes, *a1*, *a2* and *a3*, that are of equal length to each other of 120 degrees in a plane normal to *c*. These axes are either perpendicular to a plane of symmetry parallel to a two-fold axis or if there are neither two-fold axes perpendicular to *c* not plane of symmetry parallel to *c*, the a axes become the smallest unit cell. The *x*-axis coincides in direction and sense with any one of *a* axes. The z-axis is parallel to c and the *y*-axis is perpendicular to z- and *x*-axis, which form a right-handed coordinate system. Positive-sense rules for +Z, +X, +Y are listed in Table 1.2.1 for the trigonal and hexagonal system crystals. In addition, the quartz, langasite and langatate are belongs to the 32 symmetry classes which have a 3 fold rotational symmetry on one and a two-fold rotational symmetry on another axis.
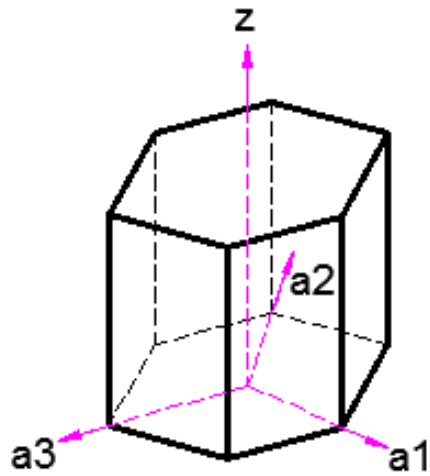
(a) Bravais-Miller system
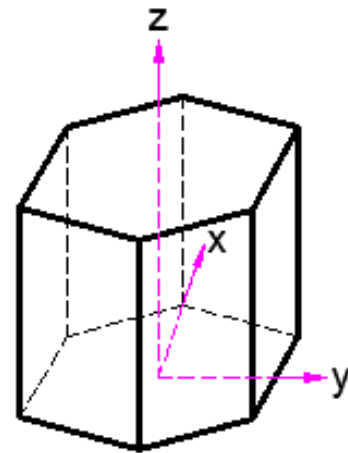
(b) Rectangular Coordinate system

Figure 1.2.1 Bravais-Miller system
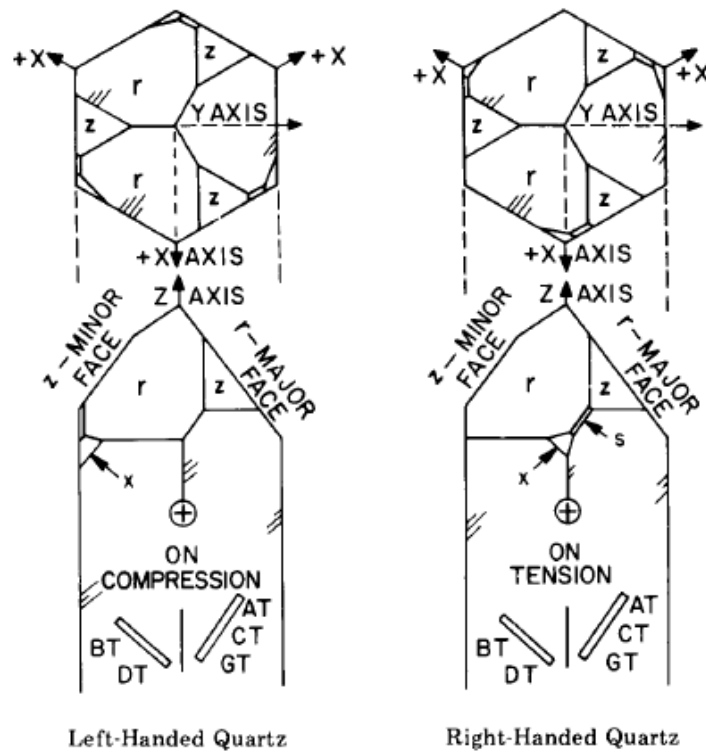
Figure 1.2.2 Left and Right-handed quartz crystals, Trigonal class 32 [IEEE

Standards on Piezoelectricity]

Class	+Z	+X	+Y
3	Positive d_{33}	Positive d_{11}	Form right-handed system
32	Arbitrary	Positive d_{11}	Form right-handed system
3m	Positive d_{33}	Form right-handed system	Positive d_{22}
6	Positive d_{33}	Arbitrary	Form right-handed system
	Form right-handed system	Positive d_{11}	Positive d_{22}
622	Arbitrary	Arbitrary	Form right-handed system
6mm	Positive d_{33}	Arbitrary	Form right-handed system
6m2	Arbitrary	Positive d_{11}	Form right-handed system

Table 1.2.1 Positive sense rules for Z, X, and Y for trigonal and hexagonal crystals

[IEEE Standards on Piezoelectricity]

1.3 Governing Equations of Piezoelectricity

The governing equations of linear and non-linear piezoelectricity are listed in this section [6] [7] [8]. These equations are implemented in COMSOL Multiphysics finite element analysis software and Matlab to analyze the gyroscopes and study the frequency-temperature behavior of langasite crystal in succeeding chapters.

1.3.1 Linear Piezoelectricity

Strain-displacement relation

$$\varepsilon_{ij} = \frac{1}{2}\left(u_{i,j} + u_{j,i}\right) \tag{1.3.1}$$

Equation of motion

$$T_{ij,j} = \rho \ddot{u}_j \tag{1.3.2}$$

$$T_{ij} = T_{ij} \tag{1.3.3}$$

Electric field-potential relation

$$E_i = -\emptyset_{,i} \tag{1.3.4}$$

Electrostatic

$$D_{i,i} = 0 \tag{1.3.5}$$

Constitutive equations

$$T_{ij} = c_{ijkl}^E \varepsilon_{kl} - e_{kij} E_k + \eta_{ijkl} \dot{\varepsilon}_{kl} \tag{1.3.6}$$

$$D_i = e_{ikl} \varepsilon_{kl} + \epsilon_{ik}^S E_k \tag{1.3.7}$$

Where T_{ij} is the Cauchy stress tensor, u_i is the component of displacement, ε_{ij} is the lagrangian strain tensor, ρ is the mass density of the material and D_i is the electric displacement. E_i is the electric field, $\emptyset$ is the electric potential, c_{ijkl}^E is the elastic moduli of an anisotropic body, e_{ikl} is the piezoelectric constant describing the effect of an electric

field on the mechanical stress, ϵ_{ik}^S is the dielectric permittivity and η_{ijkl} is the viscoelastic constant.

1.3.2 Non-linear Piezoelectricity

Strain-displacement relation

$$\varepsilon_{ij} = \frac{1}{2} \left(u_{i,j} + u_{j,i} + u_{i,k}u_{k,j} \right) \tag{1.3.8}$$

Equation of motion

$$(T_{ij} + T_{jk}u_{i,k})_{,j} = \rho \ddot{u}_j \tag{1.3.9}$$

$$T_{ij} = T_{ij} \tag{1.3.10}$$

Electric field-potential relation

$$E_i = -\emptyset_{,i} \tag{1.3.11}$$

Electrostatic

$$D_{i,i} = 0 \tag{1.3.12}$$

Constitutive equations

$$T_{ij} = (C_{ijkl} + C_{ijklmn}\varepsilon_{nm} - e_{ijklm}E_m)\varepsilon_{kl} - (e_{ijklmn}\varepsilon_{kl})E_m + \eta_{ijkl}\dot{\varepsilon}_{kl} \tag{1.3.13}$$

$$D_i = \left(-e_{ikl} - e_{ijklm}\varepsilon_{mj} \right)\varepsilon_{kl} + (\epsilon_{mi}^\varepsilon + \beta_{mki}^\varepsilon E_k)E_m \tag{1.3.14}$$

where e_{ijklm} is the nonlinear piezoelectric constants and β_{mki}^ε is the electro-optical coefficients. The constitutive equation can be written in different forms, which listed in Appendix B. The stress-charge form of the piezoelectric constitutive equations, shown in equation 1.3.13 and 1.3.14 are implemented in finite element analysis.

Chapter 2. Microelectromechanical System (MEMS) Piezoelectric Vibratory Gyroscopes

2.1 Introduction

The vibratory gyroscope is a device, which utilizes the Coriolis force to measure the changes in angular momentum or angular velocity. The Coriolis force is generates by Coriolis affect, which only be seen in rotating non-inertial reference frame.

French physicist Leon Foucault introduced the gyroscope in 1852. He named a gyroscope combining two Greek words "gyro" meaning rotation and "skopeein" meaning to see. The earlier mechanical gyroscope consists of a spinning wheel that is suspended by three gimbals. However, the mechanical gyroscope has many disadvantages such as wear and bearing friction. Modern vibratory gyroscope eliminated these problems by removing the rotating parts.

There are many different types of vibratory gyroscopes in the current market. Wine-glass resonator/hemisphere resonator gyroscopes, cylindrical resonator gyroscope (CRG), tuning fork gyroscope and vibrating wheel gyroscope/disk resonator gyroscope (DPG) are the most widely used and well known vibratory gyroscopes. Alternately, optical gyroscopes such as fiber-optic gyroscope and ring laser gyroscope are available for high performance applications. Due to the high price of the optical gyroscopes, it can only be used for high performance applications. Inertial navigation and guidance system, radar sensors and structural health monitoring are the example of aerospace industry applications. A wide range of consumer electronics and entertainment industries

applications include stabilization in digital camera, smartphone and motion sensor for game console.

   Microelectromechanical Systems (MEMS) is based on photo-lithography technology. In order to be consider as MEMS, it has to be in micrometer scale with electrical and mechanical functions. MEMS technologies became more desirable for many applications because of its lightweight, miniature size and manufacture cost.
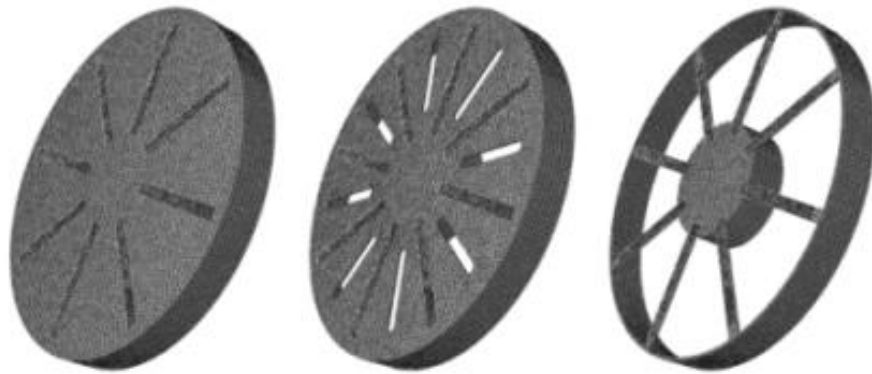
Figure 2.1.1 Schematic diagrams of the cylindrical gyroscopes [9].
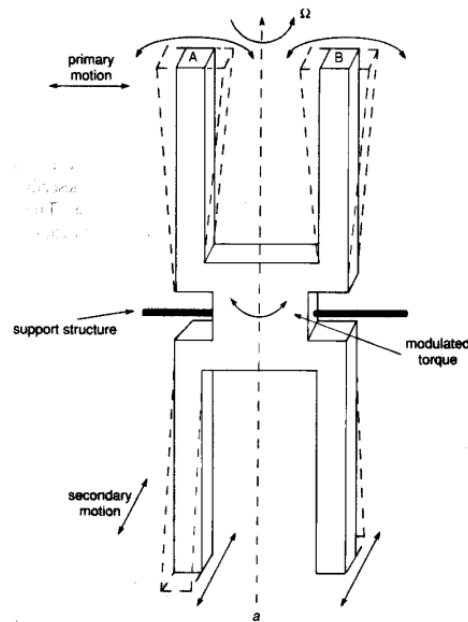
Figure 2.1.2 Schematic diagram of double tuning fork gyroscope [10].
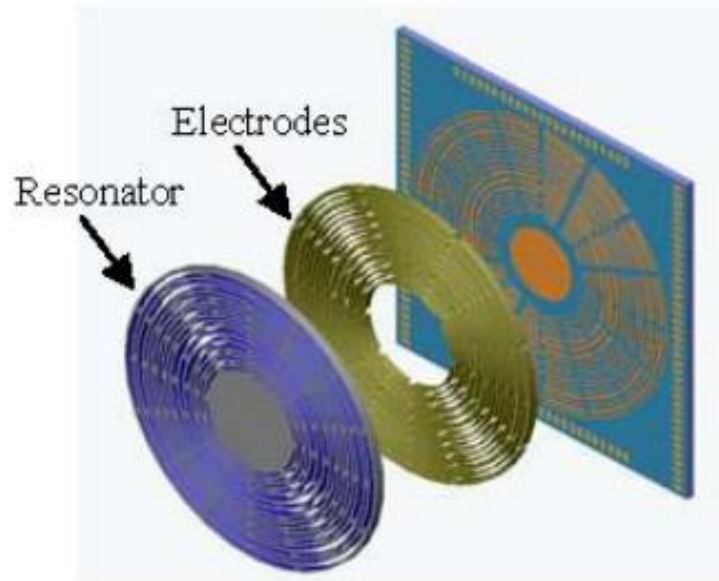
Figure 2.1.3 Schematic diagram of disk resonator gyroscope [11].

2.2   Dynamics of Vibratory Gyroscopes

The fundamental equations of the vibratory gyroscope are developed in this chapter. The simple theoretical gyroscope is comprised of a driving-mode oscillator, sensing-mode detector and the proof mass. The driving mode oscillator comprises of proof mass which oscillating in the driving direction at driving resonant frequency and it is suspended by suspension system.

The sensing mode accelerometer is comprises of proof mass suspended by suspension system. It allows the proof mass to oscillate in the sensing direction, which is perpendicular to the driving direction. The Coriolis force is generated in the sensing direction when the gyroscope is subjected to an angular rotation. The sense electrodes detect the change in angular momentum and output the signal.
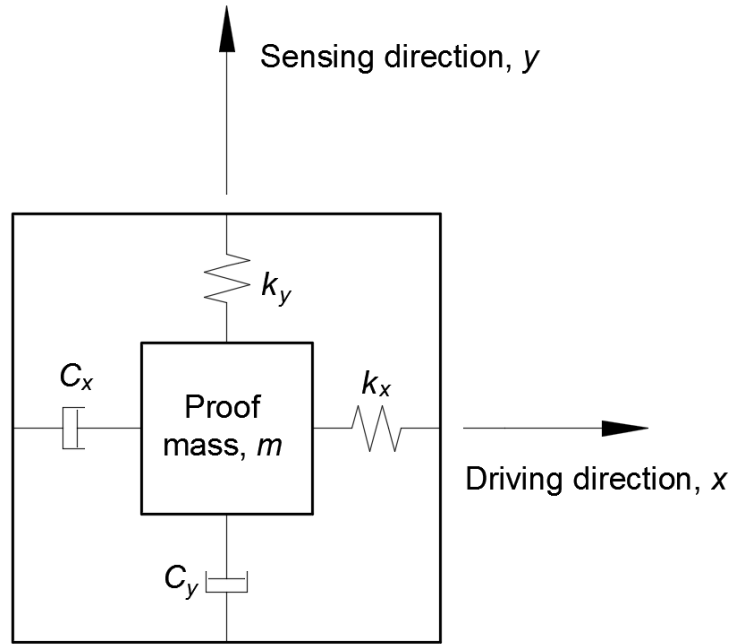
Figure 2.2.1 A structure of the simplified 2-D.O.F vibratory gyroscope.

A simple theoretical z-axis gyroscope, shown in figure 2.2.1, is used to illustrate the dynamics and operational principles of the vibratory gyroscope. The gyroscope subjected to rotation about z-axis is considered. The equation of the motion of the vibratory gyroscope can be derived by taking second time derivative of the position vector [1].

The equations of the motion of the moving body in a rotating reference frame consist of following definitions:

A : Inertial frame

B : Rotating reference frame

$\mathbf{r}_A$: Position vector relative to inertial frame A

$\mathbf{r}_B$: Position vector relative to inertial frame B

$\mathbf{v}_A$: Velocity vector relative to inertial frame A, $\mathbf{v}_A = \dot{\mathbf{r}}_A$

$\mathbf{v}_B$: Velocity vector relative to inertial frame B, $\mathbf{v}_B = \dot{\mathbf{r}}_B$
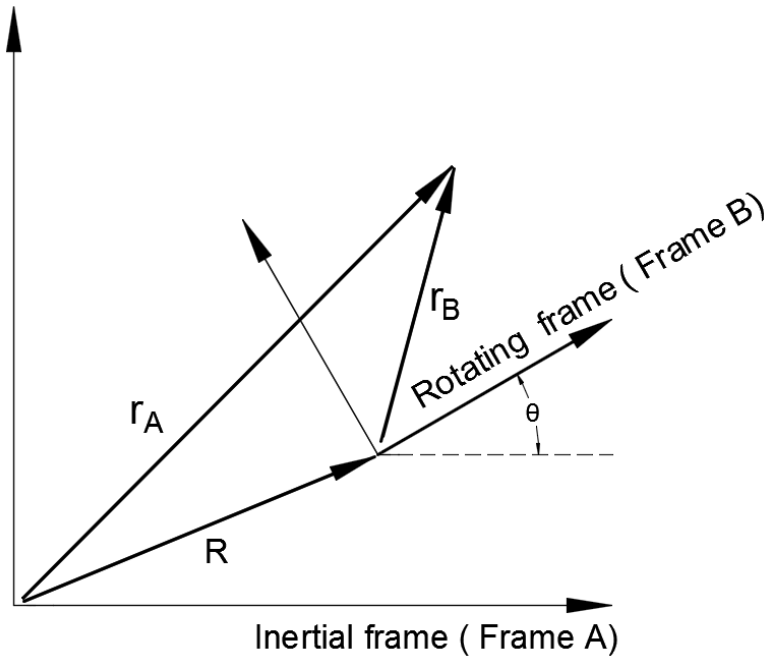
Figure 2.2.2 Illustration of the position vector relative to the inertial reference frame and the rotating reference frame.

$\mathbf{a}_A$: Acceleration vector relative to inertial frame A, $\mathbf{a}_A = \dot{\mathbf{v}}_A = \ddot{\mathbf{r}}_A$

$\mathbf{a}_B$: Acceleration vector relative to inertial frame B, $\mathbf{a}_B = \dot{\mathbf{v}}_B = \ddot{\mathbf{r}}_B$

Θ: Orientation vector of rotating reference frame relative to inertial frame

Ω: Angular velocity vector of rotating reference frame, $\Omega = \dot{\theta}$

R: Position vector of rotating frame

By taking the second time derivative of the position vector, the equations of the motions of moving body in a rotating frame is obtained and they are given as

$$\mathbf{r}_A(t) = \mathbf{R}(t) + \mathbf{r}_B(t) \tag{2.2.1}$$

$$\dot{\mathbf{r}}_A(t) = \dot{\mathbf{R}}(t) + \dot{\mathbf{r}}_B(t) + \dot{\theta} \times \mathbf{r}_B(t) \tag{2.2.2}$$

$$\ddot{\mathbf{r}}_A(t) = \ddot{\mathbf{R}}_A(t) + \ddot{\mathbf{r}}_B(t) + \dot{\theta} \times \dot{\mathbf{r}}_B(t) + \dot{\theta} \times (\dot{\theta} \times \mathbf{r}_B(t)) + \ddot{\theta} \times \mathbf{r}_B(t) + \dot{\theta} \times \dot{\mathbf{r}}_B(t)$$

$$(2.2.3)$$

The figure 2.2.2 represent the position vector relative to the inertial frame A and the rotating frame. Equation 2.2.3 can be reduced by writing the equation in terms of velocity vector, $\mathbf{v}$, acceleration vector, $\mathbf{a}$, and linear acceleration of the reference frame B, $\mathbf{A}$ and is it given as

$$\mathbf{a}_A = \mathbf{A} + \mathbf{a}_B + \dot{\Omega} \times \mathbf{r}_B + \Omega \times (\Omega \times \mathbf{r}_B) + 2\,\Omega \times \mathbf{v}_B \qquad (2.2.4)$$

Above equation 2.2.4 can be divided into three parts where first three terms are the local acceleration, $\mathbf{A} + \mathbf{a}_B + \dot{\Omega} \times \mathbf{r}_B$, following two terms are centripetal acceleration, $\Omega \times (\Omega \times \mathbf{r}_B)$, and last two terms are the Coriolis acceleration, $2\,\Omega \times \mathbf{v}_B$. The Coriolis acceleration only appears in the rotating reference frame. We can further simplify the equation by multiplying the mass with the equation 2.2.4 to find the equation of the motion of the proof mass moving with the rotating frame reference frame and it is shown as

$$\mathbf{F}_{ext} = m\,[\mathbf{A} + \mathbf{a}_B + \dot{\Omega} \times \mathbf{r}_B + \Omega \times (\Omega \times \mathbf{r}_B) + 2\,\Omega \times \mathbf{v}_B] \qquad (2.2.5)$$

where $\mathbf{F}_{ext}$ is the total external force applied on the proof mass, m is the proof mass, A is the linear acceleration and $\mathbf{v}_B$ and $\mathbf{a}_B$ are the velocity and acceleration vectors of the proof mass with respect to the reference frame.

In a simple theoretical z-axis gyroscope, the proof mass is allow to move in two principle oscillation directions which are the driving direction along the x-axis and the sense direction along the y-axis as shown in figure 2.2.1. The schematic diagram of the 2-DOF vibratory gyroscope in rotating reference frame rotation with respect to the inertial frame is shown in figure 2.2.3. The equations of the motion along the drive and sense

directions, which shown in equation 2.2.6, can be written by decomposing the motion of the proof mass into the two principle oscillation directions and neglecting the linear acceleration.

$$m\ddot{x} + c_x\dot{x} + (k_x - m(\Omega_y{}^2 + \Omega_z{}^2))x + m(\Omega_x\Omega_y - \dot{\Omega}_z)y = \tau_x + 2m\Omega_z\dot{y}$$

$$m\ddot{y} + c_y\dot{y} + (k_y - m(\Omega_x{}^2 + \Omega_z{}^2))y + m(\Omega_y\Omega_y + \dot{\Omega}_z)x = \tau_y - 2m\Omega_z\dot{x}$$

$$(2.2.6)$$

where c_x and c_y are the damping coefficient in the drive direction and sense direction, k_x and k_y are the spring constant in the drive direction and sense direction and $\dot{\Omega}_z$ is the angular acceleration rotation about z-axis. τ_x is the external harmonic excitation force that drives the proof mass, *m*, at the driving resonant frequency in the drive direction and τ_y is the total external force which comprise of parasitic and external inertial forces in the sense direction. Finally, $2m\Omega_z\dot{y}$ and $2m\Omega_z\dot{x}$ are the Coriolis terms applied to the proof mass induced by rotation of rotating reference frame with respect to inertial frame.

Equation 2.2.6 can be further simplified by assuming a constant angular rate, $\dot{\Omega}_z = 0$ and angular rate is much lower that driving resonant frequency which $\Omega_x{}^2, \Omega_y{}^2$ and $\Omega_y\Omega_y$ become negligible. In addition, the term $2m\Omega_z\dot{y}$ become negligible since sense-mode Coriolis force response is much smaller than drive-mode motion. Therefore, the simplified equations motion of 2 degrees of freedom vibratory gyroscope are

$$m\ddot{x} + c_x\dot{x} + k_xx = \tau_x$$

$$m\ddot{y} + c_y\dot{y} + k_yy = \tau_y - 2m\Omega_z\dot{x} \qquad (2.2.7)$$

The first equation of equation 2.2.7 represents the equation of motion in drive direction while the second equation of equation 2.2.7 represents the equation of motion in sense

direction. The second term of right hand side of the second equation of equation 2.2.7 is the practical Coriolis applied on the gyroscope that is proportional to the angular rate.
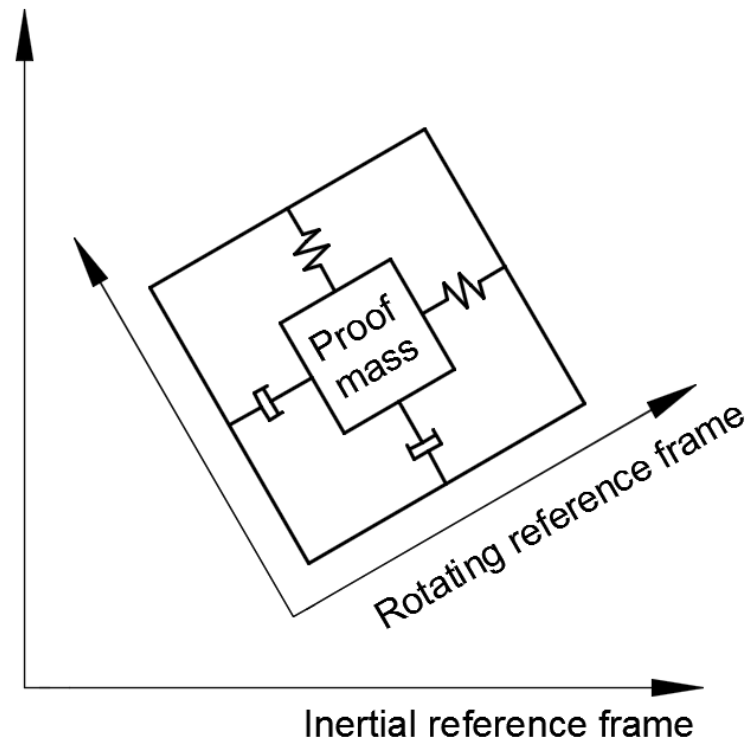
Figure 2.2.3 The schematic diagram of the 2-DOF vibratory gyroscope in rotating

reference frame rotation with respect to the inertial frame.

2.3   Drive-Mode

The vibratory gyroscope requires the momentum to detect the Coriolis force. Moment is usually generated by 1-D.O.F resonator or oscillator. The equation of motion of 1-DOF resonator along the x-axis given as

$$m\ddot{x} + c\dot{x} + kx = F(t) \tag{2.3.1}$$

If resonator generates the harmonic excitation force, $F = F_0 \sin \omega t$, the equation 2.8 can be rewritten as

$$m_d\ddot{x} + c_d\dot{x} + k_d x = F_d \sin \omega t \tag{2.3.2}$$

where m_d is drive mass proof, c_d is the viscous and thermoelastic damping and k_d is the drive-mode suspension stiffness and ω is the angular frequency. The steady state the response of above equation is

$$x = x_0 \sin(\omega t + \emptyset_d) \tag{2.3.3}$$

where x_0 is the amplitude and ϕ_d is the phase of the drive-mode stead state response.

$$x_0 = \frac{F_d}{k_d \sqrt{\left[1 - \left(\frac{\omega}{\omega_d}\right)^2\right]^2 + \left[\frac{1}{Q_d}\frac{\omega}{\omega_d}\right]^2}} \tag{2.3.4}$$

$$\emptyset_d = -\tan^{-1} \frac{\frac{1}{Q_d}\frac{\omega}{\omega_d}}{1 - \left(\frac{\omega}{\omega_d}\right)^2} \tag{2.3.5}$$

$$\omega_d = \sqrt{\frac{k_d}{m_d}} \tag{2.3.6}$$

$$Q_d = \frac{m_d \omega_d}{c_d} \tag{2.3.7}$$

where the ω_d is the drive-mode resonant frequency. Q_d is the drive-mode Quality factor, which defined as maximum ratio of the amplitude to the static deflection. The gyroscopic sensitivity of the gyroscope is directly proportional to the drive-mode oscillation amplitude, which directly scale the quality factor Q. Therefore, the gyroscopes are usually

operate at the drive resonant frequency. The phase at the resonant become -90 and the amplitude at the resonant is

$$x_{0_{res}} = Q_d \frac{F_d}{m_d \omega_d^2} \qquad (2.3.8)$$

2.4 Coriolis Response

In a vibratory gyroscope, the Coriolis force, Fc, is generated by the resonator which driving at the drive-mode resonant frequency. The equations of the motion of Coriolis response in the sense-mode direction can be derived by considering the system which drive-mode operates at drive resonant frequency, ω_d, with the drive motion regulated to be in sinusoidal form as shown in equation 2.4.1.

$$x = x_0 \sin(\omega_d t + \emptyset_d) \qquad (2.4.1)$$

$$\dot{x} = x_0 \omega_d \sin(\omega_d t + \emptyset_d) \qquad (2.4.2)$$

$$Fc = -2m_c \Omega_z \dot{x} = -2m_c \Omega_z x_0 \omega_d \cos(\omega_d t + \emptyset_d) \qquad (2.4.3)$$

where m_c is the part of the proof mass that contributed to Coriolis force. Considering sense-mode oscillator is also 1-DOF, the equation of motion in y-axis is

$$m_s \ddot{y} + c_s \dot{y} + k_s y = Fc \qquad (2.4.4)$$

By substituting equation 2.4.3 into equation 2.4.4, the equation of motion of the 1-DOF sense-mode oscillator in y-axis become

$$m_s \ddot{y} + c_s \dot{y} + k_s y = -2m_c \Omega_z x_0 \omega_d \cos(\omega_d t + \emptyset_d) \qquad (2.4.5)$$

where m_s is the part of proof mass that responds to the Coriolis force. In single-mass vibratory gyroscope system, m_c, m_s and m_d are equal. Similar to the drive-mode, amplitude and phase of the sense-mode response can be found as

$$y_0 = \Omega_z \frac{m_c \omega_d}{m_s \omega_s^2} \frac{2x_0}{k_d \sqrt{\left[1-\left(\frac{\omega_d}{\omega_s}\right)^2\right]^2 + \left[\frac{1}{Q_s}\frac{\omega_d}{\omega_s}\right]^2}} \qquad (2.4.6)$$

$$\varnothing_s = -\tan^{-1} \frac{\frac{1}{Q_s}\frac{\omega_d}{\omega_s}}{1-\left(\frac{\omega_d}{\omega_s}\right)^2} + \varnothing_d \qquad (2.4.7)$$

where

$$\omega_s = \sqrt{\frac{k_s}{m_s}} \qquad (2.4.8)$$

$$Q_s = \frac{s\omega_s}{c_s} \qquad (2.4.9)$$

The ω_s is sense-mode resonant frequency and Q_s is the sense-mode Quality factor. The phase at the sense-mode resonant frequency is -90$^\text{o}$ and the amplitude at the sense-mode resonant is

$$y_{0_{res}} = \Omega_z \frac{2Q_s x_0 m_c}{m_s \omega_s} \qquad (2.4.10)$$

Achieving the higher gyroscopic sensitivity is the most important criteria in designing a gyroscope. In order to get the maximum gyroscopic sensitivity, most of the gyroscope operates at peak or near the peak of the sense-mode resonance frequency, as illustrated in figure 2.4.1. This technical is called mode-matching. When the drive-mode resonant frequency gets closer to the sense-mode resonant frequency, the sense-mode amplitude increases dramatically. Even though matching the drive-mode and sense-mode enhance the gyroscopic sensitivity, but it makes the system unstable and shifts the resonant frequencies. Gyroscopic sensitivity can be also improve by increasing the drive-mode oscillation amplitude and increasing the quality factor Q by decreasing damping. Figure 2.4.2 and 2.4.3 illustrate how quality factor affects the sensitivity of the gyroscope. We can consider the system operating at resonant frequency of ω=1000 kHz and assume that

the drive-mode and sense-modes are mode-matched. If sense-mode is shift by 5 kHz from the resonant frequency, the gain drops by 29% when $Q = 1000$. For the same system with the higher quality factor, $Q = 10,000$, the gain drops by 90%. It is clear shows that the higher gyroscopic sensitivity can be achieve by increase of quality factor; however, the system become very sensitive. In addition, maximizing the mass m_c and minimizing m_s enhance the performance of the gyroscope [1].
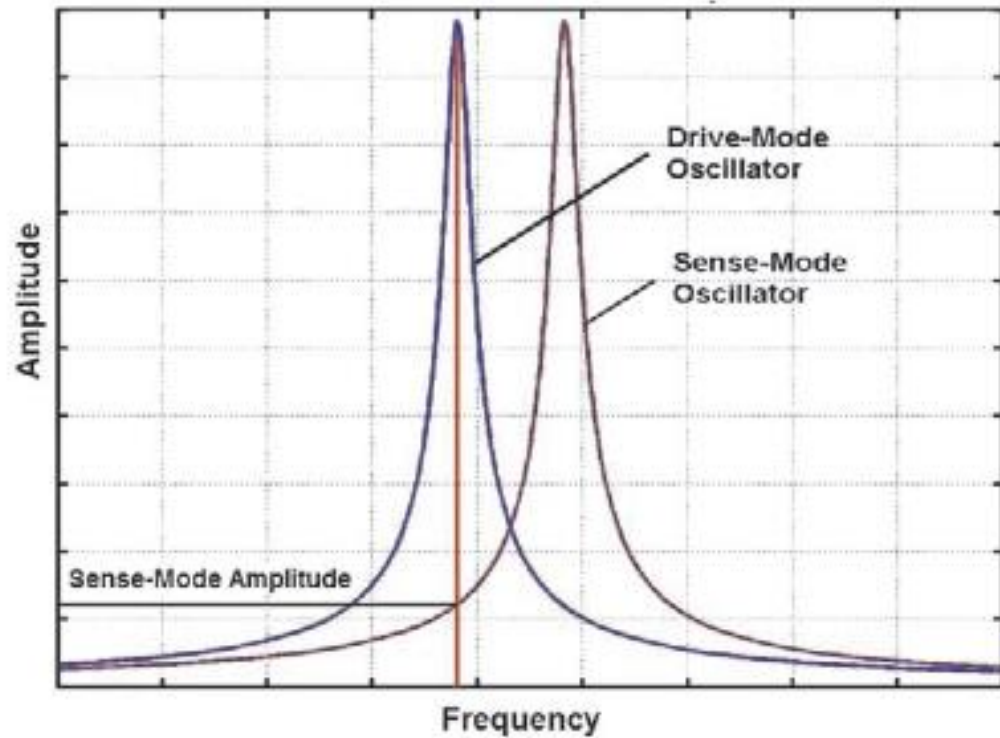
Figure 2.4.1 Drive and sense mode response of the gyroscope [1].
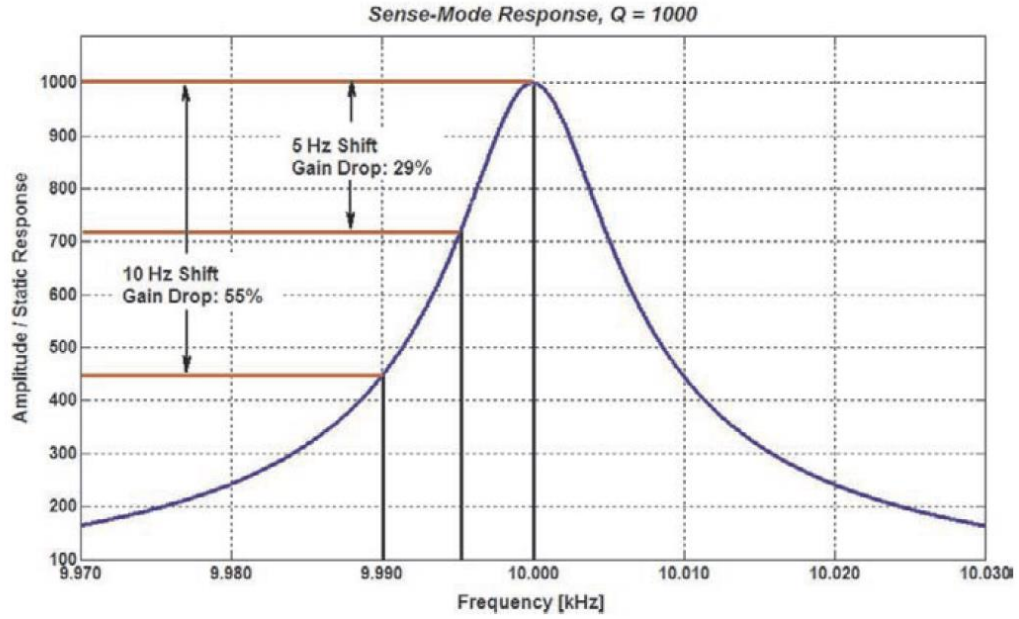
Figure 2.4.2 Sense mode response of the gyroscope at a resonant frequency of $\omega_s=10$

kHz and a $Q=1000$ [1].
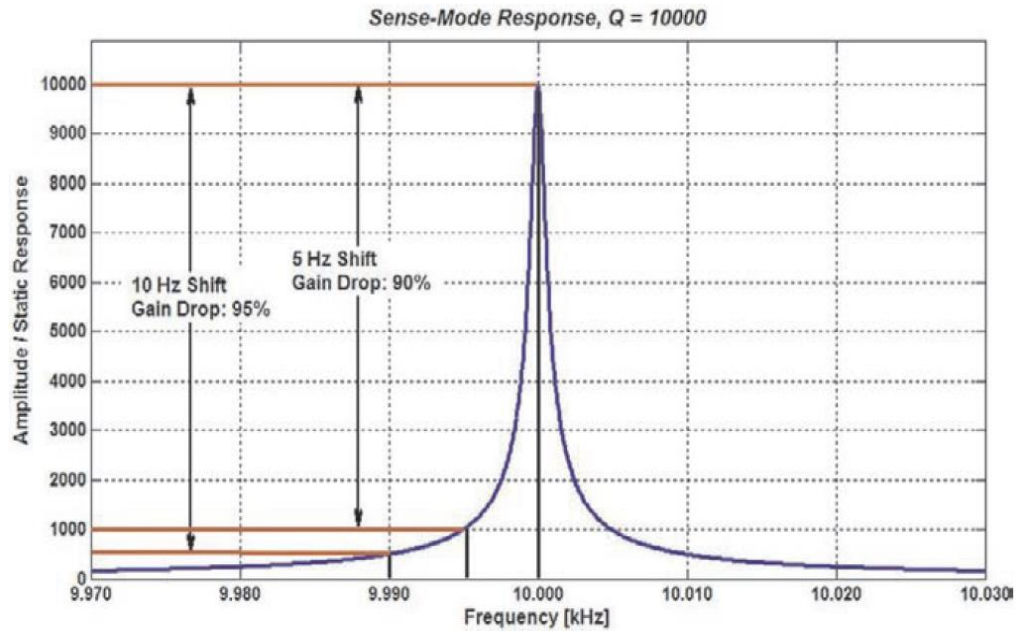
Figure 2.4.3 Sense mode response of the gyroscope at a resonant frequency of $\omega_s=10$

kHz and a $Q=10,000$ [1]

Chapter 3. Piezoelectric doubled-ended tuning fork gyroscope

3.1   Introduction

The finite element analysis has been used to design the gyroscopes for many years and they are very accurate [12]. In this chapter, the piezoelectric double-ended tuning fork gyroscope, which designed by Sato, Ono, and Tomikawa [13] [14] [15] and [16], will be analyze by finite element analysis. A piezoelectric double-ended tuning fork gyroscope has many advantages such that it can be easily manufacture due to its small size and simple geometry, it is very durable and reliable under external shock since it is made of a single quartz crystal and it has stable vibration characteristic [13]. Moreover, the gyro-sensor has flatly supports at each ends that make the tight support. Even though the gyroscope can detect the dual axis, y- and z-axes rotation, we only looked at z-axis rotation for most of this chapter. The first part of this chapter is to study the geometric the gyroscopic characteristics of gyroscope. In the second part of this chapter, the mounting and support structure will be investigate. Furthermore, we analyze the langasite and langatate double-ended tuning fork gyroscopes in addition to the quartz double-ended tuning fork gyroscope. The langasite and langatate gyroscopes will have higher gyroscopic sensitivity than quartz gyroscope due to their higher electromechanical coupling coefficient and mass density [17] [18]. Since langasite and langatate have same crystal class as quartz, the well-known methods of trapping energy of resonator can be easily and accurately applied [19] [20]. The material properties of the langasite, langatate and quartz are listed in Appendix C.

3.2 Structure of the double-ended tuning fork gyroscope

A single rotated z-cut quartz, langasite and langatate crystals are used for a double-ended tuning fork gyroscopes. The schematic diagrams of the piezoelectric double-ended tuning fork gyroscope and electrodes configuration diagram are shown in figure 3.2.1. The gyroscope is axisymmetric about both x- and y-axis. It is comprised of three main components and the mounting support. The first main component is driving arms located at the center of the gyroscope where it includes the driving electrodes. The second main component is the z-axis detecting parts that are located between the base and the driving arms. The last component is the supporting bases that are located at each end of the sensor and they are fixed with silicone rubber adhesive. Dimensions of the main components of gyroscope are listed in table 3.2.1.
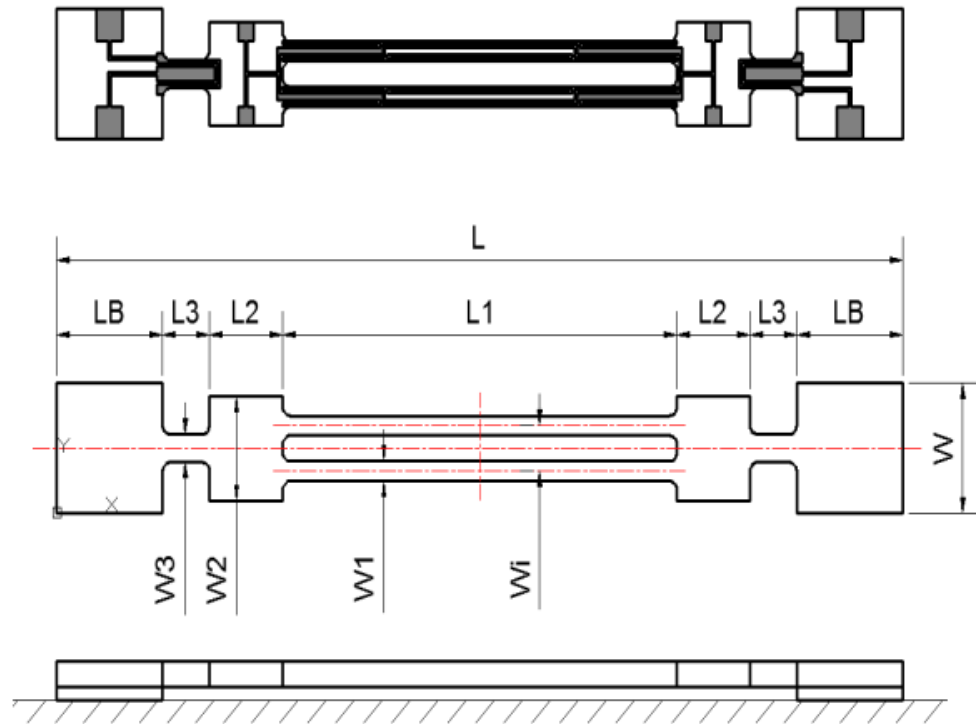
Figure 3.2.1 Structure of a double-ended tuning fork gyroscope.

Table 3.2.1 Dimensions of the double-ended tuning fork gyroscope

Component	Dimension	Component	Dimensions
L	16.0	W	2.00
L1	7.46	W1	0.31
L2	1.38	W2	1.60
L3	0.89	W3	0.451
LB	2.00	Wi	0.75
t Silicon rubber	0.03	t	0.30

Unit:*mm*

3.3 Principle of Operation of Piezoelectric Double-Ended Tuning Fork Gyroscope

The principle of operation of piezoelectric double-ended tuning fork gyroscope is shown in figure 3.3.1. It shows the two modes of vibrations that are used by the gyroscope to detect the angular velocity about *z*-axis. The driving mode is a flexure mode in the *x-y* plane, as shown in Figure 3.3.1 (a). It is a symmetrical mode driven by drive electrodes on drive arms. The *z*-axis detecting mode is an asymmetric flexure mode in the *x-y* plane, as shown in Figure 3.3.1 (b).

The driving electrodes on the drive arms are configured to vibrate the drive arms symmetrical in the *x-y* plane. When the gyroscope is subjected to a rotation about the *z*-axis, a pair of Coriolis forces F_{cz} is generated proportional to the angular velocity Ω_z and vibration velocity V_x. The moment M_{cz} are produced at each end of the driving arms and displace them in opposite direction which will cause an asymmetric mode in the horizontal *x-y* plane. The *z*-axis detection electrodes on the arm *L3* measures the change of charge or voltage to output change in angular velocity.
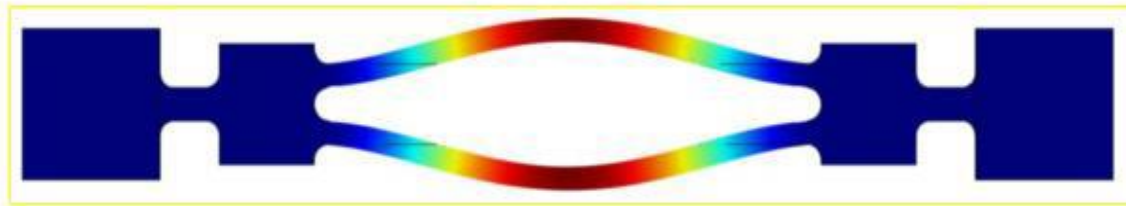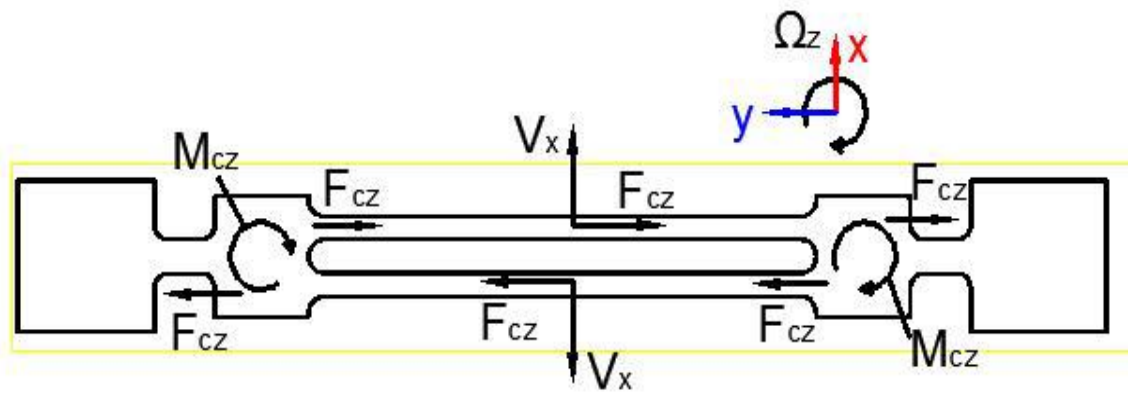
(a) Drive Mode
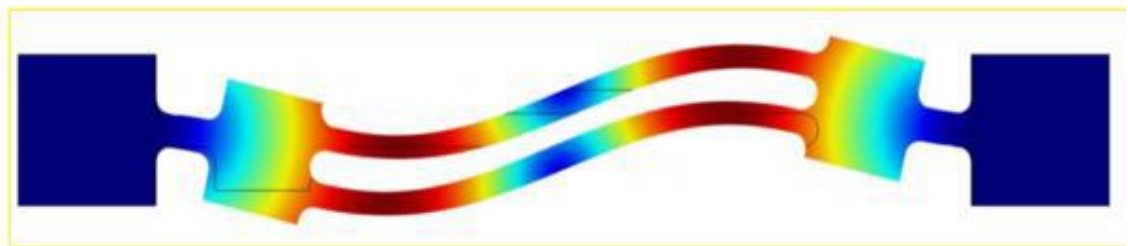
(b) z-axis detection Mode

Figure 3.3.1Operation principle of double-ended tuning fork gyroscope

3.4   Finite Element Analysis

The geometric sensitivity and gyroscopic sensitivity characteristics of the double-ended tuning fork gyroscope are simulated using Comsol Multiphyscis 4.3a. As shown in figure 3.4.1, a total 16,467 tetrahedral mesh elements and 303,770 degree of freedom are used in the FEM analysis. The gyroscopic sensitivity is dependent on the matching of the resonant frequency of drive mode and detection mode. In order to have maximum gyroscopic sensitivity of the gyro sensor, the natural frequency of the z-axis detection mode must match closely to the natural frequency of the driving mode. The drive electrodes are located at the drive arms and the sensing electrodes are located at the arm L_3, which are designed to sense the changes in electric charge or voltage. For modal analyses, all the electrodes are grounded, while for the frequency response analysis, the driving electrodes are excited at ±1 V. The thickness of 0.2μm of gold films are applied to all the electrodes.
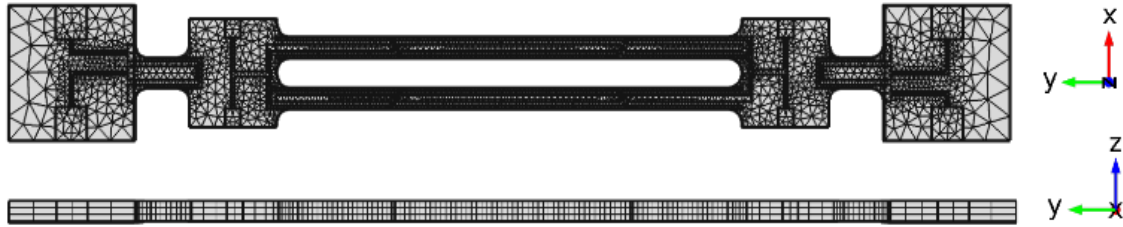
Figure 3.4.1 FEM mesh of the double-ended tuning fork gyroscope.

While the thickness of electrode films could be changed for fine-tuning of the driving or detecting frequencies, we need to determine as the first order an optimal geometry of the resonator where the driving and detecting frequencies are well matched. The frequency of the z-axis detection mode is highly dependent on the width W_3 when the detection arm

length *L3* is fixed, that is, the frequency of the detection mode increases with W_3 for a fixed L_3.

Figure 3.4.2, 3.4.3 and 3.4.4 show the frequency spectrum of the driving mode and detection mode versus the width W_3 for quartz, langasite and langatate, respectively. From the three figures, the optimal W_3 is determined for each of the material quartz, langasite and langatate. We observe that the driving mode is highly coupled to the detection mode when their modal branches intersected in the frequency spectrum. Hence, in order to reduce the coupling between the two modes but at the same time maintain adequate performance of the detection mode, we select W_3 width that is slightly away from the intersection of the two modal branches. The W_3 width chosen is shown in table 3.4.1 for each material quartz, langasite and langatate, respectively, along with their driving frequency, detection frequency, and frequency difference $\varDelta f$. The change in width W_3 has little effect on the driving frequency. The thickness, t, of the gyroscope is kept constant at 0.30 mm.
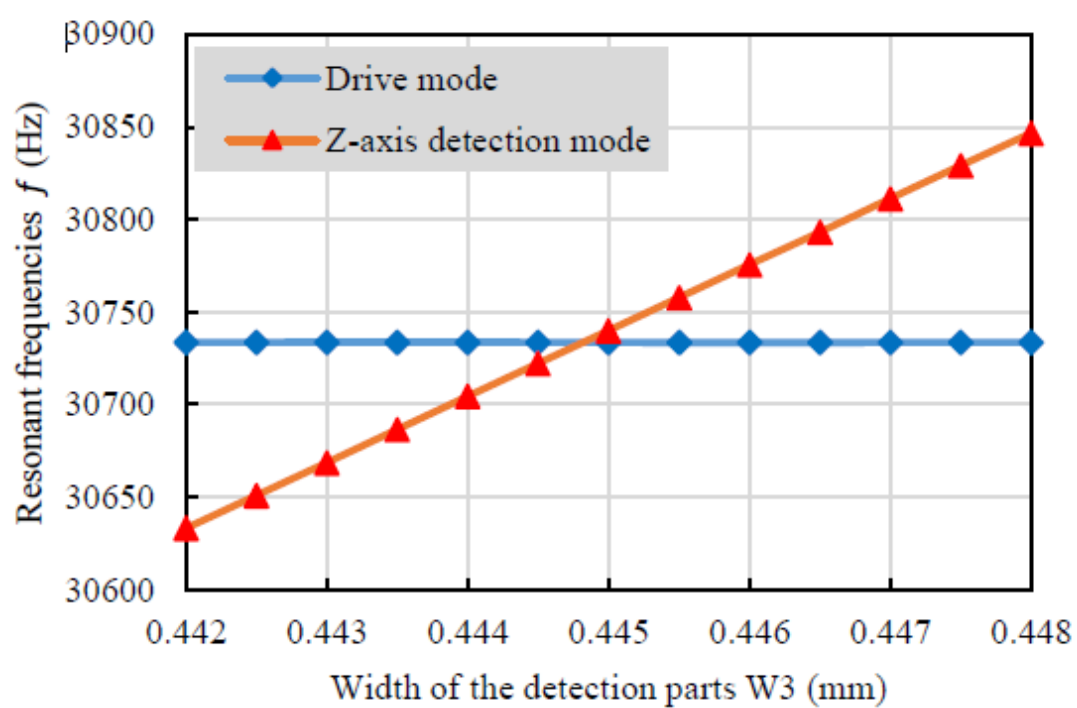
Figure 3.4.2 frequency spectrum of quartz of the driving and detecting modes as a function of W3
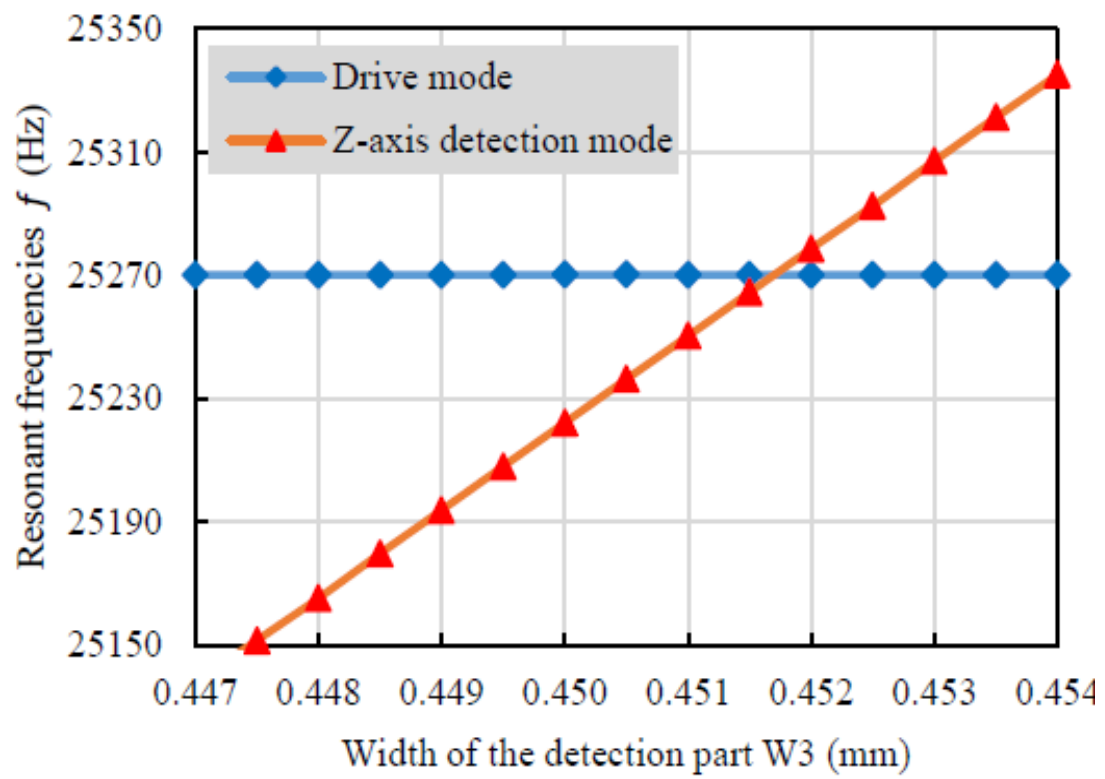
Figure 3.4.3 Frequency spectrum of langasite of the driving and detecting modes as a function of W_3.
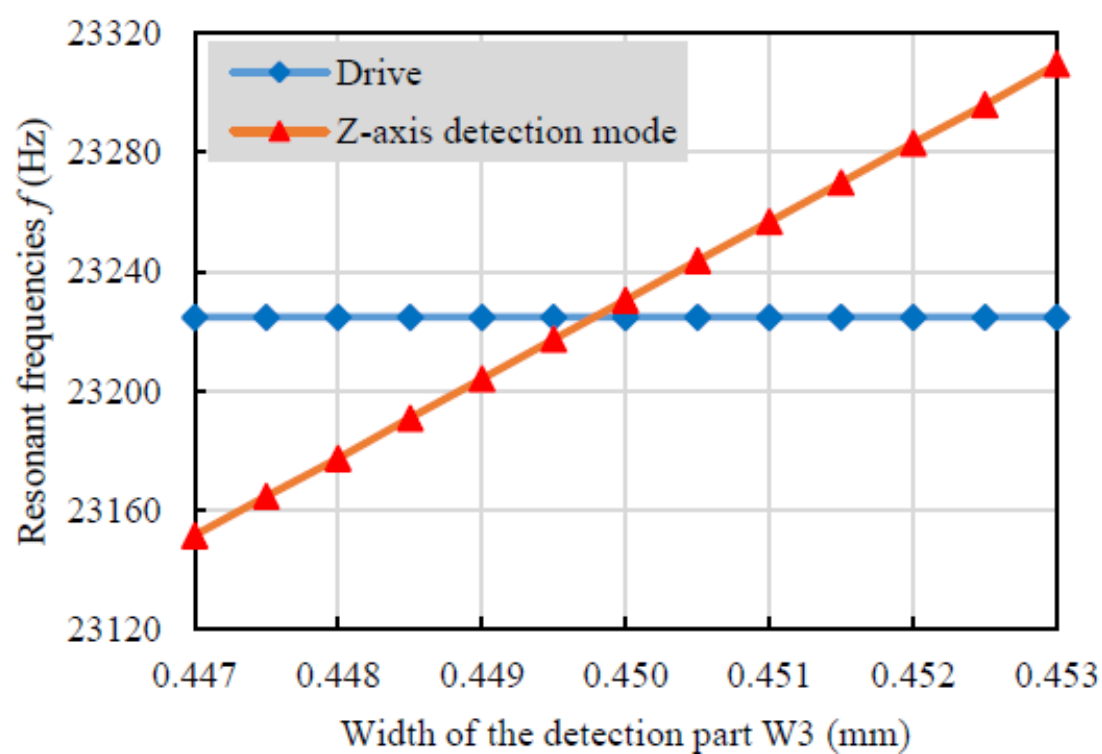
Figure 3.4.4 Frequency spectrum of langatate of the driving and detecting modes as a function of W_3.

Table 3.4.1 The driving frequency and detecting frequency of the doubled ended tuning

fork gyroscope of each material

	Quartz, $W3=0.445$mm	Langasite, $W3=0.452$mm	Langatate, $W3=0.450$mm
$f_{driving}$	30733	25270	23224
$f_{detecting}$	30740	25264	23230
Δf	7	6	6

Unit: *Hz*

The gyro-characteristics of the gyroscope also depends on the frequency separation, Δf. When driving frequency is too close to the detecting resonant frequency, the system becomes unstable which can cause a shift in detecting resonance frequency. Moreover, the coupling of driving mode and detecting mode will change the mode shapes of both modes. Operating the system too far away from the detection mode frequency will reduce the sensitivity of the gyroscope. It is very important in this simulation for comparing the relative merits of each material that we keep the same frequency separation for each material. The equation of the frequency separation is

$$\Delta f = f_{detecting} - f_{driving} \tag{3.4.1}$$

where $f_{detecting}$ and $f_{driving}$ are the detecting frequency and driving frequency in *Hz*.

3.5   The Gyroscopic Sensitivity

The gyroscopic sensitivities of the quartz, langasite and langatate double-ended tuning fork were obtained by frequency response analysis. For the models that we were analyzing are only in angular velocity about the z-axis, we applied the following gyroscopic equations in our finite element models [21].

$$f_x = F_x + \rho\omega^2 u_x + j2\rho\Omega_z\omega u_y \qquad (3.5.1)$$

$$f_y = F_y + \rho\omega^2 u_y - j2\rho\Omega_z\omega u_x \qquad (3.5.2)$$

where f is the total force acting on the element, F is the external force, ρ is the mass of the element, u_y is the displacement in y-direction and u_x is the displacement of x-direction. The third terms on the right hand side are the Coriolis forces generated by the rotation about z-axis with angular velocity Ω_z. Frequency response analyses were performed without Coriolis-body force and angular velocity, Ωz. Then, we applied the body forces F_b as Coriolis-body forces on the entire structures and these are given as

$$F_{bx} = 2\rho\omega\Omega_z u_y \qquad (3.5.3)$$

$$F_{by} = -2\rho\omega\Omega_z u_x \qquad (3.5.4)$$

$$F_{bz} = 0 \qquad (3.5.5)$$

where F_{bx}, F_{by}, and F_{bz} are the body forces applied to the structure in the x-, y-, and z-directions, respectively. The difference in voltage on the detecting electrodes were used to calculate the gyro-sensitivity. The output voltage as a function of the angular velocities, Ω_z, which represent the gyroscopic sensitivity, of each material are shown in figure 3.5.1. The sensitivity of quartz, langasite, and langatate to angular velocity Ω_z were 0.191mV/(deg/s), 0.469mV(deg/s) and 0.784mV/(deg/s), respectively. As the values indicate, sensitivity of langatate and langasite were about 4 times and 2 times higher than quartz, respectively. Also, it can be seen that all three materials exhibit a linear relationship between output voltage and angular velocity.
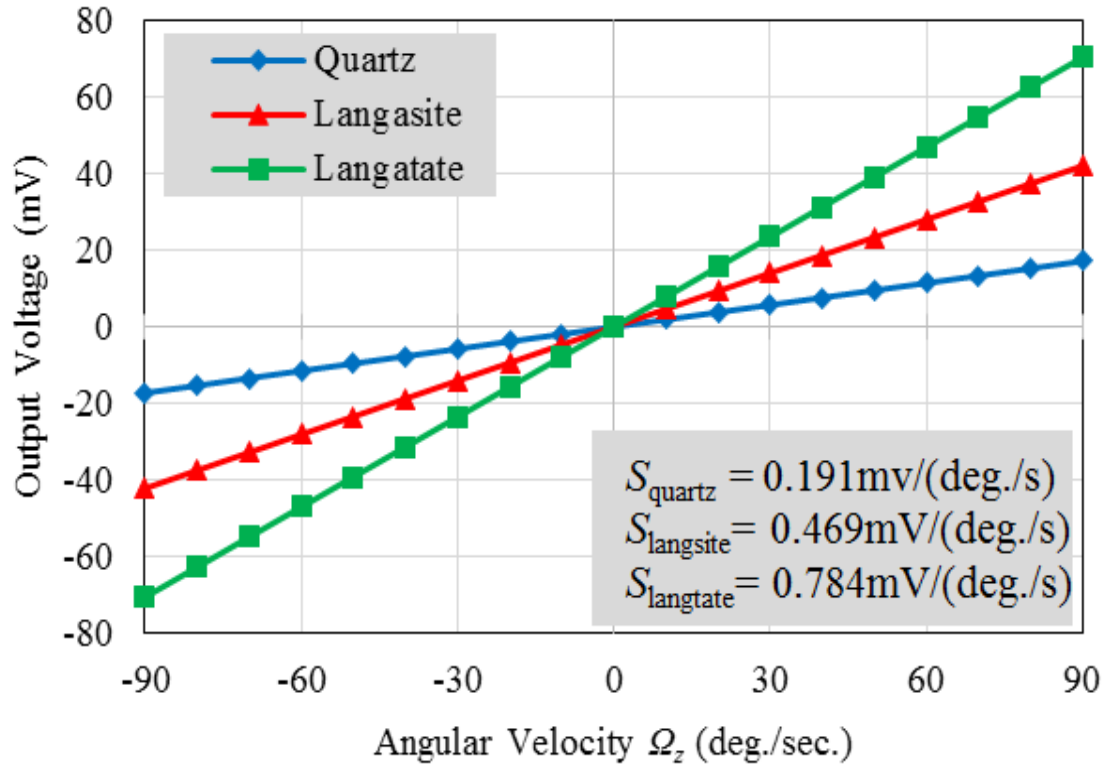
Figure 3.5.1 The gyroscopic sensitivity of quartz, langasite and langatate double-ended tuning fork gyroscope rotation about the z-axis

3.6 Effect of the mounting support of quartz double-ended tuning fork gyroscope

The vibration modes of piezoelectric crystal involve not only the geometry of the resonator or gyroscope, but also the supporting and mounting structure [22]. The quality factor of the gyroscope can decrease significantly with the small changes of mounting support. In this section, the geometry characteristics of the quartz double-ended tuning fork gyroscope with dual axis is analyzed as well as the gyroscopic sensitivity of the gyroscope rotation about z-axis as a function of thickness of mounting support. Furthermore, we look into the equivalent circuit parameter of the Butterworth Van Dyke resonator. The same double-ended tuning fork gyroscopes are used in this section except we exclude the langasite and langatate double-ended tuning fork gyroscope.

The structure of the quartz double-ended tuning fork gyroscope used in this section has the same dimension as in previous section. However, the arrangement of the electrodes has been changed so that it can detect the y- and z-axis as shown in figure 3.6.1. The electrodes are thin films made of gold. The thickness of the driving electrodes could be adjusted for fine-tuning the driving mode frequency by using the mass loading effect of the electrodes. The gyroscope was designed so that the moment and the displacement of the mounting support are minimized while the moment of the detecting arms was maximized. The driving, y-axis sense, and z-axis sense electrodes are denoted as $D_r \pm$, $D_y \pm$, and $D_z \pm$, respectively.

The operation principle of the quartz double-ended tuning fork gyroscopes is the same as in previous section except it can detect the y-axis, in addition to the z-axis. For the angular velocity rotation about z-axis, the principle of the operation is the same as in section 3.3. Figure 3.6.2 shows the three modes of vibrations that are employed by the gyroscope to detect the angular velocities about the y- and z-axes of the device: (a) At the top is the driving mode which is a flexure mode in the x-y plane, (b) at the middle is the y-axis (Ω_y) detection mode which is a flexure mode in the y-z plane, and (c) at the bottom is the z-axis (Ω_z) detection mode which is a asymmetric flexure mode in the x-y plane. The driving electrodes are designed to vibrate the center arms in the horizontal x-y plane as shown in figure 3.6.2 (a). The top arms vibrate in the opposite x-direction from the bottom arm. The Coriolis force, F_{cy}, is generated in z-direction when an angular velocity Ω_y is applied to the gyroscope. Due to the Coriolis Effect, the center arms then vibrate in y-z plane as shown in figure 3.6.2 (b). The y-axis detecting electrodes on the center arms of the gyroscope detect the Coriolis force F_{cy}.
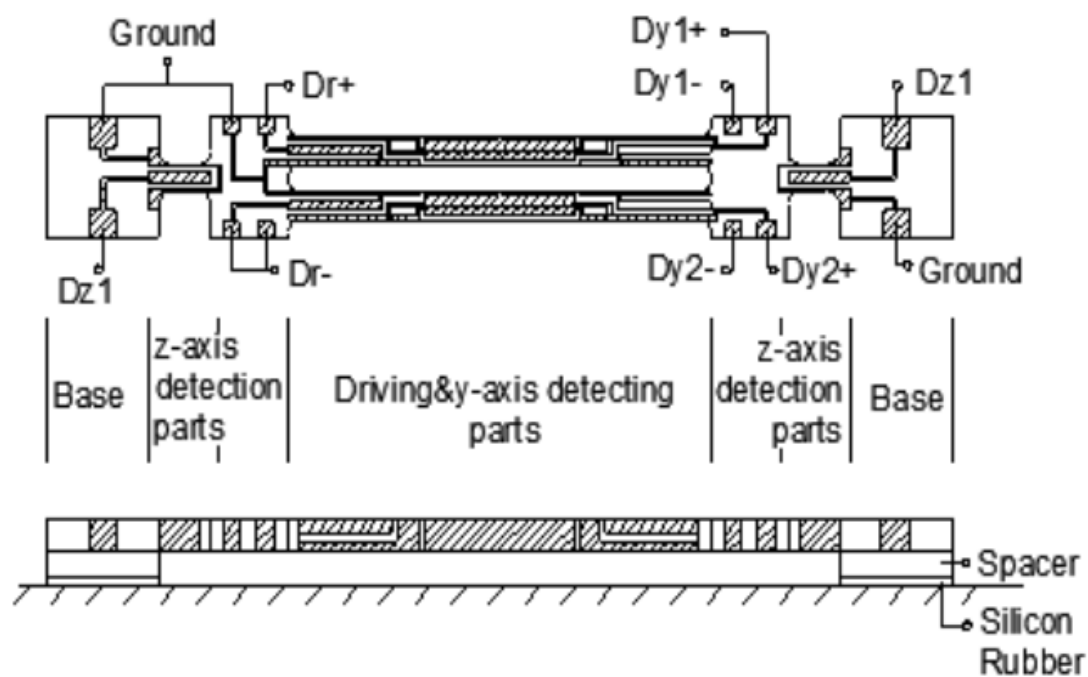
Figure 3.6.1 The electrode configuration of the double-ended tuning fork

(a) Driving Mode
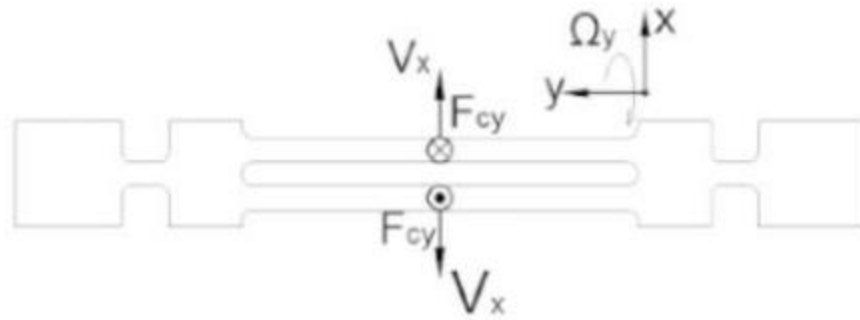
(b) y−axis detection mode
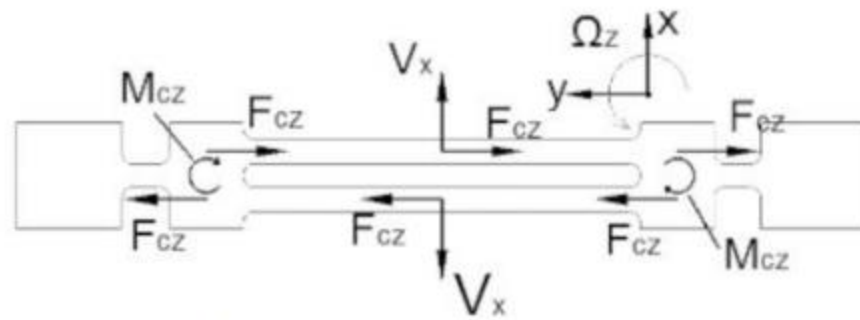
(c) z−axis detection mode

Figure 3.6.2 The three modes of vibration of the gyroscope: (a) Driving mode, (b) y-axis detection mode and (c) z-axis detection mode.

The 3-D Structural Mechanics, Piezoelectric Devices (pzd) module was employed to model the structure of the quartz gyroscope. The FEM model of the gyroscope is shown in figure 3.6.3. Tetrahedral elements were used in the mesh. There were 50,594 elements and 321,757 degrees of freedom. Both eigenfrequency and frequency response analyses were performed. The eigenfrequency analysis was employed to (1) determine the optimum gyroscope geometry for the driving mode and two detection modes, and (2) to calculate the electrical parameters of the gyroscope. The frequency response analysis was needed to calculate the Coriolis forces and the detection sensitivity of the gyroscope.
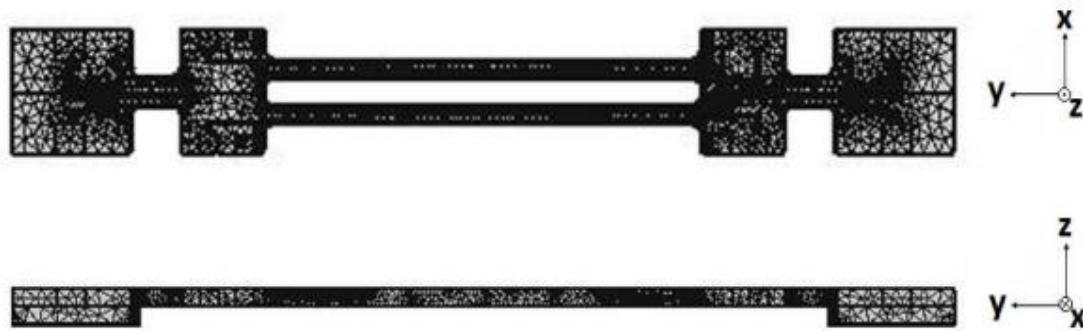
Figure 3.6.3 FEM mesh of the double-ended tuning fork gyroscope.

3.6.1 Eigenfrequency analysis

Since the sensitivity of the gyroscope is dependent on the matching of the natural frequencies of the detecting modes to the natural frequency of the driving mode, parametric eigenfrequency analyses were performed on the geometry of the tuning fork. The parameters were the height of the mounting supports and the thickness of the quartz blank. These parameters affect the frequencies of the driving mode and the detecting modes. For example, figure 3.6.4 shows the changes in the y-detection and z-detection

mode frequencies and the driving mode frequency as a function of the thickness of the resonator-gyroscope when $W_3 = 0.491$ mm. We observed that it is difficult to get all three modal frequencies to match, especially the y-detection mode frequency. At the resonator thickness t = 0.36031 mm the three modes come closest together but there is coupling of the y-detection mode with the driving and z-detection modes. This coupling creates cross-talking of the y-detection mode with the z-detection mode. Hence, in this paper we focused on a one axis detection gyroscope, namely, the z-axis angular velocity detection while putting aside for now the y-axis angular velocity detection.

The analysis also shows that it is possible to match very well the frequency of the z-detection mode to the frequency of the driving mode. Figure 3.6.5 shows that a good frequency match could be obtained at a resonator thickness of 0.3 mm. The normalized resonant frequency of the z-axis detection mode depends on the width W_3. The width W_3 is adequate at W_3=0.491mm, as shown in figure 3.6.6. The change in the width W_3 has very little effect on the driving and y-axis detection modes frequencies. We also observed that the resonant frequency of the z-axis detection mode can be tuned by the width W_3. We can further optimize the frequency matching of the z-detection mode. Figure 3.6.7 shows the change in frequency of the z-detection mode as a function of the spacer height. The blue line is for W_3=0.491 mm while the red line is for W_3=0.49 mm.

Based upon our parametric studies, we chose the resonator dimensions to be those provided in table 3.6.1. (Please see figure 3.2.1 and 3.6.1 for the definition of the dimension)

Table 3.6.1 Dimensions of the double-ended tuning fork gyroscope.

Item	Dimension	Item	Dimension
L	16.0	W	2.00
L1	7.46	W1	0.31
L3	0.89	W3	0.43
LB	2.00	Wi	0.75
t (blank thickness)	0.30	Spacer	0.28
Silicon rubber	0.03		
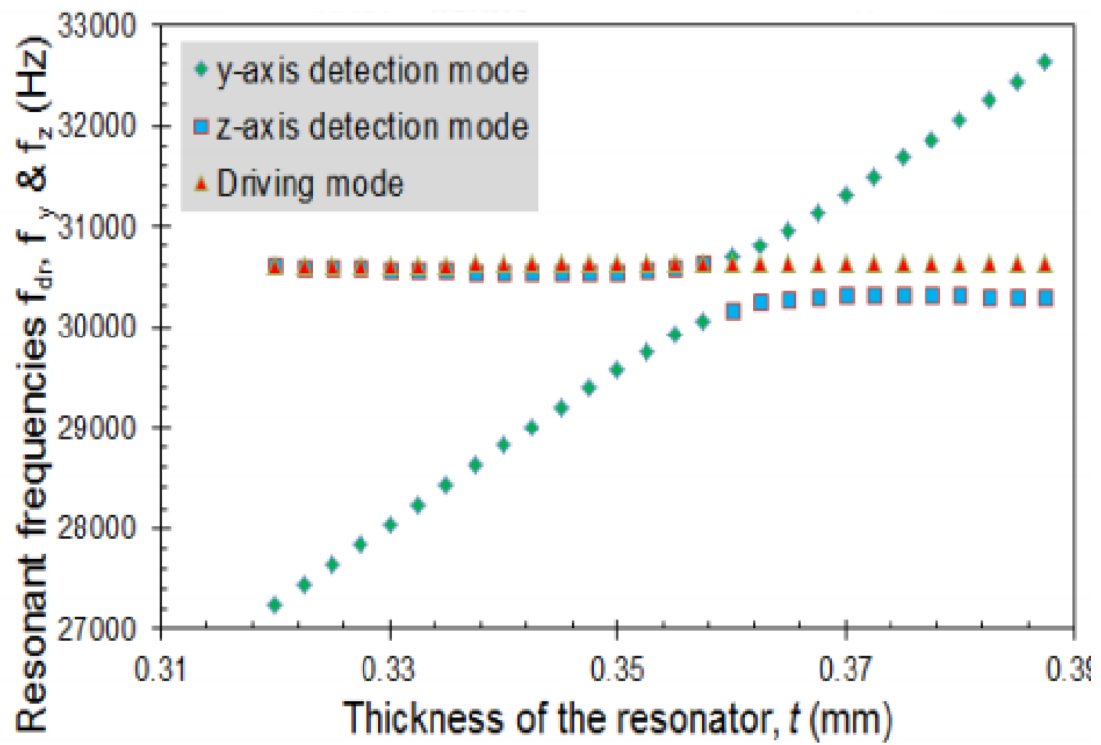
Figure 3.6.4 Resonant frequencies of the driving, y- and z-axis detection modes as a function of the resonator thickness when W3=0.491mm
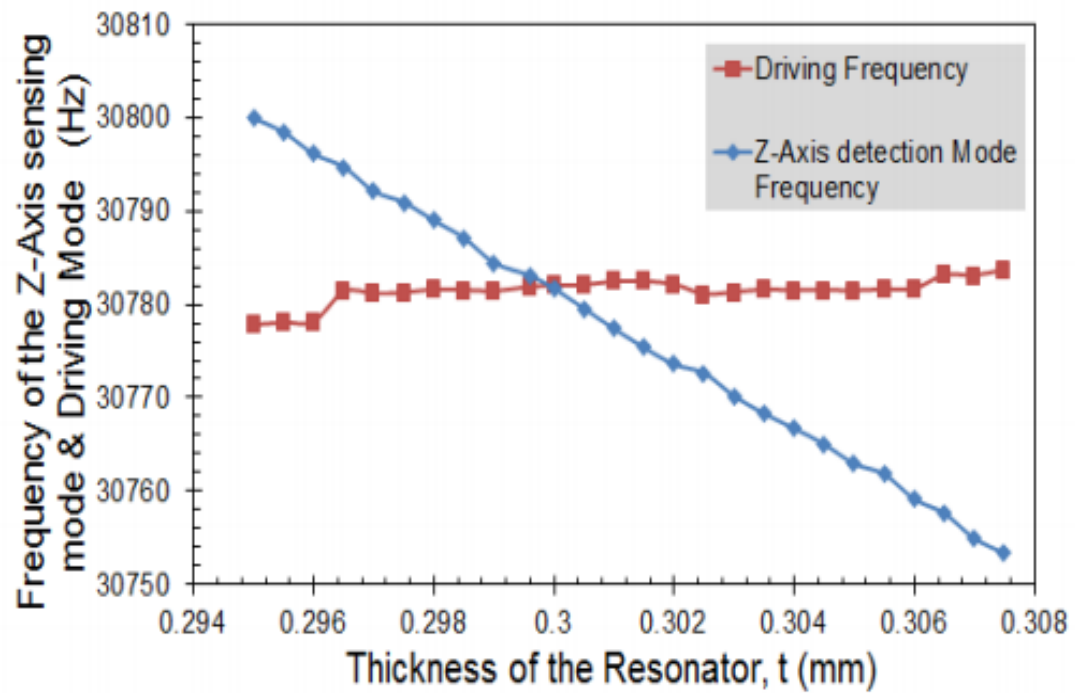
Figure 3.6.5 Resonant frequencies of the z-axis detection mode and the driving mode with the resonator thickness when W3=0.43mm
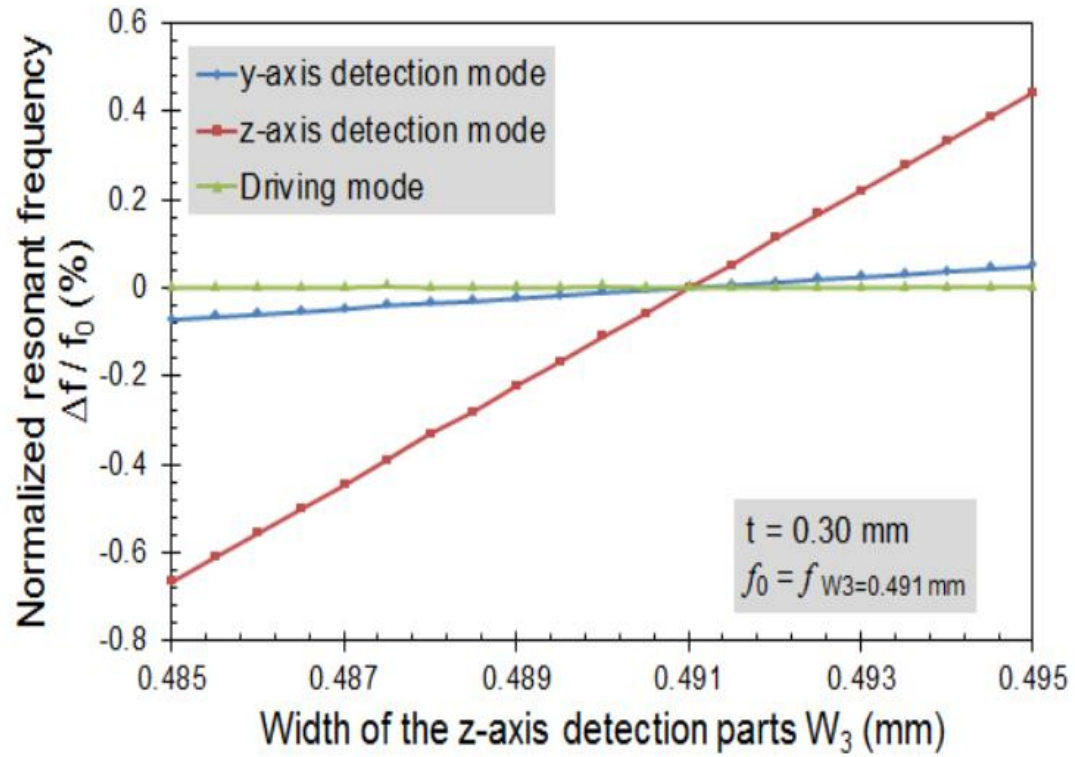
Figure 3.6.6 Resonant frequencies of the driving, z- and y-axis detection modes as function of the W3

Figure 3.6.7 Change in resonant frequencies of the z-axis detection mode for height of the

spacer
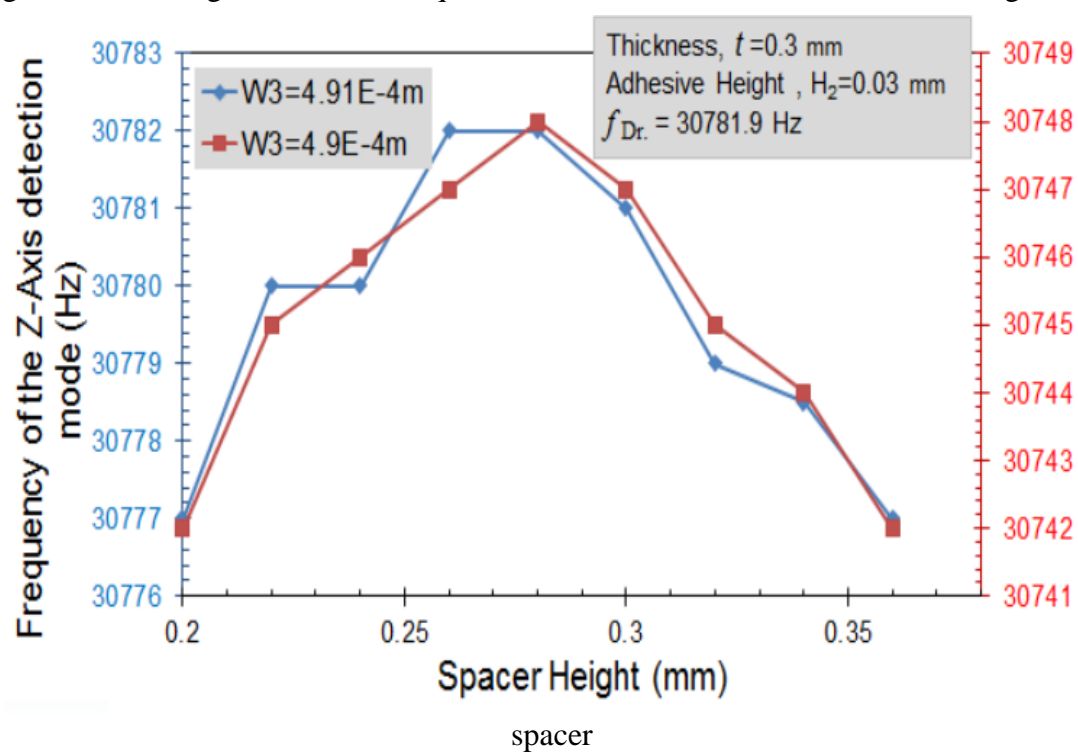
3.6.2 Butterworth Van Dyke Electrical Parameters

The piezoelectric gyroscope could be represented in an equivalent circuit parameters of the Butterworth van Dyke resonator as shown in figure 3.6.8. [23]
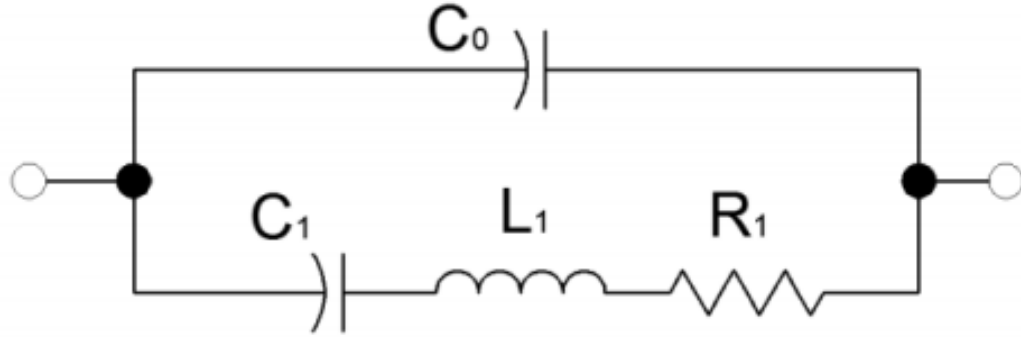
Figure 3.6.8 Equivalent electrical circuit parameters of the piezoelectric resonator-gyroscope represented as Butterworth van Dyke resonator

The static capacitance C_0 is obtained from a COMSOL electrostatic analysis by putting 1V on the drive electrodes. C_0 is then equal to the total surface charge on the drive electrodes as shown in equation 3.6.1. The electrical parameters C_1, L_1 and R_1 can be obtained from our eigenfrequency analysis of the resonator-gyroscope. The following four quantities are first obtained from the eigenfrequency analysis:

(1) ω_r , the short circuit resonance frequency,

(2) Q, the quality factor of the mode ω_r,

 (3) q, the charge on the drive electrode, and

(4) E, an energy norm.

Q and ω_r are obtained directly from the COMSOL eigenfrequency model *pzd.Q_eig* and *pzd.omega*, respectively, while q and E are calculated using equation 3.6.1 and 3.6.2, respectively

$$q = \left| \int_{drive\ electrode} (pzd.nD)dA \right| \tag{3.6.1}$$

$$E = \left| \int_{All\ domains} (pzd.rho * pdz.disp\text{\textasciicircum}2)\ d\Omega \right| \tag{3.6.2}$$

The four quantities ω_r, Q, q, and E are used to calculate the electrical parameters C_1, L_1, and R_1 using equation 3.6.3, 3.6.4 and 3.6.5 below

$$C_1 = \frac{q^2}{E\ \omega_r{}^2}$$

$$\tag{3.6.3}$$

$$L_1 = \frac{1}{C_1\ \omega_r{}^2}$$

$$\tag{3.6.4}$$

$$R_1 = \frac{1}{Q\ C_1\ \omega_r} \tag{3.6.5}$$

The calculated Butterworth van Dyke electrical parameters for our gyroscope are provided in Table 3.6.2.

Table 3.6.2 Calculated equivalent circuit elements

Frequency (Hz)	30781.69
C_1 (F)	1.0347 E -15
R_1 (Ω	3332.4965
C_0 (F)	1.8394 E -10
L_1 (H)	25837.8089

It is important that the dissipation or damping of the gyroscope be modeled because of its effect on the electrical parameters and sensitivity of the gyroscope. The quality factor Q obtained from the COMSOL model is dependent on the damping coefficients of the quartz elastic constants, and the dissipation in the silicon rubber adhesive used to bond the

gyroscope to a device substrate. Equation 3.6.5 shows that the motional resistance R_1 is inversely proportional to the Q if the motional capacitance C_1 is constant. Since the model damping will affect the coupling between resonant modes, and the resonant frequencies of the modes themselves, the dissipation at the silicon rubber adhesive bonds was studied and found to be an important factor in the sensitivity of the gyroscope when subjected to an angular velocity about the z-axis.

3.6.3   Frequency response analysis of the double-ended gyroscope

The sensitivity of the gyroscope to angular velocity about the z-axis was simulated with the frequency domain or harmonic response analysis. The frequency response of the driving mode with 1V at the drive electrodes is shown in figure 3.6.9. The simulation method is the same as in previous sections 3.5 and 3.6. We observe a change in the charge at the z-detection electrodes when the gyroscope is rotated about the z-axis. For example in a frequency response analysis shown in figure 3.6.10 we see the change in charge at the z-detection electrodes when Ωz = 120 deg. /s. Therefore, the gyroscope could sense the angular velocity Ωz about the z-axis as a change in charge at the z-axis detection electrodes. The magnitude of the change is greatest at the resonant frequency of the driving mode.

The sensitivity of the gyroscope is dependent on the matching of the resonant frequency of the z-axis detection mode to the resonant frequency of the driving mode. When the two resonant frequencies are not well matched the sensitivity of the gyroscope decreases. We studied the effect of small changes in the thickness of the silicon rubber adhesive at the bottom of the spacers of the gyroscope (please see figure 3.6.1). The adhesive thickness has significant effects on the z-axis detection mode frequency but has

little or no effect on the driving mode frequency. The change in the z-axis detection mode frequency resonator will affect the sensitivity of gyroscope when subjected to an angular velocity about its z-axis. This is shown in figure 3.6.11 where we observe that a small change of 4µm in adhesive thickness could change the sensitivity by as much as 44%. Therefore the adhesive thickness will be a significant factor in improving the production yields of this gyroscope.
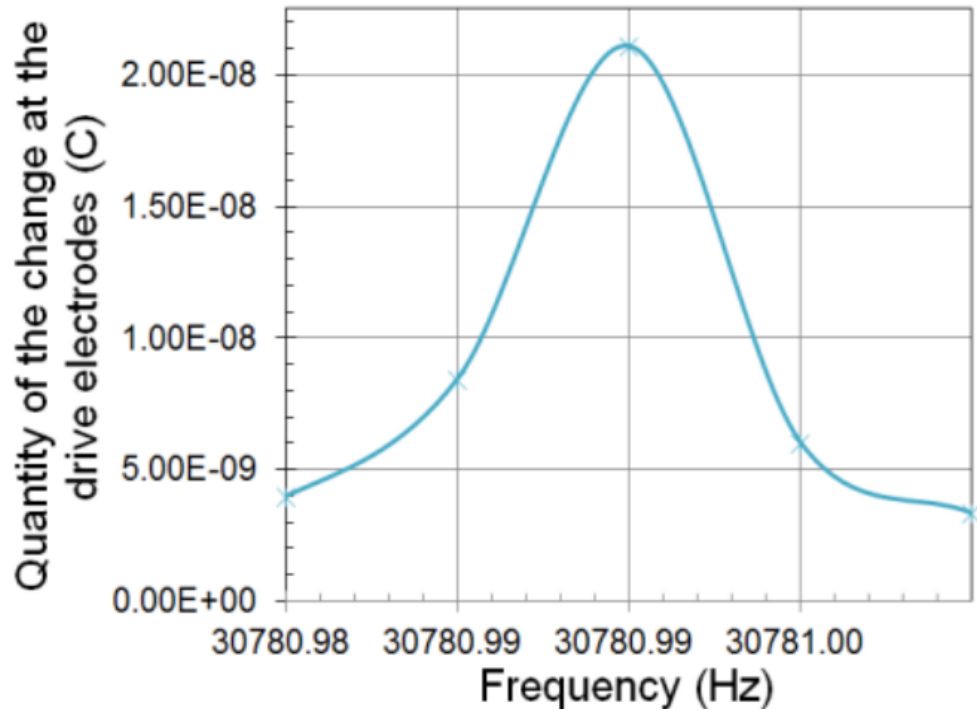
Figure 3.6.9 Frequency response of the driving mode with 1V at the drive electrodes
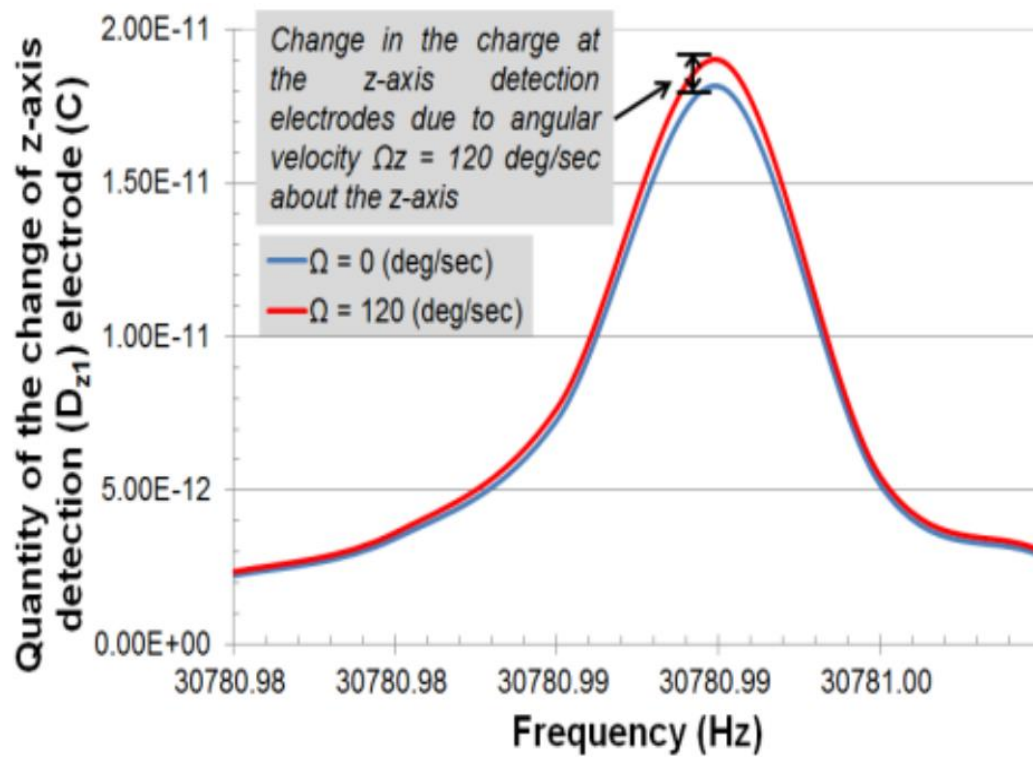
Figure 3.6.10 Change in charge at the z-axis detection electrodes when the gyroscope experiences an angular velocity $\Omega z = 120$ deg./s about z-axis
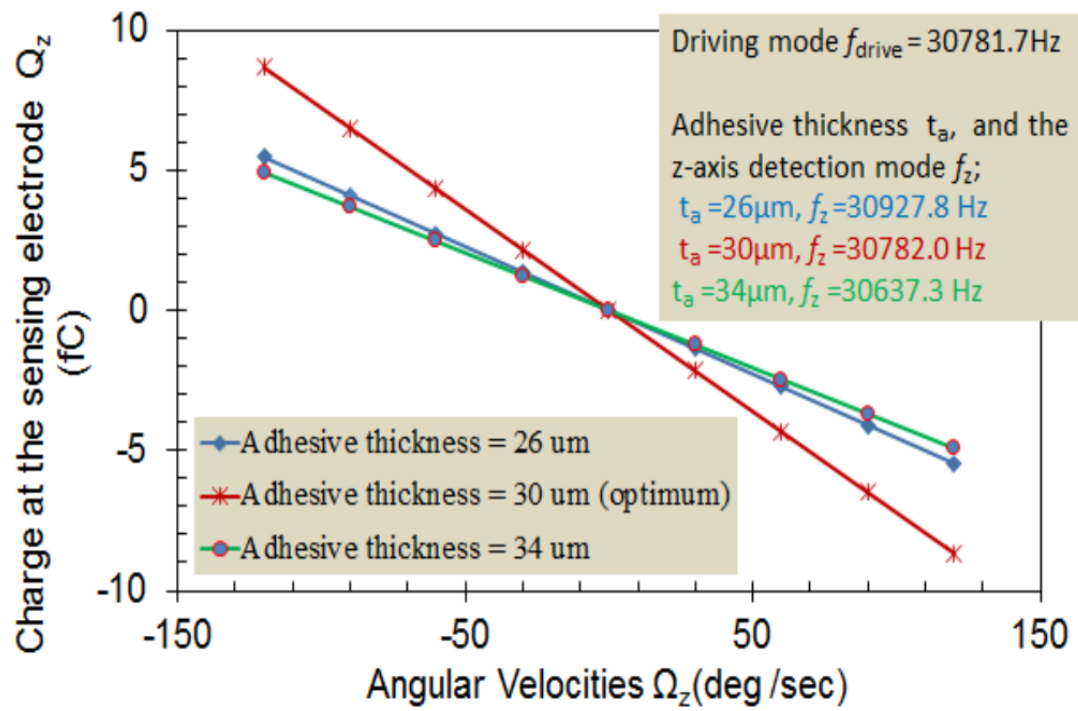
Figure 3.6.11 The z-axis detection sensitivity of the gyroscope as a function of adhesive thickness

3.1 Summary

Using FEM simulation, we have investigated the geometry of double-ended tuning fork gyroscope and gyro-characteristics of a double-ended tuning fork gyroscope that utilized either quartz, or langasite, or langatate crystal respectively. Our study confirms that the langasite and langatate gyroscopes provide higher gyro-sensitivity than the quartz gyroscope. The gyro-sensitivity is also a function of geometry and frequency separation between the driving mode frequency and the detection mode frequency. In order to achieve higher sensitivity, adequate frequency separation is needed so that both the driving mode and detection mode remain pure while at the same time the detection mode could sense the Coriolis force at the driving mode frequency. We conclude that the langasite and langatate crystals are better gyroscopic materials than quartz.

Furthermore, a COMSOL model of a piezoelectric quartz double ended tuning fork gyroscope was successfully implemented. The gyroscope has two detection modes; the first mode detects the angular velocity about a z- axis perpendicular to the tuning fork plane (X-Y plane), while the second mode detects the angular velocity about a y-axis that is the longitudinal axis along the length of the tuning fork. The quartz doubleended tuning fork gyro sensor characteristics were studied using COMOL software. Both eigenfrequency and frequency response analyses were performed. The eigenfrequency analysis was employed to (1) determine the optimum gyroscope geometry for the driving mode and two detection modes, and (2) to calculate the electrical parameters of the gyroscope. The frequency response analysis was needed to calculate the Coriolis forces and the detection sensitivity of the gyroscope. An optimal geometry of the gyroscope was found by eigenfrequency analyses with geometric parameters such as the dimensions of

the tuning fork tines, spacers, and resonator thickness. The dimensions of the gyroscope provided in Table 3.6.1 were obtained using eigenfrequency analyses. The frequency response analysis was used to simulate the response of the gyroscope to angular velocity about its z-axis. The Coriolis forces were treated as body forces in the COMSOL model, which cause change in charge at the detection electrodes. The sign and magnitude of the change in charge at the detection electrodes are proportional to the sign and magnitude of the angular velocity of the gyroscope. We observed that good frequency matching of the driving mode with the detection modes was essential for the gyroscope to function well as a sensor for angular velocity. A sensitivity analysis was performed for detection of z-axis angular velocity as a function of the silicon rubber adhesive thickness at the bottom of the spacers. The z-axis detection mode was found to be sensitive to the adhesive height. Conversely the driving mode was found to be insensitive to the adhesive height. Therefore, the adhesive height is an important factor in the matching of the z-detection mode frequency to the driving mode frequency. The adhesive height would affect the production yields of this gyroscope.

Chapter 4. Piezoelectric length-extension gyroscope

4.1   Introduction

A piezoelectric length extension gyroscope is a newly designed gyroscope, which utilizes the length extension mode and flexure mode to detect the Coriolis force [24]. The z-cut, third-overtone, extensional quartz resonator was extensively studied by Yong, Lee and Chung [25] [26]. Moreover, the length-extension mode are studied by many other researchers [27] [28]. It can be made of a single piezoelectric crystal with MEMs fabrication technology. It has small size structure that can be easily mount and manufactured. The geometry of a length extension gyroscope is very simple compared to other vibratory gyroscopes. The length extension gyroscope utilizes the length extension mode to reduce the energy dissipation that uses the symmetric mode shape with the zero displacement nodes at the center of the driving arms. In this chapter 4, the piezoelectric length extension gyroscope is analyze by finite element analysis. Furthermore, gyroscopic sensitivity of quartz, langasite and langatate length extension gyroscopes are compared.

4.2   Structure of the Piezoelectric Length Extension Vibratory Gyroscope

The piezoelectric length extension vibratory is comprises of three main components, driving parts, sensing parts and supporting arms and base, as shown in figure 4.2.1 and figure 4.2.2.

4.2.1   Driving Parts

The driving arms are located at the middles of the sensing arms. The crystallographic axis and electric polarization direction of each crystal are considered for designing the length extension gyroscopes. The driving part electrodes are placed on the side wall (y-z

plane) of the driving arms so the drive arms can extend and contract in drive direction (y-axis). In order to get maximum gyroscopic sensitivity, gyroscopes are designed so that the drive mode shape is identical to the resonant frequency mode shape, the first length extension mode. The each driving arms are driven by ± 1 V which applied on one side of the electrodes whereas opposite sides of the electrodes are ground. The advantage of using length extension mode is energy dissipation of the gyroscope. The drive-mode vibration mode has very small influence by the support conditions, which high Q-factor of the gyroscope can be easily achieved.

4.2.2   Sensing Parts

The sensing part is the part that connects the driving arms and the support part while it measures the Coriolis force signals of the gyroscope. The sensing bridge is located at the end of the supporting arms, as shown in figure 4.2.2. Similar to the driving arms, the electrodes on the sensing bridge are located on the sidewalls (x-y plane) of the sensing bridge. The electrodes are placed so that the resonant frequency mode shape, the flexure mode, is similar to the sensing mode shape. In consideration of the crystallographic axis and electric polarization direction of each crystal, the sensing electrodes, which measure and output the Coriolis force signal of a gyroscope, are placed on one side of the sidewalls and the electrodes on the other side is grounded. The result is that higher sensitivity of the gyroscope can be achieved.

4.2.3   Support Part and Base

The supporting part is located between the base and sensing part, as shown in figure 4.2.2. The length of the support part, L_2, is determined by the length of driving arm, L_D. The small gap between the end of the driving arm and the supporting part is adequate,

since the displacement of the driving arms is insignificant. The width of the length, Ws, has to be long enough so that displacement of the support part along the x-axis is minimized. The end of the base is fixed to the fixed end conditions.
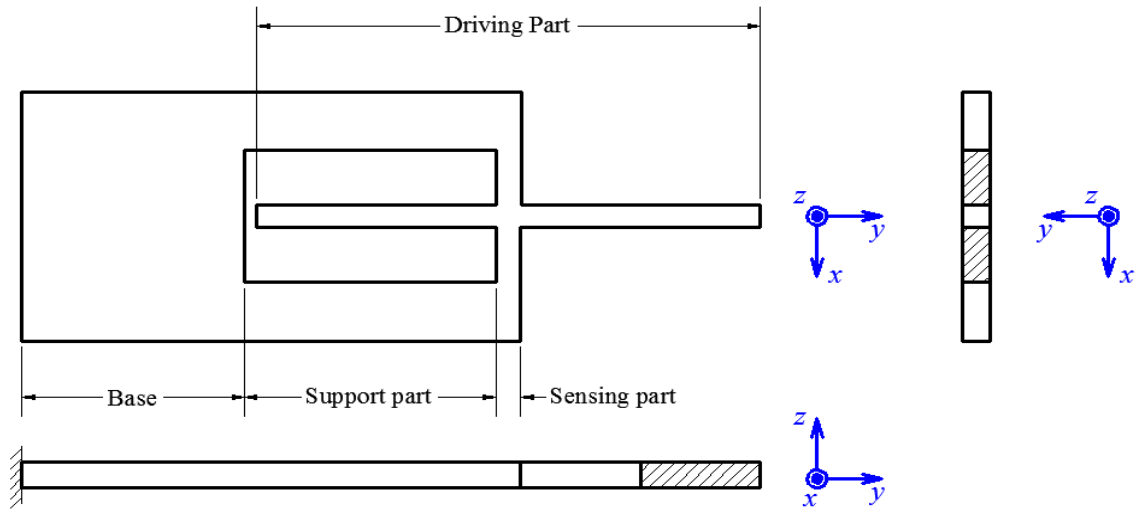
Figure 4.2.1 Structure of the piezoelectric length extension vibratory.
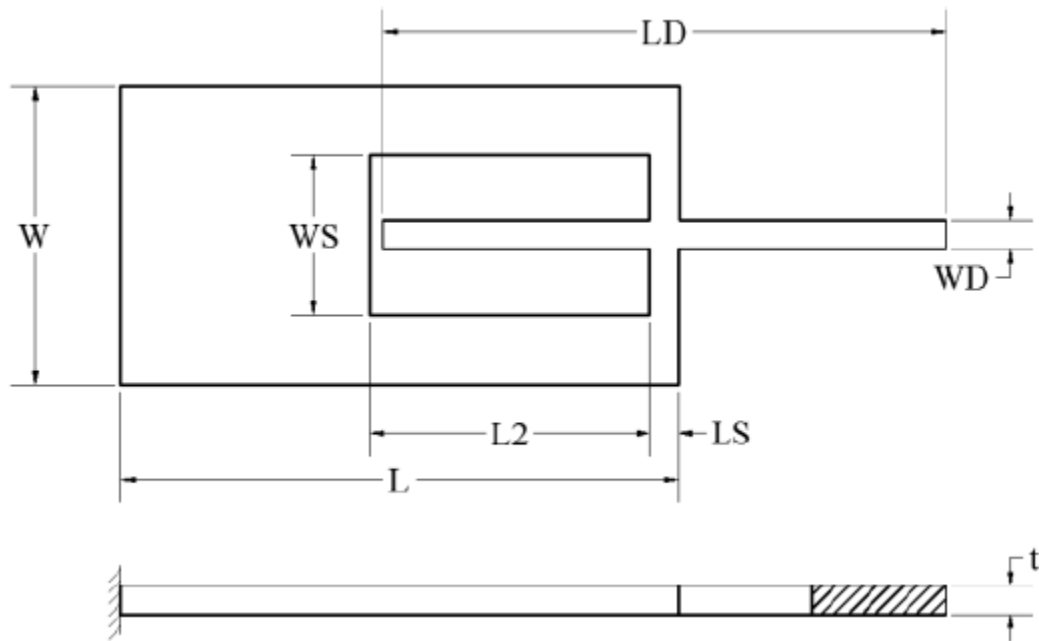
Figure 4.2.2 Dimensions of the piezoelectric length extension gyroscope

4.3   Principle of Operation of the Piezoelectric Length Extension

Gyroscope

The principle of operation of a length extension gyroscope is shown in figure 4.3.1. The each mode of two vibration modes is used as driving mode and sensing mode. Both modes are used to detect the angular velocity rotation about z-axis. The driving mode is a first extension mode of driving arm in the x-y plane. The driving arm is expands and contracts along y-axis by the external harmonic excitation force, as shown in figure 4.3.2 (a). The midpoint of the driving arm is the zero displacement node. The second vibration mode is the z-axis detection mode that is an anti-symmetric flexure mode in x-y plane, as shown in figure 4.3.2 (b). When the gyroscope is subjected to a rotation about z-axis, a pair of Coriolis forces, F_c, on the driving arms is generated proportional to the angular rate of gyroscope, Ω_z, mass density, m, and vibration velocity, V_y. A pair of equal and opposite Coriolis force on each driving arms, which generated by the rotation about z-axis, create the moment, M_c, on the center of the driving arms. The moment, M_c, induce the flexure mode of the sensing arms. The z-axis detection electrodes on the sensing arm measure the Coriolis force signals. The driving frequency, f_d, and sensing frequency, f_s, have to tuned closed to each other in order to achieve higher gyroscopic sensitivity.
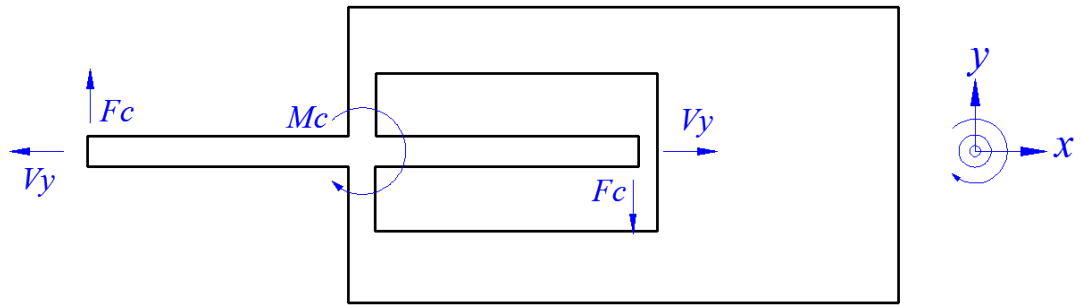
Figure 4.3.1 The principle of operation of a length extension gyroscope
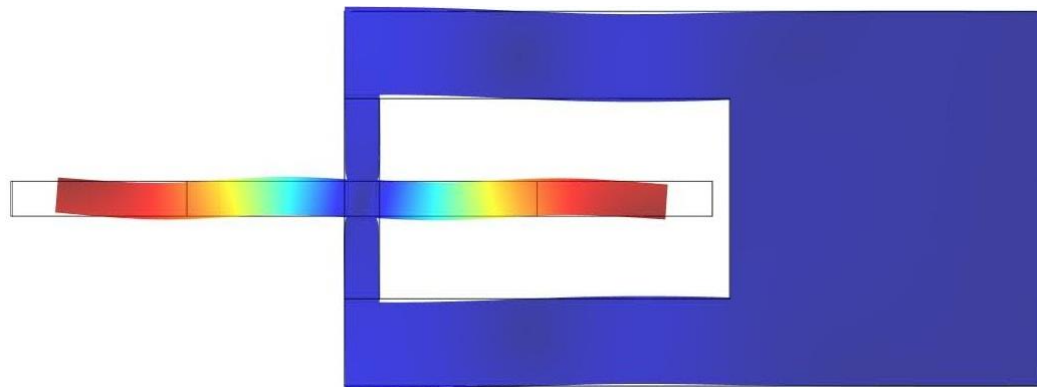
(a) Driving mode
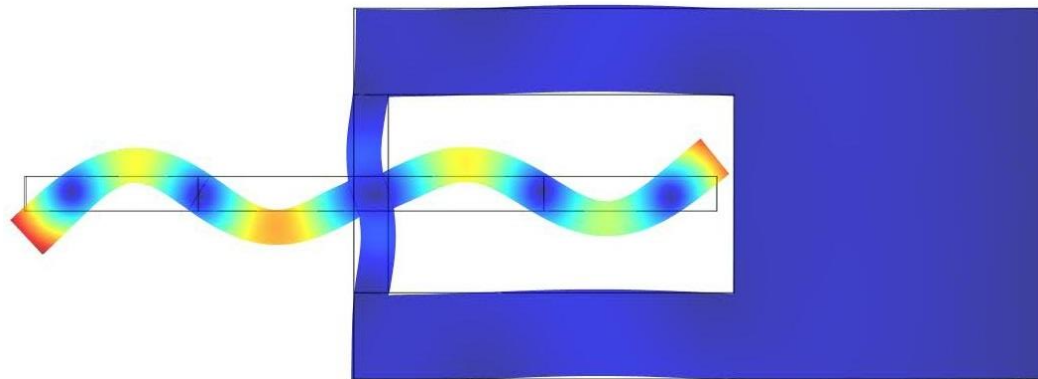
(b) Sensing mode

Figure 4.3.2 Drive-mode and sense-mode vibration modes of the piezoelectric length extension gyroscope

4.4   Finite Element Simulation

In this section, the length extension gyroscope is simulated and analyzed by finite element analysis method. Quartz, langasite and langatate crystals are used as materials for the length extension gyroscopes. The three materials can be easily compared, since they have same crystal properties. The material properties of the quartz, langasite and langatate are listed in Appendix C. The eigenfrequency analysis and frequency domain analysis are performed to study the geometric characteristics and gyro-characteristics of each gyroscope. The following equations 4.4.1, 4.4.2, 4.4.3, and 4.4.4 are implemented in COMSOL finite element method software. The equation 4.4.1 is the strain-displacement relation and the equation 4.4.2 is the electric field-potential relation.

$$S_{ij} = \frac{1}{2} (u_{j,i} + u_{i,j}) \tag{4.4.1}$$

$$E_i = -\emptyset_i \tag{4.4.2}$$

where S_{ij} is the mechanical strains, u_i is the mechanical displacements, and E_i is the electrical field and $\emptyset_i$ is the electric potential.

$$T_K = -e_{Kk}E_k + c_{KJ}^E s_J \tag{4.4.3}$$

$$D_i = \epsilon_{ik}^S E_k + e_{ij}s_J \tag{4.4.4}$$

The equation 4.4.3 and 4.4.4 are the piezoelectric constitutive equations in stress-charge form. T_k, e_{Kk}, c_{KJ}^E, D_i, ϵ_{ik}^S are the mechanical stress, piezoelectric constants, linear elastic constants, electric displacements, and dielectric permittivity, respectively.
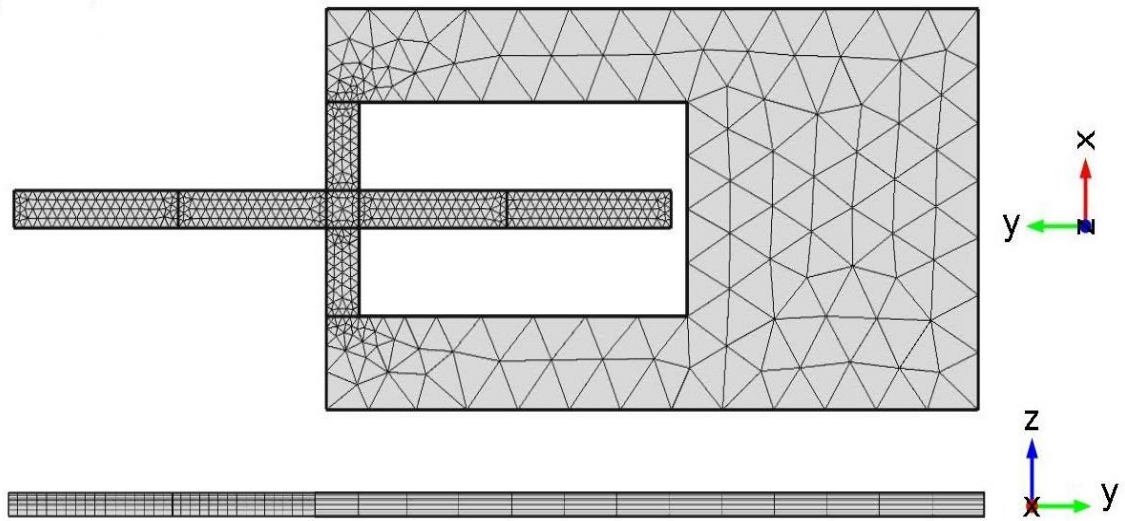
Figure 4.4.1 FEM mesh of the length extension gyroscope
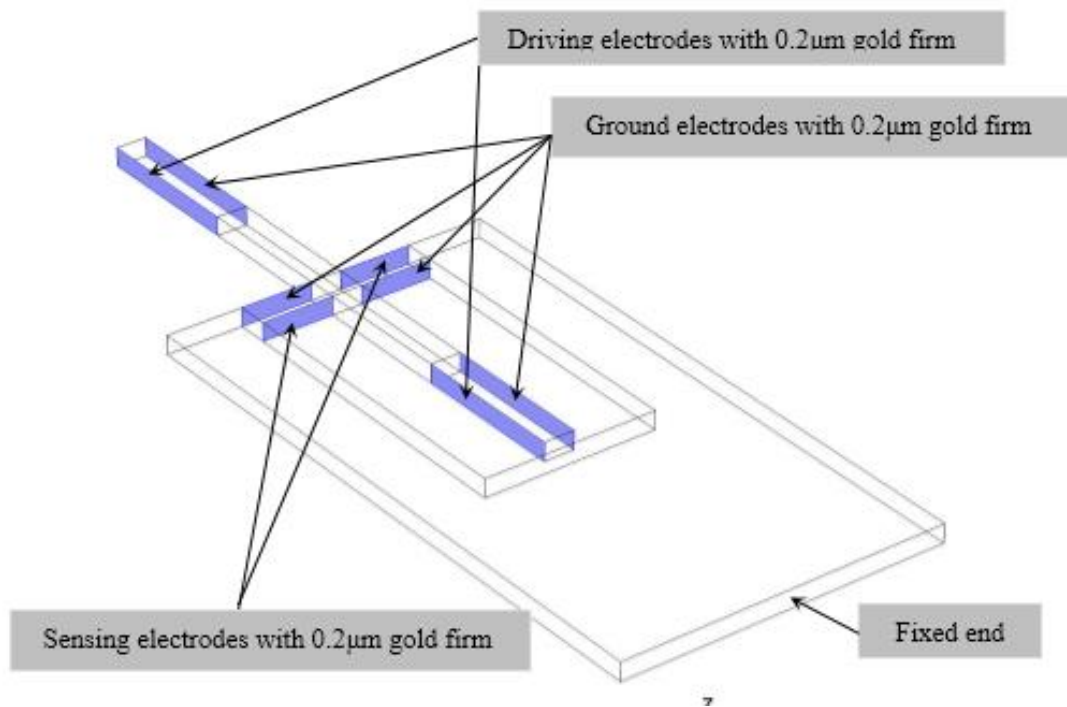
Figure 4.4.2 The locations of the drive and sensing electrodes of the gyroscope

The figure 4.4.1 shows the FEM model of the proposed gyroscope. The 10 layers of the triangle shaped elements were used in mesh for all three materials. The total number of elements and degrees of freedom which used in FEM is listed in table 4.4.1. The drive and sense electrodes are also included in the FEM simulations, which shown in figure 4.4.2. All the electrodes are coated with 0.2μm thickness gold film.

The targeted the driving frequency of the gyroscopes to be around 1 MHz. The gyroscope uses a length extension mode as a driving mode. The driving arm is symmetric along the x-axis. Hence, we considered a longitudinal vibration of elastic beam of fixed-free case to simplify the problem. The equation of the motion for free vibration of elastic beam is

$$m\frac{\partial^2 u}{\partial t^2} - EA\frac{\partial^2 u}{\partial x^2} = 0 \qquad (4.4.5)$$

Applying the fixed-free boundary conditions to the equation 4.4.5, we can obtain the equation for the frequency of a longitudinal vibration of beam when the structure is fixed at its one end.

$$f \equiv \frac{1}{2\pi}\sqrt{\frac{EA}{mL_D^2}} = \frac{1}{2\pi L}\sqrt{\frac{E}{\rho}} \qquad (4.4.6)$$

The driving frequencies of each material are depends on the length of the driving arms, L_D, elastic modulus, E, and mass density. Since elastic modulus and mass density of each materials are constant, the driving frequencies are depends on the length of the driving arms of the gyroscope. Therefore, the lengths of the drive arms of each gyroscope are different; such that the length of the driving arms of langasite and langatate gyroscopes are shorter than quartz gyroscope. Hence, overall size of the langasite and langatate gyroscopes can be minimized.

4.4.1 Eigenfrequency analysis

The eigenfrequency analyses were used to determine the length of the drive arms as well as overall size of each gyroscope. The specific sizes of each gyroscope are listed in Table 4.4.2.

Table 4.4.1 Conditions of FEM simulation

Material	Quartz	Langasite	Langatate
# of elements	26,950	10,110	5,170
# of degree of freedom	490,310	188,918	100,214

Table 4.4.2 Dimension of the length extension gyroscope of quartz, langasite and langatate.

	Quartz	Langasite	Langatate
W	2.500	1.074	1.074
W_S	1.258	0.574	0.574
W_D	0.100	0.100	0.100
L	3.000	2.000	2.000
L_D	2.510	2.016	1.998
L_2	1.400	0.300	0.300
L_S	0.100	0.100	0.100
t	0.060	0.060	0.060

Units:*mm*

In the simulation, the cut angles of each crystal are different. It is realized that the z-cut crystals are not the optimum cut angle for all materials. Hence, we analyzed the each material by rotating the geometry along the x-axis to find out the geometry where the displacement along the z-axis of the driving arm is minimum. It is not only reduces the vibration of the system but also reduce the energy dissipation which increases the

sensitivities of the gyroscopes. The optimum cut angles of the quartz, langasite and langatate are $\phi= 0^\circ$, $\theta=-9^\circ$, $\phi=0^\circ$, $\theta=24^\circ$ and $\phi=0^\circ$, $\theta=24^\circ$. respectively.

The sensitivity of the gyroscopes is depending on the matching of the driving frequency and the sensing frequency. Therefore, parametric eigenfrequency analyses were performed to obtain the optimum length of the drive arm of each material. Thus, the parameters which used in this simulation were the length of the driving arms. The changing the length of the drive arms not only affect the driving frequencies but also sensing frequencies as shown in figure 4.4.3 ,4.4.4 and 4.4.5. The rates of change of the sensing frequencies are higher than driving frequencies. The adequate length of the drive arms of the quartz gyroscope, langasite gyroscope and langatate gyroscope are 2.5 mm, 2.016 mm and 1.998 mm, respectively. The diving and sensing frequencies can be adjust by changing the length of the sensing arm, W_s or width of the sensing arm, L_s. However, changing those two parameter to match the driving and sensing frequencies cannot be accomplished due to the limitation of its geometry. Hence, it can only be used for fine tuning. The mechanical coupling between the driving mode and sensing mode of the quartz gyroscope is very small compared to the other two materials, this makes it easier to match the driving and sensing frequency very closed to each other when the length of the driving arm is around 2.515mm as shown in figure 4.4..The mechanical coupling of langasite gyroscope is larger than quartz gyroscope but it's smaller than langatate gyroscope. Two modes can be matched when the length of the driving arm is near 2.018mm as shown in figure 4.4.4. As shown in figure 4.4.5, the piezoelectric coupling factor of langatate is larger enough so that two modes are never cross each other.

Previously, we discussed that matching the driving and sensing frequencies increase the gyro-sensitivity of the gyroscope. However, the system becomes unstable when the driving frequency gets too closed to the sensing frequency which requires the frequency separation of driving and sensing frequency. The frequency separations of quartz, langasite and langatate gyroscopes are 29.4 Hz, 504 Hz and 519.5 Hz, respectively. The separation frequency equation is simple and it is

$$\Delta f = f_{detecting} - f_{driving} \tag{4.4.7}$$

where $f_{detecting}$ is the detecting frequency and $f_{driving}$ is the frequency.
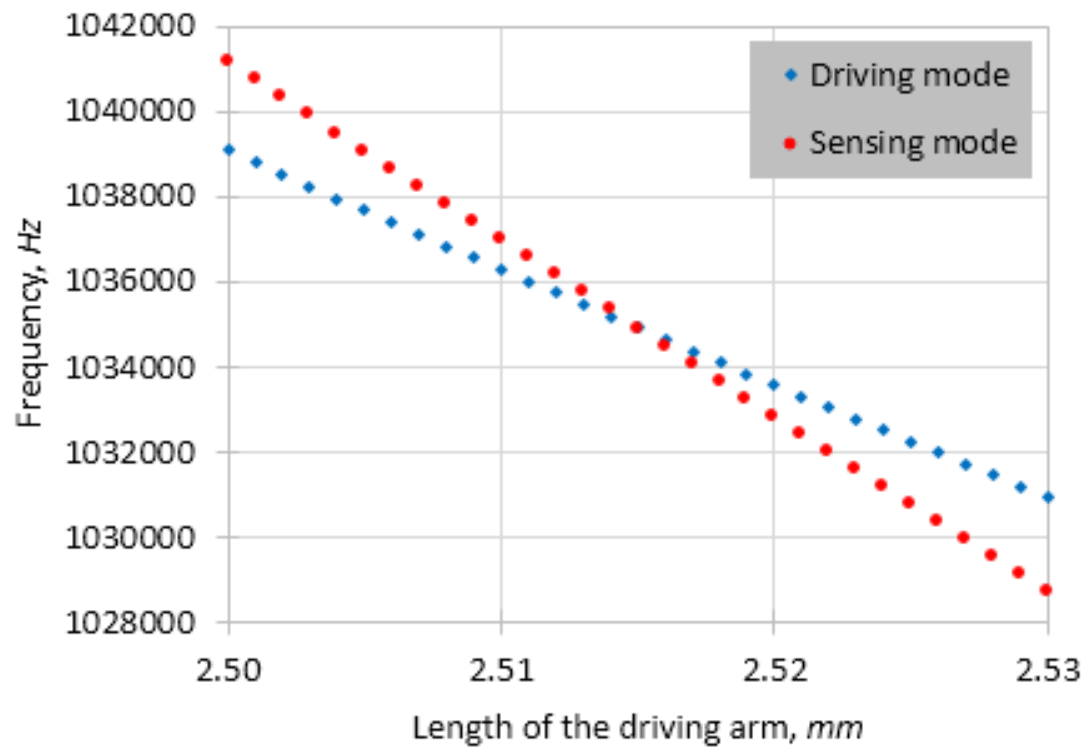
Figure 4.4.3 Frequency spectrum of the quartz gyroscope as a function of the length of the drive arm, L_D
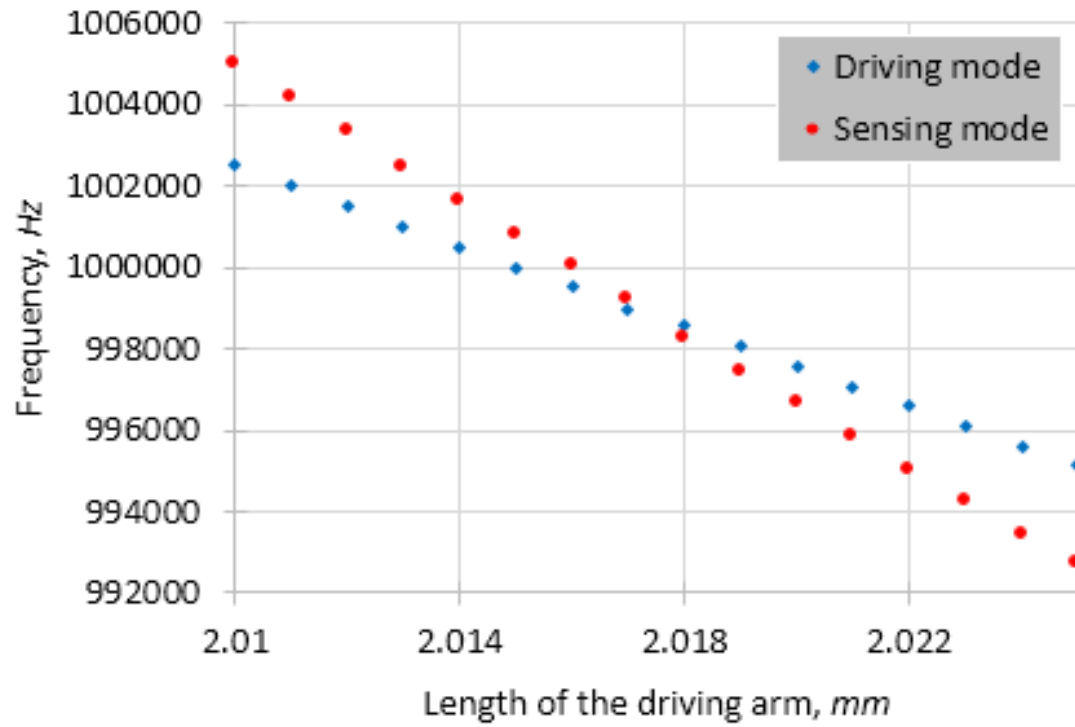
Figure 4.4.4 Frequency spectrum of the langasite gyroscope as a function of the length
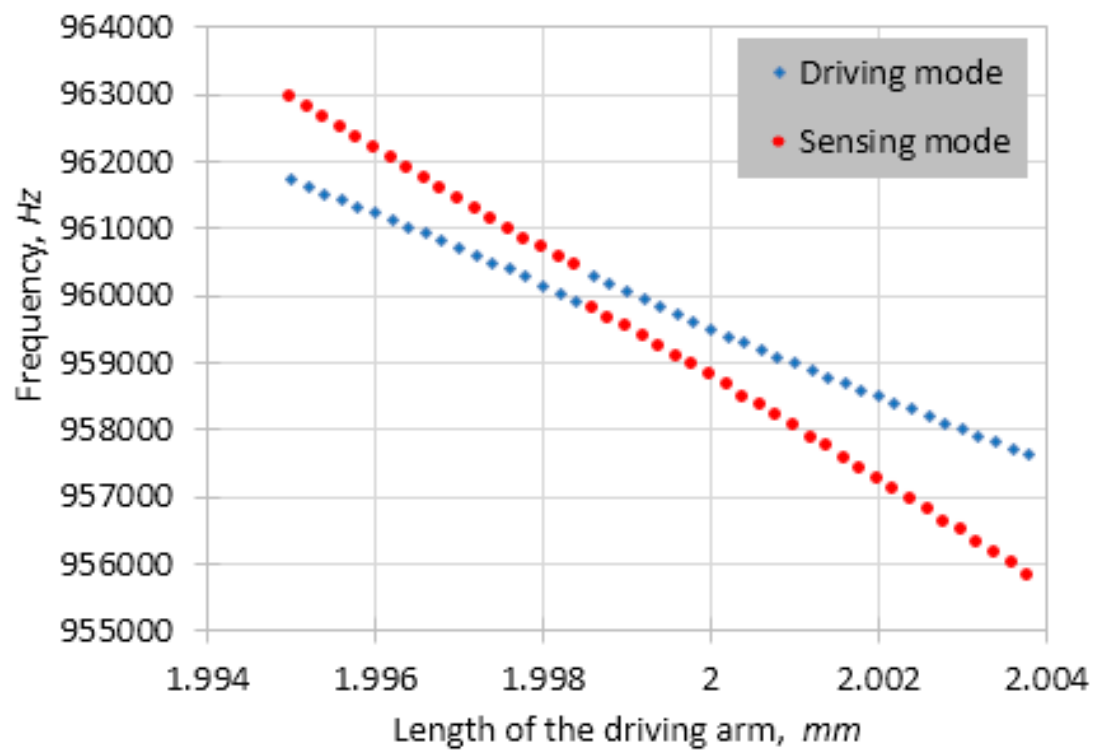
of the drive arm, L_D

Figure 4.4.5 Frequency spectrum of the langatate gyroscope as a function of the length of

the drive arm, L_D

4.4.2 Frequency response analysis

We further analyzed the length extension gyroscope with frequency response analyses using the optimized geometries of the gyroscopes of each material. The equations of the motion of the element of the rotating system rotating about z-axis are implemented in FEM simulation and they are

$$f_x = F_x + \rho\omega^2 u_x + j2\rho\Omega_z\omega u_y + \rho\Omega_z^2 x \tag{4.4.8}$$

$$f_y = F_y + \rho\omega^2 u_y - j2\rho\Omega_z\omega u_x + \rho\Omega_z^2 y \tag{4.4.9}$$

$$f_z = 0 \tag{4.4.10}$$

where f, F, u, Ω and ω are respectively the total force acting on the element, external forces, element displacement, and angular velocity and angular frequency. The x and y are the coordinates of the element. The first term and second terms of the right hand side of equation 4.4.8 and 4.4.9 are the external force and inertia forces induced by vibration. The third terms on the right hand side of equation 4.4.8 and 4.4.9 are the Coriolis force terms that we are interested in this study. Finally, the last terms of the equations are the centrifugal forces. The Coriolis forces are applied as body forces, F_b, on the entire gyroscopes in frequency response analyses to simulate the gyroscope rotation about z-axis and they are

$$F_{bx} = 2\rho\omega\Omega_z u_y \tag{4.4.11}$$

$$F_{by} = -2\rho\omega\Omega_z u_x \tag{4.4.12}$$

$$F_{bz} = 0 \tag{4.4.13}$$

where F_{bx}, F_{by} and F_{bz} are respectively the body forces applied to the entire structure in x-, y-, and z-directions. Since the vibration direction of the drive arms of the gyroscope is parallel to the angular velocity, z-axis, the Coriolis force in the z-direction is zero.

Similarly, we can also apply the Coriolis forces for rotation about x- and y-axis. The absolute values of the charges on the driving and sensing electrodes of each material as a function of the driving frequency, *fdr.,* are shown in figure 4.4.6, 4.4.7 and 4.4.8. Also, the gyroscope response of each gyroscope to angular velocity of 60 degrees/s about x-, y- and z-axis are shown in figure 4.4.9, 4.4.10 and 4.4.11. These results show that the charge are the maximum at the resonance frequency, *fdr.*, of the driving mode. It also shows that the sensitivity at the resonance will get amplified the most. The sensitivities of each gyroscope are also calculated by frequency response analyses. The electric potential was used as output signal. The gyro-sensitivities of the gyroscopes of each material are shown in figure 4.4.12, 4.4.13 and 4.4.14. The sensitivities of the quartz, langasite and langatate gyroscopes are S_z = 2.78e-4V/(deg/s), S_z = 1.60e-2V/(deg/s), S_z = -5.76e-3V/(deg/s), respectively. The sensitivity of the quartz gyroscope was calculated to be very small as expected. The sensitivities of the langasite and langatate are about 57 times and 20 times more sensitive than the quartz gyroscope. We also simulate the gyro-sensitivities of the gyroscopes rotation about the x-and y-axis. Both gyro-sensitivities were very small as expected. The quality factor, Q, is also calculated. The summary of the gyro-sensitivity of the gyroscopes are listed in Table 4.4.3. The results clearly show that the length extension gyroscope performed as a gyro-sensor.
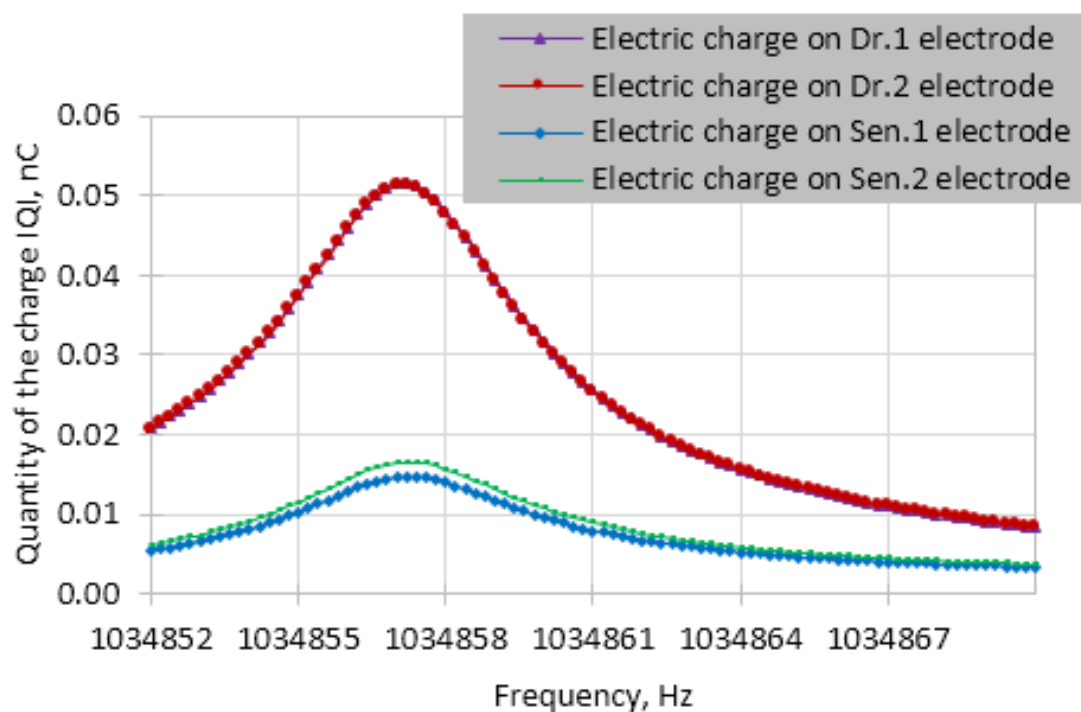
Figure 4.4.6 Frequency responses in charge at the driving and sensing electrodes for the quartz gyroscope.
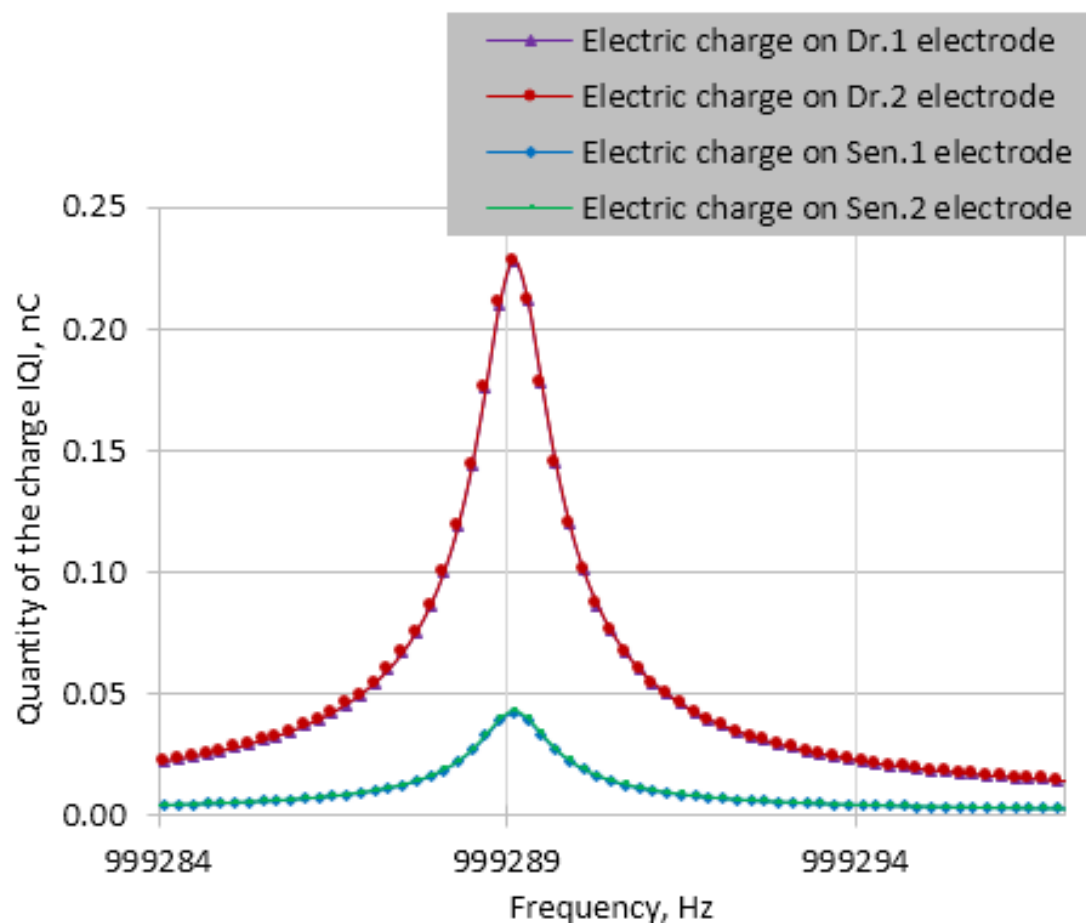
Figure 4.4.7 Frequency responses in charge at the driving and sensing electrodes for the langasite gyroscope.
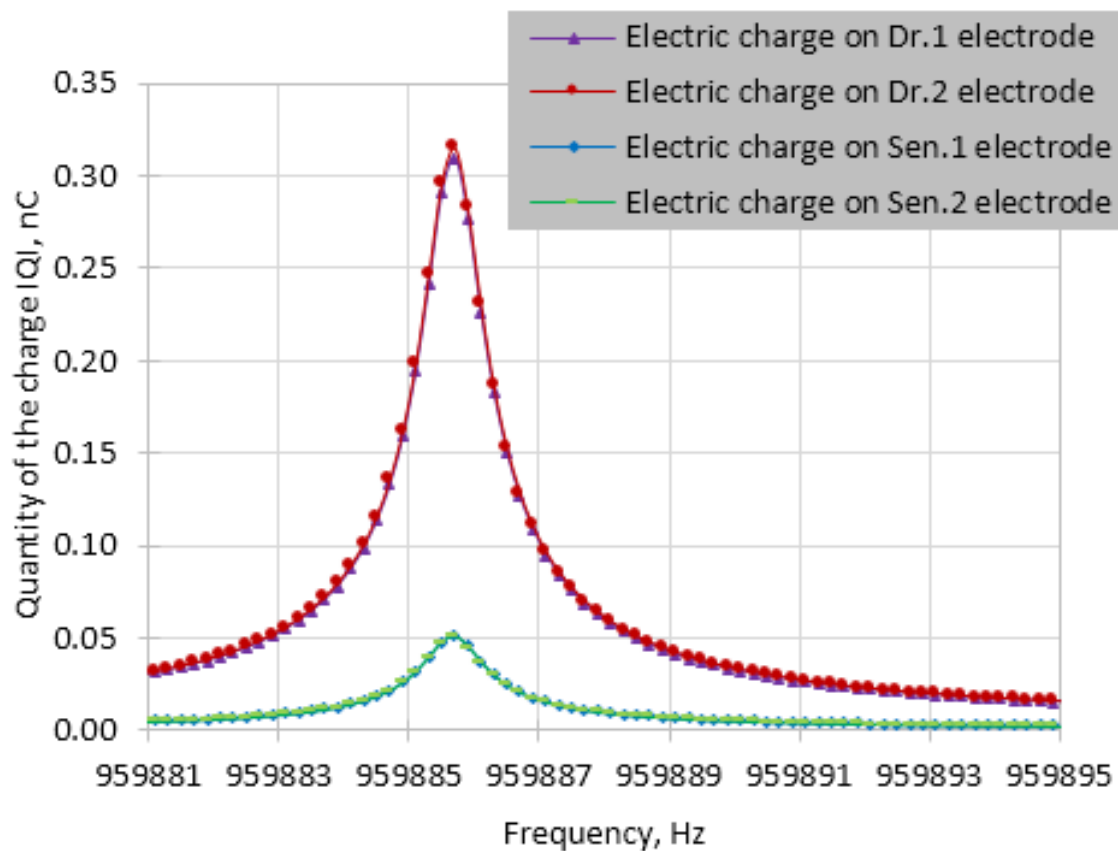
Figure 4.4.8 Frequency responses in charge at the driving and sensing electrodes for the langatate gyroscope.
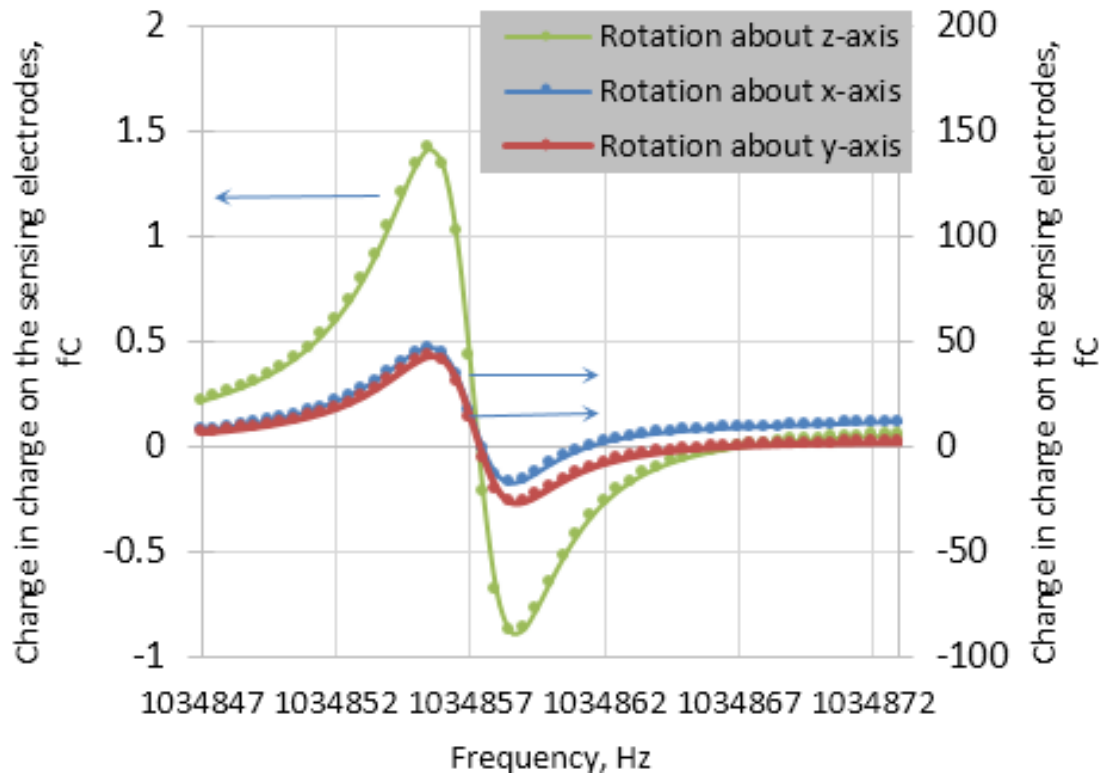
Figure 4.4.9 Gyroscope response of the quartz gyroscope to angular velocity of 60 degree/s about x-, y- and z-axis.
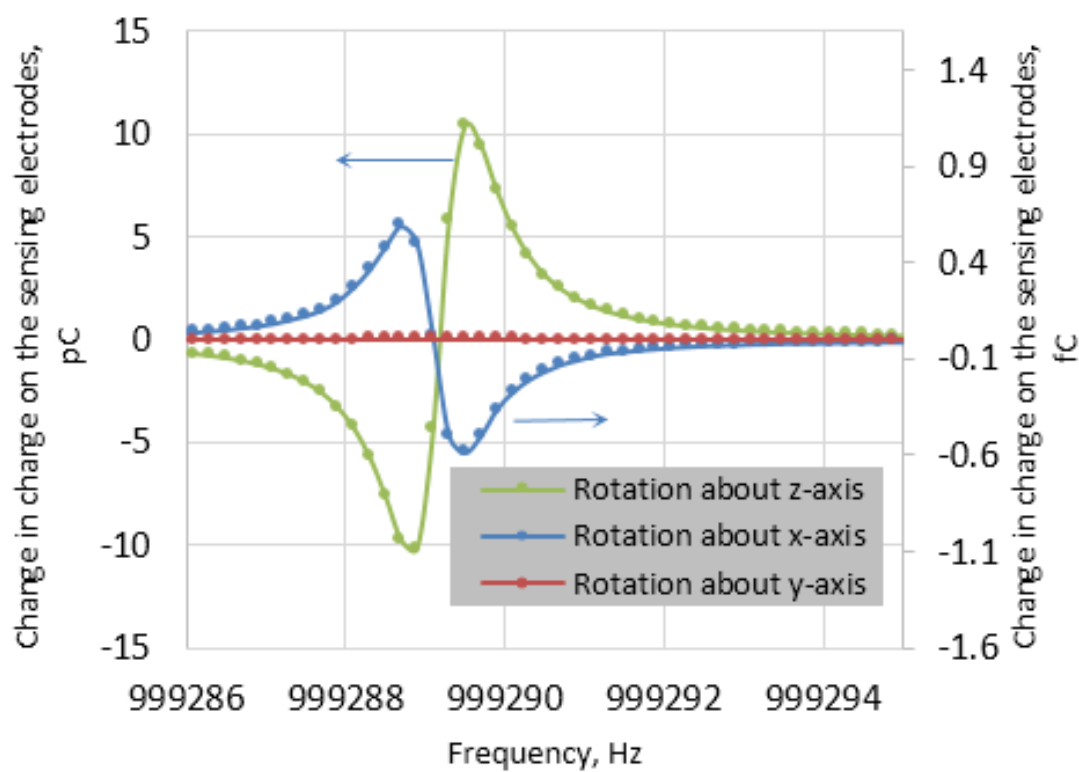
Figure 4.4.10 Gyroscope response of the langasite gyroscope to angular velocity of 60 degree/s about x-, y- and z-axis.
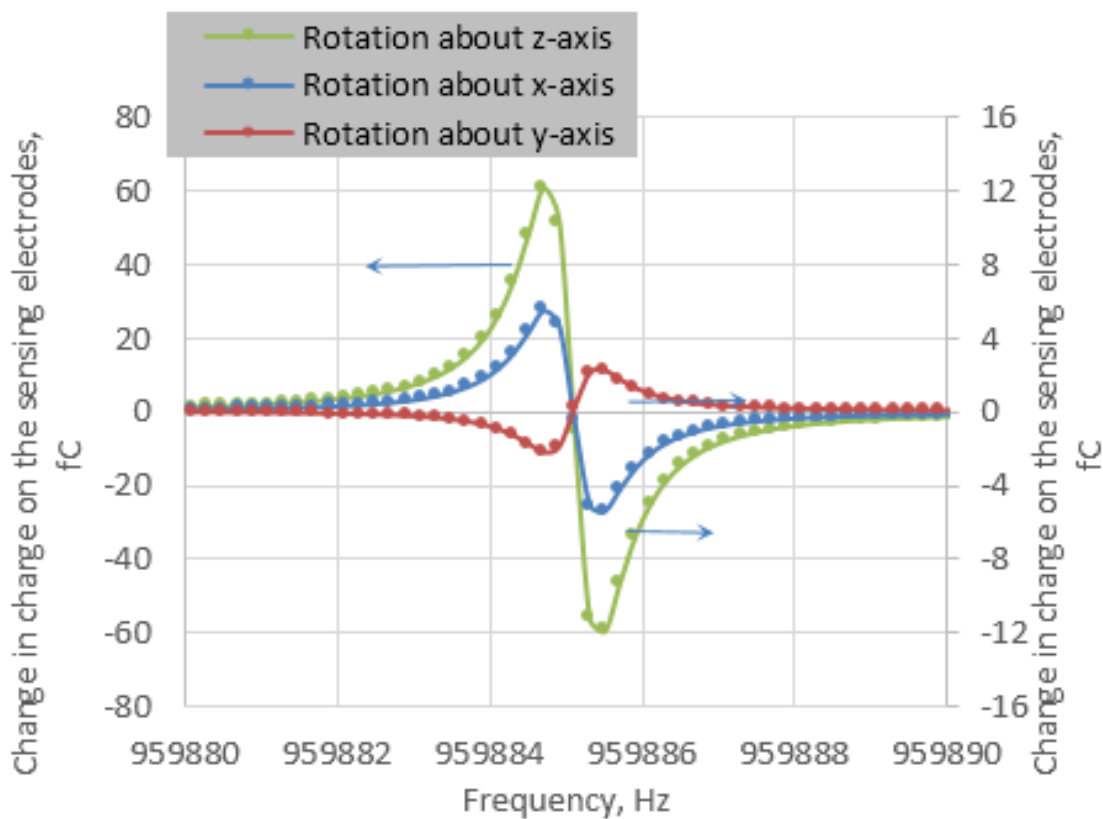
Figure 4.4.11 Gyroscope response of the langatate gyroscope to angular velocity of 60 degree/s about x-, y- and z-axis.
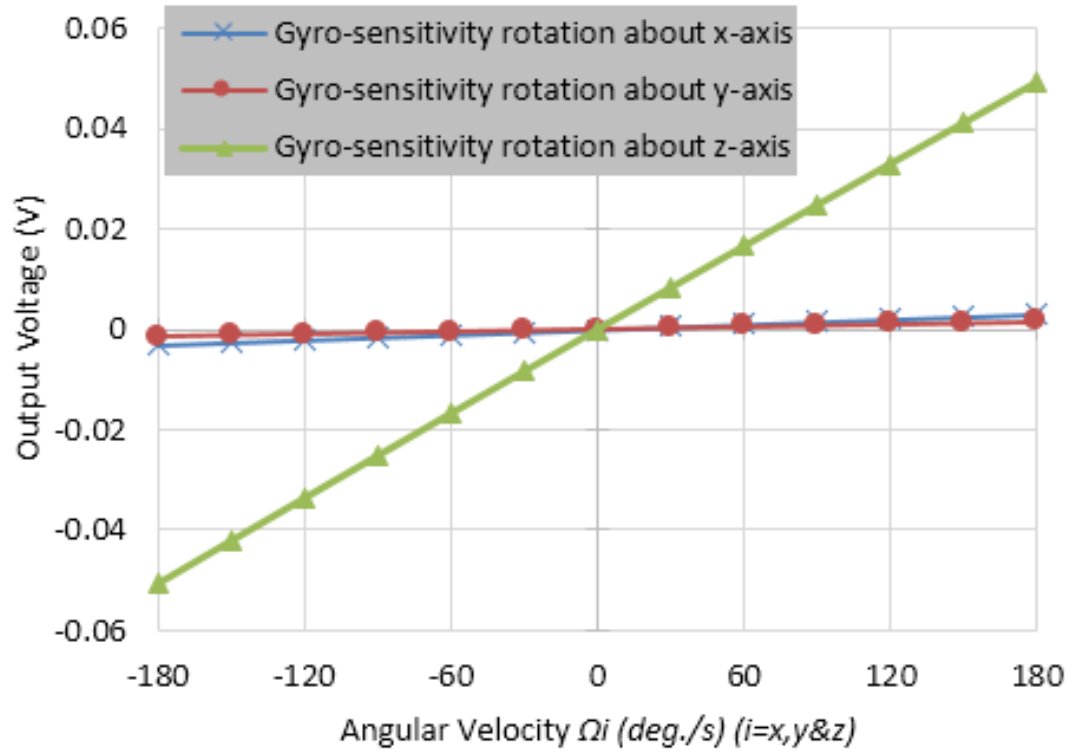
Figure 4.4.12 Gyroscopic sensitivty of the quartz gyroscope rotation about x-,y- and z-axis.
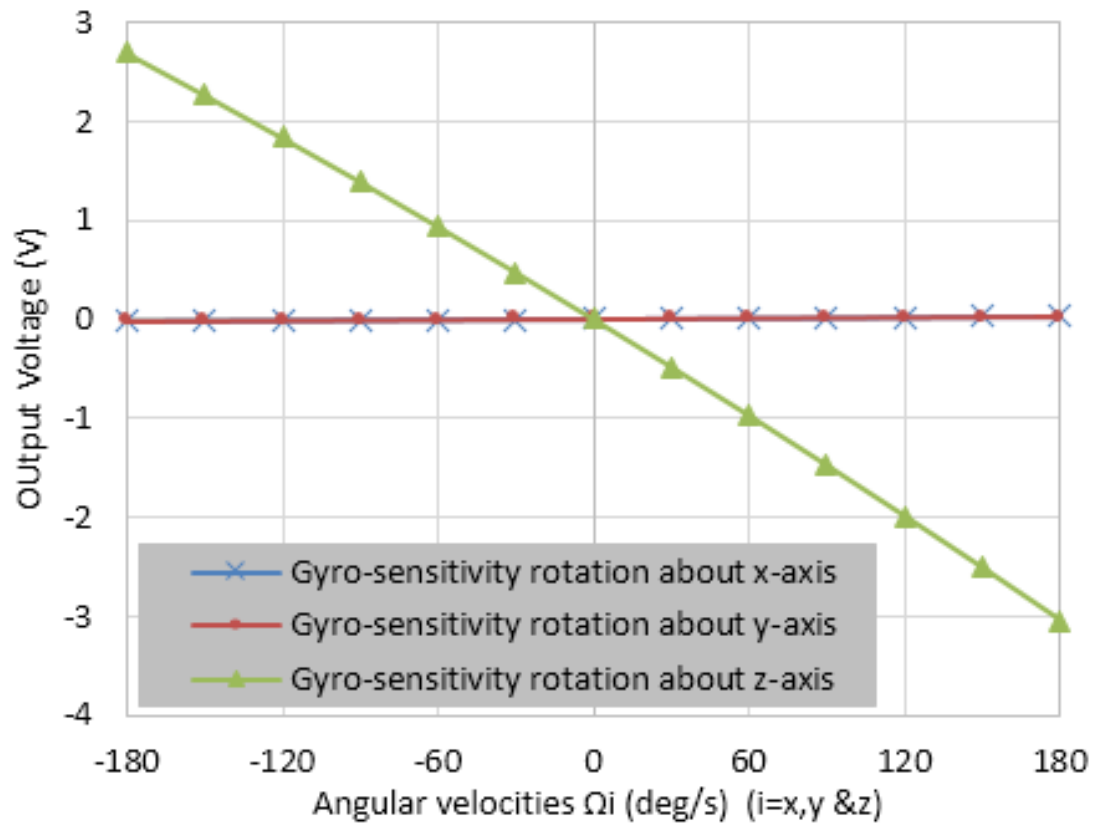
Figure 4.4.13 Gyroscopic sensitivity of the langsite gyroscope rotation about x-,y- and z-axis.
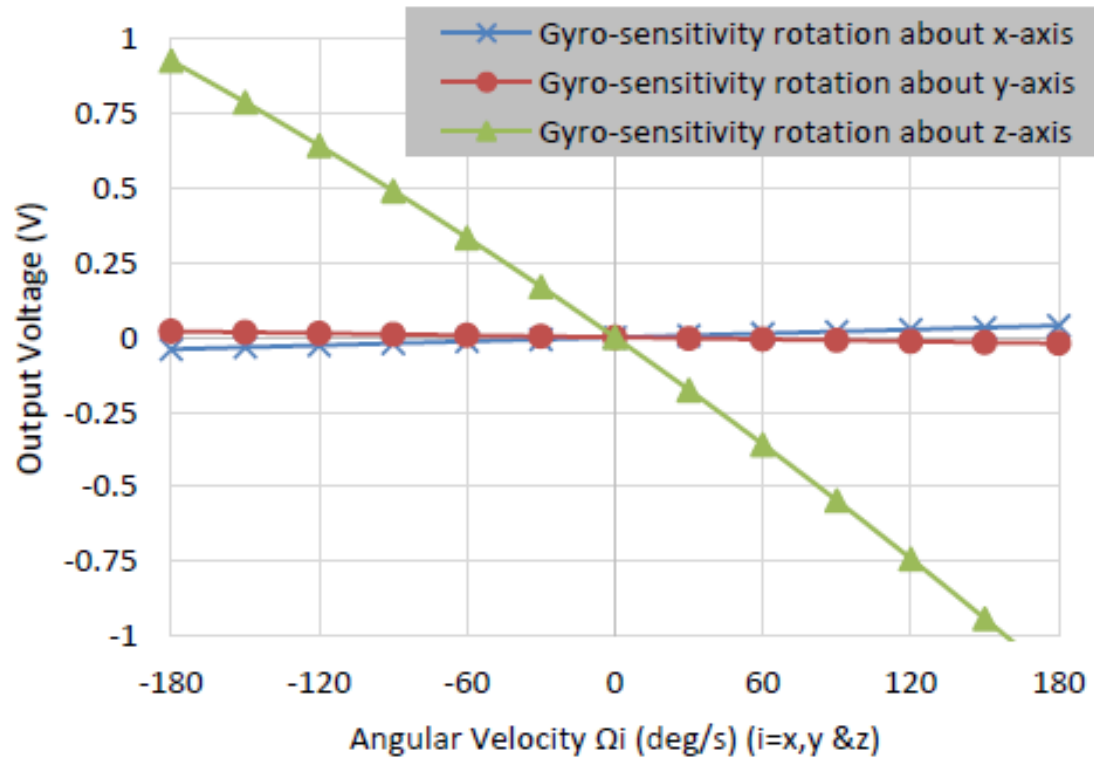
Figure 4.4.14 Gyroscopic sensitivity of the langtate gyroscope rotation about x-,y- and z-axis

Table 4.4.3 The driving and sensing frequencies of the gyroscopes and sensitivities of the gyroscopes of each material.

	Units	Quartz	Langasite	Langatate
f dr.	*Hz*	1034888	999496	960028.3
f sens.	*Hz*	1034854	999999.7	960547.6
Sx	*V/(deg/s)*	8.46e -6	1.52e-4	2.18e-4
Sy	*V/(deg/s)*	1.70e-6	8.90e-5	-1.12e-4
Sz	*V/(deg/s)*	2.78e-4	-1.6e-2	-5.76e-3
Q		230048	970375	687081

4.5   Frequency-Temperature Analysis of the Langasite

The frequency-temperature behavior of the gyroscope is an important criterion of a design of the langasite, since small shift in drive frequency can significantly reduce the gyroscopic sensitivity of the gyroscope. However, many researchers or engineers do aware of this effect when they design the gyroscope. In this chapter, the frequency-temperature behavior of the langasite length-extension gyroscope is studied. We only considered the langasite gyroscope, since we do not have all the material properties of the langatate such as third-order non-linear elastic constants or higher order temperature constants.

We implemented the non-linear questions from chapter 5 into Comsol Multiphysics softweare to compute the frequency-temperature curves of the gyroscopes. The simulation involves two steps, stationary and eigenfrequency. In the stationary analysis, only the solid mechanics module is involved, which determines the material behavior affects by the temperature chages. In the eigenfrequency analysis, the changes of drive frequency of the gyroscope as a function of temperature is calculated. Please see chapter 5 for more details.

The figure 4.5.1 and 4.5.2 show the temperature–frequency curve of the quartz and langasite length-extension gyroscope. Both gyroscopes are not temperature compensated, as the curves nearly linear. The cubic and parabolic curves can be expected for quartz and langasite gyroscopes, respectively, when the gyroscopes are temperature compensated. The langasite curve can only be parabola in this case, since we do not have third-order temperature coefficients of langasite. For more detail of the non-linear parameters and variable of Comsol sostware please see Appendix D.
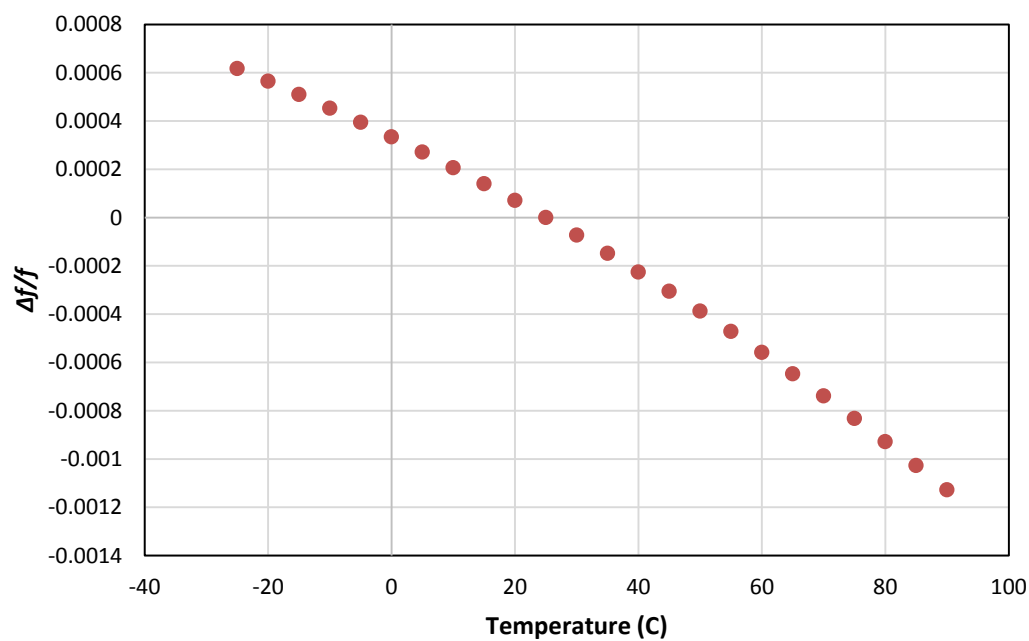
Figure 4.5.1 The temperature–frequency curve of the quartz gyroscope
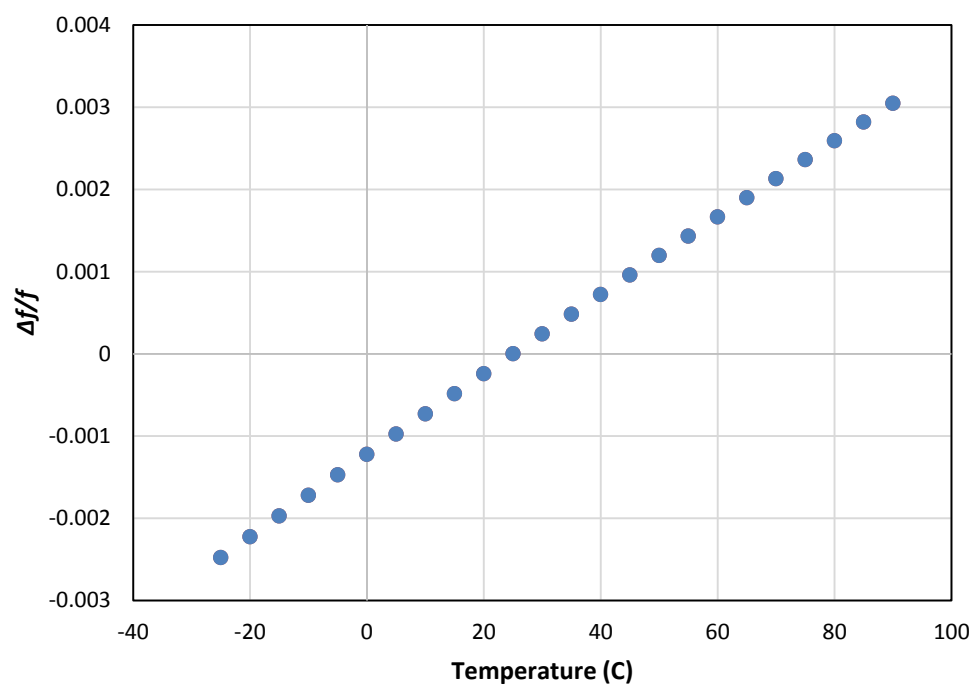
Figure 4.5.2 The temperature–frequency curve of the langasite gyroscope

4.6   SUMMARY

A novel design of the length extension gyroscope is proposed and it is analyzed with the finite element analysis software. The calculated optimum cut angle for a singly rotated quartz crystal have $\phi=0°$, $\theta=-9°$, a singly rotated langasite crystal have $\phi=0°$, $\theta=24°$ and a singly rotated langatate have $\phi=0°$, $\theta=24°$, respectively. The sizes of the gyroscopes vary due to the material properties and length of the driving arms. Overall sizes of the langasite and langatate gyroscopes are smaller than the quartz gyroscope and these two are nearly the same size. The gyro-sensitivity rotations about z-axis of quartz, langasite and langatate gyroscopes were 2.78e-4 *V/(deg/s)*, -1.60e-2 *V/(deg/s)* and -1.6e-2 *V/(deg/s)*. The results show that the finite element method to design the gyroscope are reliable and the newly designed length extension gyroscope can be used as a gyro-sensor. Moreover, the langasite and langatate gyroscope provided stronger sensitivity to angular velocity than the quartz gyroscope as we expected. The gyro- sensitivities of the gyroscopes are also a function of the geometry of the gyroscope. The length extension gyroscope is also able to detect the angular velocities about the other two axes(x- and y-axes).

Chapter 5. The Frequency-Temperature Behavior of Langasite

5.1   Introduction

Frequency control and stability of the resonator or piezoelectric sensor at high frequency or higher sensitivity is one of the most important criteria in the design of piezoelectric sensor. The quartz crystal has been used for many applications due to its temperature stability. For example, the AT-cut is the most well-known and most used type in resonator. It has a frequency temperature coefficient described by a cubic function of temperature whereas most other crystal cuts give a parabolic temperature characteristic. The frequency-temperature curve of the fundamental thickness-shear vibration of AT-cut is shown in Figure 5.1.1.

The langasite and langatate are highly attractive piezoelectric materials for the high temperature environment due to their temperature frequency coefficient (TFC) and their temperature stability. Especially, the langasite and its isomorphs have the quite unique temperature compensate property that is similar to the quartz crystal [29] [30] [31]. Therefore, these crystals are of current interest for BAW applications [32]. The complete sets of the materials properties of quartz, langasite and langastate are listed in Appendix C. The analysis on the temperature-frequency behavior of langatate has not performed in this dissertation, since third-order non-linear elastic constants of langatate have not published

The non-linear field equations of thermo-elasticity in Langrangian formulation are used to develop the three dimensional linear field equations for small vibration superposed on thermally induced deformations by stead and uniform temperature change. This Lagrangian formulation consist with three states, the natural state, initial state and final state [33] [34] [35] [36].
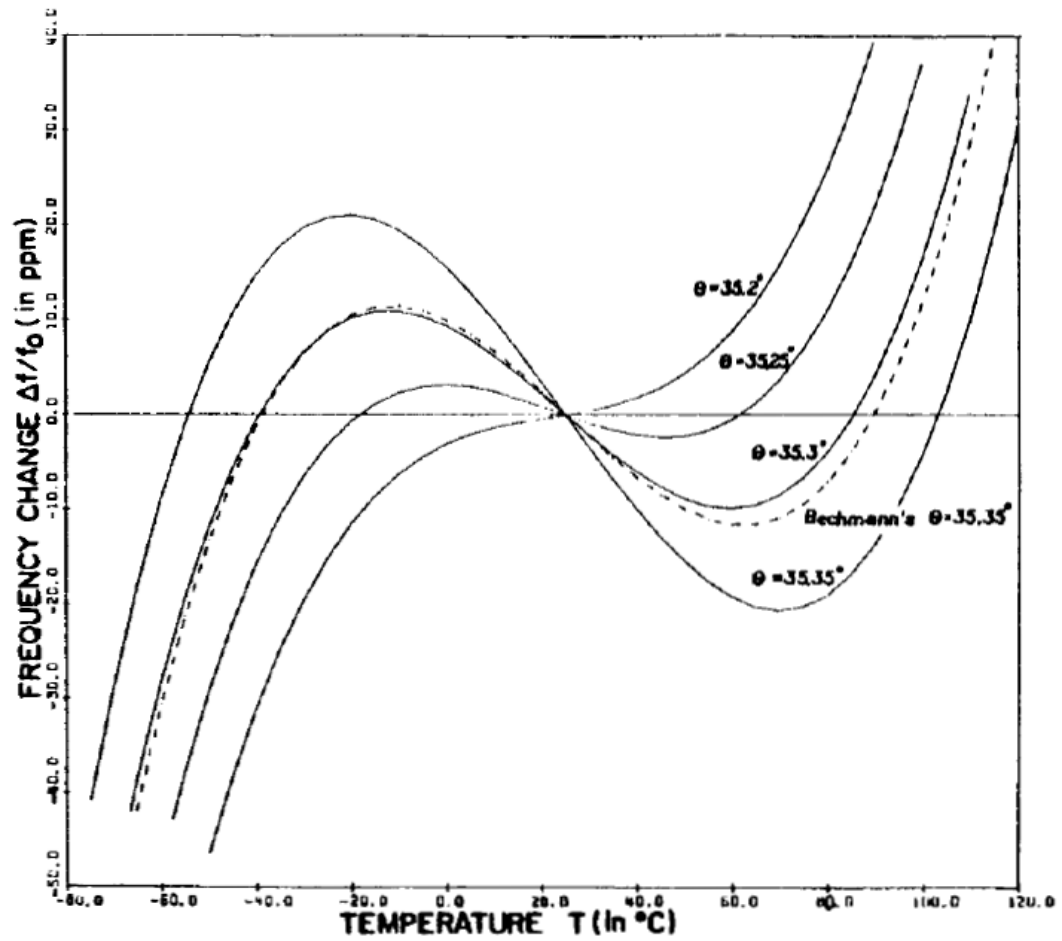
Figure 5.1.1 Frequency-temperature curves of the fundamental thickness-shear vibration of AT-cut plate. [34]
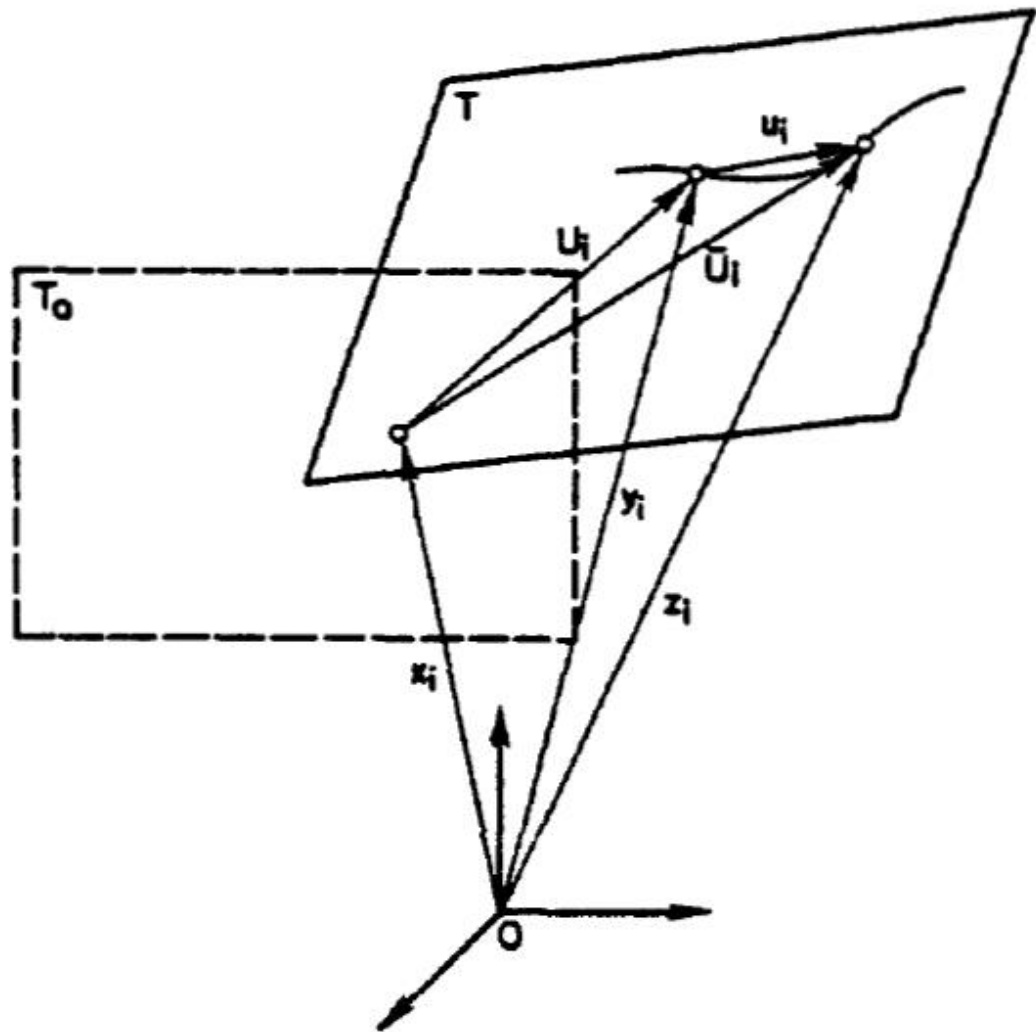
Figure 5.1.2 positions of a material point at the natural, initial and final state. [34]

5.2   Equation of Motion for Small Vibrations Superposed on Thermally Induced Deformations

The non-linear equations of thermo-elasticity in Lagrangian formation consist of three steps, natural state, initial state and final state. The incremental equations are conveniently derived with the following definitions:

T_o : Reference temperature

T : Final temperature from the reference temperature

θ : Temperature increment respect to reference temperature $T\text{-}T_0$

U_i : Displacement at initial state

$\bar{U}_i$: Total displacement from the natural state to final state

u_i : Incremental displacement

E_{ij}: Lagrangian strain tensor at initial state

$\bar{E}_{ij}$: Total strain tensor from the natural state to final state

e_{ij}: Incremental strain

T_{ij} : Kirchoff - Piola stress tensor at initial state

$\bar{T}_{ij}$: Total stress tensor from the natural state to final state

t_{ij} : Incremental stress

P_i: Surface traction at initial state

$\bar{P}_i$: Total traction from the natural state to final state

p_i: Incremental traction

n_i: Unit outward normal vector to S

C_{ijkl}: Second-order elastic stiffnesses of the crystal

C_{ijklmn}: Third-order elastic stiffnesses of the crystal

$C_{ijklmnpq}$: Four-order elastic stiffnesses of the crystal

$C_{ijkl}^{(1)}$: First temperature derivative of the second-order elastic stiffnesses of the crystal

$\tilde{C}_{ijkl}^{(2)}$: Effective Second temperature derivative of the second-order elastic stiffnesses of the crystal

λ_{ij}^{θ} : Stress coefficient of temperature

α_{ij}^{θ} : Thermal expansion coefficient

The first state is the natural state where crystal is at rest, free of stress and strain with a uniform temperature T_0 as shown in figure 5.1.2. The rectangular Cartesian coordinate system is used to illustrate the position of a material point as shown in figure 5.1.2. x_i (i=1,2,3) is the position of a material point and T_0 is the reference temperature.

Next state is the initial state which crystal is subject to a steady and uniform temperature increase from T_0 to T. In this state, the material is allows expand freely and the position of a material is moved from x_i to y_i due to the increases of the temperature. The non-linear equation of the thermo-elasticity in Lagrangian formulation can be written as:

(a) Displacement

$$U_i = y_i - x_i \tag{5.2.1}$$

(b) Strain

$$E_{ij} = \frac{1}{2}(U_{j,i} + U_{i,j} + U_{k,i}\,U_{k,j}) \tag{5.2.2}$$

(c) Stress-strain-temperature relations

$$T_{ij} =$$

$$C^{\theta}_{ijkl}E_{kl} + \frac{1}{2}C^{\theta}_{ijklmn}E_{kl}E_{mn} + \frac{1}{6}C^{\theta}_{ijklmnpq}E_{kl}E_{mn}E_{pq} +$$

$$\frac{1}{24}C^{\theta}_{ijklmnpqrs}E_{kl}E_{mn}E_{pq}E_{rs} - \lambda^{\theta}_{ij} \qquad (5.2.3)$$

(d) Stress equation of motion

$$(T_{ij} + T_{jk}U_{i,k})_{,j} = \rho \ddot{U}_i \qquad (5.2.4)$$

(e) Traction-stress tensor relation

$$P_i = n_j\,(T_{ij} + T_{jk}U_{i,k})\ \text{on}\ S \qquad (5.2.5)$$

In the stress-strain-temperature relations equation, equation 5.2.3, material properties can

be assume to be temperature dependent and have polynomial form.

$$C^{\theta}_{ijkl} = C_{ijkl} + C^{(1)}_{ijkl} + \frac{1}{2}\,C^{(2)}_{ijkl}\,\theta^2 + \frac{1}{6}\,C^{(3)}_{ijkl}\,\theta^3 \qquad (5.2.6)$$

$$C^{\theta}_{ijklmn} = C_{ijklmn} + C^{(1)}_{ijklmn}\,\theta + \frac{1}{2}C^{(2)}_{ijklmn}\,\theta \qquad (5.2.7)$$

$$C^{\theta}_{ijklmnpq} = C_{ijklmnpq} + C^{(1)}_{ijklmnpq}\theta \qquad (5.2.8)$$

$$C^{\theta}_{ijklmnpq} = C_{ijklmnpqrs} \qquad (5.2.9)$$

$$\lambda^{\theta}_{ij} = \lambda^1_{ij}\,\theta + \lambda^2_{ij}\,\theta^2 + \lambda^3_{ij}\,\theta^3 + \lambda^4_{ij}\,\theta^4 \qquad (5.2.10)$$

where

$$C^{(n)}_{ijkl} = \left.\frac{\partial^n C^{\theta}_{ijkl}}{\partial T^n}\right|_{T_0}, \qquad n = 1,2,3 \qquad (5.2.11)$$

$$C^{(n)}_{ijklmn} = \left.\frac{\partial^n C^{\theta}_{ijklmn}}{\partial T^n}\right|_{T_0}, \qquad n = 1,2 \qquad (5.2.12)$$

$$C^{(n)}_{ijklmnpq} = \left.\frac{\partial^n C^{\theta}_{ijklmn}}{\partial T^n}\right|_{T_0}, \qquad n = 1 \qquad (5.2.13)$$

The equation 5.2.11, 5.2.12 and 5.2.13 are temperature derivatives of the elastic stiffnesses evaluated at the reference temperature in the natural state. The linear thermal expansion coefficients are symmetric and have polynomial form as shown in equation 5.2.14.

$$\alpha_{ij}^{\theta} = \alpha_{ij}^{1} \, \theta + \alpha_{ij}^{2} \, \theta^2 + \alpha_{ij}^{3} \, \theta^3 \tag{5.2.14}$$

$$\frac{1}{2} \left(U_{j,i} + U_{i,j} \right) = \alpha_{ij}^{\theta} = \alpha_{ji}^{\theta} \tag{5.2.15}$$

If the equation 5.2.14 is the linear thermal expansion which measured instead of stress coefficient, λ_{ij}^{θ}, the equation 5.2.2 can be written in terms of thermal coefficient expansion.

$$E_{ij} = \alpha_{ij}^{\theta} + \frac{1}{2} \, \alpha_{ki}^{\theta} \alpha_{kj}^{\theta} \tag{5.2.16}$$

In the innitial fields the plate is at rest and allowed free exapansion. Also, any higher term are neglected since higher order terms are much smaller than first term in equation 5.2.16.

$$U_{j,i} = U_{i,j} = E_{ij} = \alpha_{ij}^{\theta} \tag{5.2.17}$$

$$T_{ij} = 0 \tag{5.2.18}$$

$$\ddot{U}_i = 0 \tag{5.2.19}$$

In the final state, small vibration is superposed with the thermally induced deformation. The governing equations for final state is similir to initial state. In this state, the material point is moved from y_i to z_i. Therefore, incremental displament can be calculated by simply taking the different between the final state displacement and the initial state displacement, $u_i = z_i - y_i$ as shown in equation 5.2.20. The variable at the final state is denoted by "barred" quantity.

$$\overline{U_i} = U_i + u_i = z_i - x_i \tag{5.2.20}$$

Similarity, strain, stress and traction at the final state can be defined as:

$$\overline{E}_{ij} = E_{ij} + e_{ij} \tag{5.2.21}$$

$$\overline{T}_{ij} = T_{ij} + t_{ij} \tag{5.2.22}$$

$$\overline{P}_i = P_i + p_i \tag{5.2.23}$$

The governing equations for final state are similir to initial state and they are:

$$\overline{E}_{ij} = \tfrac{1}{2}(\overline{U}_{j,i} + \overline{U}_{i,j} + \overline{U}_{k,i}\,\overline{U}_{k,j}) \tag{5.2.24}$$

$$\overline{T}_{ij} =$$

$$C^\theta_{ijkl}\overline{E}_{kl} + \tfrac{1}{2}C^\theta_{ijklmn}\overline{E}_{kl}\overline{E}_{mn} + \tfrac{1}{6}C^\theta_{ijklmnpq}\overline{E}_{kl}\overline{E}_{mn}\overline{E}_{pq} +$$

$$\tfrac{1}{24}C^\theta_{ijklmnpqrs}\overline{E}_{kl}\overline{E}_{mn}\overline{E}_{pq}\overline{E}_{rs} - \lambda^\theta_{ij} \tag{5.2.25}$$

$$(\overline{T}_{ij} + \overline{T}_{jk}\overline{U}_{i,k})_{,j} = \rho\ddot{U}_i \tag{5.2.26}$$

$$\overline{P}_i = n_j(\overline{T}_{ij} + \overline{U}_{i,k}) \qquad \text{on } S \tag{5.2.27}$$

As the temperature at the final state does not change, the governing equation for incremental fields can be calculated by substracting initial state from final stateas and they are defined as:

$$e_{ij} = \tfrac{1}{2}(u_{j,i} + u_{i,j} + U_{k,j}u_{k,i} + U_{k,i}u_{k,j}) \tag{5.2.28}$$

$$t_{ij} = \left(C^\theta_{ijkl} + C^\theta_{ijklmn}E_{mn} + \tfrac{1}{2}C^\theta_{ijklmnpq}E_{mn}E_{pq} + \tfrac{1}{6}C^\theta_{ijklmnpqrs}E_{mn}E_{pq}E_{rs}\right)e_{kl} \tag{5.2.29}$$

$$(t_{ij} + t_{jk}U_{i,k} + T_{jk}u_{i,k})_{,j} = \rho_0\ddot{u}_i \tag{5.2.30}$$

$$p_i = n_j(t_{ij} + t_{jk}U_{i,k} + T_{jk}u_{i,k}) \text{ on } S \tag{5.2.31}$$

In the governing equation of incremental fields, the incremental deforemation are assumed to be small and product terms are negliected.

By substituing equation 5.2.17 into 5.2.28, the incremental strain-displacement relation can be defined as:

$$e_{ij} = \frac{1}{2}\left(u_{j,i} + u_{i,j} + a_{kj}^\theta u_{k,i} + a_{ki}^\theta u_{k,j}\right) \tag{5.2.32}$$

By substituting equation 5.2.6,5.2.7 and 5.2.8 into equation 5.2.29, the stress-strain-temperature relations can be defined as:

$$t_{ij} = \left(C_{ijkl} + D_{ijkl}^{(1)}\theta + D_{ijkl}^{(2)}\theta^2 + D_{ijkl}^{(3)}\theta^3\right)e_{kl} \tag{5.2.33}$$

where

$$D_{ijkl}^{(1)} = C_{ijkl}^{(1)} + C_{ijklmn}\alpha_{mn}^{(1)}$$

$$D_{ijkl}^{(2)} = \frac{1}{2}\tilde{C}_{ijkl}^{(2)} + C_{ijklmn}\alpha_{mn}^{(2)}$$

$$D_{ijkl}^{(3)} = \frac{1}{6}\tilde{C}_{ijkl}^{(3)} + C_{ijklmn}\alpha_{mn}^{(3)}$$

$$\tilde{C}_{ijkl}^{(2)} = C_{ijkl}^{(2)} + 2C_{ijklmn}^{(1)}\alpha_{mn}^{(1)} + C_{ijklmnpq}\alpha_{mn}^{(1)}\alpha_{pq}^{(1)}$$

$$\tilde{C}_{ijkl}^{(3)}$$

$$= C_{ijkl}^{(3)} + 3C_{ijklmn}^{(2)}\alpha_{mn}^{(1)} + 6C_{ijklmn}\alpha_{mn}^{(2)}$$

$$+ 6C_{ijklmnpq}\alpha_{mn}^{(1)}\alpha_{pq}^{(2)} + 3C_{ijklmnpq}^{(1)}\alpha_{mn}^{(1)}\alpha_{pq}^{(1)}$$

$$+ C_{ijklmnpqrs}\alpha_{mn}^{(1)}\alpha_{pq}^{(1)}\alpha_{rs}^{(1)}$$

Similary, the stress equations of motion can be caluclated and they are defined as:

$$(t_{ij} + \alpha_{ik}^{\theta} t_{jk})_{,j} = \rho_0 \ddot{u}_i \tag{5.2.34}$$

$$p_i = n_j(t_{ij} + \alpha_{ik}^{\theta} t_{jk}) \text{ on } S \tag{5.2.35}$$

Finally , the incremental displacment euqation of the motion and the traction boundary condition can be defined by substituting equation 5.2.16 and 5.2.32 into equation 5.2.33 and then, equation 5.2.34 into 5.2.35.

$$G_{ijkl} u_{k.jl} = \rho_0 \ddot{u}_i \tag{5.2.36}$$

$$p_i = n_j G_{ijkl} u_{k,l} \qquad \text{on } S \tag{5.2.37}$$

where

$$G_{ijkl} = C_{ijkl} + G_{ijkl}^{(1)} \theta + G_{ijkl}^{(2)} \theta^2 \tag{5.2.38}$$

$$G_{ijkl}^{(1)} = G_{sjkl} \alpha_{is}^{(1)} + G_{ijsl} \alpha_{ks}^{(1)} + G_{ijklmn} \alpha_{mn}^{(1)} + G_{ijkl}^{(1)} \tag{5.2.39}$$

$$G_{ijkl}^{(2)} = C_{sjtl} \alpha_{is}^{(1)} \alpha_{kt}^{(1)} + C_{sjkl} \alpha_{is}^{(2)} + C_{ijsl} \alpha_{ks}^{(2)} + C_{sjkl}^{(1)} \alpha_{is}^{(1)} + C_{ijsl}^{(1)} \alpha_{ks}^{(1)} +$$
$$C_{sjklmn} \alpha_{is}^{(1)} \alpha_{mn}^{(1)} + C_{ijslmn} \alpha_{ks}^{(1)} \alpha_{mn}^{(1)} + C_{ijklmn} \alpha_{mn}^{(2)} + \frac{1}{2} \tilde{C}_{ijkl}^{(2)} \tag{5.2.40}$$

$$G_{ijkl}^{(3)} = \frac{1}{6} \tilde{C}_{ijkl}^{(3)} + C_{ijklmn} \alpha_{mn}^{(3)} + C_{ijsl} \alpha_{ks}^{(3)} + C_{sjkl} \alpha_{is}^{(3)} + C_{ijsl}^{(1)} \alpha_{ks}^{(2)} + C_{sjkl}^{(1)} \alpha_{is}^{(2)} +$$
$$C_{ijslmn} \alpha_{mn}^{(1)} \alpha_{ks}^{(2)} + C_{sjklmn} \alpha_{mn}^{(2)} \alpha_{ks}^{(1)} + \frac{1}{2} \tilde{C}_{ijsl}^{(2)} \alpha_{is}^{(1)} + C_{ijslmn} \alpha_{mn}^{(2)} \alpha_{ks}^{(1)} +$$
$$C_{sjklmn} \alpha_{mn}^{(2)} \alpha_{is}^{(1)} + C_{sjtl} \alpha_{is}^{(1)} \alpha_{kt}^{(2)} + C_{sjtl} \alpha_{is}^{(2)} \alpha_{kt}^{(1)} + C_{sjtl}^{(1)} \alpha_{is}^{(1)} \alpha_{kt}^{(1)} +$$
$$C_{sjtlmn} \alpha_{mn}^{(1)} \alpha_{is}^{(1)} \alpha_{ky}^{(1)} \tag{5.2.41}$$

Since the $D_{ijkl}^{(n)}$ and $\tilde{C}_{ijkl}^{(2)}$ have same symmetry as C_{ijkl} from equation 5.2.33, 5.2.36, 5.2.37 and 5.2.38, we can say

$$G_{ijkl}^{(n)} = G_{klij}^{(n)} \tag{5.2.42}$$

but

$$G_{ijkl}^{(n)} \neq G_{jikl}^{(n)} \neq G_{ijkl}^{(n)}$$

The non-llinear equations become to linear euqations when $\theta=0$. For the small vibration supeorsed on homogeneous thermal strain only required $C_{ijkl}^{(1)}$ and $\tilde{C}_{ijkl}^{(2)}$ to describe the temperature dependence of elastic stiffnesses up to the second power of θ based on above equations. As previously mentioned , we cannot calculate highter than second power of θ since there is no measured values of effective third-order temperautre derivative.

5.2.1 Thickness Vibration

We let x_i ($i = 1,2,3$) be the cystallographical axes of the crystals. By IEEE,a doubly rotated crystal plate is defined by (y,x,ω,l) ϕ, θ. The crystal plate has thickness of $2b$ as shown in figure 5.3 which n_i denote the unit outward normal to the faces of the plate in the natural state. Refer to the crysallographic axes and the figure 5.3, the unit normal components are:

$$n_1 = -\cos\theta\sin\emptyset$$

$$n_2 = \cos\theta\sin\emptyset$$

$$n_3 = \sin\theta \tag{5.2.43}$$

For traction free face conditions, equation 5.2.37 becomes

$$p_i = n_j G_{ijkl} u_{k,l} = 0 \quad \text{at } n_j X_j = \pm b \tag{5.2.44}$$

For solution of equation 5.2.36, for harmonic and antisymmetric thickness vibrations

$$u_k = A_k \sin\xi n_p X_p e^{i\omega t} \tag{5.2.45}$$

By substituting equation 5.2.45 into the 5.2.36 and 5.2.44, we can get

$$(Q_{ik} - \lambda\delta_{ik})A_k = 0 \tag{5.2.46}$$

where

$$\xi = \frac{n\pi}{2b}, \quad n = 1,3,5\ldots$$

$$Q_{ik} = Q_{ki} = G_{ijkl}n_j n_l$$

$$\lambda = \rho_0 \frac{\omega^2}{\xi^2} = \rho_0 \left(\frac{2b\omega}{n\pi}\right)^2$$

The equation 5.2.46 is the eigenvalue problem with the measured quantity, Q_{ik}. The amplitutute A_k and eignenvalue λ are temperature dependent with the equation 5.2.46.

$$A_k = A_k^{(0)} + A_k^{(1)}\theta + A_k^{(2)}\theta^2 + A_k^{(3)}\theta^3$$

$$\lambda = \lambda^{(0)} + \lambda^{(1)}\theta + \lambda^{(2)}\theta^2 + \lambda^{(3)}\theta^3 \qquad (5.2.47)$$

By inseting equation 5.2.47 into equation 5.2.46, the eigenvalue problems of powers of θ can be obtained.

$$\theta^0 : \quad \left[Q_k^{(0)} - \lambda^{(0)}\delta_{ik}\right]A_k^{(0)} = 0$$

$$\theta^1 : \quad \left[Q_k^{(0)} - \lambda^{(0)}\delta_{ik}\right]A_k^{(1)} + \left[Q_k^{(1)} - \lambda^{(1)}\delta_{ik}\right]A_k^{(0)} = 0$$

$$\theta^2 : \quad \left[Q_k^{(0)} - \lambda^{(0)}\delta_{ik}\right]A_k^{(2)} + \left[Q_k^{(1)} - \lambda^{(1)}\delta_{ik}\right]A_k^{(2)} + \left[Q_k^{(2)} - \lambda^{(2)}\delta_{ik}\right]A_k^{(0)} = 0$$

$$(5.2.48)$$

where

$$Q_{ik}^{(0)} = G_{ijkl}^{(0)} n_j n_l$$

$$Q_{ik}^{(1)} = G_{ijkl}^{(1)} n_j n_l$$

$$Q_{ik}^{(2)} = G_{ijkl}^{(2)} n_j n_l \qquad (5.2.49)$$

The $\lambda^{(0)}$ can be easily calculate by solving the eigenvalue problem which is the first equation of 5.2.48 and $A_k^{(0)}$ can be solve uniquely by requiring normalization

$$A_k^{(0)} A_k^{(0)} = 1 \qquad (5.2.50)$$

By utilizing equation 5.2.50 and second equation of 5.2.48, we can get following relation:

$$\lambda^{(1)} = A_i^{(0)} Q_{ik}^{(1)} A_k^{(0)} \qquad (5.2.51)$$

$A_k^{(1)}$ can be solve uniquely by requiring $A_k^{(1)}$ orthogonal to $A_k^{(0)}$, since

$\left[Q_k^{(1)} - \lambda^{(1)}\delta_{ik}\right]A_k^{(0)}$ term in equation 5.2.48 is orthogonal to the eigenvector of $\left[Q_k^{(0)} - \lambda^{(0)}\delta_{ik}\right]$.

$$A_k^{(0)}A_k^{(1)} = 0 \tag{5.2.52}$$

We can solve $\lambda^{(2)}$ by multiplying $A_i^{(0)}$ with the third equation of 5.2.48.

$$\lambda^{(2)} = A_i^{(0)}\ Q_{ik}^{(2)}\ A_k^{(0)} + \ A_i^{(0)}\ Q_{ik}^{(1)}\ A_k^{(1)} \tag{5.2.53}$$

Similarity, multiplying third equation of 5.2.47 by $A_i^{(0)}$ and utilizing

$$A_k^{(0)} = -\frac{1}{2}\ A_k^{(1)}A_k^{(1)} \tag{5.2.54}$$

We get

$$\lambda^{(3)} = A_i^{(0)}\ Q_{ik}^{(3)}\ A_k^{(0)} + \ A_i^{(0)}\ (Q_{ik}^{(1)} - \lambda^{(1)}\delta_{ik})\ A_k^{(2)} + \ A_i^{(0)}\ Q_{ik}^{(2)}\ A_k^{(1)} \tag{5.2.55}$$

Further substituting the $\omega = 2\pi f$ into the fourth equation of 5.2.46, we can get following relation:

$$f^2 = \frac{n^2}{4\rho_0 b^2}[\lambda^0 + \lambda^{(1)}\theta + \lambda^{(2)}\theta^2 + \lambda^{(3)}\theta^3] \tag{5.2.56}$$

where

$$f_0^2 = \frac{n^2\lambda^{(0)}}{4\rho_0 b^2}$$

By taking the first, second and third derivatives of equation 5.2.56 with repect to temperature T and substituiting Bechmann's temperature coefficient of frequency, we can obtain $\lambda^{(1)}$, $\lambda^{(2)}$ and $\lambda^{(3)}$ in terms of $Tf^{(n)}$.

$$\lambda^{(1)} = 2\,\lambda^{(0)}Tf^{(1)} \tag{5.2.57}$$

$$\lambda^{(2)} = 2\,\lambda^{(0)}Tf^{(2)} + \ \lambda^{(0)}[Tf^{(1)}]^2 \tag{5.2.58}$$

$$\lambda^{(2)} = 2\,\lambda^{(0)}Tf^{(3)} + \; 2\lambda^{(0)}Tf^{(1)}Tf^{(2)} \tag{5.2.59}$$

where

$$Tf^{(n)} = \frac{1}{n!\,f_0}\frac{\partial^n f}{\partial T^n}\bigg|_{T_0}$$

Futher substituting equation 5.2.51, 5.2.53 and 5.2.55 into equation 5.2.57, 5.2.58 and 5.2.59 and reranging the in terms of known measured values, we have

$$2\lambda^{(0)}Tf^{(1)} = [C_{ijkl}^{(1)}n_j n_l A_i^{(0)} A_k^{(0)} + \left[C_{ijsl}\alpha_{ks}^{(1)} + \; C_{sjkl}\alpha_{is}^{(1)} + \; C_{ijklmn}\alpha_{mn}^{(1)}\right]n_j n_l A_i^{(0)} A_k^{(0)}] \tag{5.2.60}$$

$$4\lambda^{(0)}Tf^{(2)} = \; \tilde{C}_{ijkl}^{(2)}n_j n_l A_i^{(0)} A_k^{(0)} + 2\lambda^{(0)}\left[Tf^{(1)}\right]^2$$

$$+ 2\Big[C_{sjkl}\alpha_{is}^{(2)} + \; C_{ijsl}\alpha_{ks}^{(2)} + \; C_{sjtl}\alpha_{is}^{(1)}\alpha_{kt}^{(1)} + \; C_{sjkl}^{(1)}\alpha_{is}^{(1)} + C_{ijsl}^{(1)}\alpha_{ks}^{(1)}$$

$$+ \; C_{sjklmn}\alpha_{is}^{(1)} + C_{ijslmn}\alpha_{ks}^{(1)}\alpha_{mn}^{(1)} + C_{ijklmn}\alpha_{mn}^{(2)}\Big]\, n_j\, n_l\, A_i^{(0)} A_k^{(0)}$$

$$+ 2\Big[C_{sjkl}\alpha_{is}^{(1)} + \; C_{ijsl}\alpha_{ks}^{(1)} + \; C_{ijklmn}\alpha_{mn}^{(1)} + C_{ijkl}^{(1)}\Big]n_j n_l A_i^{(0)} A_k^{(1)} \tag{5.2.61}$$

$$12\lambda^{(0)}Tf^{(3)} = \; \tilde{C}_{ijkl}^{(3)}n_j n_l A_i^{(0)} A_k^{(0)} - 12\lambda^{(0)}Tf^{(1)}Tf^{(2)}$$

$$+ 6\Big(A_i^{(0)}Q_{ik}^{(1)}A_k^{(2)} + A_i^{(0)}Q_{ik}^{(2)}A_k^{(1)} + \lambda^{(0)}Tf^{(1)}A_k^{(1)}A_k^{(1)}\Big)$$

$$+ 6\Big[\alpha_{mn}^{(3)} + 2C_{ijsl}\alpha_{ks}^{(3)} + 2\Big(C_{ijsl}^{(1)} + C_{ijslmn}\alpha_{mn}^{(1)}\Big)\alpha_{ks}^{(2)}$$

$$+ 2\Big(\frac{1}{2}\tilde{C}_{ijsl}^{(2)} + C_{ijslmn}\alpha_{mn}^{(2)}\Big)\alpha_{ks}^{(1)} + 2C_{sjtl}\alpha_{is}^{(1)}\alpha_{kt}^{(2)}$$

$$+ \Big(C_{sjtl}^{(1)} + D_{sjtlmn}\alpha_{mn}^{(1)}\Big)\alpha_{is}^{(1)}\,\alpha_{kt}^{(1)}\Big]\,n_j\,n_i\,A_i^{(0)}A_k^{(0)} \tag{5.2.62}$$
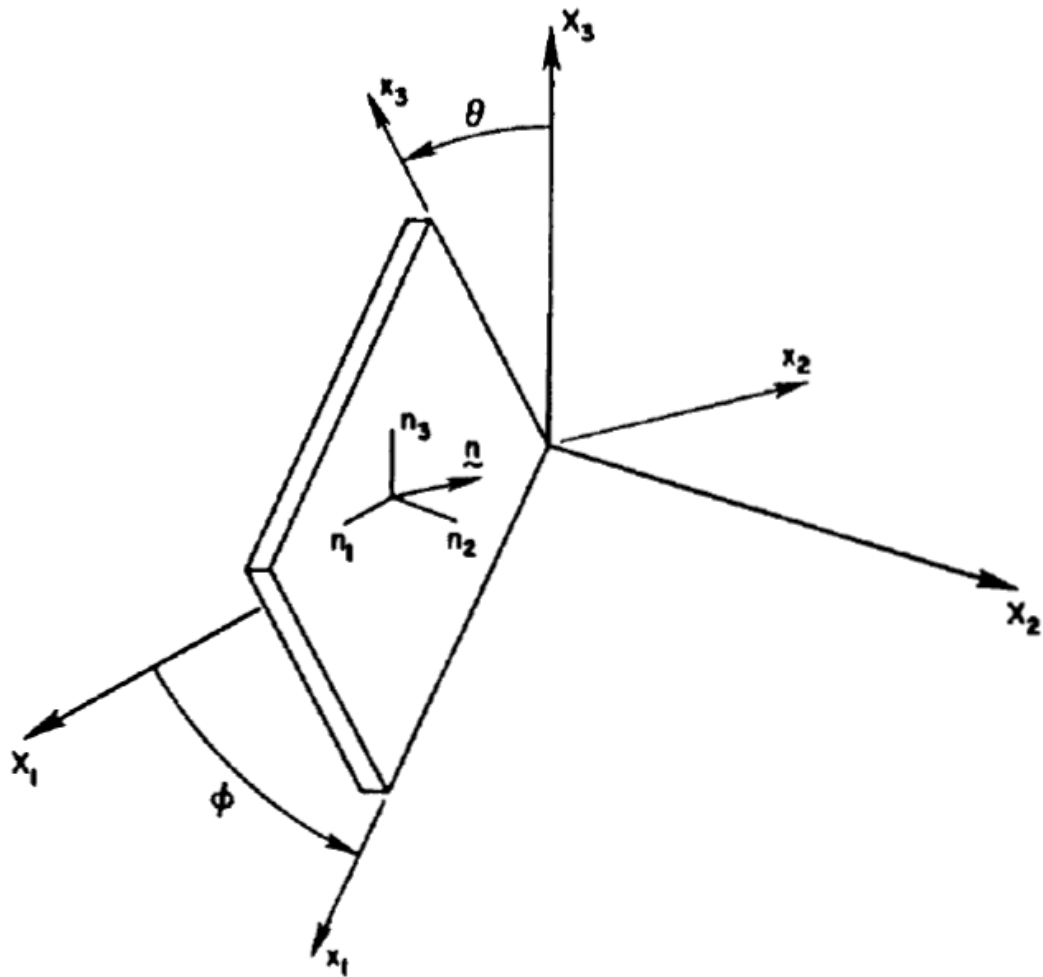
Figure 5.2.1 A doubly rotated crystal plate and normal with respect to crystallographic axes. [34]

5.3 Equation of Motion for Small Vibrations Superposed on Thermally Induced Deformations with the Piezoelectric Effect.

In recent study, researcher found that the langasite is better material for BAW application than quartz crystal due to its piezoelectric properties and temperature stability. In temperature frequency analysis of quartz crystal, the piezoelectric effects are neglected since effects are marginal. On the other hand, the piezoelectric coefficient of langasite is much larger than quartz crystal. In this chapter, we will derive the three-dimensional equation of motion for small vibration superposed on thermally induced deformations with the piezoelectric effect.

The equations of motion for small vibrations superposed on thermally induced deformations with the piezoelectric effect are conveniently derived with the following definitions:

θ : Temperature increment respect to reference temperature T-T_0

s_{ij} : Incremental strain

t_{ij} : Incremental stress

p_i : Incremental traction

E_k : Electric field

$\emptyset_{,k}$: Electrical potential

D_i : Electric charge density displacement

e_{kij} : Piezoelectric coupling coefficients

ϵ_{ik} : Dielectric coefficients

n_i : Unit outward normal vector to S

C_{ijkl} : Second-order elastic stiffnesses of the crystal

C_{ijklmn}: Third-order elastic stiffnesses of the crystal

$C_{ijklmnpq}$: Four-order elastic stiffnesses of the crystal

$C_{ijkl}^{(1)}$: First temperature derivative of the second-order elastic stiffnesses of the crystal

$\tilde{C}_{ijkl}^{(2)}$: Effective Second temperature derivative of the second-order elastic stiffnesses of the crystal

$\tilde{C}_{ijkl}^{(3)}$: Effective third temperature derivative of the second-order elastic stiffnesses of the crystal

λ_{ij}^{θ} : Stress coefficient of temperature

α_{ij}^{θ} : Thermal expansion coefficient

The Lagrangian formulation of incremental equations, which derived from previous section, will be used in this section. The following incremental equations and constitutive equations include piezoelectric effect and they are similar to the ones in previous section.

(a) Strain- displacement relation

$$s_{kl} = \frac{1}{2}(u_{k,l} + u_{l,k} + \alpha_{rk}^{\theta}u_{r,l} + \alpha_{rl}^{\theta}u_{r,k}) \tag{5.3.1}$$

(b) Electric field – potential relation

$$E_k = -\emptyset_{,k} \tag{5.3.2}$$

(c) Constitutive equations

$$t_{ij} = C_{ijkl}^{\theta}s_{kl} - e_{kij}E_k \tag{5.3.3}$$

$$D_i = e_{ikl}s_{kl} - \epsilon_{ik}E_k \tag{5.3.4}$$

(d) Stress equation of motion

$$(t_{ij} + \alpha_{ir}^\theta t_{rj})_{,j} = \rho \ddot{u}_i \tag{5.3.5}$$

$$p_i = n_j(t_{ij} + \alpha_{ik}^\theta t_{jk}) \qquad \text{on } S \tag{5.3.6}$$

(e) Electrostatics

$$D_{i,i} = 0 \tag{5.3.7}$$

The constitutive equations can be express in terms of displacement by substituting equation (5.3.1) into equation (5.3.3) and (5.3.4).

$$t_{ij} = C_{ijkl}^\theta \left(u_{k,l} + \alpha_{rk}^\theta u_{r,l} \right) - e_{kij} E_k \tag{5.3.8}$$

$$D_i = e_{ikl} \left(u_{k,l} + \alpha_{rk}^\theta u_{r,l} \right) + \epsilon_{ik} k \tag{5.3.9}$$

where

$$C_{ijkl}^\theta = C_{pij} + D_{ijkl}^{(1)} \theta + D_{ijkl}^{(2)} \theta^2 + D_{ijkl}^{(3)} \theta^3$$

$$D_{ijkl}^{(1)} = C_{ijkl}^{(1)} + C_{ijklmn} \alpha_{mn}^{(1)}$$

$$D_{ijkl}^{(2)} = \frac{1}{2} \tilde{C}_{ijkl}^{(2)} + C_{ijklmn} \alpha_{mn}^{(2)}$$

$$D_{ijkl}^{(3)} = \frac{1}{6} \tilde{C}_{ijkl}^{(3)} + C_{ijklmn} \alpha_{mn}^{(3)}$$

$$\alpha_{ri}^\theta = \alpha_{ri}^{(1)} \theta + \alpha_{ri}^{(2)} \theta^2 + \alpha_{ri}^{(3)} \theta^3$$

Further substituting the equation (5.3.8) into equation (5.3.5), we obtain

$$\left[C_{ijkl}^\theta + \alpha_{rk}^\theta C_{ijrl}^\theta + \alpha_{ri}^\theta C_{rjkl}^\theta + \alpha_{ri}^\theta \alpha_{sk}^\theta C_{rjsl}^\theta \right] u_{k,lj} - \left[e_{kij} + \alpha_{ri}^\theta e_{krj} \right] E_{k,j} = \rho \ddot{u}_i$$

or

$$G_{ijkl}^\theta \, u_{k,lj} - H_{kij}^\theta \, E_{k,j} = \rho \ddot{u}_i \tag{5.3.10}$$

where

$$G_{ijkl}^{\theta} = C_{ijkl}^{\theta} + \alpha_{rk}^{\theta} C_{ijrl}^{\theta} + \alpha_{ri}^{\theta} C_{rjkl}^{\theta} + \alpha_{ri}^{\theta} \alpha_{sk}^{\theta} C_{rjsl}^{\theta}$$

$$G_{ijkl}^{\theta} = C_{ijkl} + G_{ijkl}^{(1)} \theta + G_{ijkl}^{(2)} \theta^2 + G_{ijkl}^{(3)} \theta^3$$

$$G_{ijkl}^{(1)} = D_{ijkl}^{(1)} + \alpha_{rk}^{(1)} C_{ijrl} + \alpha_{ri}^{(1)} C_{rjkl}$$

$$G_{ijkl}^{(2)} = D_{ijkl}^{(2)} + \alpha_{rk}^{(2)} C_{ijrl} + \alpha_{ri}^{(2)} C_{rjkl} + D_{ijrl}^{(1)} \alpha_{rk}^{(1)} + D_{rjkl}^{(1)} \alpha_{ri}^{(1)}$$

$$+ C_{rjsl} \alpha_{ri}^{(1)} \alpha_{sk}^{(1)}$$

$$G_{ijkl}^{(3)} = D_{ijkl}^{(3)} + \alpha_{rk}^{(3)} C_{ijrl} + \alpha_{ri}^{(3)} C_{rjkl} + D_{ijrl}^{(2)} \alpha_{rk}^{(1)} + D_{rjkl}^{(2)} \alpha_{ri}^{(1)} + D_{ijrl}^{(1)} \alpha_{rk}^{(2)}$$

$$+ D_{rjkl}^{(1)} \alpha_{ri}^{(2)} + C_{rjsl} \alpha_{ri}^{(1)} \alpha_{sk}^{(2)} + C_{rjsl} \alpha_{ri}^{(2)} \alpha_{sk}^{(1)} + D_{rjsl}^{(1)} \alpha_{ri}^{(1)} \alpha_{sk}^{(1)}$$

$$H_{kij}^{\theta} = e_{kij} + \alpha_{ri}^{\theta} e_{krj}$$

In the equation (5.3.10), the piezoelectric coupling coefficient, the material properties are assumed to be temperature dependent. By further substituting equation (5.3.9) into equation (5.3.4), we get

$$\left(e_{ikl} + \alpha_{rk}^{\theta} e_{irl}\right) u_{k,li} + \epsilon_{ik} E_{k,i} = 0 \tag{5.3.11}$$

or

$$H_{kij}^{\theta} u_{k,li} + \epsilon_{ik} E_{k,i} = 0 \tag{5.3.12}$$

where

$$H_{ikl}^{\theta} = e_{ikl} + \alpha_{rk}^{\theta} e_{irl}$$

$$= e_{ikl} + e_{irl} \alpha_{rk}^{(1)} \theta + e_{ikl} \alpha_{rk}^{(2)} \theta^2 + e_{ikl} \alpha_{rk}^{(3)} \theta^3$$

$$= e_{iikl} + H_{ikl}^{(1)} \theta + H_{ikl}^{(2)} \theta^2 + H_{ikl}^{(3)} \theta^3$$

5.3.1 Thickness Vibration

Similar to the section 5.2.1, we kept the same notation so that x_i ($i = 1,2,3$) be the cystallographical axes of the crystals. By conventional IEEE notation, a doubly rotated crystal plate is defined by (y,x,ω,l) ϕ, θ. The crystal plate has thickness of $2b$ as shown in figure 5.3 which n_i denote the unit outward normal to the faces of the plate in the natural state. Refer to the crysallographic axes and the figure 5.3, the unit normal components are same as equation 5.4.1:

$$n_1 = -\cos\theta \, \sin\emptyset$$

$$n_2 = \cos\theta \cos\emptyset$$

$$n_3 = \sin\theta \tag{5.3.12}$$

For traction free face boundary conditions, the equation 5.3.2 and 5.3.6 becomes

$$p_i = n_j\left[G^\theta_{ijkl}u_{k,l} + H^\theta_{kij}\emptyset_{,k}\right] = 0 \quad \text{at} \quad n_jX_j = \pm b \tag{5.3.13}$$

$$\emptyset = V \quad \text{at} \quad n_jX_j = \pm b \tag{5.3.14}$$

The solution for harmonic and anti-symmetric thickness vibrations are

$$u_k = A_k \sin\xi n_p X_p e^{i\omega t} \tag{5.3.15}$$

$$\emptyset = V \sin\xi n_p X_p e^{i\omega t} \tag{5.3.16}$$

and

$$u_{k,l} = \xi\, n_l \cos\xi n_p X_p e^{i\omega t} \cdot A_k \tag{5.3.17}$$

$$u_{k,lj} = -\xi^2\, n_l\, n_j \sin\xi n_p X_p e^{i\omega t} \cdot A_k \tag{5.3.18}$$

$$\ddot{u}_i = -\omega^2\, \sin\xi\, n_p X_p e^{i\omega t} \cdot A_k \tag{5.3.19}$$

$$\emptyset_{,k} = V\,\xi\, n_k \cos\xi n_p X_p e^{i\omega t} \tag{5.3.20}$$

$$\emptyset_{,kj} = -V\,\xi^2\, n_k n_j \sin\xi n_p X_p e^{i\omega t} \tag{5.3.21}$$

By further substituting equation 5.3.18 and 5.3.21into equation 5.3.11, we get

$$H^{\theta}_{kij} \left[-A_i \, \xi^2 \, n_j \, n_k \, \sin \xi \, n_p X_p e^{i\omega t} \right] - \epsilon_{jk} \left[-V\xi^2 n_j n_k \sin \xi n_p X_p e^{i\omega t} \right] = 0$$

$$(5.3.22)$$

By simplifying the equation 5.322, we obtain electric potential in terms of piezoelectric coupling coefficient, dielectric coefficient and amplitude.

$$V = \gamma^{\theta}_i \, A_i \tag{5.3.23}$$

where

$$V = \frac{n_j \, n_k \, H^{\theta}_{kij}}{n_r \, n_s \, \epsilon_{rs}} \, A_i \tag{5.3.24}$$

$$\gamma^{\theta}_i = \frac{n_m n_n \, H^{\theta}_{nim}}{n_r n_s \epsilon_{rs}} \tag{5.3.25}$$

The equation 5.3.21 can be written in terms of γ^{θ}_i by substituting 5.3.23 into equation 5.3.21.

$$\emptyset_{,kj} = -\gamma^{\theta}_q A_q \xi^2 n_k n_j \sin \xi n_p X_p e^{i\omega t} \tag{5.3.26}$$

Now, we can substitute equation 5.3.18, 5.3.19 and 5.3.26 into equation 5.3.10 to setup the eigenvalue problem.

$$\xi^2 \, Q_{ik} \, A_k = \rho \omega^2 A_i \tag{5.3.27}$$

where

$$Q_{ik} = G^{\theta}_{ijkl} \, n_j \, n_l + H^{\theta}_{qip} \, \gamma^{\theta}_k \, n_p \, n_q \tag{5.3.28}$$

$$H^{\theta}_{qip} \gamma^{\theta}_k n_p n_q = \frac{H^{\theta}_{pij} \, H^{\theta}_{qkl}}{\epsilon_{rs} \, n_r \, n_s} \, n_p \, n_q \, n_j \, n_l \tag{5.3.29}$$

Further substituting the equation 5.3.29 into 5.3.28, we obtain piezoelectrically stiffened Christoffel constant $\bar{G}^{\theta}_{ijkl}$.

$$Q_{ik} = \bar{G}^{\theta}_{ijkl}\, n_j n_l = Q_{ki} \tag{5.3.30}$$

$$\bar{G}^{\theta}_{ijkl} = G^{\theta}_{ijkl} + \frac{H^{\theta}_{pij}\, H^{\theta}_{qkl}\, n_p n_q}{\epsilon_{rs} n_r n_s} \tag{5.3.31}$$

where

$$\bar{G}^{\theta}_{ijkl} = \bar{G}_{ijkl} + \bar{G}^{(1)}_{ijkl}\, \theta + \bar{G}^{(2)}_{ijkl}\, \theta^2 + \bar{G}^{(3)}_{ijkl}\, \theta^3$$

$$\bar{G}_{ijkl} = C_{ijkl} + \frac{e_{pij}\, e_{qkl}\, n_p\, n_q}{\epsilon_{rs}\, n_r\, n_s}$$

$$\overline{G}^{(1)}_{ijkl} = C^{(1)}_{ijkl} + \frac{e_{pij}\, H^{(1)}_{qkl}\, n_p\, n_q}{\epsilon_{rs}\, n_r\, n_s} + \frac{H^{(1)}_{pij}\, e_{qkl}\, n_p\, n_q}{\epsilon_{rs}\, n_r\, n_s}$$

$$\overline{G}^{(2)}_{ijkl} = C^{(2)}_{ijkl} + \frac{e_{pij}\, H^{(2)}_{qkl}\, n_p\, n_q}{\epsilon_{rs}\, n_r\, n_s} + \frac{H^{(2)}_{pij}\, e_{qkl}\, n_p\, n_q}{\epsilon_{rs}\, n_r\, n_s} + \frac{H^{(1)}_{pij}\, H^{(1)}_{qkl}\, n_p\, n_q}{\epsilon_{rs}\, n_r\, n_s}$$

$$\overline{G}^{(3)}_{ijkl} = C^{(3)}_{ijkl} + \frac{e_{pij}\, H^{(3)}_{qkl}\, n_p\, n_q}{\epsilon_{rs}\, n_r\, n_s} + \frac{H^{(3)}_{pij}\, e_{qkl}\, n_p\, n_q}{\epsilon_{rs}\, n_r\, n_s} + \frac{H^{(1)}_{pij}\, H^{(2)}_{qkl}\, n_p\, n_q}{\epsilon_{rs}\, n_r\, n_s}$$

$$+ \frac{H^{(2)}_{pij}\, H^{(1)}_{qkl}\, n_p\, n_q}{\epsilon_{rs}\, n_r\, n_s}$$

Upon substituting the equation 5.3.31 and 5.3.30 into equation 5.3.27, we find

$$\left[\xi^2\, \bar{G}^{\theta}_{ijkl}\, n_j\, n_l \right] A_k = \rho \omega^2 A_i$$

or

$$\left[Q_{ik} - \lambda \delta_{ik} \right] A_k = 0 \tag{5.3.32}$$

where

$$\lambda = \rho\, \frac{\omega^2}{\xi^2}, \qquad \xi = n\pi/2b, \quad n{=}1,3,5\ldots\,. \tag{5.3.33}$$

The equation 5.3.32 is the eigenvalue problem including the temperature effect and piezoelectric effect on crystal. The traction free boundary condition can be further simplify by substituting equation 5.3.17 and 5.3.20 into equation 5.3.13.

$$p_i = n_j \left[A_k G^\theta_{ijkl} \, \xi \, n_l \cos \xi \, n_p \, X_p \, e^{i\omega t} + H^\theta_{kij} V \, \xi \, n_k \, \cos \xi \, n_p \, X_p \, e^{i\omega t} \right]$$

$$= n_j \left[A_k G^\theta_{ijkl} \, \xi \, n_l + H^\theta_{kij} V \, \xi \, n_k \right] \cos \xi \, n_p \, X_p \, e^{i\omega t} =$$

$$0 \quad at \quad n_j X_n = \pm b$$

$$(5.3.34)$$

We let

$$t_i = [\, G^\theta_{ijkl} \, n_j \, n_l \, A_k + H^\theta_{kil} \, n_k \, V] \tag{5.3.35}$$

and then,

$$p_i = \xi \, t_i \, \cos \xi \, n_p \, X_p \, e^{i\omega t} = 0 \quad at \quad n_j X_j = \pm b \tag{5.3.36}$$

Since $e^{i\omega t}$, ξ and t_i cannot equal to zero, $\cos \xi \, b$ has to be zero. Therefore,

$$\xi = \frac{\pi}{2b}, \frac{3\pi}{2b}, \frac{5\pi}{2b} \dots$$

$$\lambda = \rho \left(\frac{2b\omega}{n\pi}\right)^2, \qquad n = 1,2,3 \dots \tag{5.3.37}$$

Now, we can repeat the same procedure as in section 5.2.1 and solve the eigenvalue

problem.

From the equation 5.3.32, the amplitutute A_k and eignenvalue λ are assumed to be

temperature dependent and utilizing Rayleigh-Schrodinger's pertubation method, we get

$$A_k = A_k^{(0)} + A_k^{(1)} \theta + A_k^{(2)} \theta^2$$

$$\lambda = \lambda^{(0)} + \lambda^{(1)} \theta + \lambda^{(2)} \theta^2 \tag{5.3.38}$$

By substituting the equation 5.3.28 into equation 5.3.32, the eigenvalue problems of

powers of θ can be obtained and they are

$$\theta^0 : \quad \left[Q_k^{(0)} - \lambda^{(0)} \delta_{ik} \right] A_k^{(0)} = 0$$

$$\theta^1 : \quad \left[Q_k^{(0)} - \lambda^{(0)} \delta_{ik} \right] A_k^{(1)} + \left[Q_k^{(1)} - \lambda^{(1)} \delta_{ik} \right] A_k^{(0)} = 0$$

$$\theta^2 : \quad \left[Q_k^{(0)} - \lambda^{(0)}\delta_{ik}\right]A_k^{(2)} + \left[Q_k^{(1)} - \lambda^{(1)}\delta_{ik}\right]A_k^{(2)} + \left[Q_k^{(2)} - \lambda^{(2)}\delta_{ik}\right]A_k^{(0)} = 0$$

$$\theta^3 : \quad \left[Q_k^{(0)} - \lambda^{(0)}\delta_{ik}\right]A_k^{(3)} + \left[Q_k^{(1)} - \lambda^{(1)}\delta_{ik}\right]A_k^{(2)} + \left[Q_k^{(2)} - \lambda^{(2)}\delta_{ik}\right]A_k^{(1)} +$$

$$\left[Q_k^{(3)} - \lambda^{(3)}\delta_{ik}\right]A_k^{(0)} = 0$$

$$(5.3.39)$$

where

$$Q_{ik}^{(0)} = G_{ijkl}^{(0)} n_j n_l$$

$$Q_{ik}^{(1)} = G_{ijkl}^{(1)} n_j n_l$$

$$Q_{ik}^{(2)} = G_{ijkl}^{(2)} n_j n_l$$

$$Q_{ik}^{(3)} = G_{ijkl}^{(3)} n_j n_l \tag{5.3.40}$$

Similar to the previous section 5.2.1, the each eigenvalues $\lambda^{(n)}$ are uniqlely calculated.

The $\lambda^{(0)}$ and $A_k^{(0)}$ can be easily calculate by solving the first eigenvalue problem of equation 5.3.39 and satifying the equation 5.3.41.

$$A_k^{(0)} A_k^{(0)} = 1 \tag{5.3.41}$$

By multiplying $A_i^{(0)}$ with the second equation of 5.3.39 and utilizing equation 5.3.41 and first euquation of 5.3.39, we can get following relation:

$$\lambda^{(1)} = A_i^{(0)} Q_{ik}^{(1)} A_k^{(0)} \tag{5.3.42}$$

$A_k^{(1)}$ can be solve uniquely by requiring $A_k^{(1)}$ orthogonal to $A_k^{(0)}$, since $\left[Q_k^{(1)} - \lambda^{(1)}\delta_{ik}\right]A_k^{(0)}$ term in equation 5.3.39 is orthogonal to the eigenvector of $\left[Q_k^{(0)} - \lambda^{(0)}\delta_{ik}\right]$.

$$A_k^{(0)} A_k^{(1)} = 0 \tag{5.3.43}$$

We further multiply the $A_i^{(0)}$ with the third equation of 5.3.39 and utilizing equation

5.3.41 and 5.3.43, we obtain

$$\lambda^{(2)} = A_i^{(0)} Q_{ik}^{(2)} A_k^{(0)} + A_i^{(0)} Q_{ik}^{(1)} A_k^{(1)} \tag{5.3.44}$$

Finally, $\lambda^{(3)}$ can be calculated by repeating the same procedure, which is multiplying

$A_i^{(0)}$ with the forth equation of 5.3.39, and employing the constraint, equation 5.3.45.

$$A_k^{(2)} A_k^{(1)} = -\frac{1}{2} A_k^{(1)} A_k^{(1)} \tag{5.3.45}$$

$$\lambda^{(3)} = A_i^{(0)} Q_{ik}^{(3)} A_k^{(0)} + A_i^{(0)} \left(Q_k^{(1)} - \lambda^{(1)} \delta_{ik} \right) A_k^{(2)} + A_i^{(0)} Q_{ik}^{(2)} A_k^{(1)} \tag{5.3.46}$$

These above formulations are the normal procedures to compute the $\lambda^{(n)}$ and $A_k^{(n)}$ when

$Q_k^{(n)}$ are known. In the next chapter, we are going to compute the temperature coefficient

of frequency using the calculated quantity, such as $\lambda^{(n)}$ and $A_k^{(n)}$, from this section.

5.3.2   Temperature coefficient of frequency

In this section, we will utilize the same method, which previously used in section 5.2.1

by Yong ,Lee and Tiersten, to find the relation between Bechmann' temperature

coefficient of frequency Tf^n and the eigen value $\lambda^{(n)}$.

$$\lambda^{(1)} = 2 \lambda^{(0)} Tf^{(1)} \tag{5.3.47}$$

$$\lambda^{(2)} = 2 \lambda^{(0)} Tf^{(2)} + \lambda^{(0)} [Tf^{(1)}]^2 \tag{5.3.48}$$

$$\lambda^{(3)} = 2 \lambda^{(0)} Tf^{(3)} + 2\lambda^{(0)} Tf^{(1)} Tf^{(2)} \tag{5.3.49}$$

where

$$Tf^{(n)} = \frac{1}{n! f_0} \frac{\partial^n f}{\partial T^n}\bigg|_{T_0}$$

The above equations can be rearrange so that $Tf^{(n)}$ are a function of $\lambda^{(n)}$ and they are

$$Tf^{(1)} = \frac{1}{2}\frac{\lambda^{(1)}}{\lambda^{(0)}} \tag{5.3.50}$$

$$Tf^{(2)} = \frac{1}{2}\frac{\lambda^{(2)} - \lambda^{(0)}(Tf^{(1)})^2}{\lambda^{(0)}} = \frac{4\,\lambda^{(2)} - \lambda^{(1)}\,\lambda^{(1)}}{8\,\lambda^{(0)}\,\lambda^{(0)}} \tag{5.3.51}$$

$$Tf^{(3)} = \frac{1}{2}\frac{\lambda^{(3)} - 2\lambda^{(0)}Tf^{(1)}Tf^{(2)}}{\lambda^{(0)}} = \frac{\lambda^{(3)}}{\lambda^{(0)}} + \frac{1}{4}\frac{\lambda^{(2)}\,\lambda^{(1)}}{\lambda^{(0)}\,\lambda^{(0)}} + \frac{1}{16}\frac{\lambda^{(1)}\,\lambda^{(1)}\,\lambda^{(1)}}{\lambda^{(0)}\,\lambda^{(0)}\,\lambda^{(0)}} \tag{5.3.52}$$

5.4   Temperature Compensated Cuts of Langasite

In this chapter, the temperature coefficients of frequency Tf^n are computed at the entire region of the langasite crystal. From the computational results, the temperature compensated cuts of all three thickness vibration modes, the thickness-extensional or A-mode, fast thickness - shear modes or B-mode and slow thickness- shear or C-mode are identified by loci plots. The calculated lamda, λ, values from equation 5.3.40 are directly related to each mode of vibration, such that lamda and resonance frequencies follow below relations,

$$f_A > f_B > f_C \tag{5.4.1}$$

$$\lambda_1^0 > \lambda_2^0 > \lambda_3^0 \tag{5.4.2}$$

where

$$\lambda_1^0 = f_A \qquad \& \qquad \lambda_2^0 = f_B \qquad \& \qquad \lambda_3^0 = f_C$$

The temperature compensated cut of $Tf3$ cannot be calculated, since the third-order temperature derivative of the langasite has not been reported. [37] Therefore, the analysis of the temperature compensated cut of $Tf1$ and $Tf2$ are only included in this works. We implemented the equations from the previous section to calculate thee $Tf1$ and $Tf2$ of each

vibration mode. The complete sets of the material properties of the langasite obtain by Bourquin [38] and Molocha [39] are listed in Appendix C.

The temperature coefficients of frequency are calculate with the data obtained by Bourquin. The calculated values of each temperature coefficient of frequency are shown in figure 5.4.1, 5.4.2, 5.4.3, 5.4.4, 5.4.5 and 5.4.6. The figure 5.4.1 and 5.4.2 represent the first- and second- order temperature coefficient of frequency for A-mode. The figure 5.4.3 and 5.4.4 represent the first- and second-order temperature coefficient of frequency for B-mode. The figure 5.4.5 and 5.4.6 show the first- and second-order temperature coefficient of frequency for C-mode. There are no zero-valued temperature coefficients for A- and B-mode are found based on our calculation. Figure 5.4.7 shows the loci of C-mode temperature compensated orientations for langasite. A more than sufficient number of the zero-temperature compensated orientations of first-order temperature coefficient of frequency of langasite for C-mode have been identified. Figure 5.4.8 and 5.4.9 show a typical examples of the behavior of first- and second-order frequency-temperature coefficient of langasite for C-mode when $\theta = 10°$, 20° and 30°. The blue, red and green curves are represent the temperature coefficient of frequencies when $\theta = 10°$, 20° and 30°, respectively. No zero values of second-order temperature of frequency of langasite are found.
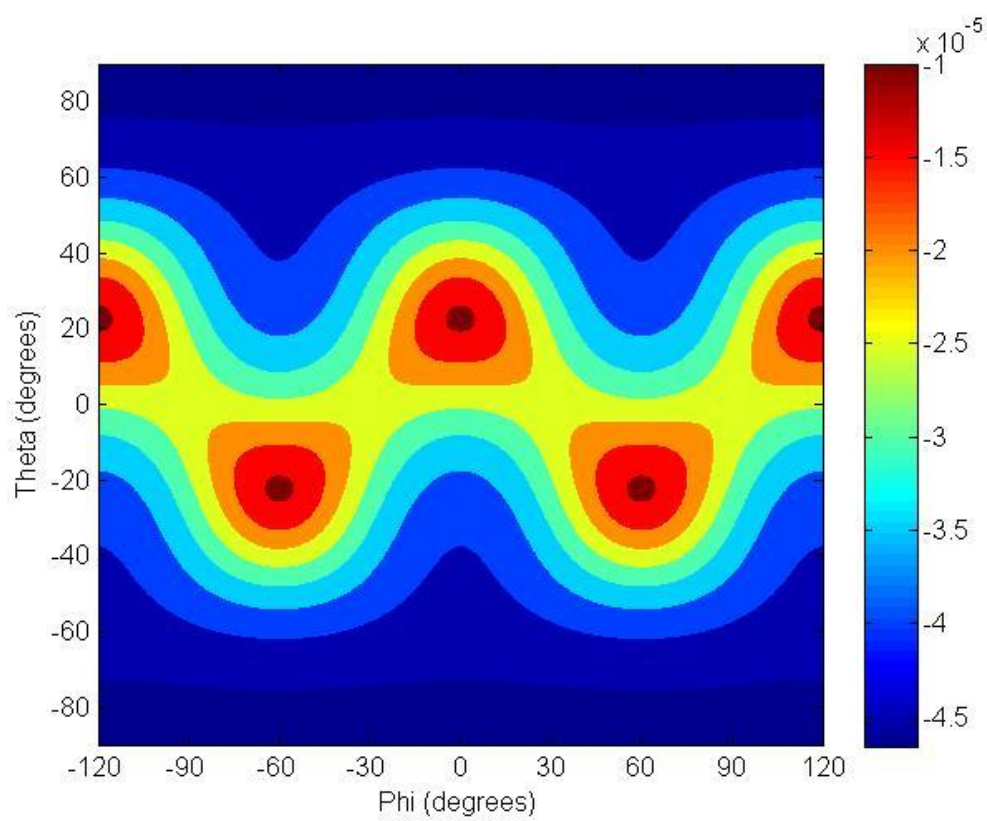
Figure 5.4.1 First-order temperature coefficient of frequency of langasite for A-mode
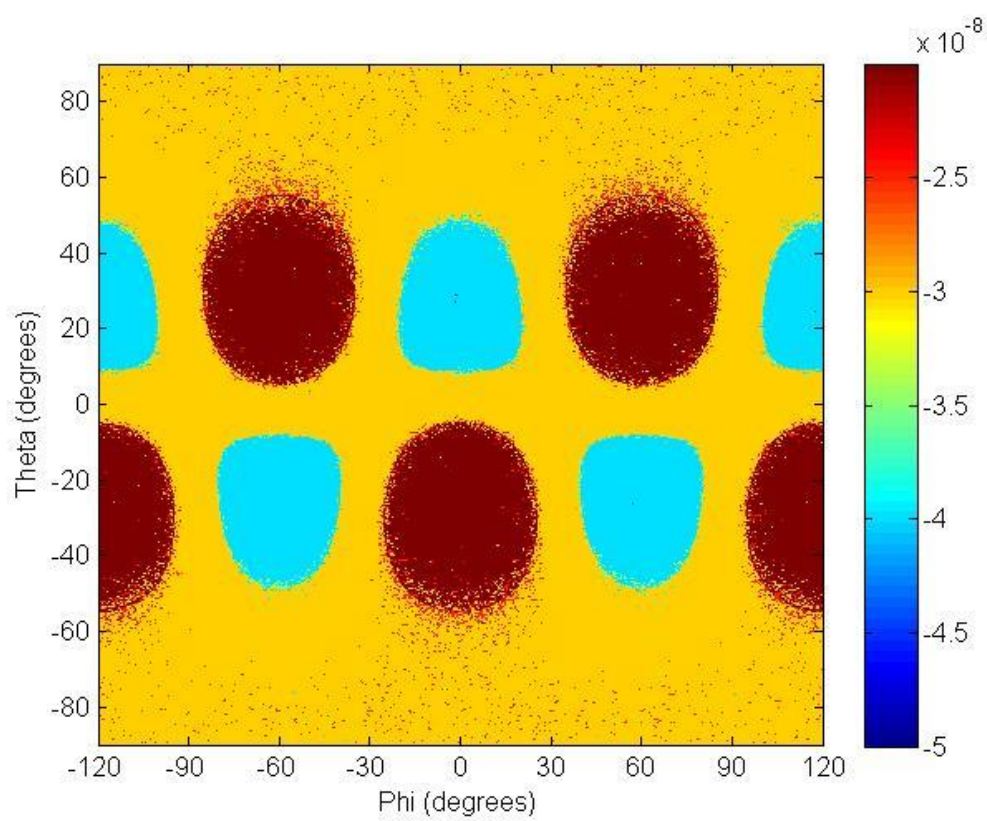
Figure 5.4.2 Second-order temperature coefficient of frequency of langasite for A-mode
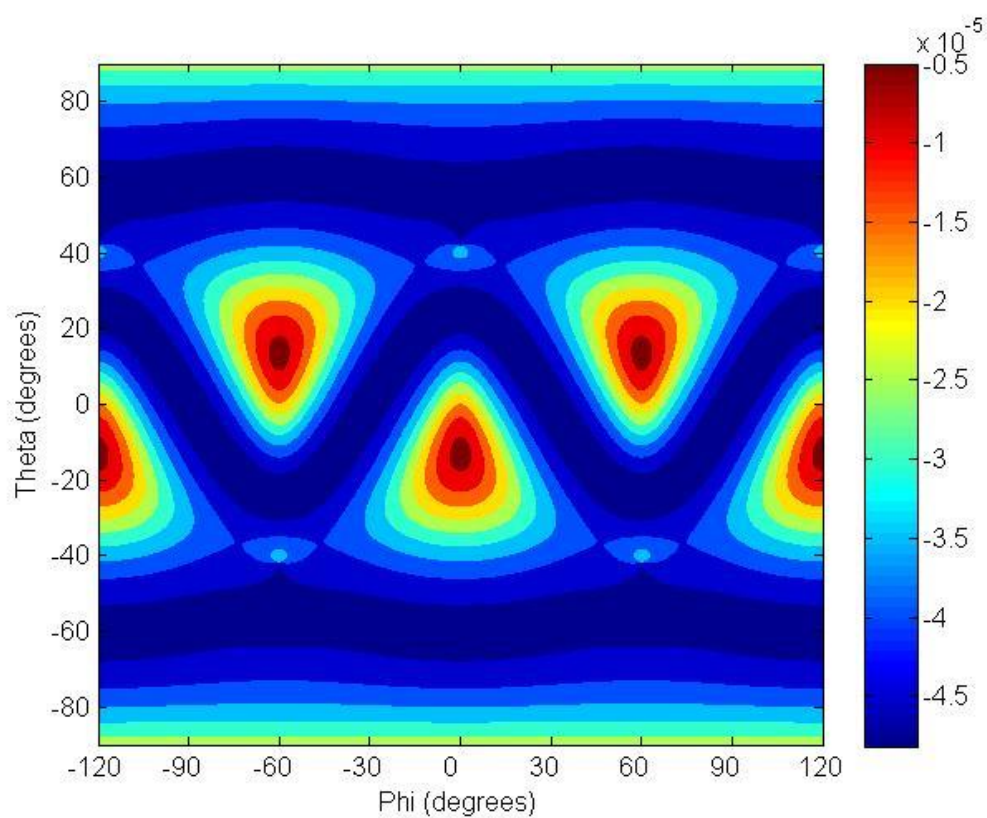
Figure 5.4.3 First-order temperature coefficient of frequency of langasite for B-mode
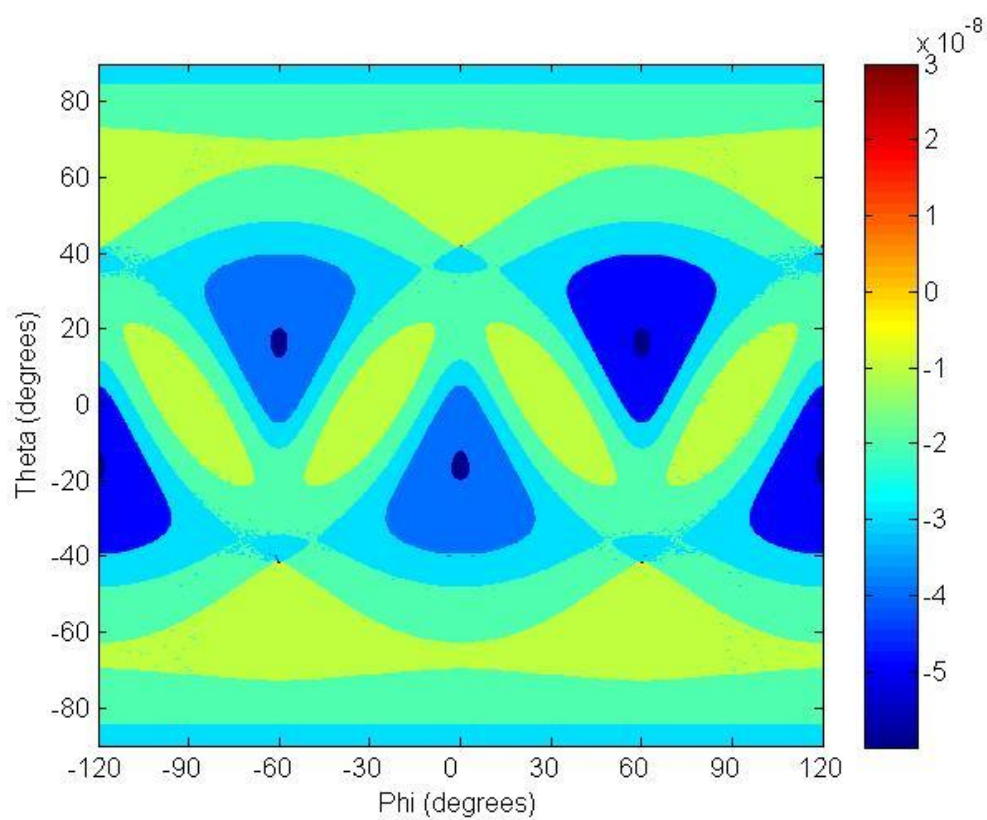
Figure 5.4.4 Second-order temperature coefficient of frequency of langasite for B-mode
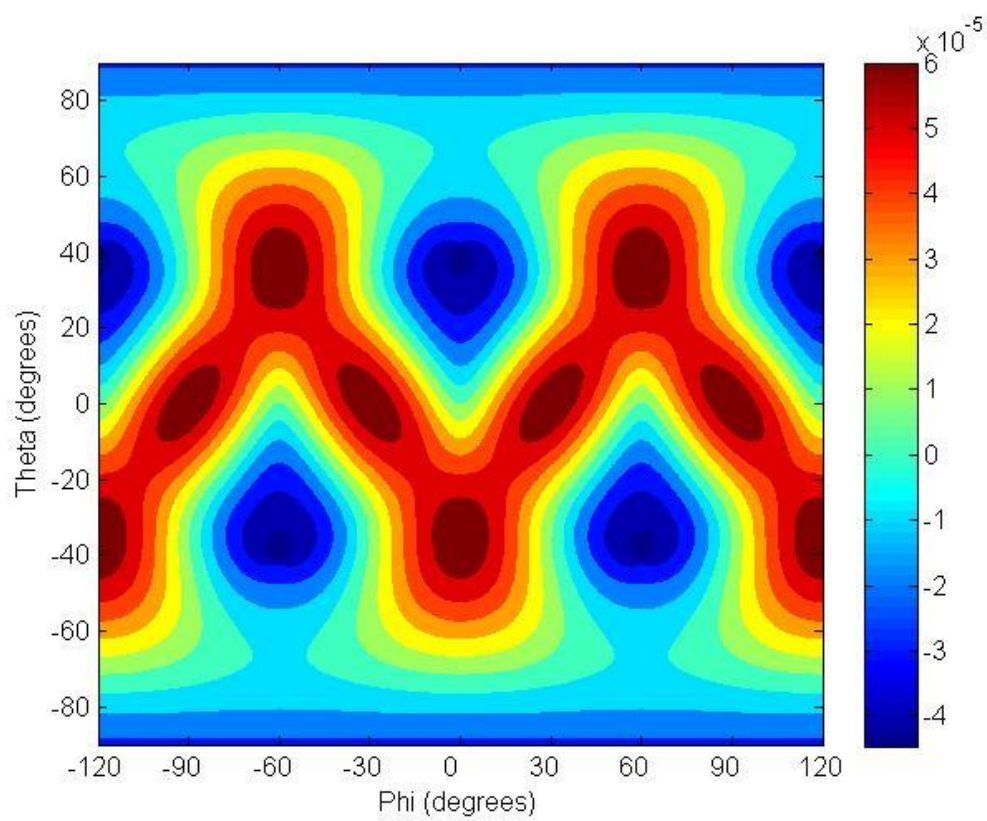
Figure 5.4.5 First-order temperature coefficient of frequency of langasite for C-mode
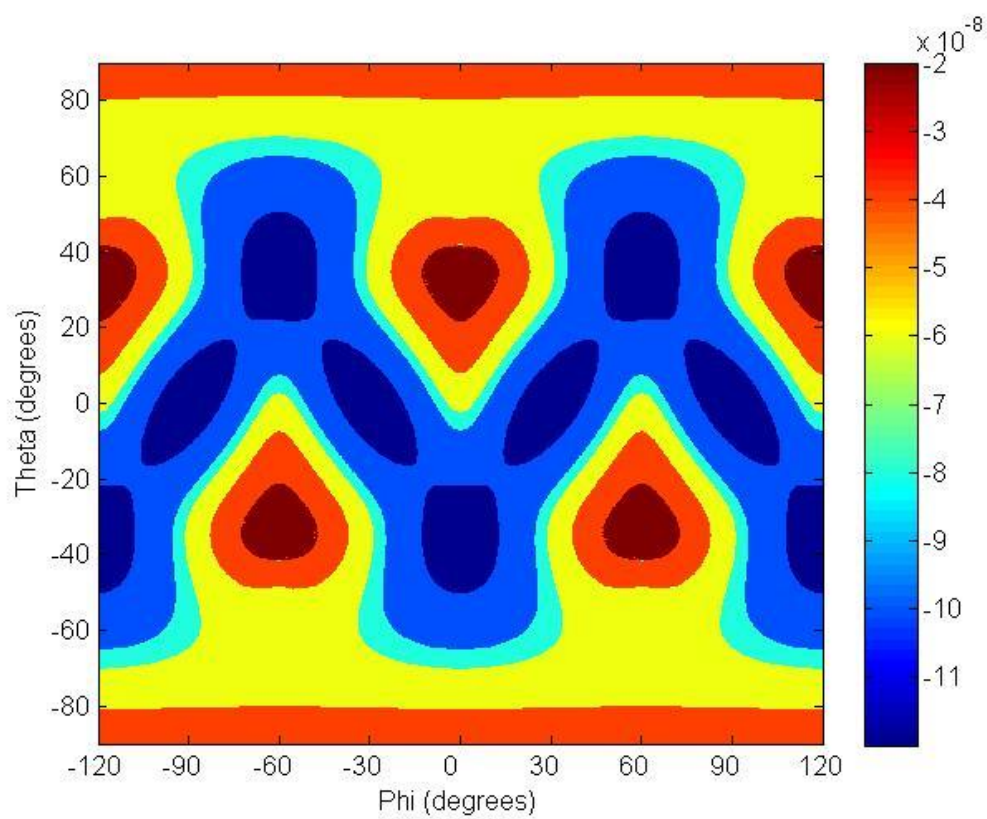
Figure 5.4.6 Second-order temperature coefficient of frequency of langasite for C-mode
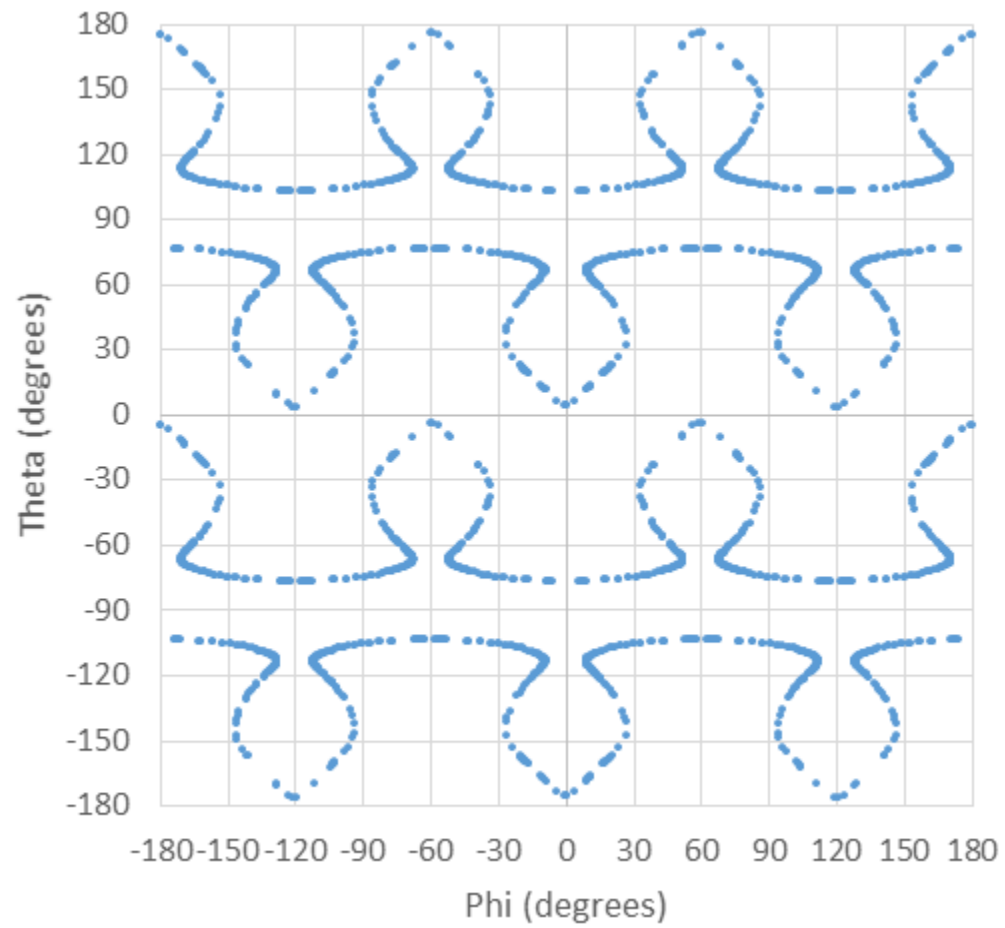
Figure 5.4.7 Temperature compensated loci of langasite for C-mode.
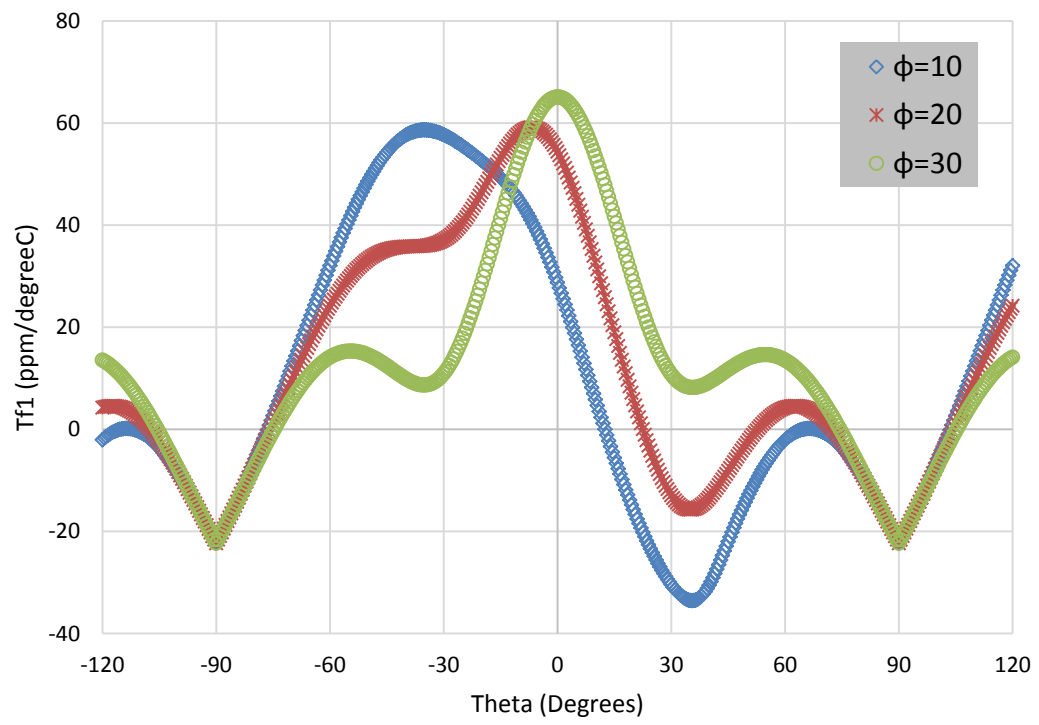
Figure 5.4.8 First-order of temperature coefficient of frequency of the C-mode for langasite when θ = 10 °, 20 ° and 30 °
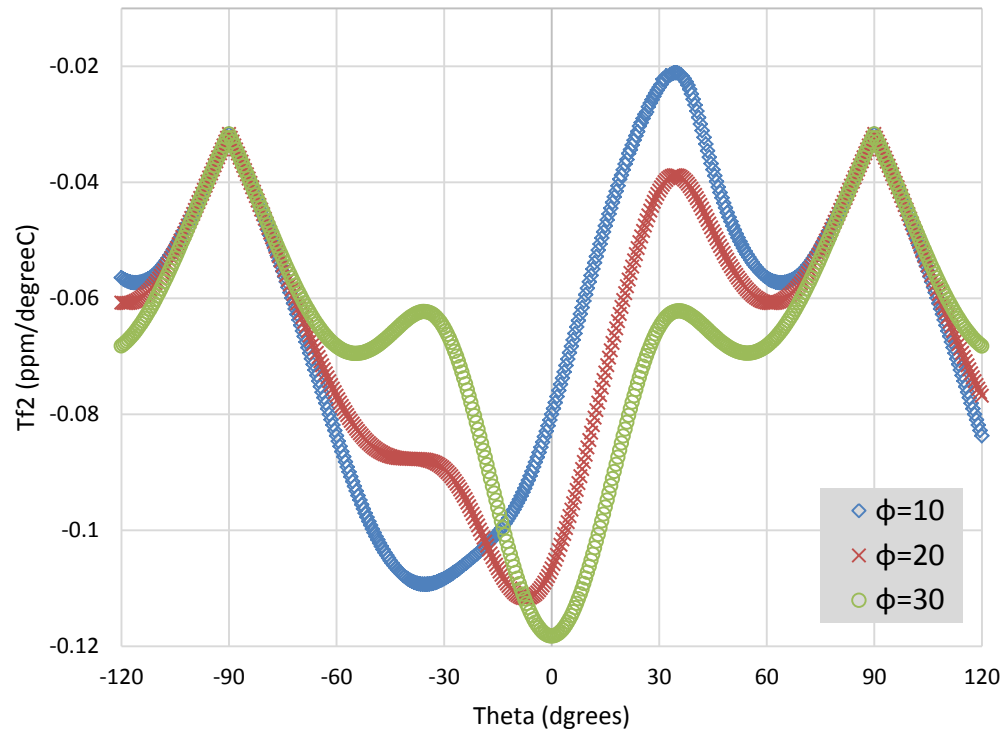
Figure 5.4.9 Second-order of temperature coefficient of frequency of the C-mode for langasite when θ = 10 °, 20 ° and 30 °

In addition, the temperature coefficients of frequency are calculated with the data obtained by Molacha [39]. The calculated values of each temperature coefficient of frequency are shown in figure 5.4.10, 5.4.11, 5.4.12, 5.4.13, 5.4.14 and 5.4.15. The figure 5.4.10 and 5.4.11 represent the first- and the second- order temperature coefficients of frequency for A-mode. The figure 5.4.12 and 5.4.13 represent the first- and second-order temperature coefficient of frequency for B-mode. The figure 5.4.14 and 5.4.15 show the first- and second-order temperature coefficient of frequency for C-mode. There are no zero-valued temperature coefficients for A- and B-mode are found based on the calculation. Figure 5.4.16 shows the first-order temperature compensated loci of the langasite for C-mode. The red crosses and the green diamonds represent the calculated temperature coefficients of frequency with the data obtained from ref. [38] and [39], respectively. The temperature compensated cuts are closely matched except when $\theta \approx \pm 70^{\mathbf{o}}$ and $\phi \approx \pm 40^{\mathbf{o}}$ to $60^{\mathbf{o}}$. Figure 5.4.17 shows the first- and the second-order temperature compensated loci of the langasite for C mode. The green circles and red crosses represent the first-order temperature coefficient of frequency, which computed with the data obtain by Bourquin [38] and Malocha [39], and the blue diamonds represent the second-order temperature coefficient of frequency with the data obtain from ref. [40]. A more than sufficient number of the temperature compensated orientations up to the second-order of langasite for C-mode have been identified. Our computation shows that no zero values of the second-order temperature coefficients of frequency are identify with the data obtain from ref. [38]. The points, where the red crosses and the blue diamonds intersect, are the crystal orientations, which the first- and the second-order temperature coefficient of frequencies equal to zero. These intersect points provide the ideal langasite cuts for a

resonator which operates at extremely high temperature. Figure 5.4.18 and 5.4.19 show the behavior of the first- and second-order temperature coefficient of langasite for C-mode when ϕ varies from $10°$ to $30°$ at increment of $10°$ and θ varies from $-120°$ to $120°$. As calculated results illustrate in fig.5.4.18 and 5.4.19, the number of zero-valued temperature coefficient of frequency are identified.

Figure 5.4.20 shows the examples of the frequency-temperature behavior of the langasite. The θ is fixed at -35^0, while ϕ varies from 30.36^0 to 30.40^0 at increment of 0.02^0. The results show that the langasite has excellent frequency-temperature stability.
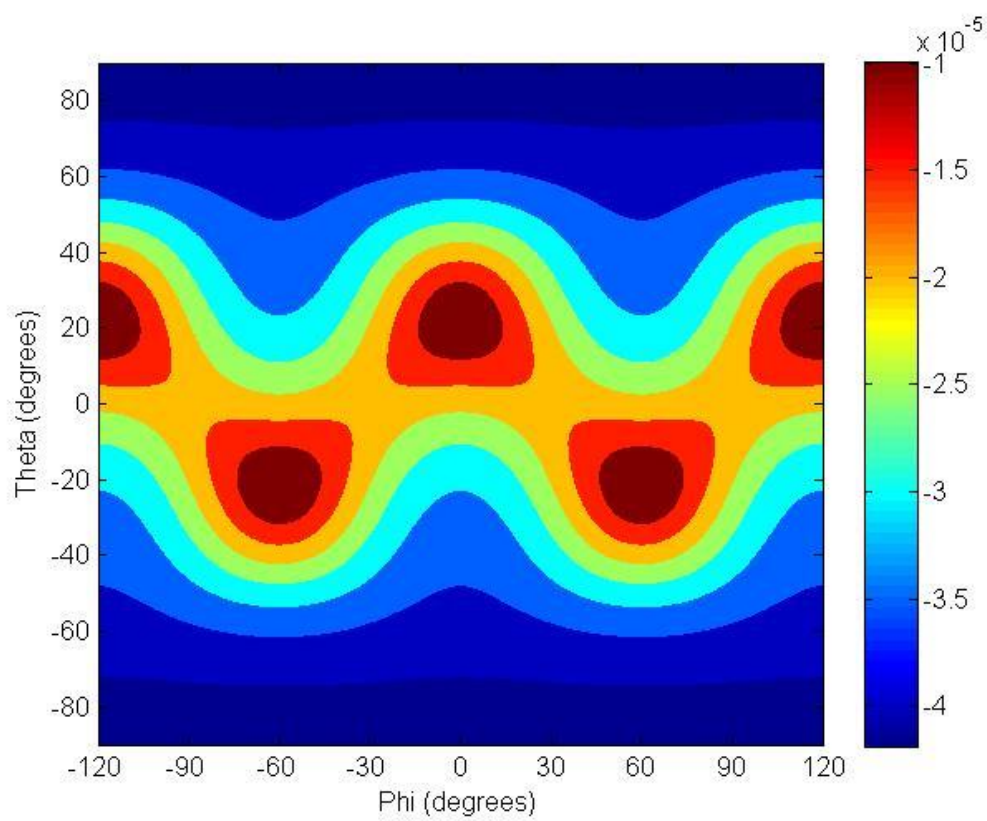
Figure 5.4.10 The first-order temperature coefficient of frequency of langasite for A-mode
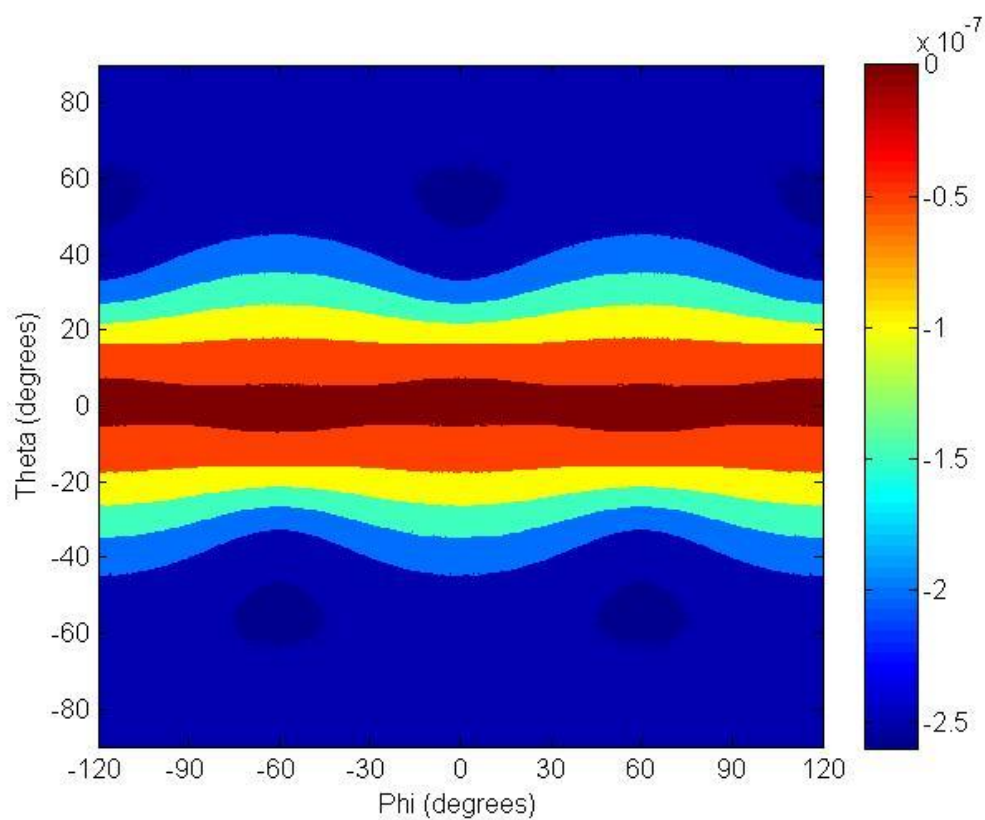
Figure 5.4.11 The second-order temperature coefficient of frequency of langasite for A-mode
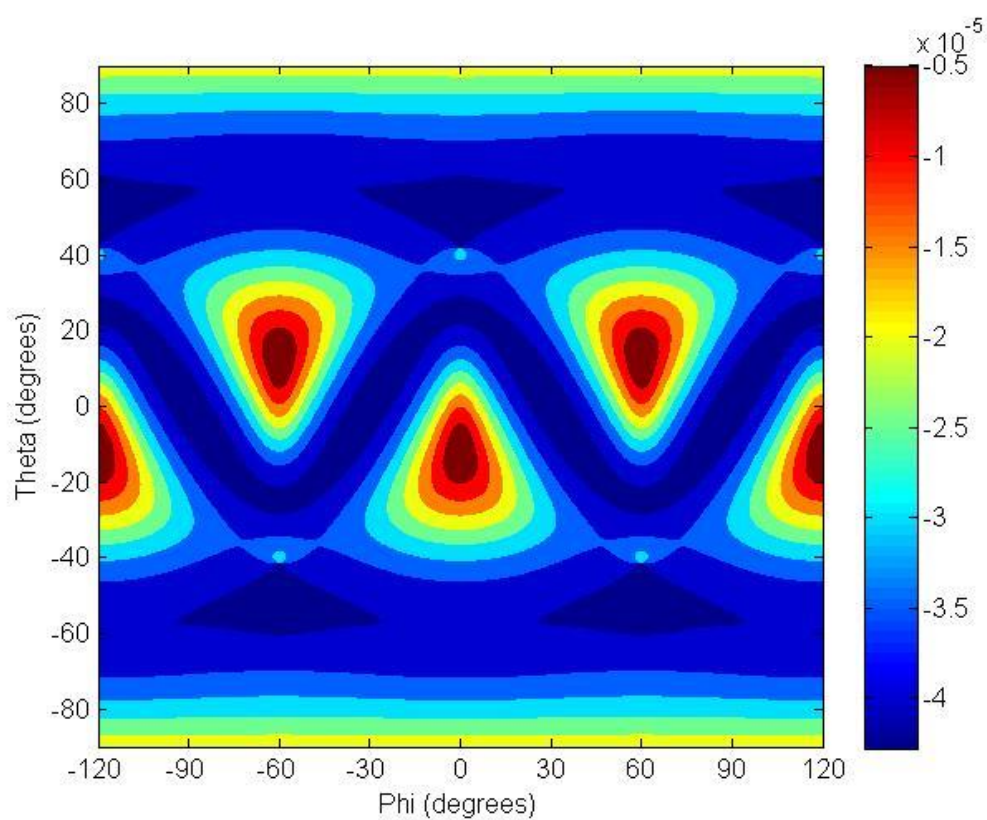
Figure 5.4.12 The first-order temperature coefficient of frequency of langasite for B-mode
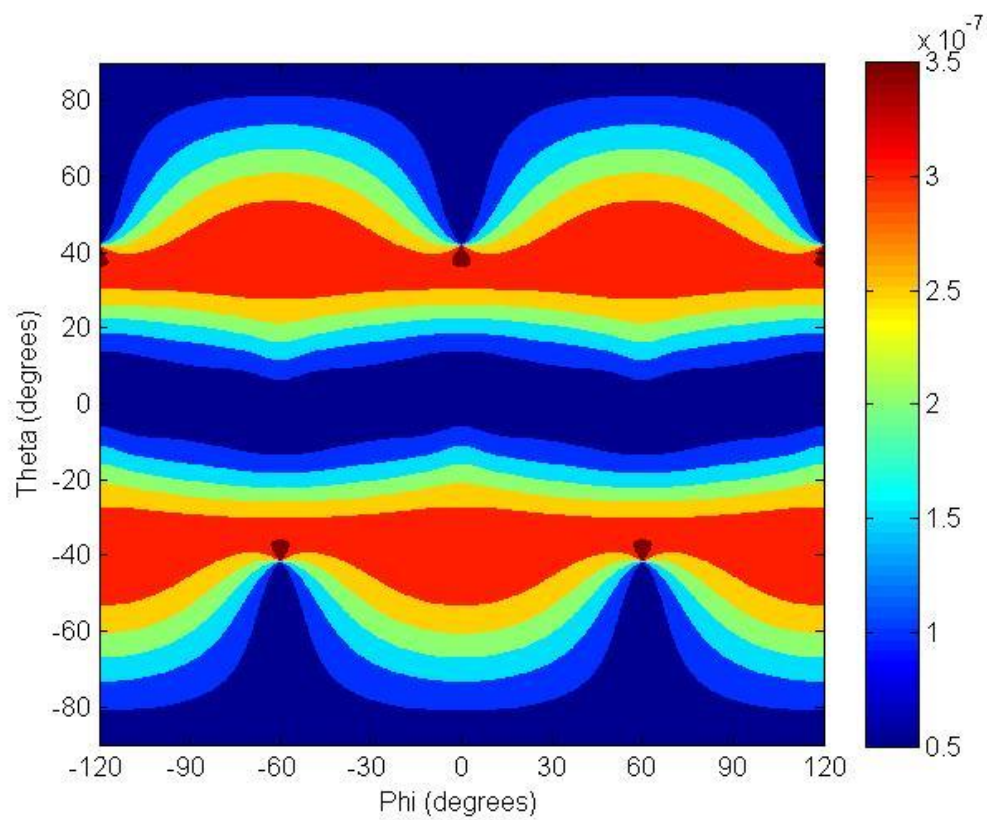
Figure 5.4.13 The second-order temperature coefficient of frequency of langasite for B-mode
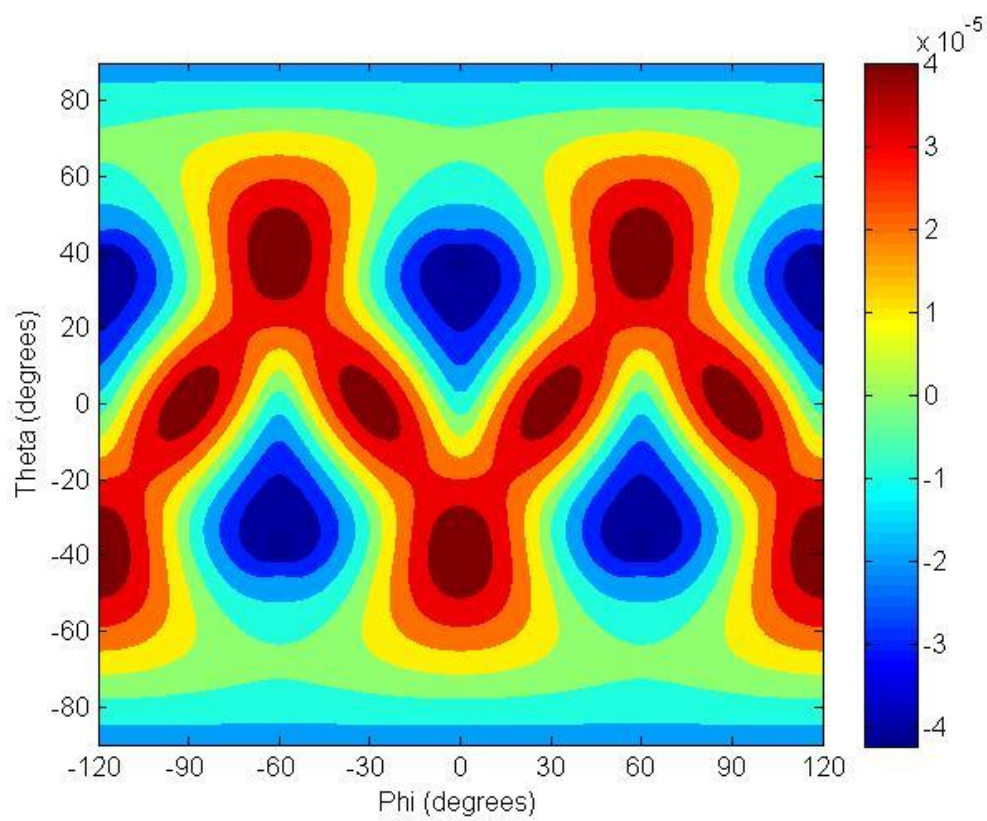
Figure 5.4.14 The first-order temperature coefficient of frequency of langasite for C-mode
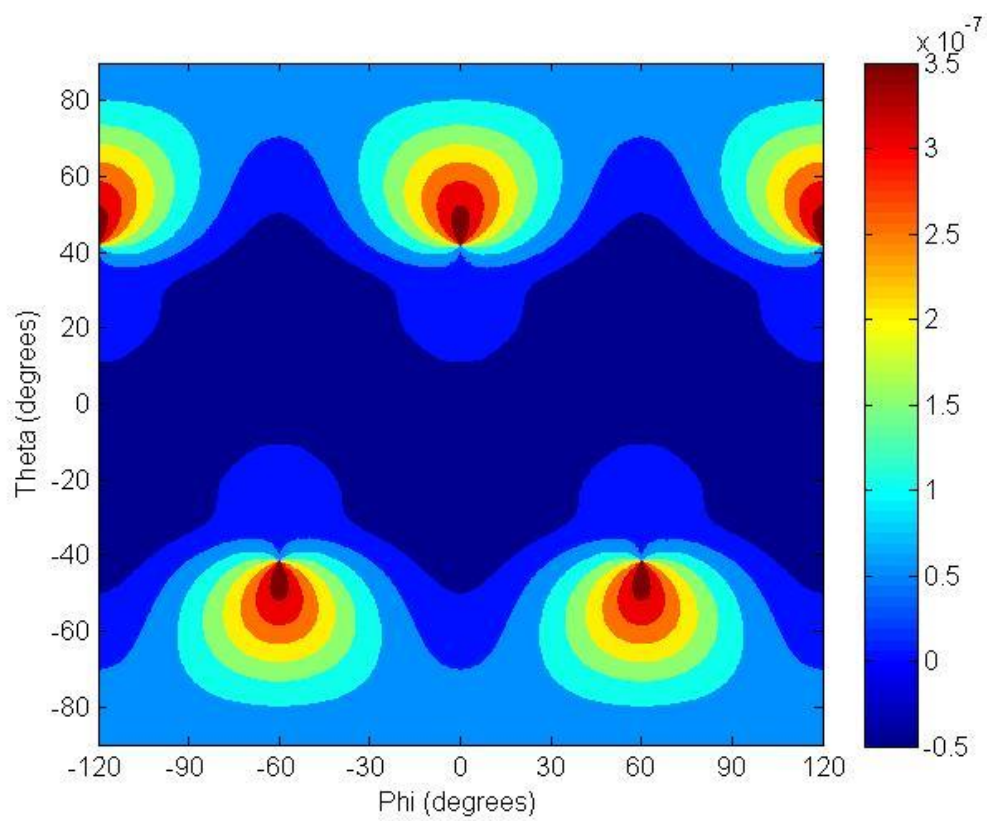
Figure 5.4.15 The first-order temperature coefficient of frequency of langasite for C-mode
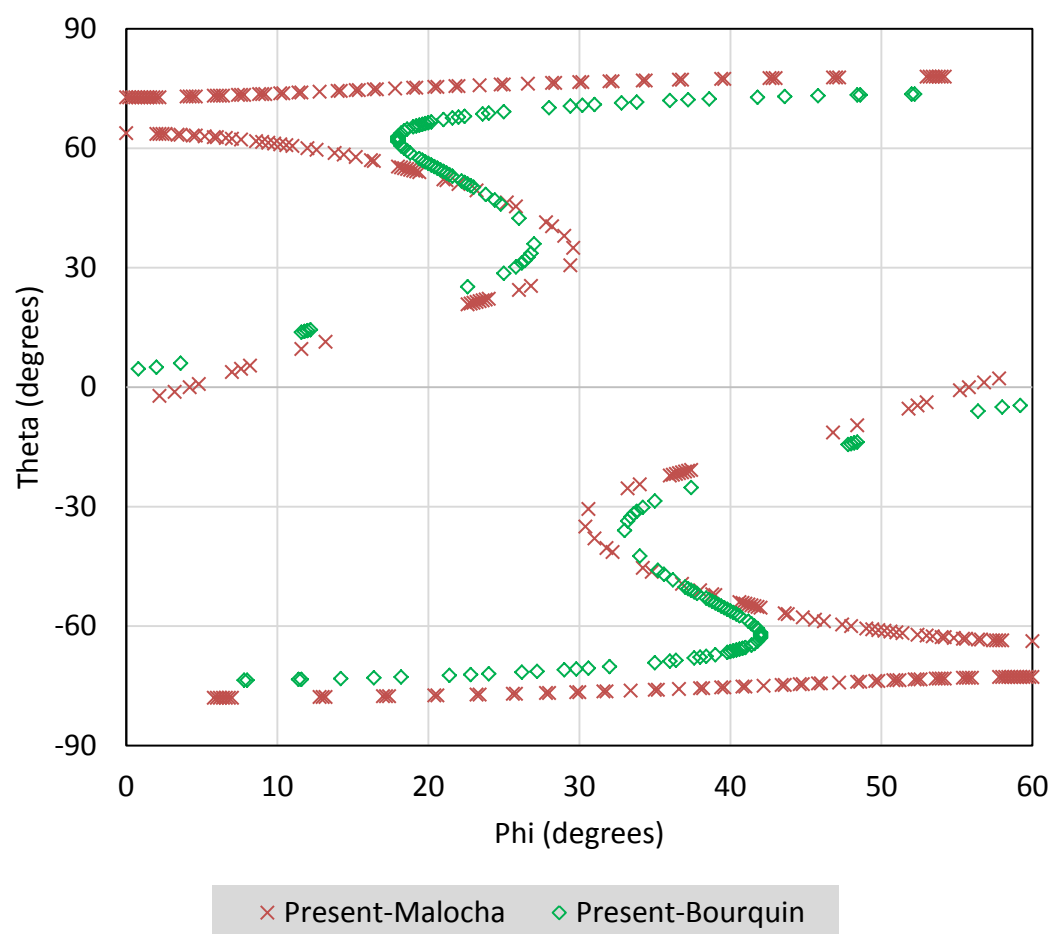
Figure 5.4.16 Loci of Tf1=0 for the thickness mode C of langasite
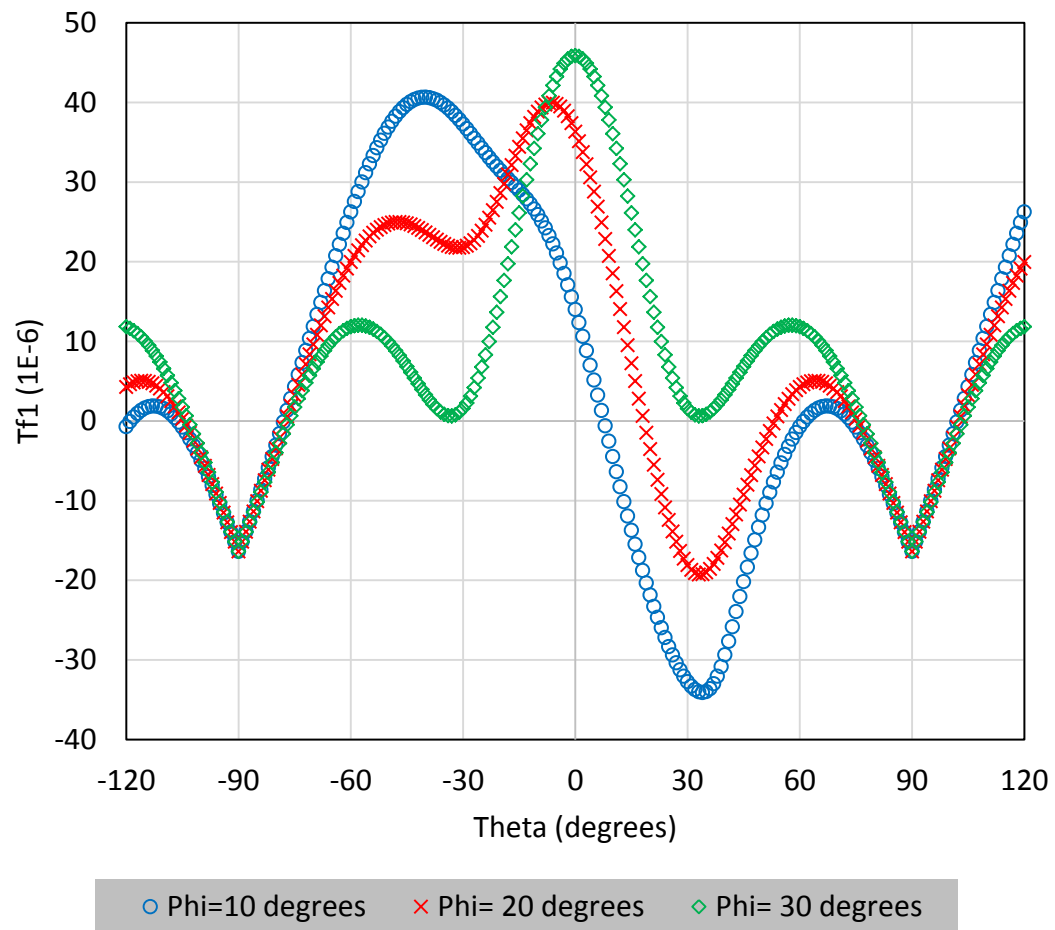
Figure 5.4.17 Loci of *Tf1* =0 and *Tf* 2=0 for the thickness mode C of langasite

Figure 5.4.18 Calculated first-order temperature coefficient of frequency of langasite
when ϕ=10, 20, 30
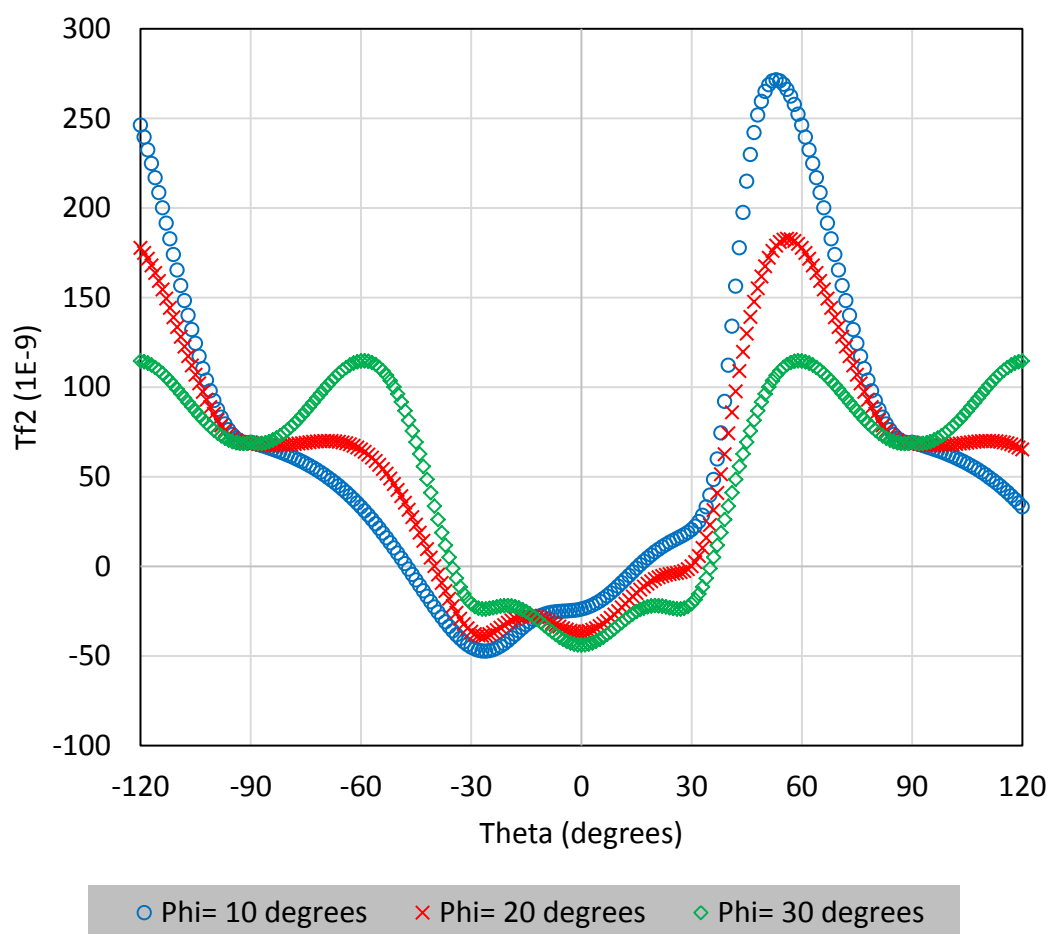
Figure 5.4.19 Calculated second-order temperature coefficient of frequency of langasite when ϕ=10, 20, 30
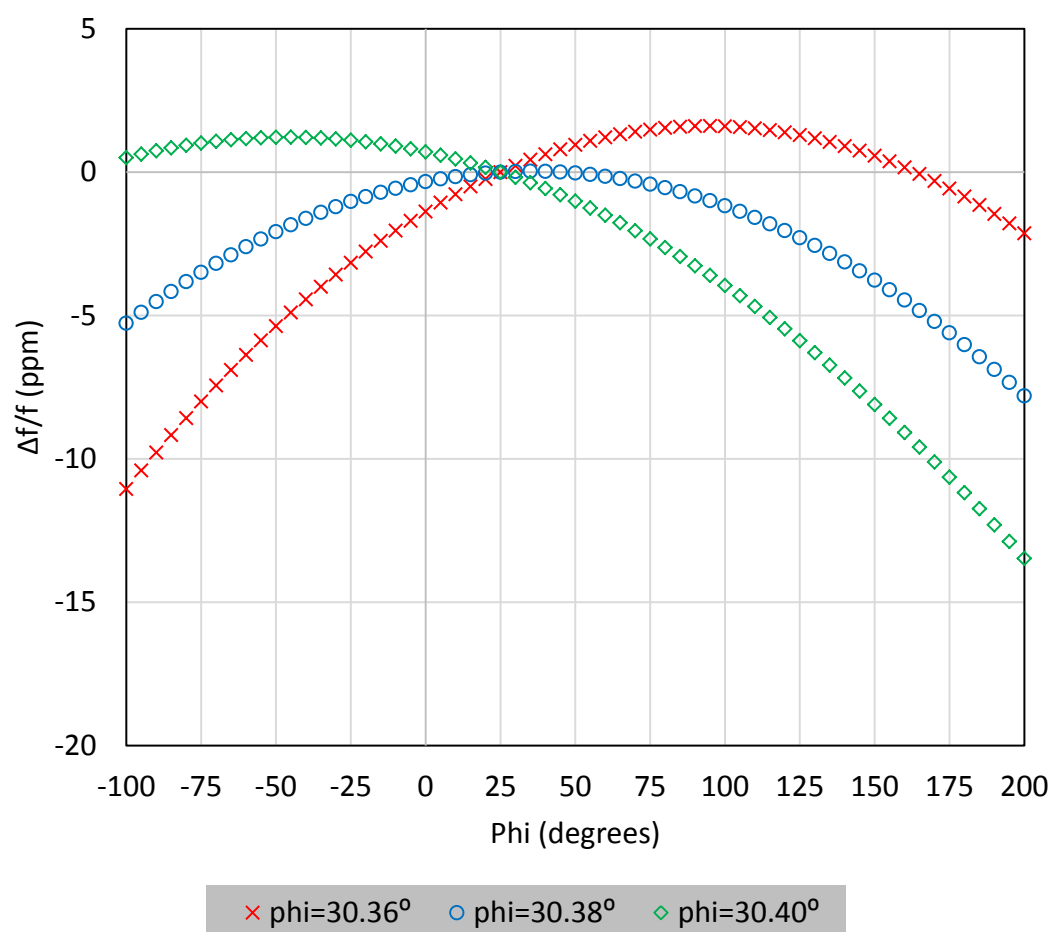
Figure 5.4.20 Frequency – temperature curve when $\theta = 33.5$

5.5   The Material Properties at High Temperature

It is well known that the resonant frequency of the piezoelectric resonators or devices not only depends on its crystalline orientations, material anisotropy and mounting support, but also on temperature. The resonant frequency shifting due to the changes of the temperature can be compensated or corrected with a known temperature dependence of the resonant frequencies or by measuring the temperature of the piezoelectric crystal by some independent means. The temperature coefficients are usually measured at the room temperature, $25℃$ and those material properties values that associate with the reference temperature are only valid under a relatively small temperature range around the room temperature. For example, the oil and gas industry requires reliable and stable sensors to operate at high temperatures because the temperature is a function of depth. The langasite sensor has the potential to allow the oil/gas companies to drill deeper as they seek to find sources of production.

In this section, the Lagrangian equations, which previously derived in Chapter 5.2 and 5.3, are used to predict the material properties at the elevated temperature. Only the effective elastic constants are temperature dependent and requires the computation of the material constants. The six-independent second-order linear elastic constants and the thermal expansion coefficients are analytically calculated with the data obtain from [41] by shifting the reference temperature from $25℃$ to $600℃$. The newly calculated materials constants are used to compute the temperature coefficient of frequency. The temperature compensated orientations of the langasite for C-mode at reference temperature are compared with the temperature compensated orientations that are calculated in a wide temperature range.

By assuming the relationship between the temperature and the elastic constant of langasite at any reference temperature is the same, each second-order linear elastic constant is computed with the first equation of Eq. 5.2.6. The Taylor series expansion is used to predict the second-order linear elastic constants at high temperatures. The changes of each elastic constant of the langasite as a function of temperature are shown in fig. 5.5.1 to 5.59. Each second-order elastic constant of langasite and thermal expansion coefficients are computed from -50℃ to 500℃ at increments of 25℃. Base on the calculation of the stiffness of langasite, C_{11}, C_{12}, C_{13}, C_{14}, C_{33} and C_{44} decrease when temperature increases. C_{66} is the only second-order linear elastic constant that increases when temperature increases.

Similarly, the thermal expansion coefficients at a wide temperature range, from -50℃ to 600℃, are computed with Eq. 5.1.14. Figure 5.5.8 and 5.5.9 show the changes of the thermal expansion coefficient as a function of temperature. Both thermal expansion coefficients increase when the temperature increases. In addition, the rate of change in the thermal expansion coefficient increases with the temperature.

By shifting the reference temperature using the regression analysis technique, we obtained new set of second-order elastic constants: first-and second-order temperature derivative of the elastic constants and thermal expansion coefficients at temperatures from 25℃ to 600℃. The calculated second order elastic constants are compared with the data obtained by Weihnacht [42], as shown in Fig. 5.5.10. The comparison between the newly calculated sets of second-order elastic constants agrees well with experimental data, except elastic constant C_{33}. Figure 5.5.11 and 5.5.12 show the first order temperature derivative of second-order elastic constant and thermal expansion

coefficients of langasite as a function of reference temperature. The second temperature derivative of second order elastic constants and the second order thermal expansion coefficients are temperature independent due to the nature of the curve fitting process. Once the third-order temperature coefficients are determined, the second-order temperature derivative and second-order thermal expansion coefficients of langasite can be calculated as a function of temperature.

The temperature coefficient of frequency of the langasite plates is calculated with the present sets of elastic constants and the thermal expansion coefficients at high temperatures. The temperature compensated orientations of langasite are investigated in the entire region of the crystalline. The fast- and slow-thickness shear modes are not included in this study, as zero-valued temperature coefficient of frequency of those two modes are not found. Figure5.5.13 shows a loci of C-mode temperature compensated orientations for langasite at various temperatures from 25℃ to 315℃. The results shows that when the reference temperature increases, the zero-valued temperature coefficient of frequency curves get smaller until it reaches the temperature of around 315℃. At any temperature above 350 ℃, the temperature compensated orientations do not exist. Figure 5.5.14, 5.5.15 and 5.5.16 show the typical examples of the behavior of the temperature coefficient of frequency for the C-mode of langasite when ϕ=30°, 45° and 60°, respectively. The number of points crossing the zero-value of temperature coefficient of frequency decreases as the reference temperature increases as shown in fig. 5.5.14, 5.5.15 and 5.5.16.
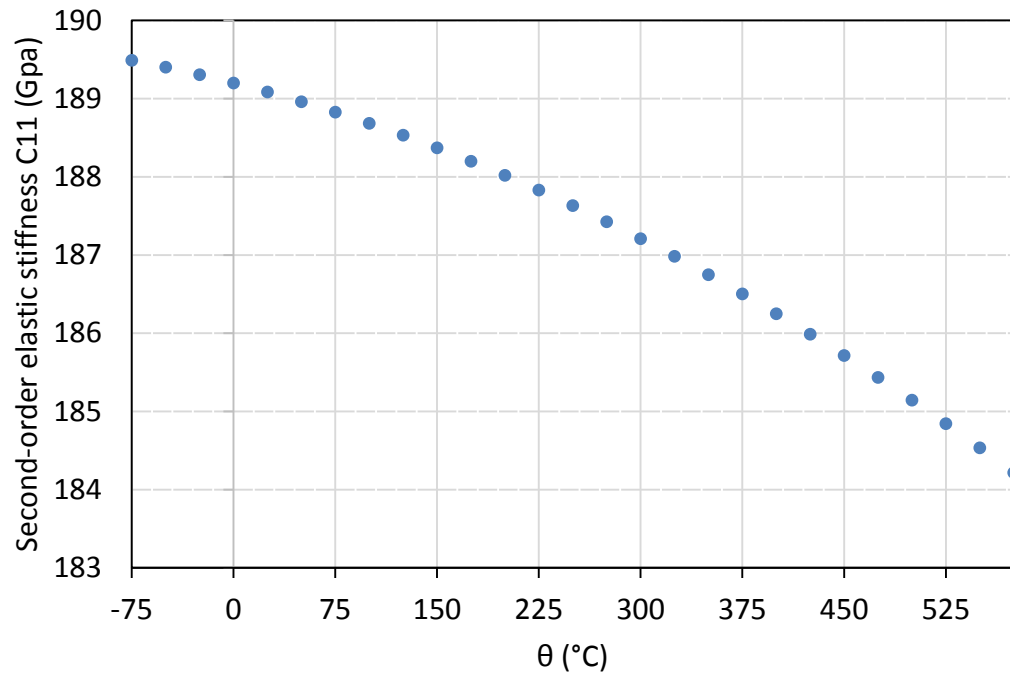
Figure 5.5.1 The second-order linear elastic constant C_{11} as a function of temperature
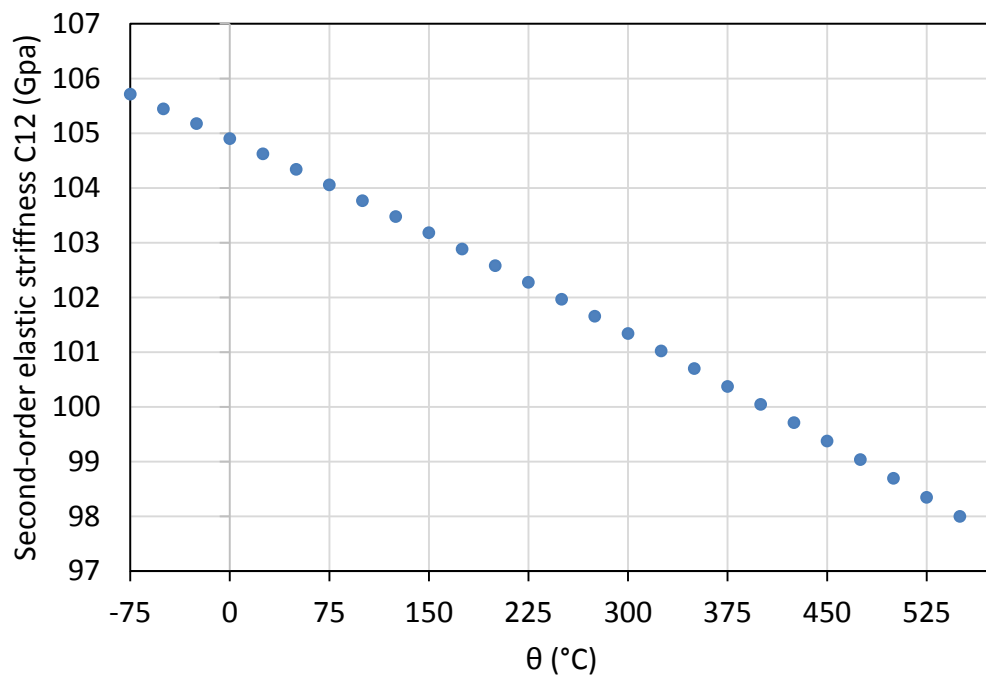
Figure 5.5.2 The second-order linear elastic constant C_{12} as a function of temperature
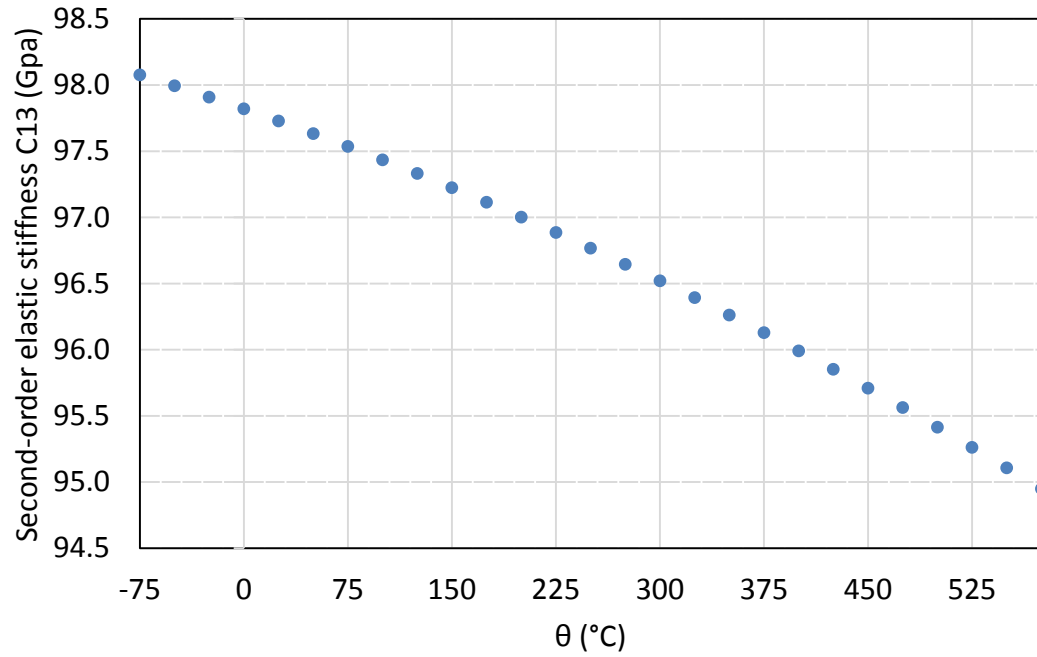
Figure 5.5.3 The second-order linear elastic constant C_{13} as a function of temperature
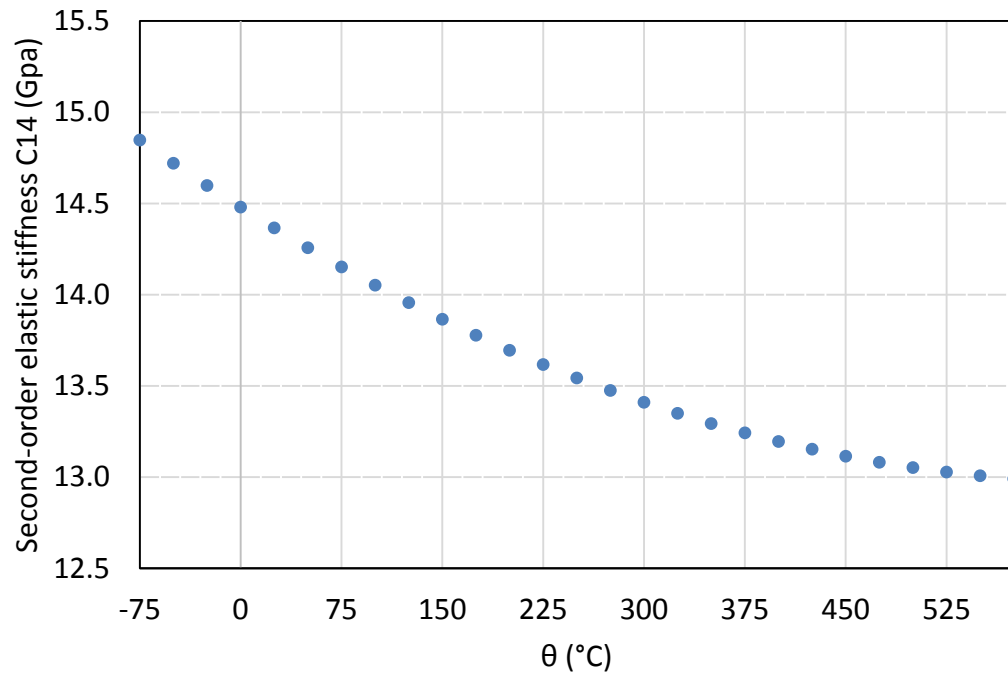
Figure 5.5.4 The second-order linear elastic constant C_{14} as a function of temperature
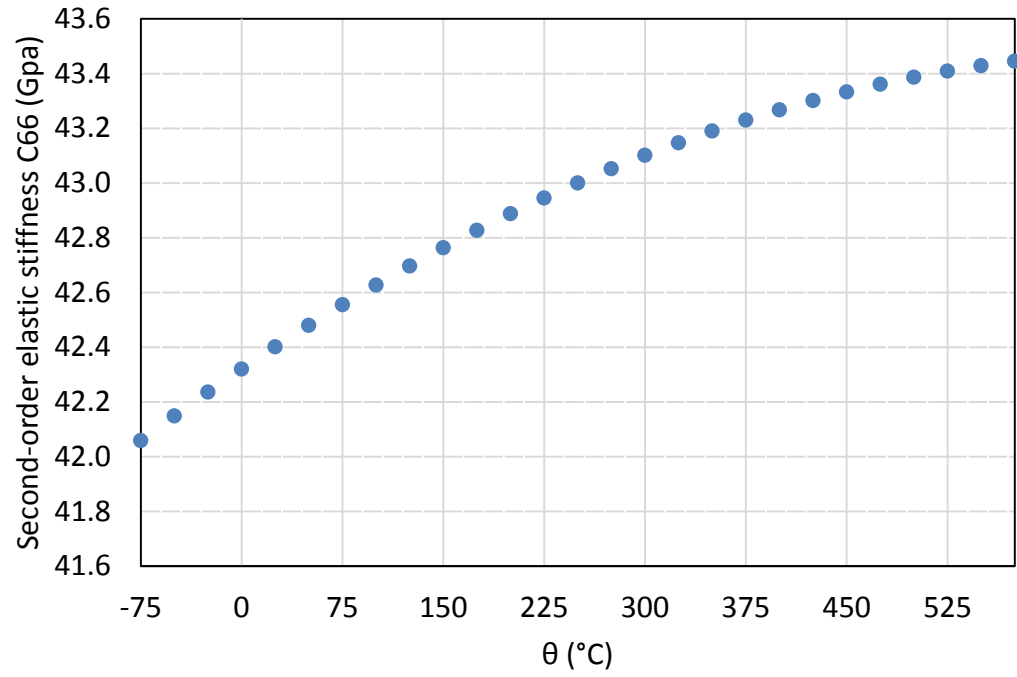
Figure 5.5.5 The second-order linear elastic constant C_{66} as a function of temperature
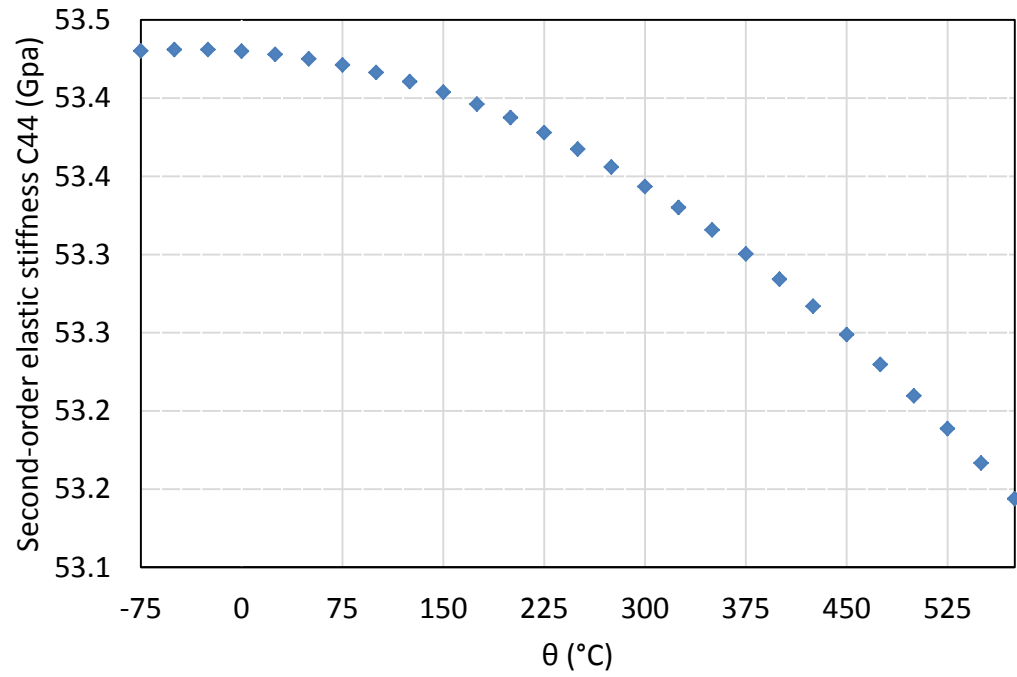
Figure 5.5.6 The second-order linear elastic constant C_{44} as a function of temperature
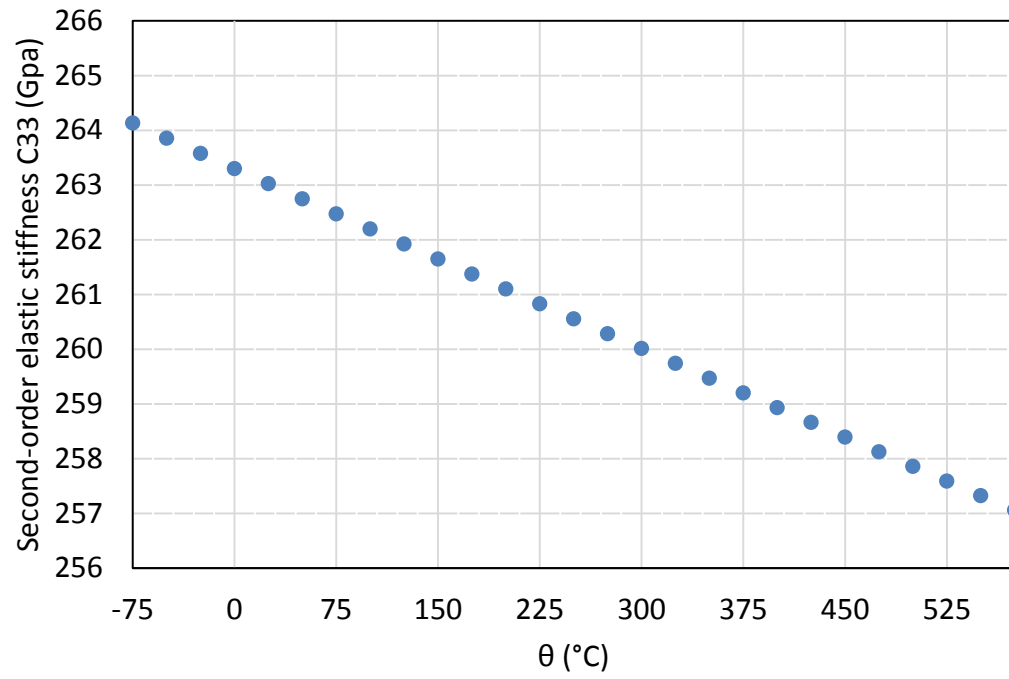
Figure 5.5.7 The second-order linear elastic constant C_{33} as a function of temperature
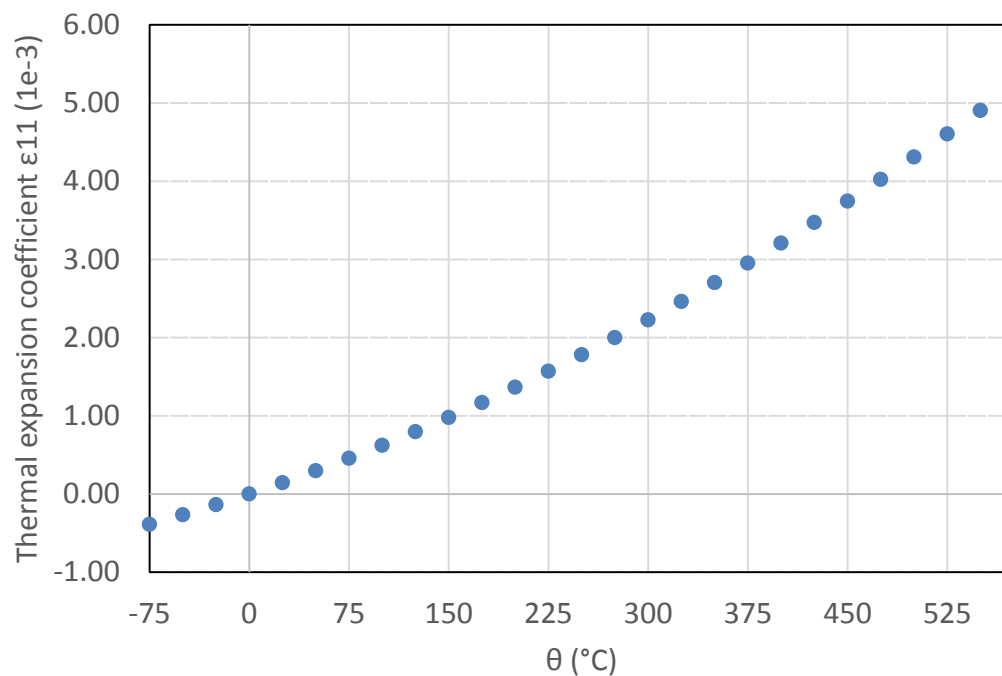
Figure 5.5.8 Thermal expansion coefficient ε_{11} as a function of temperature
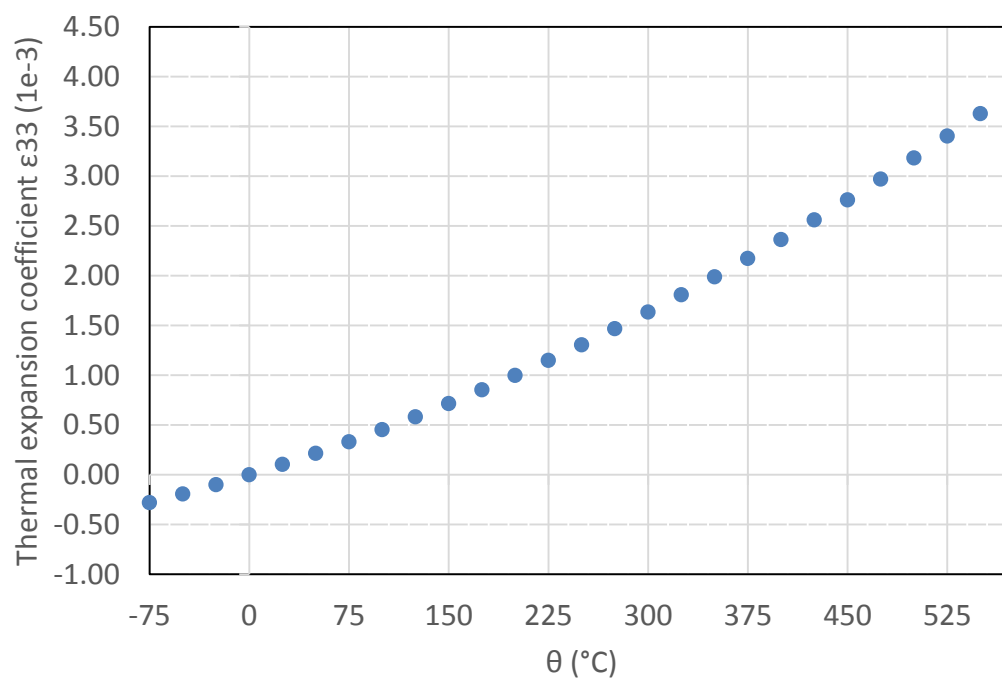
Figure 5.5.9 Thermal expansion coefficient ε_{33} as a function of temperature
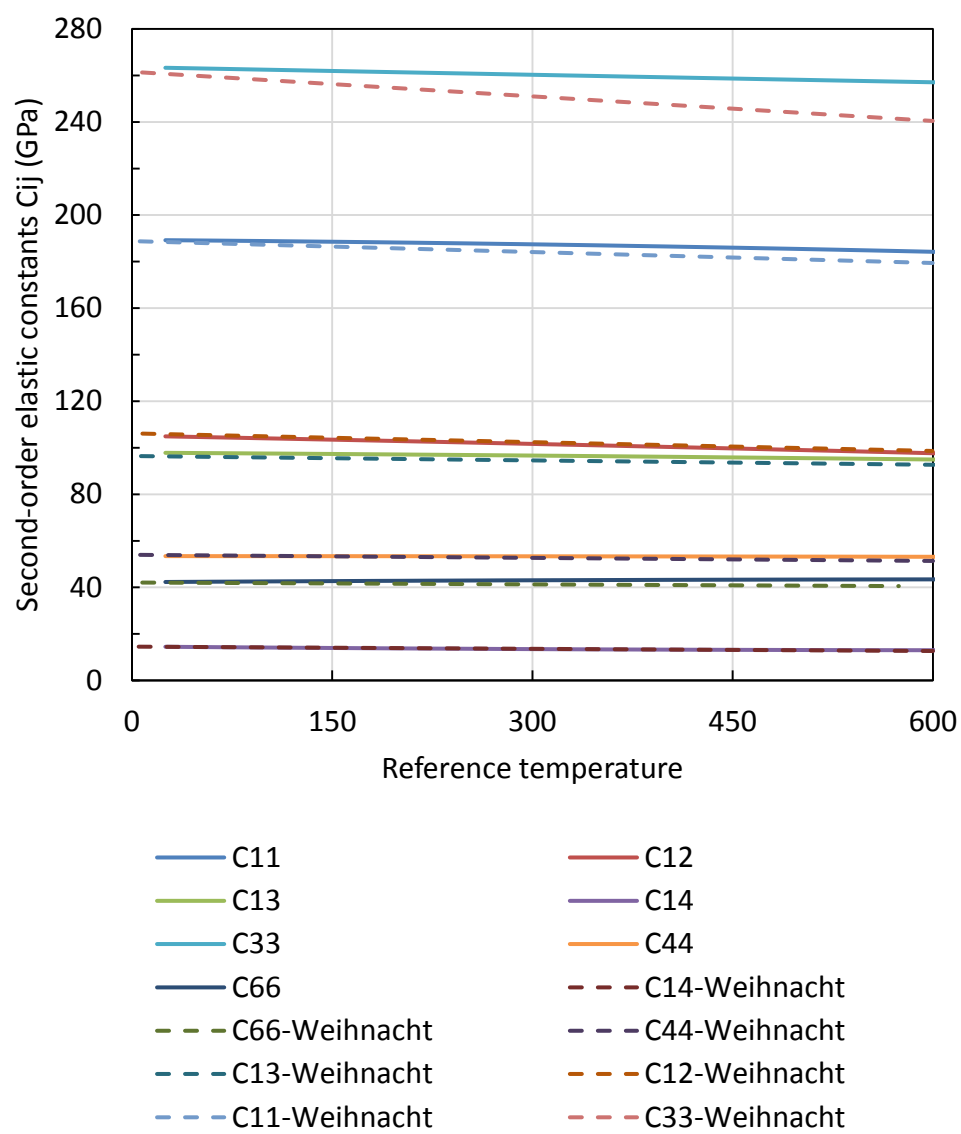
Figure 5.5.10 Temperature dependence of the second-order elastic constants of langasite
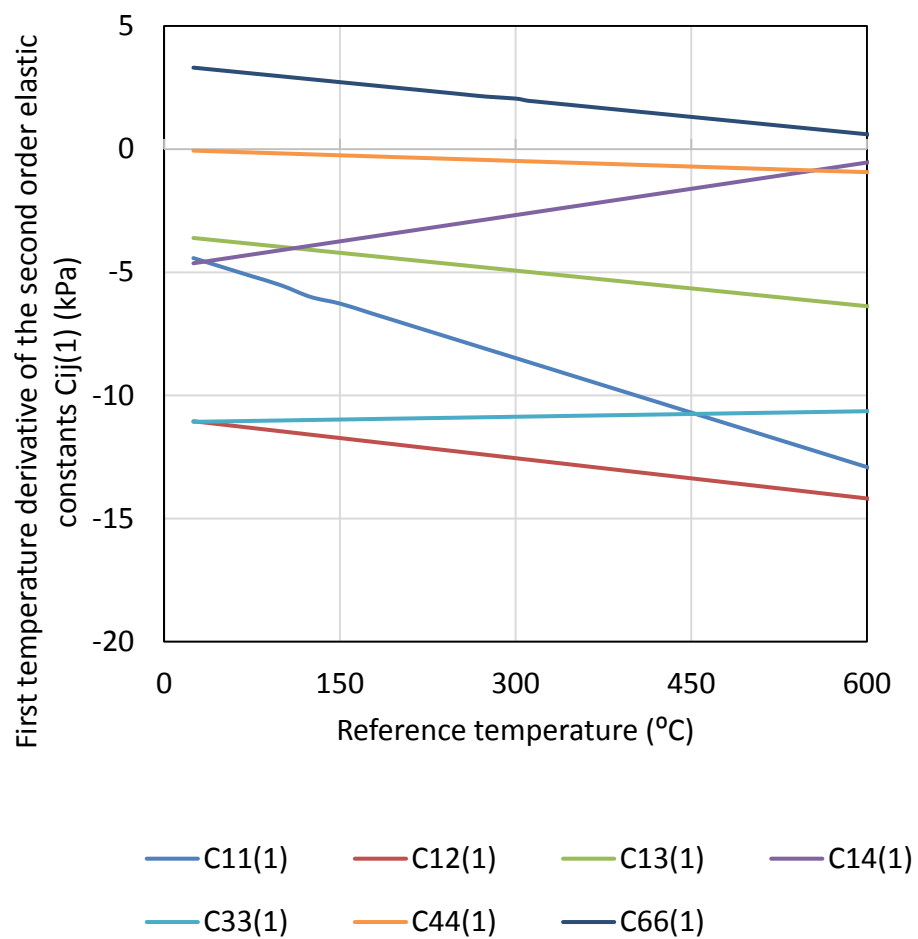
Figure 5.5.11 Temperature dependence of first temperature derivative of the second-order linear elastic constant of langasite
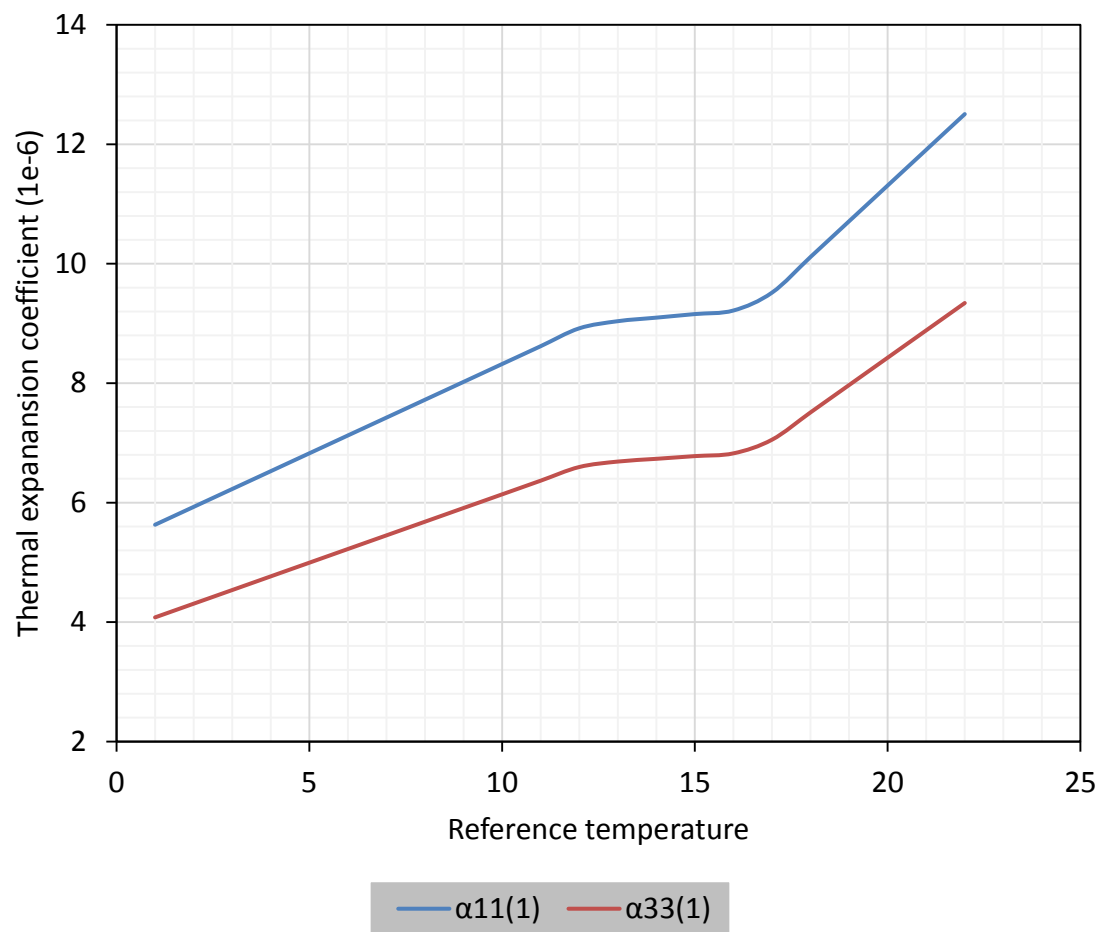
Figure 5.5.12 Temperature dependence of thermal expansion coefficients
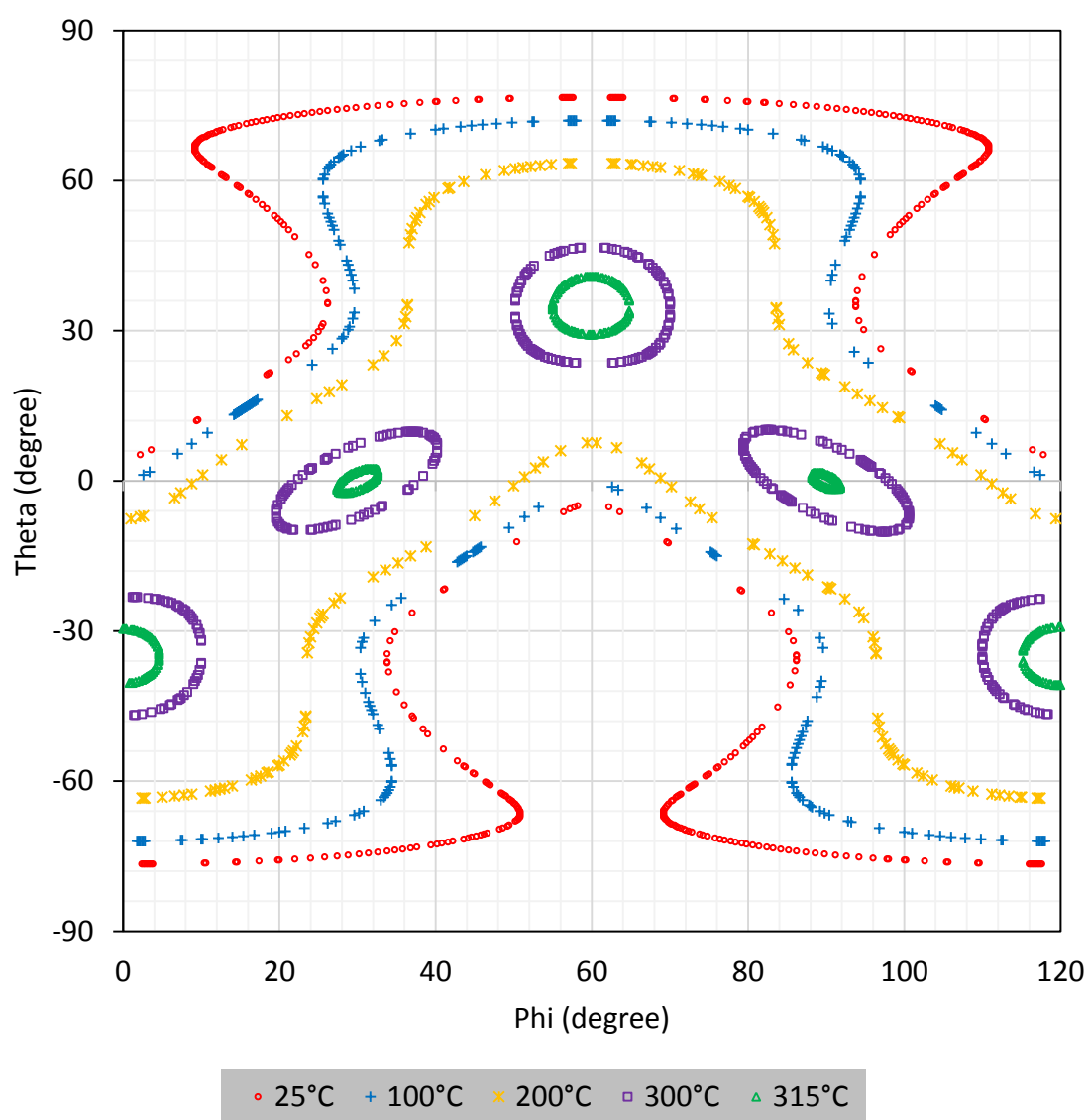
Figure 5.5.13 Loci of C-mode temperature compensated orientation for langasite
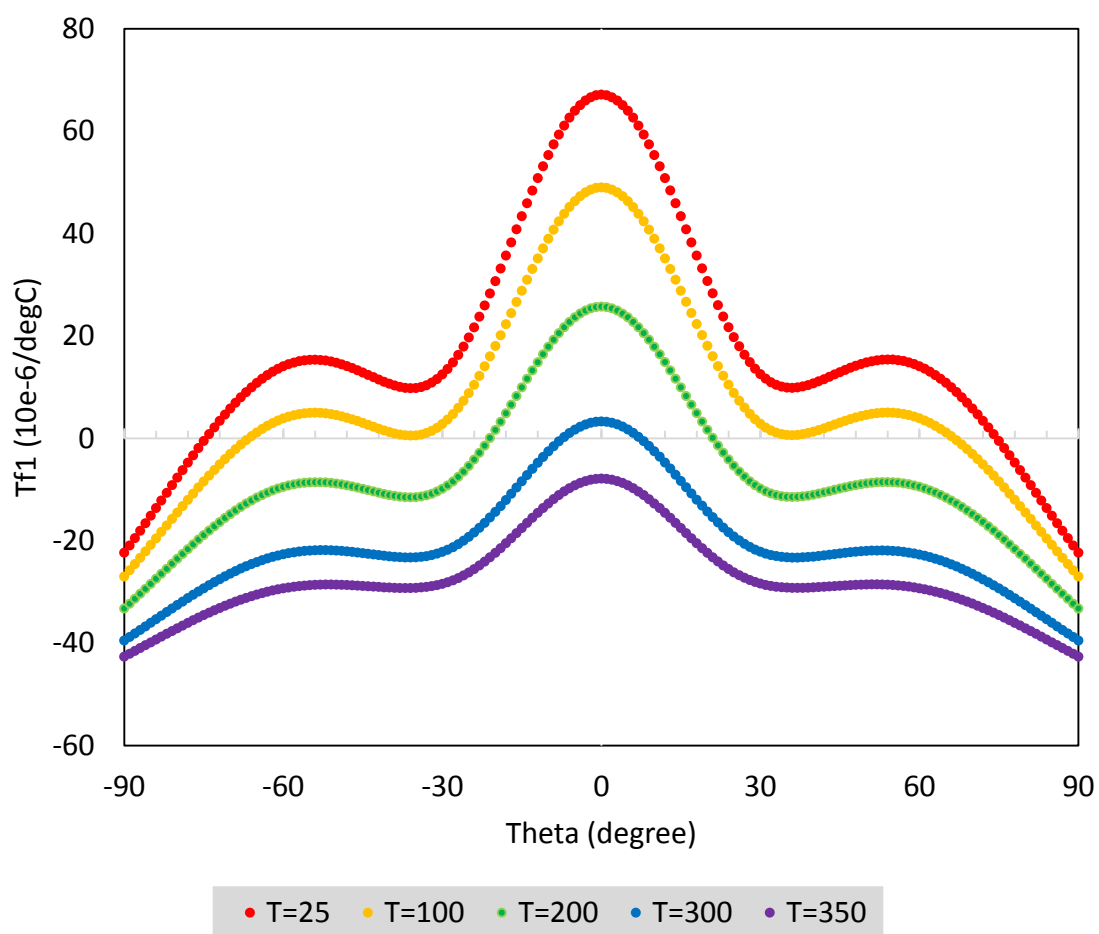
Figure 5.5.14 Temperature dependence of the temperature coefficient of frequency of the C-mode for langasite when φ=30°
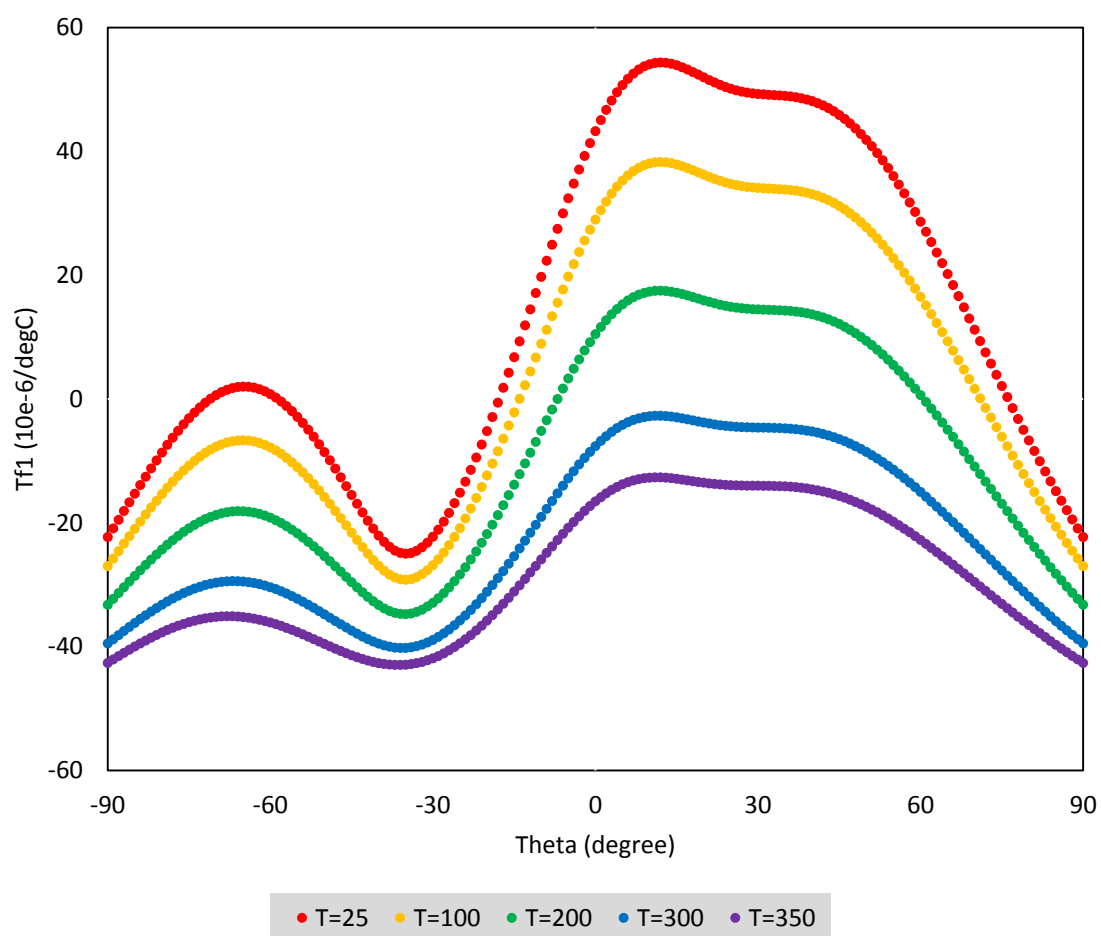
Figure 5.5.15 Temperature dependence of the temperature coefficient of frequency of the C-mode for langasite when $\phi=45°$
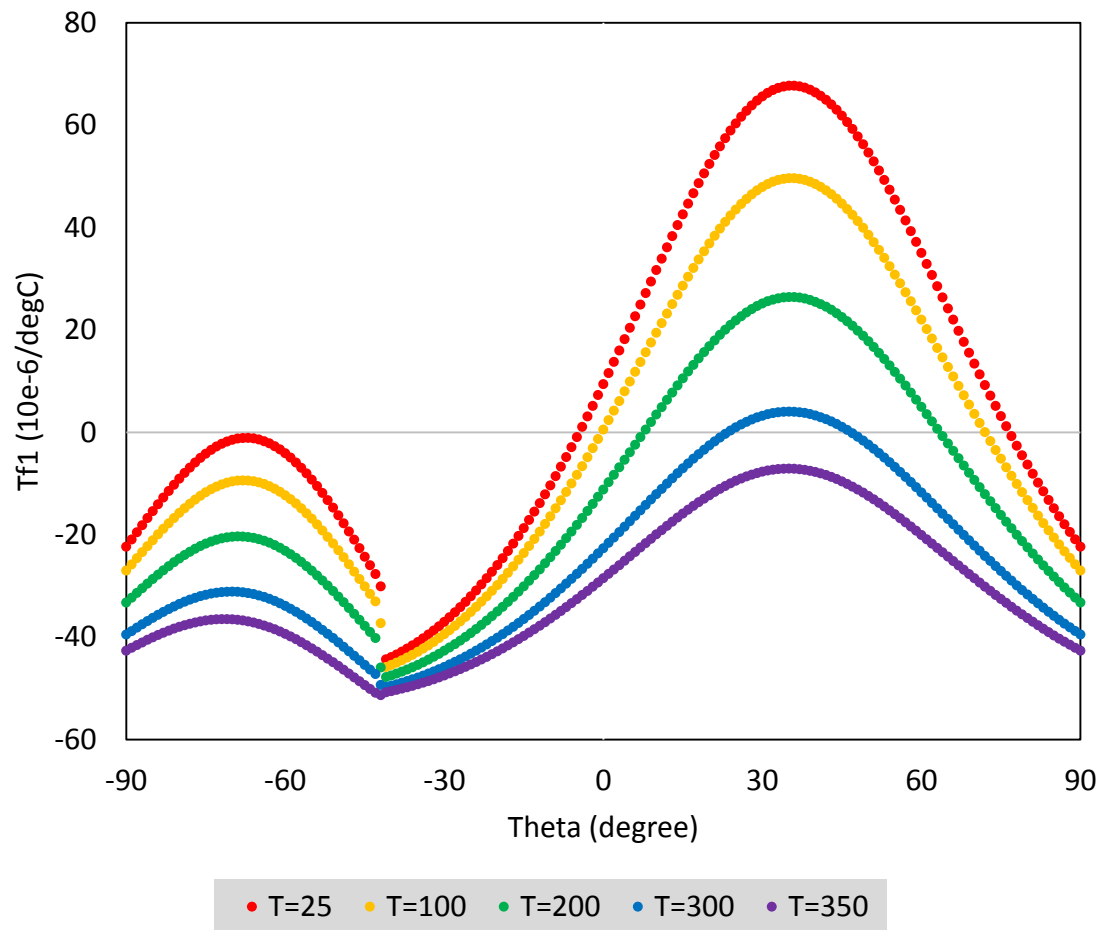
Figure 5.5.16 Temperature dependence of the temperature coefficient of frequency of the C-mode for langasite when $\phi=60°$

5.6   Summary

The frequency-temperature behavior of the langasite crystal is studied with the three-dimensional equations of incremental motion superposed on homogeneous thermal strain including piezoelectric effect. Normally, the piezoelectric effect is neglected in analysis of quartz crystal due to their very small piezoelectric coupling. The piezoelectric coupling factor of the langasite crystal is much larger than its quartz crystal and cannon be ignore. However, the analysis shows that piezoelectric effect on the frequency-temperature behavior of langasite is negligible. The temperature coefficient of frequency of langasite of all three modes of vibration, A-, B- and C-mode, is calculated. The results show that no temperature compensated orientation of the A- and B-modes exist. For C-mode, the temperature compensated cuts are found at several locations.

Only the effective elastic constants are a function of the temperature in the equations for small vibrations superposed on thermally-induced deformations by steady and uniform temperature changes. The effective elastic constants consist of the second-order elastic constants, first-and effective second-order temperature derivative of second-order elastic constants, third-order elastic constant, and the first-and second-order thermal expansion coefficient, in addition to piezoelectric and dielectric coefficients. These values are measured at the room temperature, but they can change when measured at different temperatures. The second order elastic constants and the thermal expansion coefficients are calculated with regression analysis at high temperatures. The results show that this theoretical method can be used to predict the elastic constants and the thermal expansion coefficient at high temperatures as newly computed elastic constants agree very well with the experimental data, except C_{33}. This theoretical method to predict the

temperature dependency of the material properties of langasite can be more accurately implemented once higher-order temperature coefficients are known. The loci shows that the temperature compensated orientations change as temperature increases. No temperature compensated orientations can be found at temperatures above 350℃. The loci can be used for design of sensors or devices that operates at high temperatures.

Chapter 6. Future works

In this dissertation, we studied double-ended tuning fork gyroscope and introduced the newly designed gyroscope called, length-extension gyroscope. Using quartz, langasite and langatate crystals, we simulated each gyroscope and compared the geometric and gyroscopic characteristics. Furthermore, frequency-temperature behavior of the langasite has been investigated at the reference temperature, as well as elevated temperatures.

In the future study, the third-order temperature coefficient of frequency of langasite can be calculated once the full set of the third-order temperature coefficient are measured. This will provide more accurate results. The temperature coefficient of frequency of langatate can be investigated when the third-order nonlinear elastic constants are reported.

Bibliography

[1] C. Acar and A. Shkel, MEMS Vibratory Gyroscopes Structure Approaches to Improve Robustness, New York: Springer Verlag, 2009, pp. 4-5,14-35.

[2] J. Peters, An introduction to piezoelectric materials and applications, Apeldoorn: Stichting Applied Piezo, 2013, p. Chapter 3.

[3] J. Nye, Physical Properties of Crystals, Oxford: The Clarendon Press, 1960, pp. Chapter 4, section 5.

[4] R. Newnham, Properties of matrials, New York: Oxford university press, 2005.

[5] A.Sehirlioglu, A.Sayir and C.Klemenz, "High-Temperature Properties of Piezoelectric Langatate Single Crystals," NASA Glenn Research Center and Case Western Reserve University , Cleveland,Ohio, 2007.

[6] M. Patel, Nonlinear behavior in quarz resonators and its stability, New Brunswick: Rutgers University, 2008.

[7] J. Rosenbaum, Bulk Acoustic Wave Theory and Devices, Norwood,MA: Artech house Inc., 1988, pp. 57-66,125-157.

[8] T. H.F, Linear Piezoelectric plate vibration, New York: Plenum Press, 1969, pp. Chapter9,section 2.

[9] K. Fujiwara, H. Hida and I. Kanno, "Design of MEMS cylindrical gyroscope integrated with piezoelectric thin film," in *Micro-NanoMechatronics and Human Science (MHS)*, Nagoya, 2013.

[10] J. Burdess, A. Harris, J. Cruickshank, D. Wood and G. Cooper, "A review of vibratory gyroscopes," *Engineering Science and Education Journal,* pp. 249 - 254, 1994.

[11] D. Keymeulen, C. Peay, D. Foor, T. Trung, A. Bakhshi, P. Withington, K. Yee and R. Terrile, "Control of MEMS Disc Resonance Gyroscope (DRG) using a FPGA Platform," in *Aerospace Conference, 2008 IEEE*, Big Sky, MT, 2008.

[12] R. Oria, J. Otero, L. González, L. Botaya, M. Carmona and M. Puig-Vidal, "Finite element analysis of electrically excited quartz tuning fork devices," *Sensor,* vol. 13, pp. 7156-7169, 2013.

[13] K. Sato, A. Ono and Y. Tomikawa, "Finite Element Method Simulation of Double-Ended Tuning-Fork Quartz Resonator for Application to Vibratory Gyro-Sensor," *Japanese Journal of Applied Physics,* vol. 42, pp. 3115-3119, 2003.

[14] K. Sato, A. Ono and Y. Tomikawa, "Simulation of quartz crystal gyro-sensor using double-ended tuning fork resonator for detection of two-axial angular velocities," in *Ultrasonics, 2003 IEEE Symposium*, Honolulu, 2003.

[15] K. Sato, A. Ono and Y. Tomikawa, "Experimental study of gyro sensor using double-ended tuning fork quartz resonator," in *Frequency Control Symposium and Exposition, 2004 IEEE International*, 2004.

[16] G. Choi and Y. Yong, "Langatate and langasite microacoustic gyro sensors," in *Ultrasonics Symposium (IUS), 2014 IEEE International*, Chicago, IL, 2014.

[17] J. Yang, "Some analytical results on piezoelectric gyroscopes," in *Frequency*

Control Symposium, 1998 IEEE International, Pasadena, CA, 1988.

[18] Y. Y.K. and Y. Kim, "Analysis and comparison of langasite versus quartz for a thickness shear vibratory gyroscope," in *Frequency Control Symposium (FCS), 2010 IEEE International*, Newport Beach, CA, 2010.

[19] R. Smythe, "Material and resonator properties of langasite and langtate: A progress report," in *IEEE International frequency control symposium*, Pasadena, CA, 1998.

[20] J.Yang and J.Kosinski, "Effects of Piezoelectric Coupling on Energy Trapping of thickness-Shear Modes," *IEEE UFFC,* vol. 51, no. 9, pp. 1047-1049, 2004.

[21] Y. Kagawa, T. Tsuchiya and T. Kawashima, "Finite element simulation of piezoelectric vibrator gyroscopes," *Ultrasonics, Ferroelectrics, and Frequency Control, IEEE Transactions on,* vol. 43, no. 4, pp. 509 - 518, 1996.

[22] Y. Tomikawa, S. Oyama and M. Konno, "A Quartz Crystal Tuning Fork with Modified Basewidth for a High Quality Factor: Finite Element Analysis and Experiments," *Sonics and Ultrasonics, IEEE Transactions on,* vol. 29, no. 4, pp. 217 - 223, 1982.

[23] A. Ballato, "Equivalent ciruits for resonators and transducers driven piezoelectrically," US army laboratory command, Fort Monmouth, 1990.

[24] G. choi and Y. Yong, "Design of a novel length extension vibratory gyroscope," in *Frequency Control Symposium & the European Frequency and Time Forum (FCS), 2015 Joint Conference of the IEEE International*, Denver, CO, 2015.

[25] Y. Yong, P.C.Y.Lee and S. Chuang, "Vibrations of a z-cut quartz resonator-structure in the vicinity of the third overtone of extensional mode," *Computers & Structures,* vol. 38, no. 1, pp. 93-106, 1991.

[26] Y. Yong, P. Lee and S. Chuang, "Vibrations of z-cut resonator structure by finite element analysis," in *Frequency Control Symposium, 1988., Proceedings of the 42nd Annual*, Baltimore, MD, 1988.

[27] J. Hermann, "Determination of the electromechanical coupling factor of quartz bars vibrating in flexure or length extension," in *IEEE 29th Annual Symposium on Frequency Control. 1975*, 1975.

[28] H. Kawashima, "Forced vibrations of KT-cut width-extensional mode quartz crystal resonators," in *Frequency Control Symposium, 1993. 47th., Proceedings of the 1993 IEEE International*, Salt Lake City, UT, 1993.

[29] G. Kuzmicheva, E. Domoroschina, V. Rybakov, A. Dubovsky and T. E.A., "A family of langasite: growth and structure," *Journal of Crystal Growth,* vol. 275, no. 1-2, pp. 715-719, 2005.

[30] I. Mateescu, J. Zelenka, J. Nosek and G. Johnson, "Frequency-temperature characteristics of the langasite resonators," in *Frequency Control Symposium and PDA Exhibition, 2001. Proceedings of the 2001 IEEE International*, Seattle, WA, 2001.

[31] Y. Pisarevsky, P. Senushencov, P. Popov and B. Mill, "New strong piezoelectric La3Ga5.5Nb0.5O14 with temperature compensation cuts," in *Frequency Control Symposium, 1995. 49th., Proceedings of the 1995 IEEE International*, San Francisco, CA, 1995.

[32] O. Buzanov, A. Naumov, V. Nechaev and S. Knyazev, "A new approach to the growth of langasite crystals," in *Frequency Control Symposium, 1996. 50th., Proceedings of the 1996 IEEE International.*, Honolulu, HI, 1996.

[33] P. Lee and Y. Yong, "Temperature Derivatives of Elastic Stiffnesses Derived from the Frequency-Temperature Behavior of Quartz Plates," in *37th Annual Symposium on Frequency Control. 1983*, Philadelphia, Pennsylvania, 1983.

[34] P. Lee and Y. Yong, "Frequency-Temperature Behavior of Thickness Vibrations of Doubly-Rotated Quartz Plates Affected by Plate Dimensions and Orientations," in *38th Annual Symposium on Frequency Control*, 1984.

[35] J. Yang, Analysis of Piezoelectric Devices, Hackensack, New Jersey: World Scientific, 2006, pp. 16-21.

[36] B. K. Sinha and H. F. Tiersten, "First temperature derivatives of the fundamental elastic constants of quartz," *Journal of Applied Physics,* vol. 50, pp. 2732-2739, 1979.

[37] M. Patel and B. Sinha, "Stress and temperature compensated orientations for thickness-shear langasite resonators for high temperature and high pressure environment," *Ultrasonics, Ferroelectrics, and Frequency Control, IEEE Transactions on,* vol. 62, no. 6, pp. 1095 - 1103, 2014.

[38] R. Bourquin and B. Dulmet, "New sets of data for the thermal sensitivity of elastic coefficients of langasite and langatate," in *Frequency and Time Forum (EFTF), 2006 20th European*, Braunschweig, 2006.

[39] D. Malocha, M. da Cunha, E. Adler, R. Smythe, S. Frederick, M. Chou, R. Helmbold and Y. Zhou, "Recent measurements of material constants versus temperature for langatate, langanite and langasite," in *Frequency Control Symposium and Exhibition, 2000. Proceedings of the 2000 IEEE/EIA International*, Kansas City, MO, 2000.

[40] D. Malocha, H. Francois-Saint-Cyr, K. Richardson and R. Helmbold, "Measurements of LGS, LGN, and LGT thermal coefficients of expansion and density," *IEEE Transactions on Ultrasonics, Ferroelectrics, and Frequency Control,* vol. 49, no. 3, pp. 350-355, 2002.

[41] R. Bourquin and B. Dulmet, "Thermal sensitivity of elastic coefficients of langasite and langatate," *IEEE Transactions on Ultrasonics, Ferroelectrics, and Frequency Control,* vol. 56, no. 10, pp. 2079 - 2085, 2009.

[42] M.Weihnacht, A..Sotnikov, H.Schmidt, B.Wall and R.Grunwald, "Langasite:High temperature Properties and SAW Simulations," *IEEE International Ultrasonics Symposium,* pp. 1549-1552, 2012.

[43] R. Thuston, H. McSkimin and J. P. Andreatch, "Third-Order Elastic Coefficients of Quartz," *Journal of applied physics,* vol. 37, pp. 267-275, 1966.

[44] R.Bechmann, A.D.Ballato and T. Luzaszek, "Higher order temeprature coefficients of the elastic stiffnesses and comopliances of alpha-quartz," U.S.Army Electronics Research and, Fort Monmouth, NJ, 1963.

[45] J. lamb and J. Richter, "Anisotropic Acoustic Attenuation with New Measurements for Quartz Room Temperature," *Proceedings of the Royal Society of London,*

Mathematical and Physical Sciences, vol. 293A, pp. 479-492, 1633.

[46] F. Sergeev, S. Alekseev, I. Kotelyanskii, G. Mansfeld and N. Polzikova, "Viscosity tensor components of the langatate and langasite," in *Ultrasonics Symposium, 2008. IUS 2008. IEEE*, Beijing, 2008.

[47] B.P.Sorokin, P.P.Turchin, S.I.Burkov and D.A.Glushkov, "Influece of Static Electric Field, Mechanical Pressure and Temperature on the Propgation of Acoustic Waves in La3Ga5SiO14 Piezeoelectric Single Crystals," *IEEE International Frequency Control Symposium,* pp. 161-169, 1996.

[48] H. Zhang, "Optimal cuts to extract the third-order piezoelectric constants and electrostictive constants of langasite single crystals through the electroelastic effect," *IEEE Transactions on Ultrasonics, Ferroelectrics, and Frequency Control,* vol. 60, no. 7, pp. 1453-1466, 2013.

[49] F. A. Radwan, "Some Properties of Copper – Gold and Silver –Gold Alloys at Different % of Gold," in *Proceedings of the International MultiConference of Engineerings and Computer Scientists*, Hong Kong, 2011.

[50] I. t. committees, "IEEE Standard on Piezoelectricity," The Institute of Electrical and Electronics Engineers,Inc, New York, NY, 1987.

Appendix A.

A.1   Matrix Notation

Einstein tensor notation	Voigt notation
ij or *kl*	*p* or *q*
11 (*xx*)	11
22 (*yy*)	2
33 (*zz*)	3
23 or 32 (*yz* or *zy*)	4
31 or 13 (*zy* or *yz*)	5
12 or 21 (*xy* or *yx*)	6

The Voigt notation is an alternative way of representing and simplifying higher-order

tensor. The notation is often used in continuum mechanics.

Appendix B.

B.1   Alternate forms of Constitution equations

The standard constitutive equations can be written in four different forms.

Stress-Charge form

$$T_{ij} = c^E_{ijkl}S_{kl} - e_{kij}E_k$$

$$D_i = e_{ikl}S_{kl} + \varepsilon^S_{ik}E_k$$

Stress-Voltage form

$$T_{ij} = c^D_{ijkl}S_{kl} - h_{kij}D_k$$

$$E_i = -h_{ikl}s_{kl} + \beta^S_{ik}D_k$$

Strain-Charge form

$$S_{ij} = s^E_{ijkl}T_{kl} + d_{kij}E_k$$

$$D_i = d_{ikl}T_{kl} + \varepsilon^T_{ik}E_k$$

Strain –Voltage form

$$S_{ij} = s^D_{ijkl}T_{kl} + g_{kij}D_k$$

$$D_i = -g_{ikl}T_{kl} + \beta^T_{ik}D_k$$

The relations between coefficients appearing in the constitutive equations are

$$c^E_{pr}s^E_{qr} = \delta_{pg} \qquad\qquad c^D_{pr}s^D_{qr} = \delta_{pg}$$

$$\beta^S_{ik}\varepsilon^S_{jk} = \delta_{ij} \qquad\qquad \beta^T_{ik}\varepsilon^T_{jk} = \delta_{ij}$$

$$c^D_{pq} = c^E_{pq} + e_{kp}h_{kq} \qquad\qquad s^D_{pq} = s^E_{pq} - d_{kp}g_{kq}$$

$$\varepsilon^T_{ij} = \varepsilon^S_{ij} + D_{iq}e_{jq} \qquad\qquad \beta^T_{ij} = \beta^S_{ij} - g_{iq}h_{jq}$$

$$e_{ip} = d_{iq}c_{qp}^{E} \qquad\qquad d_{ip} = \varepsilon_{ik}^{T}g_{kp}$$

$$g_{ip} = \beta_{ik}^{T}d_{kp} \qquad\qquad h_{ip} = g_{iq}c_{qp}^{D}$$

where i,j,k = 1,2,3 and p,q,r = 1,2,3,4,5,6

Appendix C. Properties of Materials

C.1 Quartz

The material properties of quartz is determined by Yong [34] [33], Thurston [43], Bechmann [44] and Lamb and Richter [45].

The mass density of quartz is 2649 kg/m^3

Second-order elastic constant: (10^{10} N/m^2)

C_{pq}						
p \ q	1	2	3	4	5	6
1	8.674	0.6980	1.191	-1.791	0.000	0.000
2	6.980	8.674	1.191	1.791	0.000	0.000
3	1.191	1.191	1.072	0.000	0.000	0.000
4	-1.791	1.791	0.000	5.794	0.000	0.000
5	0.000	0.000	0.000	0.000	5.794	-1.791
6	0.000	0.000	0.000	0.000	-1.791	3.998

Viscosity constant: (10^{-3} N-sec/m^2)

n_{pg}						
p \ q	1	2	3	4	5	6
1	1.370	0.730	0.710	0.010	0.000	0.000
2	0.730	1.370	0.710	-0.010	0.000	0.000
3	0.710	0.710	0.960	0.000	0.000	0.000
4	0.010	-0.010	0.000	0.360	0.000	0.000
5	0.000	0.000	0.000	0.000	0.360	0.010
6	0.000	0.000	0.000	0.000	0.010	0.320

First-order temperature derivative of elastic constants: (10^6 N/m^2/°C)

$C^{(1)}_{pq}$						
p \ q	1	2	3	4	5	6
1	1.5976	-8.5518	-2.1983	0.91675	0.0000	0.0000
2	-8.5518	1.5976	-2.1983	-0.91675	0.0000	0.0000
3	-2.1983	-2.1983	-6.5255	0.0000	0.0000	0.0000
4	0.91675	-0.91675	0.0000	-5.3780	0.0000	0.0000
5	0.0000	0.0000	0.0000	0.0000	-5.3780	0.91675
6	0.0000	0.0000	0.0000	0.0000	0.91675	5.0747

Effective second-order temperature derivative of elastic constants: (10^3 N/m^2/ (°C)^2)

$C^{(2)}{}_{pq}$						
p \ q	1	2	3	4	5	6
1	-12.989	-35.121	-18.806	4.2849	0.000	0.000
2	-35.121	-12.989	-18.806	-4.2849	0.000	0.000
3	-18.806	-18.806	-20.835	0.000	0.000	0.000
4	4.2849	-4.2849	0.000	-26.505	0.000	0.000
5	0.000	0.000	0.000	0.000	-26.505	4.2849
6	0.000	0.000	0.000	0.000	4.2849	11.066

Effective third-order temperature derivative of elastic constants: $(N/m^2/(^{\circ}C)^3)$

$C^{(3)}{}_{pq}$						
p \ q	1	2	3	4	5	6
1	-38.1450	73.5030	-8.9302	0.0000	0.0000	0.0000
2	73.5030	-38.1450	-8.9302	-85.7730	0.0000	0.0000
3	-8.9302	-8.9302	46.2550	0.0000	0.0000	0.0000
4	85.7730	-85.7730	0.0000	-20.4680	0.0000	0.0000
5	0.0000	0.0000	0.0000	0.0000	-20.4680	85.7730
6	0.0000	0.0000	0.0000	0.0000	85.7730	-55.8240

Third-order non-linear of elastic constants: $(10^{10}\ N/m^2)$

r =1	C_{pqr}					
p \ q	1	2	3	4	5	6
1	-21.000	-34.500	1.200	-16.300	0.000	0.000
2	-34.500	-22.300	-29.40	-1.500	0.000	0.000
3	1.200	-29.400	-31.20	0.200	0.000	0.000
4	-16.300	-1.500	0.200	-13.400	0.000	0.000
5	0.000	0.000	0.000	0.000	-20.00	-10.40
6	0.000	0.000	0.000	0.000	-10.400	-5.775

r =2	C_{pqr}					
p \ q	1	2	3	4	5	6
1	-34.500	-22.300	-29.400	-1.500	0.000	0.000
2	-22.300	-33.200	1.200	19.300	0.000	0.000
3	-29.400	1.200	-31.200	-0.200	0.000	0.000
4	-1.500	19.300	-0.200	-20.00	0.000	0.000
5	0.000	0.000	0.000	0.000	-13.400	-7.400
6	0.000	0.000	0.000	0.000	-7.400	6.425

$r = 3$	C_{pqr}					
p \ q	1	2	3	4	5	6
1	1.200	-29.400	-31.200	0.200	0.000	0.000
2	-29.400	1.200	-31.200	-0.200	0.000	0.000
3	-31.200	-31.200	-81.500	0.000	0.000	0.000
4	0.200	-0.200	0.000	-11.000	0.000	0.000
5	0.000	0.000	0.000	0.000	-11.000	0.200
6	0.000	0.000	0.000	0.000	0.200	15.300

$r = 4$	C_{pqr}					
p \ q	1	2	3	4	5	6
1	-16.300	-15.000	0.200	-13.400	0.000	0.000
2	-1.500	19.300	-0.200	-20.000	0.000	0.000
3	0.200	-0.200	0.000	-11.00	0.000	0.000
4	-13.400	-20.000	-11.000	-27.600	0.000	0.000
5	0.000	0.000	0.000	0.000	27.600	-3.300
6	0.000	0.000	0.000	0.000	-3.300	-1.500

$r = 5$	C_{pqr}					
p \ q	1	2	3	4	5	6
1	0.000	0.000	0.000	0.000	-20.000	-10.400
2	0.000	0.000	0.000	0.000	-13.400	-7.400
3	0.000	0.000	0.000	0.000	-11.000	0.200
4	0.000	0.000	0.000	0.000	27.600	-3.300
5	-20.000	-13.400	-11.000	27.600	0.000	0.000
6	-10.400	-7.400	0.200	-3.300	0.300	0.300

$r = 6$	C_{pqr}					
p \ q	1	2	3	4	5	6
1	0.000	0.000	0.000	0.000	-10.400	-5.775
2	0.000	0.000	0.000	0.000	-7.400	6.425
3	0.000	0.000	0.000	0.000	0.200	15.300
4	0.000	0.000	0.000	0.000	-3.300	-1.500
5	-10.400	-7.400	0.200	-3.300	0.000	0.000
6	-5.775	6.425	15.300	-1.500	0.300	0.300

First-order thermal expansion coefficients: (10^{-6} 1/C)

$\alpha^{(1)}_{ij}$			
i \ j	1	2	3
1	13.71	0.00	0.00
2	0.00	13.71	0.00
3	0.00	0.00	7.48

Second-order thermal expansion coefficients: (10^{-9} 1/C^2)

$\alpha^{(2)}_{ij}$			
i \ j	1	2	3
1	6.50	0.00	0.00
2	0.00	6.50	0.00
3	0.00	0.00	2.90

Third-order thermal expansion coefficients: (10^{-12} 1/C^3)

$\alpha^{(2)}_{ij}$			
i \ j	1	2	3
1	-1.90	0.00	0.00
2	0.00	-1.90	0.00
3	0.00	0.00	-1.50

Dielectric constant: (10^{-12} Coulombs/(Volts*m))

ε_{ip}			
i \ p	1	2	3
1	39.215	0.000	0.000
2	0.000	39.215	0.000
3	0.000	0.000	41.038

Piezoelectric constants: (10^{-3} Coulombs/m^2)

e_{ij}						
i \ j	1	2	3	4	5	6
1	171.00	-171.00	0.00	-40.67	0.00	0.00
2	0.00	0.00	0.00	0.00	40.67	-171.00
3	0.00	0.00	0.00	0.00	0.00	0.00

C.2 Langasite

The material constants for langasite have been determined by Molocha [39], Sergeev [46]

Bourquin [41] and Sorokin [47].

Mass density of langasite: $\rho = 5743$ kg/m^3

Second-order linear elastic constant: (10^{10} N/m^2) [39]

C_{pq}						
p \ q	1	2	3	4	5	6
1	18.849	10.407	9.688	1.415	0.000	0.000
2	10.407	18.849	9.688	-1.415	0.000	0.000
3	9.688	9.688	26.168	0.000	0.000	0.000
4	1.415	9.688	0.000	5.371	0.000	0.000
5	0.000	0.000	0.000	0.000	5.371	1.415
6	0.000	0.000	0.000	0.000	1.415	4.221

First-order temperature derivative of elastic constants: (10^6 N/m^2/°C)

$C^{(1)}_{pq}$						
p \ q	1	2	3	4	5	6
1	-2.370	-6.4586	-2.4585	-3.9250	0.0000	0.0000
2	-6.4586	-2.3701	-2.4585	3.9250	0.0000	0.0000
3	-2.4585	-2.4585	-8.4501	0.0000	0.0000	0.0000
4	-3.9250	3.9250	0.0000	5.6096	0.0000	0.0000
5	0.0000	0.0000	0.0000	0.0000	5.6096	-3.9250
6	0.0000	0.0000	0.0000	0.0000	-3.9250	2.0443

Effective second-order temperature derivative of elastic constants: $(10^3 \, \text{N/m}^2/ \, (°\text{C})^2)$

$C^{(2)}_{pq}$						
p \ q	1	2	3	4	5	6
1	9.5165	7.6227	-2.7230	8.3625	0.000	0.000
2	7.6227	9.5165	-2.7230	-8.3625	0.000	0.000
3	-2.7230	-2.7230	-2.2310	0.000	0.000	0.000
4	8.3625	-8.3625	0.000	2.0063	0.000	0.000
5	0.000	0.000	0.000	0.000	2.0063	8.3625
6	0.000	0.000	0.000	0.000	8.3625	946.8962

Second-order linear elastic constant: $(10^{10} \, \text{N/m}^2)$ [41]

C_{pq}						
p \ q	1	2	3	4	5	6
1	18.920	10.490	9.782	1.448	0.000	0.000
2	10.490	18.920	9.688	-1.415	0.000	0.000
3	9.782	9.688	26.330	0.000	0.000	0.000
4	1.448	9.688	0.000	5.343	0.000	0.000
5	0.000	0.000	0.000	0.000	5.343	1.448
6	0.000	0.000	0.000	0.000	1.448	4.232

First-order temperature derivative of elastic constants: $(10^6 \, \text{N/m}^2/°\text{C})$

$C^{(1)}_{pq}$						
p \ q	1	2	3	4	5	6
1	-4.4242	-11.0486	-3.6073	-4.6337	0.0000	0.0000
2	-11.0486	-4.4242	-3.6073	4.6337	0.0000	0.0000
3	-3.6073	-3.6073	11.0729	0.0000	0.0000	0.0000
4	-4.6337	4.6337	0.0000	-0.0601	0.0000	0.0000
5	0.0000	0.0000	0.0000	0.0000	-0.0601	-4.6337
6	0.0000	0.0000	0.000	0.0000	-4.6337	3.3089

Effective second-order temperature derivative of elastic constants: $(10^3 \, \text{N/m}^2/ \, (°\text{C})^2)$

$C^{(2)}_{pq}$						
p \ q	1	2	3	4	5	6
1	-14.757	-5.453	-4.817	7.113	0.000	0.000
2	-5.453	-14.757	-4.817	-7.113	0.000	0.000
3	-4.817	-4.817	0.751	0.000	0.000	0.000
4	7.113	-7.113	0.000	-1.522	0.000	0.000
5	0.000	0.000	0.000	0.000	-1.522	7.113
6	0.000	0.000	0.000	0.000	7.1135	-4.704

Third-order non-linear of elastic constants: (10^{10} N/m^2) [47]

$C_{pqr\,(r=1)}$						
p \ q	1	2	3	4	5	6
1	-97.20	0.70	-11.60	-2.20	0.00	0.00
2	0.70	0.00	0.90	-2.80	0.00	0.00
3	-11.60	0.90	-72.10	-4.10	0.00	0.00
4	-2.20	-2.80	-4.10	-4.00	0.00	0.00
5	0.00	0.00	0.00	0.00	-19.80	-5.30
6	0.00	0.00	0.00	0.00	-5.30	48.95

$C_{pqr\,(r=2)}$						
p \ q	1	2	3	4	5	6
1	0.70	0.00	0.90	-2.80	0.00	0.00
2	0.00	-96.50	-11.60	7.80	0.00	0.00
3	0.90	-11.60	-72.10	4.10	0.00	0.00
4	-2.80	7.80	4.10	-19.80	0.00	0.00
5	0.00	0.00	0.00	0.00	-4.00	0.30
6	0.00	0.00	0.00	0.00	0.30	-24.650

$C_{pqr\,(r=3)}$						
p \ q	1	2	3	4	5	6
1	-11.60	0.90	-72.10	-4.10	0.00	0.00
2	0.90	-11.60	-72.10	0.410	0.00	0.00
3	-72.10	-72.10	-183.40	0.00	0.00	0.00
4	-4.10	4.10	0.00	-38.90	0.00	0.00
5	0.00	0.00	0.00	0.00	-38.90	-4.10
6	0.00	0.00	0.00	0.00	-4.10	-6.250

$C_{pqr\,(r=4)}$						
p \ q	1	2	3	4	5	6
1	-2.20	-2.80	-4.10	-4.00	0.00	0.00
2	-2.80	7.80	4.10	-19.80	0.00	0.00
3	-4.10	4.10	0.00	-38.90	0.00	0.00
4	-4.00	-19.80	-38.90	20.20	0.00	0.00
5	0.00	0.00	0.00	0.00	-20.20	-7.90
6	0.00	0.00	0.00	0.00	-7.90	-2.80

$C_{pqr\ (r=5)}$						
p \ q	1	2	3	4	5	6
1	0.00	0.00	0.00	0.00	-19.80	-5.30
2	0.00	0.00	0.00	0.00	-4.00	0.30
3	0.00	0.00	0.00	0.00	-38.90	-4.10
4	0.00	0.00	0.00	0.00	-20.20	-7.90
5	-19.80	-4.00	-38.90	-20.20	0.00	0.00
6	-5.30	0.30	-4.10	-7.90	0.00	0.00

$C_{pqr\ (r=6)}$						
p \ q	1	2	3	4	5	6
1	0.00	0.00	0.00	0.00	-5.30	-23.95
2	0.00	0.00	0.00	0.00	0.30	-24.65
3	0.00	0.00	0.00	0.00	-4.10	-6.25
4	0.00	0.00	0.00	0.00	-7.90	-2.80
5	-5.30	-0.30	-4.10	-7.90	0.00	0.00
6	-23.95	-24.65	-6.25	-2.80	0.00	0.00

Viscosity constant: (10^{-3} N-sec/m^2)

n_{pg}						
p \ q	1	2	3	4	5	6
1	0.443	0.139	0.041	-0.082	0.000	0.000
2	0.139	0.443	0.041	0.082	0.000	0.000
3	0.041	0.041	0.462	0.000	0.000	0.000
4	-0.082	0.082	0.000	0.196	0.000	0.000
5	0.000	0.000	0.000	0.000	0.196	-0.082
6	0.000	0.000	0.000	0.000	-0.082	0.152

First-order thermal expansion coefficients: (10^{-6} 1/C)

$\alpha^{(1)}_{ij}$			
i \ j	1	2	3
1	5.630	0.000	0.000
2	0.000	5.630	0.000
3	0.000	0.000	4.577

Second-order thermal expansion coefficients: $(10^{-9} \, 1/C^2)$

		$\alpha^{(2)}_{ij}$	
i \ j	1	2	3
1	5.979	0.000	0.000
2	0.000	5.979	0.000
3	0.000	0.000	4.577

Dielectric constant: $(10^{-12} \, \text{Coulombs/(Volts*m)})$

		ε_{ip}	
p \ i	1	2	3
1	167.52	0.00	0.00
2	0.00	167.52	0.00
3	0.00	0.00	448.92

Piezoelectric constants: $(10^{-3} \, \text{Coulombs/m}^2)$

			e_{ij}			
i \ j	1	2	3	4	5	6
1	-402	402	0	130	0	0
2	0	0	0	0	-130	402
3	0	0	0	0	0	0

C.3   Langatate

The material constants for langatate have been determined by Molocha [39], Sergeev [46] Bourquin [41] and Zhang [48].

Mass density of langatate: $\rho = 6150 \, \text{kg/m}^3$

Second-order elastic constant: $(10^{10} \, \text{N/m}^2)$

			C_{pq}			
p \ q	1	2	3	4	5	6
1	18.852	10.788	10.336	1.351	0.000	0.000
2	10.788	18.852	10.336	-1.351	0.000	0.000
3	10.336	10.336	26.180	0.000	0.000	0.000
4	1.351	-1.351	0.000	5.110	0.000	0.000
5	0.000	0.000	0.000	0.000	5.110	1.351
6	0.000	0.000	0.000	0.000	1.351	4.032

Viscosity constant: $(10^{-3}$ N-sec/m$^2)$

n_{pg}						
p \ q	1	2	3	4	5	6
1	0.490	0.290	0.093	0.093	0.000	0.000
2	0.290	0.490	0.093	-0.093	0.000	0.000
3	0.093	0.093	0.320	0.000	0.000	0.000
4	0.093	-0.093	0.000	0.185	0.000	0.000
5	0.000	0.000	0.000	0.000	0.185	0.093
6	0.000	0.000	0.000	0.000	0.093	0.100

First-order thermal expansion coefficients: $(10^{-6}$ 1/C)

$\alpha^{(1)}_{ij}$		
i \ j	1	2	3
1	6.087	0.000	0.000
2	0.000	6.087	0.000
3	0.000	0.000	3.827

Second-order thermal expansion coefficients: $(10^{-9}$ 1/C$^2)$

$\alpha^{(2)}_{ij}$		
i \ j	1	2	3
1	4.736	0.000	0.000
2	0.000	4.736	0.000
3	0.000	0.000	5.030

Dielectric constant: $(10^{-12}$ Coulombs/(Volts*m))

ε_{ip}		
i \ p	1	2	3
1	161.77	0.00	0.00
2	0.00	161.77	0.00
3	0.00	0.00	699.02

Piezoelectric constants: $(10^{-3}$ Coulombs/m$^2)$

e_{ij}						
i \ j	1	2	3	4	5	6
1	-456	456	0	94	0	0
2	0	0	0	0	-94	456
3	0	0	0	0	0	0

C.4 Gold

The material constants for langatate have been determined by Radwan [49].

Mass density of gold : $\rho = 19{,}300 \text{ kg/m}^3$

Elastic constants (Gpa)

	C_{ij}					
i \ j	1	2	3	4	5	6
1	190.0	161.0	161.0	0.0	0.0	0.0
2	161.0	190.0	161.0	0.0	0.0	0.0
3	161.0	161.0	190.0	0.0	0.0	0.0
4	0.0	0.0	0.0	42.3	0.0	0.0
5	0.0	0.0	0.0	0.0	42.3	0.0
6	0.0	0.0	0.0	0.0	0.0	42.3

Appendix D.   Comsol Parameters and Variable

D.1   Variable

Theta= T-Tref Temperature in Celcius

theta2= theta^2

theta3= theta^3

alf11= alfa11+alfb11*theta+alfc11*theta2 1/K Thermal expansion coefficient

alf12= alfa12+alfb12*theta+alfc12*theta2 1/K Thermal expansion coefficient

alf13= alfa13+alfb13*theta+alfc13*theta2 1/K Thermal expansion coefficient

alf22= alfa22+alfb22*theta+alfc22*theta2 1/K Thermal expansion coefficient

alf23= alfa23+alfb23*theta+alfc23*theta2 1/K Thermal expansion coefficient

alf33= alfa33+alfb33*theta+alfc33*theta2 1/K Thermal expansion coefficient

CT11

=N111*solid.eX+N112*solid.eY+N113*solid.eZ+2*(N114*solid.eYZ+N115*solid.eXZ+N116*solid.eXY)

CT12

=N121*solid.eX+N122*solid.eY+N123*solid.eZ+2*(N124*solid.eYZ+N125*solid.eXZ+N126*solid.eXY)

CT13

=N131*solid.eX+N132*solid.eY+N133*solid.eZ+2*(N134*solid.eYZ+N135*solid.eXZ+N136*solid.eXY)

CT14

=N141*solid.eX+N142*solid.eY+N143*solid.eZ+2*(N144*solid.eYZ+N145*solid.eXZ+N146*solid.eXY)

CT15

=N151*solid.eX+N152*solid.eY+N153*solid.eZ+2*(N154*solid.eYZ+N155*solid.eXZ+N156*solid.eXY)

CT16

=N161*solid.eX+N162*solid.eY+N163*solid.eZ+2*(N164*solid.eYZ+N165*solid.eXZ+N166*solid.eXY)

CT22

=N221*solid.eX+N222*solid.eY+N223*solid.eZ+2*(N224*solid.eYZ+N225*solid.eXZ+N226*solid.eXY)

CT23

=N231*solid.eX+N232*solid.eY+N233*solid.eZ+2*(N234*solid.eYZ+N235*solid.eXZ+N236*solid.eXY)

CT24

=N241*solid.eX+N242*solid.eY+N243*solid.eZ+2*(N244*solid.eYZ+N245*solid.eXZ+N246*solid.eXY)

CT25

=N251*solid.eX+N252*solid.eY+N253*solid.eZ+2*(N254*solid.eYZ+N255*solid.eXZ+N256*solid.eXY)

CT26

=N261*solid.eX+N262*solid.eY+N263*solid.eZ+2*(N264*solid.eYZ+N265*solid.eXZ+N266*solid.eXY)

CT33

=N331*solid.eX+N332*solid.eY+N333*solid.eZ+2*(N334*solid.eYZ+N335*solid.eXZ+N336*solid.eXY)

CT34

=N341*solid.eX+N342*solid.eY+N343*solid.eZ+2*(N344*solid.eYZ+N345*solid.eXZ+N346*solid.eXY)

CT35

=N351*solid.eX+N352*solid.eY+N353*solid.eZ+2*(N354*solid.eYZ+N355*solid.eXZ+N356*solid.eXY)

CT36

=N361*solid.eX+N362*solid.eY+N363*solid.eZ+2*(N364*solid.eYZ+N365*solid.eXZ+N366*solid.eXY)

CT44

=N441*solid.eX+N442*solid.eY+N443*solid.eZ+2*(N444*solid.eYZ+N445*solid.eXZ+N446*solid.eXY)

CT45

=N451*solid.eX+N452*solid.eY+N453*solid.eZ+2*(N454*solid.eYZ+N455*solid.eXZ+N456*solid.eXY)

CT46

=N461*solid.eX+N462*solid.eY+N463*solid.eZ+2*(N464*solid.eYZ+N465*solid.eXZ+N466*solid.eXY)

CT55

=N551*solid.eX+N552*solid.eY+N553*solid.eZ+2*(N554*solid.eYZ+N555*solid.eXZ+N556*solid.eXY)

CT56

=N561*solid.eX+N562*solid.eY+N563*solid.eZ+2*(N564*solid.eYZ+N565*solid.eXZ+N566*solid.eXY)

CT66

=N661*solid.eX+N662*solid.eY+N663*solid.eZ+2*(N664*solid.eYZ+N665*solid.eXZ+N666*solid.eXY)

C11=   C011+Ca11*theta+0.5*Cb11*theta2+0.1666666666*Cc11*theta3+CT11   Pa   Nonlinear   elastic

constants with damping

C12= C012+Ca12*theta+0.5*Cb12*theta2+0.1666666666*Cc12*theta3+CT12 Pa Nonlinear elastic
constants with damping

C13= C013+Ca13*theta+0.5*Cb13*theta2+0.1666666666*Cc13*theta3+CT13 Pa Nonlinear elastic
constants with damping

C14= C014+Ca14*theta+0.5*Cb14*theta2+0.1666666666*Cc14*theta3+CT14 Pa Nonlinear elastic
constants with damping

C15= C015+Ca15*theta+0.5*Cb15*theta2+0.1666666666*Cc15*theta3+CT15 Pa Nonlinear elastic
constants with damping

C16= C016+Ca16*theta+0.5*Cb16*theta2+0.1666666666*Cc16*theta3+CT16 Pa Nonlinear elastic
constants with damping

C22= C022+Ca22*theta+0.5*Cb22*theta2+0.1666666666*Cc22*theta3+CT22 Pa Nonlinear elastic
constants with damping

C23= C023+Ca23*theta+0.5*Cb23*theta2+0.1666666666*Cc23*theta3+CT23 Pa Nonlinear elastic
constants with damping

C24= C024+Ca24*theta+0.5*Cb24*theta2+0.1666666666*Cc24*theta3+CT24 Pa Nonlinear elastic
constants with damping

C25= C025+Ca25*theta+0.5*Cb25*theta2+0.1666666666*Cc25*theta3+CT25 Pa Nonlinear elastic
constants with damping

C26= C026+Ca26*theta+0.5*Cb26*theta2+0.1666666666*Cc26*theta3+CT26 Pa Nonlinear elastic
constants with damping

C33= C033+Ca33*theta+0.5*Cb33*theta2+0.1666666666*Cc33*theta3+CT33 Pa Nonlinear elastic
constants with damping

C34= C034+Ca34*theta+0.5*Cb34*theta2+0.1666666666*Cc34*theta3+CT34 Pa Nonlinear elastic
constants with damping

C35= C035+Ca35*theta+0.5*Cb35*theta2+0.1666666666*Cc35*theta3+CT35 Pa Nonlinear elastic
constants with damping

C36= C036+Ca36*theta+0.5*Cb36*theta2+0.1666666666*Cc36*theta3+CT36 Pa Nonlinear elastic
constants with damping

C44= C044+Ca44*theta+0.5*Cb44*theta2+0.1666666666*Cc44*theta3+CT44 Pa Nonlinear elastic constants with damping

C45= C045+Ca45*theta+0.5*Cb45*theta2+0.1666666666*Cc45*theta3+CT45 Pa Nonlinear elastic constants with damping

C46= C046+Ca46*theta+0.5*Cb46*theta2+0.1666666666*Cc46*theta3+CT46 Pa Nonlinear elastic constants with damping

C55= C055+Ca55*theta+0.5*Cb55*theta2+0.1666666666*Cc55*theta3+CT55 Pa Nonlinear elastic constants with damping

C56= C056+Ca56*theta+0.5*Cb56*theta2+0.1666666666*Cc56*theta3+CT56 Pa Nonlinear elastic constants with damping

C66= C066+Ca66*theta+0.5*Cb66*theta2+0.1666666666*Cc66*theta3+CT66 Pa Nonlinear elastic constants with damping

e11= e011+ea11*theta+eb11*theta2+ec11*theta3 C/m^2 Piezoelectric stress constant

e12= e012+ea12*theta+eb12*theta2+ec12*theta3 C/m^2 Piezoelectric stress constant

e13= e013+ea13*theta+eb13*theta2+ec13*theta3 C/m^2 Piezoelectric stress constant

e14= e014+ea14*theta+eb14*theta2+ec14*theta3 C/m^2 Piezoelectric stress constant

e15= e015+ea15*theta+eb15*theta2+ec15*theta3 C/m^2 Piezoelectric stress constant

e16= e016+ea16*theta+eb16*theta2+ec16*theta3 C/m^2 Piezoelectric stress constant

e21= e021+ea21*theta+eb21*theta2+ec21*theta3 C/m^2 Piezoelectric stress constant

e22= e022+ea22*theta+eb22*theta2+ec22*theta3 C/m^2 Piezoelectric stress constant

e23= e023+ea23*theta+eb23*theta2+ec23*theta3 C/m^2 Piezoelectric stress constant

e24= e024+ea24*theta+eb24*theta2+ec24*theta3 C/m^2 Piezoelectric stress constant

e25= e025+ea25*theta+eb25*theta2+ec25*theta3 C/m^2 Piezoelectric stress constant

e26= e026+ea26*theta+eb26*theta2+ec26*theta3 C/m^2 Piezoelectric stress constant

e31= e031+ea31*theta+eb31*theta2+ec31*theta3 C/m^2 Piezoelectric stress constant

e32= e032+ea32*theta+eb32*theta2+ec32*theta3 C/m^2 Piezoelectric stress constant

e33= e033+ea33*theta+eb33*theta2+ec33*theta3 C/m^2 Piezoelectric stress constant

e34= e034+ea34*theta+eb34*theta2+ec34*theta3 C/m^2 Piezoelectric stress constant

e35= e035+ea35*theta+eb35*theta2+ec35*theta3 C/m^2 Piezoelectric stress constant

e36= e036+ea36*theta+eb36*theta2+ec36*theta3 C/m^2 Piezoelectric stress constant

eps11= eps011+epsa11*theta+epsb11*theta2+epsc11*theta3 F/m Dielectric permittivity

eps12= eps012+epsa12*theta+epsb12*theta2+epsc12*theta3 F/m Dielectric permittivity

eps13= eps013+epsa13*theta+epsb13*theta2+epsc13*theta3 F/m Dielectric permittivity

eps22= eps022+epsa22*theta+epsb22*theta2+epsc22*theta3 F/m Dielectric permittivity

eps23= eps023+epsa23*theta+epsb23*theta2+epsc23*theta3 F/m Dielectric permittivity

eps33= eps033+epsa33*theta+epsb33*theta2+epsc33*theta3 F/m Dielectric permittivity

D.2   Parameters

C_freq 1e6 Center frequency of device, Hz

C_omega C_freq*2*pi C_freq in rad/s

T 25 Temperature in Celcius

Tref 25 Reference temperature in Celcius

gold_rho 19300

gold_thickness 0.2e-6

C011 1.884900e+11+i*C_omega*4.430000e-04 Pa Elastic constants with damping

C012 1.133960e+11+i*C_omega*6.184952e-05 Pa Elastic constants with damping

C013 8.755398e+10+i*C_omega*1.181505e-04 Pa Elastic constants with damping

C014 6.796592e+09+i*C_omega*-9.128281e-05 Pa Elastic constants with damping

C015 0.000000e+00+i*C_omega*0.000000e+00 Pa Elastic constants with damping

C016 0.000000e+00+i*C_omega*0.000000e+00 Pa Elastic constants with damping

C022 1.773070e+11+i*C_omega*4.859546e-04 Pa Elastic constants with damping

C023 1.096556e+11+i*C_omega*-5.594175e-06 Pa Elastic constants with damping

C024 4.435348e+09+i*C_omega*4.699347e-05 Pa Elastic constants with damping

C025 0.000000e+00+i*C_omega*0.000000e+00 Pa Elastic constants with damping

C026 0.000000e+00+i*C_omega*0.000000e+00 Pa Elastic constants with damping

C033 2.473117e+11+i*C_omega*4.377302e-04 Pa Elastic constants with damping

C034 1.329184e+10+i*C_omega*3.016958e-05 Pa Elastic constants with damping

C035 0.000000e+00+i*C_omega*0.000000e+00 Pa Elastic constants with damping

C036 0.000000e+00+i*C_omega*0.000000e+00 Pa Elastic constants with damping

C044 6.648565e+10+i*C_omega*1.866576e-04 Pa Elastic constants with damping

C045 0.000000e+00+i*C_omega*0.000000e+00 Pa Elastic constants with damping

C046 0.000000e+00+i*C_omega*0.000000e+00 Pa Elastic constants with damping

C055 4.129200e+10+i*C_omega*2.191898e-04 Pa Elastic constants with damping

C056 1.374128e+10+i*C_omega*-5.208517e-05 Pa Elastic constants with damping

C066 5.462800e+10+i*C_omega*1.288102e-04 Pa Elastic constants with damping

Ca11 -4.424200e+06 Pa/K 1st temperature derivative of C0

Ca12 -1.325355e+07 Pa/K 1st temperature derivative of C0

Ca13 -1.393350e+06 Pa/K 1st temperature derivative of C0

Ca14 -3.389128e+05 Pa/K 1st temperature derivative of C0

Ca15 0.000000e+00 Pa/K 1st temperature derivative of C0

Ca16 0.000000e+00 Pa/K 1st temperature derivative of C0

Ca22 1.939984e+06 Pa/K 1st temperature derivative of C0

Ca23 -3.964216e+06 Pa/K 1st temperature derivative of C0

Ca24 2.433941e+06 Pa/K 1st temperature derivative of C0

Ca25 0.000000e+00 Pa/K 1st temperature derivative of C0

Ca26 0.000000e+00 Pa/K 1st temperature derivative of C0

Ca33 5.422548e+06 Pa/K 1st temperature derivative of C0

Ca34 6.424904e+06 Pa/K 1st temperature derivative of C0

Ca35 0.000000e+00 Pa/K 1st temperature derivative of C0

Ca36 0.000000e+00 Pa/K 1st temperature derivative of C0

Ca44 -4.170158e+05 Pa/K 1st temperature derivative of C0

Ca45 0.000000e+00 Pa/K 1st temperature derivative of C0

Ca46 0.000000e+00 Pa/K 1st temperature derivative of C0

Ca55 3.940561e+06 Pa/K 1st temperature derivative of C0

Ca56 -4.351932e+06 Pa/K 1st temperature derivative of C0

Ca66 -6.929611e+05 Pa/K 1st temperature derivative of C0

Cb11 -1.475700e+04 Pa/K^2 2nd temperature derivative of C0

Cb12 -3.691453e+04 Pa/K^2 2nd temperature derivative of C0

Cb13 -1.751347e+04 Pa/K^2 2nd temperature derivative of C0

Cb14 2.140374e+04 Pa/K^2 2nd temperature derivative of C0

Cb15 0.000000e+00 Pa/K^2 2nd temperature derivative of C0

Cb16 0.000000e+00 Pa/K^2 2nd temperature derivative of C0

Cb22 -2.125137e+04 Pa/K^2 2nd temperature derivative of C0

Cb23 -1.043062e+03 Pa/K^2 2nd temperature derivative of C0

Cb24 6.598400e+02 Pa/K^2 2nd temperature derivative of C0

Cb25 0.000000e+00 Pa/K^2 2nd temperature derivative of C0

Cb26 0.000000e+00 Pa/K^2 2nd temperature derivative of C0

Cb33 -3.025106e+02 Pa/K^2 2nd temperature derivative of C0

Cb34 3.429790e+02 Pa/K^2 2nd temperature derivative of C0

Cb35 0.000000e+00 Pa/K^2 2nd temperature derivative of C0

Cb36 0.000000e+00 Pa/K^2 2nd temperature derivative of C0

Cb44 2.251938e+03 Pa/K^2 2nd temperature derivative of C0

Cb45 0.000000e+00 Pa/K^2 2nd temperature derivative of C0

Cb46 0.000000e+00 Pa/K^2 2nd temperature derivative of C0

Cb55 -3.673167e+03 Pa/K^2 2nd temperature derivative of C0

Cb56 -2.281400e+03 Pa/K^2 2nd temperature derivative of C0

Cb66 1.957817e+04 Pa/K^2 2nd temperature derivative of C0

Cc11 0.000000e+00 Pa/K^3 3rd temperature derivative of C0

Cc12 0.000000e+00 Pa/K^3 3rd temperature derivative of C0

Cc13 0.000000e+00 Pa/K^3 3rd temperature derivative of C0

Cc14 0.000000e+00 Pa/K^3 3rd temperature derivative of C0

Cc15 0.000000e+00 Pa/K^3 3rd temperature derivative of C0

Cc16 0.000000e+00 Pa/K^3 3rd temperature derivative of C0

Cc22 0.000000e+00 Pa/K^3 3rd temperature derivative of C0

Cc23 0.000000e+00 Pa/K^3 3rd temperature derivative of C0

Cc24 0.000000e+00 Pa/K^3 3rd temperature derivative of C0

Cc25 0.000000e+00 Pa/K^3 3rd temperature derivative of C0

Cc26 0.000000e+00 Pa/K^3 3rd temperature derivative of C0

Cc33 0.000000e+00 Pa/K^3 3rd temperature derivative of C0

Cc34 0.000000e+00 Pa/K^3 3rd temperature derivative of C0

Cc35 0.000000e+00 Pa/K^3 3rd temperature derivative of C0

Cc36 0.000000e+00 Pa/K^3 3rd temperature derivative of C0

Cc44 0.000000e+00 Pa/K^3 3rd temperature derivative of C0

Cc45 0.000000e+00 Pa/K^3 3rd temperature derivative of C0

Cc46 0.000000e+00 Pa/K^3 3rd temperature derivative of C0

Cc55 0.000000e+00 Pa/K^3 3rd temperature derivative of C0

Cc56 0.000000e+00 Pa/K^3 3rd temperature derivative of C0

Cc66 0.000000e+00 Pa/K^3 3rd temperature derivative of C0

N111 -9.720000e+11 Pa Nonlinear elastic constant

N112 -2.969765e+10 Pa Nonlinear elastic constant

N113 -7.930235e+10 Pa Nonlinear elastic constant

N114 -6.042428e+10 Pa Nonlinear elastic constant

N115 0.000000e+00 Pa Nonlinear elastic constant

N116 0.000000e+00 Pa Nonlinear elastic constant

N121 -2.969765e+10 Pa Nonlinear elastic constant

N122 -8.415077e+10 Pa Nonlinear elastic constant

N123 -7.740464e+10 Pa Nonlinear elastic constant

N124 -8.573777e+10 Pa Nonlinear elastic constant

N125 0.000000e+00 Pa Nonlinear elastic constant

N126 0.000000e+00 Pa Nonlinear elastic constant

N131 -7.930235e+10 Pa Nonlinear elastic constant

N132 -7.740464e+10 Pa Nonlinear elastic constant

N133 -4.640400e+11 Pa Nonlinear elastic constant

N134 -2.283359e+11 Pa Nonlinear elastic constant

N135 0.000000e+00 Pa Nonlinear elastic constant

N136 0.000000e+00 Pa Nonlinear elastic constant

N141 -6.042428e+10 Pa Nonlinear elastic constant

N142 -8.573777e+10 Pa Nonlinear elastic constant

N143 -2.283359e+11 Pa Nonlinear elastic constant

N144 -1.264046e+11 Pa Nonlinear elastic constant

N145 0.000000e+00 Pa Nonlinear elastic constant

N146 0.000000e+00 Pa Nonlinear elastic constant

N151 0.000000e+00 Pa Nonlinear elastic constant

N152 0.000000e+00 Pa Nonlinear elastic constant

N153 0.000000e+00 Pa Nonlinear elastic constant

N154 0.000000e+00 Pa Nonlinear elastic constant

N155 -1.654789e+11 Pa Nonlinear elastic constant

N156 -2.004367e+10 Pa Nonlinear elastic constant

N161 0.000000e+00 Pa Nonlinear elastic constant

N162 0.000000e+00 Pa Nonlinear elastic constant

N163 0.000000e+00 Pa Nonlinear elastic constant

N164 0.000000e+00 Pa Nonlinear elastic constant

N165 -2.004367e+10 Pa Nonlinear elastic constant

N166 -2.720211e+11 Pa Nonlinear elastic constant

N211 -2.969765e+10 Pa Nonlinear elastic constant

N212 -8.415077e+10 Pa Nonlinear elastic constant

N213 -7.740464e+10 Pa Nonlinear elastic constant

N214 -8.573777e+10 Pa Nonlinear elastic constant

N215 0.000000e+00 Pa Nonlinear elastic constant

N216 0.000000e+00 Pa Nonlinear elastic constant

N221 -8.415077e+10 Pa Nonlinear elastic constant

N222 -9.756775e+11 Pa Nonlinear elastic constant

N223 -2.447772e+11 Pa Nonlinear elastic constant

N224 -1.727253e+11 Pa Nonlinear elastic constant

N225 0.000000e+00 Pa Nonlinear elastic constant

N226 0.000000e+00 Pa Nonlinear elastic constant

N231 -7.740464e+10 Pa Nonlinear elastic constant

N232 -2.447772e+11 Pa Nonlinear elastic constant

N233 -5.777157e+11 Pa Nonlinear elastic constant

N234 -9.965539e+10 Pa Nonlinear elastic constant

N235 0.000000e+00 Pa Nonlinear elastic constant

N236 0.000000e+00 Pa Nonlinear elastic constant

N241 -8.573777e+10 Pa Nonlinear elastic constant

N242 -1.727253e+11 Pa Nonlinear elastic constant

N243 -9.965539e+10 Pa Nonlinear elastic constant

N244 -4.388714e+11 Pa Nonlinear elastic constant

N245 0.000000e+00 Pa Nonlinear elastic constant

N246 0.000000e+00 Pa Nonlinear elastic constant

N251 0.000000e+00 Pa Nonlinear elastic constant

N252 0.000000e+00 Pa Nonlinear elastic constant

N253 0.000000e+00 Pa Nonlinear elastic constant

N254 0.000000e+00 Pa Nonlinear elastic constant

N255 5.133600e+10 Pa Nonlinear elastic constant

N256 6.532915e+10 Pa Nonlinear elastic constant

N261 0.000000e+00 Pa Nonlinear elastic constant

N262 0.000000e+00 Pa Nonlinear elastic constant

N263 0.000000e+00 Pa Nonlinear elastic constant

N264 0.000000e+00 Pa Nonlinear elastic constant

N265 6.532915e+10 Pa Nonlinear elastic constant

N266 -2.358255e+11 Pa Nonlinear elastic constant

N311 -7.930235e+10 Pa Nonlinear elastic constant

N312 -7.740464e+10 Pa Nonlinear elastic constant

N313 -4.640400e+11 Pa Nonlinear elastic constant

N314 -2.283359e+11 Pa Nonlinear elastic constant

N315 0.000000e+00 Pa Nonlinear elastic constant

N316 0.000000e+00 Pa Nonlinear elastic constant

N321 -7.740464e+10 Pa Nonlinear elastic constant

N322 -2.447772e+11 Pa Nonlinear elastic constant

N323 -5.777157e+11 Pa Nonlinear elastic constant

N324 -9.965539e+10 Pa Nonlinear elastic constant

N325 0.000000e+00 Pa Nonlinear elastic constant

N326 0.000000e+00 Pa Nonlinear elastic constant

N331 -4.640400e+11 Pa Nonlinear elastic constant

N332 -5.777157e+11 Pa Nonlinear elastic constant

N333 -1.866844e+12 Pa Nonlinear elastic constant

N334 -6.860074e+10 Pa Nonlinear elastic constant

N335 0.000000e+00 Pa Nonlinear elastic constant

N336 0.000000e+00 Pa Nonlinear elastic constant

N341 -2.283359e+11 Pa Nonlinear elastic constant

N342 -9.965539e+10 Pa Nonlinear elastic constant

N343 -6.860074e+10 Pa Nonlinear elastic constant

N344 -1.336214e+11 Pa Nonlinear elastic constant

N345 0.000000e+00 Pa Nonlinear elastic constant

N346 0.000000e+00 Pa Nonlinear elastic constant

N351 0.000000e+00 Pa Nonlinear elastic constant

N352 0.000000e+00 Pa Nonlinear elastic constant

N353 0.000000e+00 Pa Nonlinear elastic constant

N354 0.000000e+00 Pa Nonlinear elastic constant

N355 -4.322443e+11 Pa Nonlinear elastic constant

N356 -1.353448e+11 Pa Nonlinear elastic constant

N361 0.000000e+00 Pa Nonlinear elastic constant

N362 0.000000e+00 Pa Nonlinear elastic constant

N363 0.000000e+00 Pa Nonlinear elastic constant

N364 0.000000e+00 Pa Nonlinear elastic constant

N365 -1.353448e+11 Pa Nonlinear elastic constant

N366 -1.212661e+11 Pa Nonlinear elastic constant

N411 -6.042428e+10 Pa Nonlinear elastic constant

N412 -8.573777e+10 Pa Nonlinear elastic constant

N413 -2.283359e+11 Pa Nonlinear elastic constant

N414 -1.264046e+11 Pa Nonlinear elastic constant

N415 0.000000e+00 Pa Nonlinear elastic constant

N416 0.000000e+00 Pa Nonlinear elastic constant

N421 -8.573777e+10 Pa Nonlinear elastic constant

N422 -1.727253e+11 Pa Nonlinear elastic constant

N423 -9.965539e+10 Pa Nonlinear elastic constant

N424 -4.388714e+11 Pa Nonlinear elastic constant

N425 0.000000e+00 Pa Nonlinear elastic constant

N426 0.000000e+00 Pa Nonlinear elastic constant

N431 -2.283359e+11 Pa Nonlinear elastic constant

N432 -9.965539e+10 Pa Nonlinear elastic constant

N433 -6.860074e+10 Pa Nonlinear elastic constant

N434 -1.336214e+11 Pa Nonlinear elastic constant

N435 0.000000e+00 Pa Nonlinear elastic constant

N436 0.000000e+00 Pa Nonlinear elastic constant

N441 -1.264046e+11 Pa Nonlinear elastic constant

N442 -4.388714e+11 Pa Nonlinear elastic constant

N443 -1.336214e+11 Pa Nonlinear elastic constant

N444 -1.084232e+11 Pa Nonlinear elastic constant

N445 0.000000e+00 Pa Nonlinear elastic constant

N446 0.000000e+00 Pa Nonlinear elastic constant

N451 0.000000e+00 Pa Nonlinear elastic constant

N452 0.000000e+00 Pa Nonlinear elastic constant

N453 0.000000e+00 Pa Nonlinear elastic constant

N454 0.000000e+00 Pa Nonlinear elastic constant

N455 6.422266e+10 Pa Nonlinear elastic constant

N456 -6.271507e+10 Pa Nonlinear elastic constant

N461 0.000000e+00 Pa Nonlinear elastic constant

N462 0.000000e+00 Pa Nonlinear elastic constant

N463 0.000000e+00 Pa Nonlinear elastic constant

N464 0.000000e+00 Pa Nonlinear elastic constant

N465 -6.271507e+10 Pa Nonlinear elastic constant

N466 -9.103381e+09 Pa Nonlinear elastic constant

N511 0.000000e+00 Pa Nonlinear elastic constant

N512 0.000000e+00 Pa Nonlinear elastic constant

N513 0.000000e+00 Pa Nonlinear elastic constant

N514 0.000000e+00 Pa Nonlinear elastic constant

N515 -1.654789e+11 Pa Nonlinear elastic constant

N516 -2.004367e+10 Pa Nonlinear elastic constant

N521 0.000000e+00 Pa Nonlinear elastic constant

N522 0.000000e+00 Pa Nonlinear elastic constant

N523 0.000000e+00 Pa Nonlinear elastic constant

N524 0.000000e+00 Pa Nonlinear elastic constant

N525 5.133600e+10 Pa Nonlinear elastic constant

N526 6.532915e+10 Pa Nonlinear elastic constant

N531 0.000000e+00 Pa Nonlinear elastic constant

N532 0.000000e+00 Pa Nonlinear elastic constant

N533 0.000000e+00 Pa Nonlinear elastic constant

N534 0.000000e+00 Pa Nonlinear elastic constant

N535 -4.322443e+11 Pa Nonlinear elastic constant

N536 -1.353448e+11 Pa Nonlinear elastic constant

N541 0.000000e+00 Pa Nonlinear elastic constant

N542 0.000000e+00 Pa Nonlinear elastic constant

N543 0.000000e+00 Pa Nonlinear elastic constant

N544 0.000000e+00 Pa Nonlinear elastic constant

N545 6.422266e+10 Pa Nonlinear elastic constant

N546 -6.271507e+10 Pa Nonlinear elastic constant

N551 -1.654789e+11 Pa Nonlinear elastic constant

N552 5.133600e+10 Pa Nonlinear elastic constant

N553 -4.322443e+11 Pa Nonlinear elastic constant

N554 6.422266e+10 Pa Nonlinear elastic constant

N555 0.000000e+00 Pa Nonlinear elastic constant

N556 0.000000e+00 Pa Nonlinear elastic constant

N561 -2.004367e+10 Pa Nonlinear elastic constant

N562 6.532915e+10 Pa Nonlinear elastic constant

N563 -1.353448e+11 Pa Nonlinear elastic constant

N564 -6.271507e+10 Pa Nonlinear elastic constant

N565 0.000000e+00 Pa Nonlinear elastic constant

N566 0.000000e+00 Pa Nonlinear elastic constant

N611 0.000000e+00 Pa Nonlinear elastic constant

N612 0.000000e+00 Pa Nonlinear elastic constant

N613 0.000000e+00 Pa Nonlinear elastic constant

N614 0.000000e+00 Pa Nonlinear elastic constant

N615 -2.004367e+10 Pa Nonlinear elastic constant

N616 -2.720211e+11 Pa Nonlinear elastic constant

N621 0.000000e+00 Pa Nonlinear elastic constant

N622 0.000000e+00 Pa Nonlinear elastic constant

N623 0.000000e+00 Pa Nonlinear elastic constant

N624 0.000000e+00 Pa Nonlinear elastic constant

N625 6.532915e+10 Pa Nonlinear elastic constant

N626 -2.358255e+11 Pa Nonlinear elastic constant

N631 0.000000e+00 Pa Nonlinear elastic constant

N632 0.000000e+00 Pa Nonlinear elastic constant

N633 0.000000e+00 Pa Nonlinear elastic constant

N634 0.000000e+00 Pa Nonlinear elastic constant

N635 -1.353448e+11 Pa Nonlinear elastic constant

N636 -1.212661e+11 Pa Nonlinear elastic constant

N641 0.000000e+00 Pa Nonlinear elastic constant

N642 0.000000e+00 Pa Nonlinear elastic constant

N643 0.000000e+00 Pa Nonlinear elastic constant

N644 0.000000e+00 Pa Nonlinear elastic constant

N645 -6.271507e+10 Pa Nonlinear elastic constant

N646 -9.103381e+09 Pa Nonlinear elastic constant

N651 -2.004367e+10 Pa Nonlinear elastic constant

N652 6.532915e+10 Pa Nonlinear elastic constant

N653 -1.353448e+11 Pa Nonlinear elastic constant

N654 -6.271507e+10 Pa Nonlinear elastic constant

N655 0.000000e+00 Pa Nonlinear elastic constant

N656 0.000000e+00 Pa Nonlinear elastic constant

N661 -2.720211e+11 Pa Nonlinear elastic constant

N662 -2.358255e+11 Pa Nonlinear elastic constant

N663 -1.212661e+11 Pa Nonlinear elastic constant

N664 -9.103381e+09 Pa Nonlinear elastic constant

N665 0.000000e+00 Pa Nonlinear elastic constant

N666 0.000000e+00 Pa Nonlinear elastic constant

e011 -4.020000e-01 C/m^2 Piezoelectric stress constant

e012 4.328472e-01 C/m^2 Piezoelectric stress constant

e013 -3.084722e-02 C/m^2 Piezoelectric stress constant

e014 -6.171600e-02 C/m^2 Piezoelectric stress constant

e015 0.000000e+00 C/m^2 Piezoelectric stress constant

e016 0.000000e+00 C/m^2 Piezoelectric stress constant

e021 0.000000e+00 C/m^2 Piezoelectric stress constant

e022 0.000000e+00 C/m^2 Piezoelectric stress constant

e023 0.000000e+00 C/m^2 Piezoelectric stress constant

e024 0.000000e+00 C/m^2 Piezoelectric stress constant

e025 -2.587002e-01 C/m^2 Piezoelectric stress constant

e026 2.868193e-01 C/m^2 Piezoelectric stress constant

e031 0.000000e+00 C/m^2 Piezoelectric stress constant

e032 0.000000e+00 C/m^2 Piezoelectric stress constant

e033 0.000000e+00 C/m^2 Piezoelectric stress constant

e034 0.000000e+00 C/m^2 Piezoelectric stress constant

e035 1.151807e-01 C/m^2 Piezoelectric stress constant

e036 -1.277002e-01 C/m^2 Piezoelectric stress constant

ea11 3.290000e-04 C/(m^2.K) 1st temperature coefficient of e0

ea12 -5.287275e-04 C/(m^2.K) 1st temperature coefficient of e0

ea13 1.997275e-04 C/(m^2.K) 1st temperature coefficient of e0

ea14 -1.065953e-04 C/(m^2.K) 1st temperature coefficient of e0

ea15 0.000000e+00 C/(m^2.K) 1st temperature coefficient of e0

ea16 0.000000e+00 C/(m^2.K) 1st temperature coefficient of e0

ea21 0.000000e+00 C/(m^2.K) 1st temperature coefficient of e0

ea22 0.000000e+00 C/(m^2.K) 1st temperature coefficient of e0

ea23 0.000000e+00 C/(m^2.K) 1st temperature coefficient of e0

ea24 0.000000e+00 C/(m^2.K) 1st temperature coefficient of e0

ea25 4.076687e-04 C/(m^2.K) 1st temperature coefficient of e0

ea26 -1.474942e-04 C/(m^2.K) 1st temperature coefficient of e0

ea31 0.000000e+00 C/(m^2.K) 1st temperature coefficient of e0

ea32 0.000000e+00 C/(m^2.K) 1st temperature coefficient of e0

ea33 0.000000e+00 C/(m^2.K) 1st temperature coefficient of e0

ea34 0.000000e+00 C/(m^2.K) 1st temperature coefficient of e0

ea35 -1.815058e-04 C/(m^2.K) 1st temperature coefficient of e0

ea36 6.566866e-05 C/(m^2.K) 1st temperature coefficient of e0

eb11 1.990000e-07 C/(m^2.K^2) 2nd temperature coefficient of e0

eb12 1.533494e-06 C/(m^2.K^2) 2nd temperature coefficient of e0

eb13 -1.732494e-06 C/(m^2.K^2) 2nd temperature coefficient of e0

eb14 1.604245e-06 C/(m^2.K^2) 2nd temperature coefficient of e0

eb15 0.000000e+00 C/(m^2.K^2) 2nd temperature coefficient of e0

eb16 0.000000e+00 C/(m^2.K^2) 2nd temperature coefficient of e0

eb21 0.000000e+00 C/(m^2.K^2) 2nd temperature coefficient of e0

eb22 0.000000e+00 C/(m^2.K^2) 2nd temperature coefficient of e0

eb23 0.000000e+00 C/(m^2.K^2) 2nd temperature coefficient of e0

eb24 0.000000e+00 C/(m^2.K^2) 2nd temperature coefficient of e0

eb25 -1.834708e-06 C/(m^2.K^2) 2nd temperature coefficient of e0

eb26 -1.015865e-06 C/(m^2.K^2) 2nd temperature coefficient of e0

eb31 0.000000e+00 C/(m^2.K^2) 2nd temperature coefficient of e0

eb32 0.000000e+00 C/(m^2.K^2) 2nd temperature coefficient of e0

eb33 0.000000e+00 C/(m^2.K^2) 2nd temperature coefficient of e0

eb34 0.000000e+00 C/(m^2.K^2) 2nd temperature coefficient of e0

eb35 8.168646e-07 C/(m^2.K^2) 2nd temperature coefficient of e0

eb36 4.522921e-07 C/(m^2.K^2) 2nd temperature coefficient of e0

ec11 1.955179e-12 C/(m^2.K^3) 3rdd temperature coefficient of e0

ec12 -5.118842e-12 C/(m^2.K^3) 3rdd temperature coefficient of e0

ec13 3.163663e-12 C/(m^2.K^3) 3rdd temperature coefficient of e0

ec14 -2.413324e-12 C/(m^2.K^3) 3rdd temperature coefficient of e0

ec15 0.000000e+00 C/(m^2.K^3) 3rdd temperature coefficient of e0

ec16 0.000000e+00 C/(m^2.K^3) 3rdd temperature coefficient of e0

ec21 0.000000e+00 C/(m^2.K^3) 3rdd temperature coefficient of e0

ec22 0.000000e+00 C/(m^2.K^3) 3rdd temperature coefficient of e0

ec23 0.000000e+00 C/(m^2.K^3) 3rdd temperature coefficient of e0

ec24 0.000000e+00 C/(m^2.K^3) 3rdd temperature coefficient of e0

ec25 4.642588e-12 C/(m^2.K^3) 3rdd temperature coefficient of e0

ec26 1.118344e-13 C/(m^2.K^3) 3rdd temperature coefficient of e0

ec31 0.000000e+00 C/(m^2.K^3) 3rdd temperature coefficient of e0

ec32 0.000000e+00 C/(m^2.K^3) 3rdd temperature coefficient of e0

ec33 0.000000e+00 C/(m^2.K^3) 3rdd temperature coefficient of e0

ec34 0.000000e+00 C/(m^2.K^3) 3rdd temperature coefficient of e0

ec35 -2.067013e-12 C/(m^2.K^3) 3rdd temperature coefficient of e0

ec36 -4.979188e-14 C/(m^2.K^3) 3rdd temperature coefficient of e0

eps011 1.962000e+01 F/m Dielectric permittivity

eps012 0.000000e+00 F/m Dielectric permittivity

eps013 0.000000e+00 F/m Dielectric permittivity

eps022 2.454830e+01 F/m Dielectric permittivity

eps023 1.106914e+01 F/m Dielectric permittivity

eps033 4.448170e+01 F/m Dielectric permittivity

epsa11 3.229000e-04 F/(m.K) 1st temperature coefficient of eps0

epsa12 0.000000e+00 F/(m.K) 1st temperature coefficient of eps0

epsa13 0.000000e+00 F/(m.K) 1st temperature coefficient of eps0

epsa22 1.475558e-04 F/(m.K) 1st temperature coefficient of eps0

epsa23 -3.938296e-04 F/(m.K) 1st temperature coefficient of eps0

epsa33 -5.616558e-04 F/(m.K) 1st temperature coefficient of eps0

epsb11 -1.073000e-06 F/(m.K^2) 2nd temperature coefficient of eps0

epsb12 0.000000e+00 F/(m.K^2) 2nd temperature coefficient of eps0

epsb13 0.000000e+00 F/(m.K^2) 2nd temperature coefficient of eps0

epsb22 -8.055086e-07 F/(m.K^2) 2nd temperature coefficient of eps0

epsb23 6.007954e-07 F/(m.K^2) 2nd temperature coefficient of eps0

epsb33 2.764086e-07 F/(m.K^2) 2nd temperature coefficient of eps0

epsc11 0.000000e+00 F/(m.K^3) 3rd temperature coefficient of eps0

epsc12 0.000000e+00 F/(m.K^3) 3rd temperature coefficient of eps0

epsc13 0.000000e+00 F/(m.K^3) 3rd temperature coefficient of eps0

epsc22 0.000000e+00 F/(m.K^3) 3rd temperature coefficient of eps0

epsc23 0.000000e+00 F/(m.K^3) 3rd temperature coefficient of eps0

epsc33 0.000000e+00 F/(m.K^3) 3rd temperature coefficient of eps0

alfa11 5.630000e-06 1/K 1st thermal expansion coefficient

alfa12 0.000000e+00 1/K 1st thermal expansion coefficient

alfa13 0.000000e+00 1/K 1st thermal expansion coefficient

alfa22 5.455797e-06 1/K 1st thermal expansion coefficient

alfa23 -3.912658e-07 1/K 1st thermal expansion coefficient

alfa33 4.751203e-06 1/K 1st thermal expansion coefficient

alfb11 5.979000e-09 1/K^2 2nd thermal expansion coefficient

alfb12 0.000000e+00 1/K^2 2nd thermal expansion coefficient

alfb13 0.000000e+00 1/K^2 2nd thermal expansion coefficient

alfb22 5.595921e-09 1/K^2 2nd thermal expansion coefficient

alfb23 -4.536528e-10 1/K^2 2nd thermal expansion coefficient

alfb33 4.778979e-09 1/K^2 2nd thermal expansion coefficient

alfc11 0.000000e+00 1/K^3 3rd thermal expansion coefficient

alfc12 0.000000e+00 1/K^3 3rd thermal expansion coefficient

alfc13 0.000000e+00 1/K^3 3rd thermal expansion coefficient

alfc22 0.000000e+00 1/K^3 3rd thermal expansion coefficient

alfc23 0.000000e+00 1/K^3 3rd thermal expansion coefficient

alfc33 0.000000e+00 1/K^3 3rd thermal expansion coefficient

ang_freq_factor 2*pi

omega_radian omega_degree*pi/180

omega_degree 90

rho_langasite 5743

ext_damping 1.92e6/2